A SEARCH FOR EVIDENCE OF PHYSICS BEYOND THE STANDARD MODEL WITH NEW LIGHT BOSONS DECAYING INTO PAIRS OF MUONS AT $\sqrt{S} = 13$ TEV USING THE CMS DETECTOR

A Dissertation

by

SVEN DILDICK

Submitted to the Office of Graduate and Professional Studies of
Texas A&M University
in partial fulfillment of the requirements for the degree of

DOCTOR OF PHILOSOPHY

Chair of Committee,	Alexei Safonov
Co-Chair of Committee,	Dirk Ryckbosch
Committee Members,	Teruki Kamon
	Bhaskar Dutta
	Sherry Yennello
Head of Department,	Grigory Rogachev

August 2019

Major Subject: Physics

ABSTRACT

The standard model (SM) of particle physics is to date the most accurate description of fundamental particles and the interactions between them. While there are strong motivations for physics beyond the SM, experimental evidence has yet to be established. Searches for new light bosons can offer insight into the nature of the Higgs boson, dark matter and the possible existence of hidden sectors. New light bosons are introduced in many extensions of the SM, such as supersymmetry (SUSY) and models with hidden sectors. This dissertation presents a search for pair production of new light bosons, each of which decays into a pair of muons. Proton-proton collision data corresponding to an integrated luminosity of $35.9\ \mathrm{fb}^{-1}$ have been collected with the Compact Muon Solenoid detector at the CERN Large Hadron Collider at a center-of-mass energy of $\sqrt{s} = 13\ \mathrm{TeV}$. The search is uniquely sensitive to signatures with multimuon final states and is designed to be quasi model independent. The data are found to be consistent with the SM prediction. A model independent upper limit is set on the product of the production cross section, the branching fraction to dimuons squared and the acceptance as a function of the light boson mass. This limit varies between 0.15 and $0.39\ \mathrm{fb}$ over a light boson mass range from 0.25 to $8.5\ \mathrm{GeV}$. The limit is interpreted in the context of the next-to-minimal supersymmetric SM and a minimal SUSY model with a $U(1)_{\mathrm{D}}$ hidden sector that allows for nonnegligible light boson lifetimes. More stringent limits are set for both scenarios compared to earlier studies conducted on proton-proton collision data at $\sqrt{s} = 8\ \mathrm{TeV}$ by CMS.

DEDICATION

Deze thesis is opgedragen aan mijn vrouw Carolyn en mijn ouders Tania en Peter.

ACKNOWLEDGMENTS

This work would not have been possible without the support of many people inside and outside the CMS collaboration.

First of all I want to thank my thesis advisors Dr. Alexei Safonov and Dr. Dirk Ryckbosch for their support during my graduate studies and for immersing me in a learning environment with many interesting and challenging projects.

I would like to express my gratitude to Dr. Teruki Kamon and Dr. Bhaskar Dutta for the fruitful discussions in the final stages of my graduate studies and for providing many useful references.

I owe a debt of gratitude to Dr. Vadim Khotilovich and Dr. Vyacheslav Krutelyov whose technical expertise helped me perform the data analysis.

I am indebted to current and former CMS colleagues who contributed to this analysis: Dr. Aysen Tatarinov, Dr. Yuriy Pakhotin, Dr. Anthony Rose, Dr. Alfredo Castaneda, Dr. Luca Pernie, Dr. Paul Padley, Dr. Jamal Rorie, Dr. Benjamin Michlin and Wei Shi.

I thank my colleagues Dr. Jason Gilmore, Tao Huang and Ryan Mueller for their contribution to a positive working environment.

The computational aspects of this analysis could not be performed without the excellent work of IT managers from the various CMS data centers around the world. In particular, I would to thank Dr. David Toback, Katrina Colletti, Jorge Morales, Richard Lawrence and the managers of the Texas A& M University Brazos HPC cluster.

Finally, I would like to thank my wife Carolyn, my parents Tania and Peter, my family and friends for their unconditional love and support.

CONTRIBUTORS AND FUNDING SOURCES

Contributors

This work has been supervised by a dissertation committee consisting of Dr. Alexei Safonov (advisor) of the Department of Physics and Astronomy (TAMU), Dr. Dirk Ryckbosch (co-advisor) of the Department of Physics and Astronomy (Ghent University), Dr. Teruki Kamon and Dr. Bhaskar Dutta of the Department of Physics and Astronomy (TAMU), and Dr. Sherry Yennello of the Department of Chemistry (TAMU).

All work for the dissertation has been completed by the student, in collaboration with Dr. Alexei Safonov (TAMU), Dr. Teruki Kamon (TAMU), Dr. Paul Padley (Rice University), Dr. Alfredo Castaneda (University of Sonora), Dr. Luca Pernie (TAMU), Dr. Jamal Rorie (Rice University) and Wei Shi (Rice University).

Funding Sources

This work has been made possible in part by the US Department of Energy grant “High Energy Physics Program at Texas A&M University”.

NOMENCLATURE

CERN	European Centre for Nuclear Research
LHC	Large Hadron Collider
EW	Electroweak
SM	Standard Model of particle physics
BSM	Beyond the Standard Model of particle physics
SUSY	Supersymmetry
MSSM	Minimal Supersymmetric Standard Model
NMSSM	Next-to Minimal Supersymmetric Standard Model
CMS	Compact Muon Solenoid
IP	Interaction Point
CSC	Cathode Strip Chamber
RPC	Resistive Plate Chamber
DT	Drift Tube
ECAL	Electromagnetic Calorimeter
HCAL	Hadronic Calorimeter
L1T	L1 Trigger
HLT	High Level Trigger
MC	Monte Carlo
POG	Physics Object Group

TABLE OF CONTENTS

Page

LIST OF FIGURES

FIGURE Page

LIST OF TABLES

TABLE Page

1. INTRODUCTION

Particle physics is the science that studies the subatomic building blocks of the Universe and the interactions between them. The current understanding of subatomic interactions is contained within a theoretical framework called the *standard model* (SM) of particle physics [1–6]. Since it has been conceived in the 1960s and 1970s, precision measurements [7] have shown that the SM accurately describes phenomena at the smallest distance scales. Since the startup of the CERN Large Hadron Collider (LHC) [8] in 2010, experiments at the LHC have produced a wealth of new results, consistent with SM predictions.

However, there are strong arguments that support physics beyond the SM. Theoretical arguments such as the hierarchy problem and the unification of the fundamental forces, and astronomical and cosmological observations such as the large excess of matter over antimatter in the Universe suggest that new particles or new mechanisms must exist in nature. Extensions beyond the SM provide theoretical and phenomenological frameworks to search for new physics. Many extensions beyond the SM predict massive new light bosons to appear at the LHC. Some examples include supersymmetry (SUSY), string theory and models with hidden sectors. Because these bosons can couple to Higgs bosons, SUSY particles or hidden sector particles, research into new light bosons is a particularly interesting topic.

Searches for light bosons have been carried out since the 1980s at various experiments around the world [9–43] . Since the startup of the CERN LHC in 2010, searches have been carried out by CMS [44–54], ATLAS [55–64] and LHCb [65,66]. So far, no new light bosons have been observed experimentally.

This dissertation describes a search for a pair of new light bosons, each of which decaying into a pair of muons. The data analysis is designed to be (quasi) model independent. If a significant excess in the data is found, an observation of new physics can be claimed. In absence of an excess, a model-independent upper limit can be set on the product of the cross section, branching ratio and acceptance for light bosons decaying into pair of muons. The model-independent upper limit

can then be interpreted in the context of different benchmark models with light bosons decaying into pairs of muons. The benchmark models used in this analysis are the next-to minimal supersymmmetric standard model (NMSSM) [67] and an extension of SUSY with hidden $U(1)_{\mathrm{D}}$ sector (MSSMD) [68–70]. In the MSSMD scenario the light bosons can have a nonnegligible lifetime, resulting in displaced muons in the detector.

The search presented in this dissertation improves the previous search for a pair of light bosons decaying into muons by the CMS Collaboration [47]. The data have been collected with the CMS detector at $\sqrt{s} = 13\ \mathrm{TeV}$ during the 2016 data proton-proton (pp) collision run of the LHC and correspond to an integrated luminosity of $35.9\ \mathrm{fb}^{-1}$, compared to $20.7\ \mathrm{fb}^{-1}$ at $\sqrt{s} = 8\ \mathrm{TeV}$. Various upgrades have been made to the CMS detector, which are described in Ref. [71]. These upgrades include a new L1 trigger system, extra muon detection chambers in the endcap region of the detector, and improved electronics for the Cathode Strip Chamber detectors close to the interaction point. The data have been taken with a new high level trigger algorithm which has increased sensitivity to signatures with displaced muons. In addition, the selection criteria have been improved so that the search is more sensitive to NMSSM bosons (a_1) with a mass between 0.25 and $3.55\ \mathrm{GeV}$, and to MSSMD dark photons (γ_{D}) with a mass between 0.25 and $8.5\ \mathrm{GeV}$ and a lifetime between $c\tau_{\gamma_{\mathrm{D}}} = 0\ \mathrm{mm}$ and $100\ \mathrm{mm}$. These improvements enhance the detection sensitivity and model parameter space coverage.

This dissertation is organized as follows. Chapters 2 and 3 introduce the reader to the SM of particle physics and extensions thereof. The LHC and the CMS experiment are described in chapters 4 and 5. Chapter 6 discusses the offline reconstruction of real and Monte Carlo simulated data, with the emphasis on muon reconstruction. Finally, the search for light bosons decaying into pairs of muons is documented in chapter 7. Consecutively we describe the event selection, background estimation, treatment of the systematic uncertainties, results and interpretation in the context of NMSSM and MSSMD. Conclusions and outlook of this analysis are provided in chapter 8.

2. THE STANDARD MODEL OF PARTICLE PHYSICS

The standard model (SM) of particle physics [1–6, 72–74] is a theory that describes how subatomic particles interact with each other at the smallest distance scales. In the current framework of the SM, three of the four known interactions are included, namely electromagnetism, the strong nuclear interaction and the weak nuclear interaction. The fourth interaction - gravity - is not included since a renormalizable quantum version of gravity has yet to be developed. However, since gravity is much weaker than the other three interactions, gravitational effects are generally negligible.

Twelve matter particles exist in the standard model: six quarks and six leptons. Each of the matter particles also has a corresponding antimatter particle. The most familiar quarks are the *up* (u) and *down* (d) quark which make up the protons and neutrons in atomic nuclei. The most familiar lepton is the electron which combines with a proton to form a hydrogen atom. The four remaining quarks appear to be heavier *cousins* of the up and down quark, and are called *charm* (c), *strange* (s), *top* (t) and *bottom* (b). The five remaining leptons are two charged leptons, muon (μ) and tau (τ); and three neutral leptons, electron neutrino (ν_e), muon neutrino (ν_μ) and tau neutrino (ν_τ). Quarks and leptons are fermions carrying one half unit of quantum mechanical spin.

The quarks and leptons interact with each other by exchanging *gauge bosons*. The gauge bosons are a natural consequence of the requirement that the SM is invariant under transformations of the symmetry group $SU(3)_{\rm C} \times SU(2)_{\rm L} \times U(1)_{\rm Y}$. The gauge bosons for the strong, weak and electromagnetic interactions are the gluons, $W^{\pm}$ and Z bosons, and the photon (γ) respectively. In contrast to fermions, gauge bosons carry one unit of spin.

Quarks, leptons and gauge bosons are required to be massless in the SM. However, since most particles have a physical mass, particle mass must be generated with other means. In the SM, particle mass is generated dynamically through spontaneous symmetry breaking (SSB) [75, 76] in the electroweak part of the SM symmetry group, $SU(2)_{\rm L} \times U(1)_{\rm Y}$. SSB, also known as the Brout-Englert-Higgs mechanism, has been proposed in 1964 by Brout, Englert, Higgs, Guralnik, Hagen and Kibble [72–74]. The Higgs boson, that emerges after SSB, couples to fermions and

gauge bosons so they acquire physical mass.

The particles in the SM and their properties are given in Tab. 2.1. In the next sections we go deeper into the properties of these particles. We will pay particular attention to the Higgs boson and its importance in the SM. The last section of this chapter summarizes the status of the SM.

Table 2.1: Particles in the SM and their quantum numbers. Right-handed neutrinos are not taken into consideration.

	Spin	Color	Weak isospin		Hypercharge	Charge
	J	C	T	T_3	Y	Q
Higgs boson						
h	0	$-$	$1/2$	$-1/2$	1	0
Quarks						
$\begin{pmatrix} u \\ d' \end{pmatrix}_L$	$1/2$	$r/g/b$	$1/2$	$1/2$	$1/3$	$2/3$
$\begin{pmatrix} c \\ s' \end{pmatrix}_L$	$1/2$		$1/2$	$-1/2$	$1/3$	$-1/3$
$\begin{pmatrix} t \\ b' \end{pmatrix}_L$	$1/2$		$1/2$	$-1/2$	$1/3$	$-1/3$
u_R	$1/2$	$r/g/b$	0	0	$4/3$	$2/3$
c_R	$1/2$		0	0	$4/3$	$2/3$
t_R	$1/2$		0	0	$4/3$	$2/3$
d_R	$1/2$	$r/g/b$	0	0	$-2/3$	$-1/3$
s_R	$1/2$		0	0	$-2/3$	$-1/3$
b_R	$1/2$		0	0	$-2/3$	$-1/3$
Leptons						
$\begin{pmatrix} \nu_e \\ e \end{pmatrix}_L$	$1/2$	$-$	$1/2$	$1/2$	-1	0
$\begin{pmatrix} \nu_\mu \\ \mu \end{pmatrix}_L$	$1/2$		$1/2$	$-1/2$	-1	-1
$\begin{pmatrix} \nu_\tau \\ \tau \end{pmatrix}_L$	$1/2$		$1/2$	$-1/2$	-1	-1
e_R	$1/2$	$-$	0	0	-2	-1
μ_R	$1/2$		0	0	-2	-1
τ_R	$1/2$		0	0	-2	-1
Gauge bosons						
8 Gluons (g)	1	$r/g/b$	0	0	0	0
W^+	1	$-$	1	1	0	1
W^-	1	$-$	1	-1	0	-1
Z	1	$-$	1	0	0	0
Photon γ	1	$-$	0	0	0	0

2.1 Particles in the SM

2.1.1 Quarks and Leptons

Quarks and antiquarks do not appear singly in nature. Instead, they form combinations called hadrons. The most familiar hadrons are the proton (uud) and the neutron (udd). Many more hadrons exist in nature. However, most have a very short lifetime and decay almost instantly. A unique feature of quarks is that they carry a fractional unit of electromagnetic charge as shown

in Tab. 2.1. They also carry strong charge (color) and weak charge. Unlike quarks, leptons do not interact strongly. In addition, the neutral leptons (neutrinos) only interact weakly. Neutrinos are considered massless in the SM. However, the observation of neutrino oscillation demands that neutrinos have a nonzero mass [77]. Massive neutrinos are described in a minimal extension of the SM through the Pontecorvo-Maki-Nakagawa-Sakata matrix [78, 79].

2.1.2 Gauge bosons

Gluons are the gauge bosons of strong interaction. They bind together with up and down quarks to form protons and neutrons. Gluons appear naturally in the theory by requiring that the SM is invariant under transformations of the $SU(3)_{\mathrm{C}}$ symmetry group. A direct consequence is that gluons also couple to other gluons, so they interact among themselves. That coupling becomes asymptotically weaker as the distance scale decreases, allowing quarks to move quasi-free inside hadrons.

The $W^{\pm}$ and Z bosons are exchanged in weak interactions. An example of such interaction is the beta decay of the neutron, $n \rightarrow p + e + \bar{\nu}_e$, where $\bar{\nu}_e$ denotes an electron antineutrino. The $W^{\pm}$ and Z are very heavy compared to up and down quark, with masses $m_W = 80.379 \pm 0.012\ \mathrm{GeV}$ and $m_Z = 91.1876 \pm 0.0021\ \mathrm{GeV}$ [7]. Like gluons, the weak bosons self-interact - due to invariance of the SM under $SU(2)_{\mathrm{L}}$ transformations. However, unlike gluons, weak bosons only couple to left-handed helicity quarks and leptons.

The massless photon is the gauge boson of the electromagnetic interaction. Protons and electrons exchange photons to form hydrogen atoms. In contrast to gluons and weak bosons, photons do not self-interact. This is due to the invariance of the SM under $U(1)_{\mathrm{EM}}$ transformations.

2.1.3 The Higgs Boson

The Higgs boson is the particle in the SM that generates mass for the quarks, leptons and weak bosons. The Brout-Englert-Higgs mechanism [72–74] has been proposed in 1964 and applied in 1967 by Weinberg and Salam [2, 3] to the electroweak theory which had been developed six years earlier in 1961 by Glashow [1]. The electroweak theory provides a unified description of weak

bosons and the photon using the $SU(2)_{\mathrm{L}} \times U(1)_{\mathrm{Y}}$ symmetry group. The symbol Y denotes the *hypercharge* given by the expression $Y = 2(Q - T_3)$, with Q the EM charge and T_3 the third component of the weak isospin. The electroweak theory experiences problems at high energy without a Higgs boson. An example is the process $W^+W^- \to W^+W^-$. Its scattering amplitude violates unitarity at $\sqrt{s} \sim 1$ TeV, i.e. the probability of this process becomes greater than unity. The Feynman diagrams in Fig. 2.1 associated with the process $W^+W^- \to W^+W^-$ must be complemented by two additional diagrams in Fig. 2.2 so that the process amplitude does not diverge at high energy.

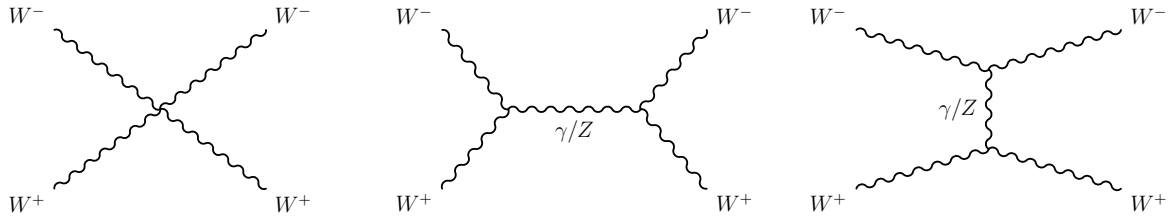

(a) W^+W^- scattering through a four-point interaction

(b) W^+W^- scattering through the s-channel

(c) W^+W^- scattering through the t-channel

Figure 2.1: Feynman diagrams for the process $W^+W^- \to W^+W^-$ in the electroweak theory.

(a) W^+W^- scattering through the s-channel with a Higgs boson

(b) W^+W^- scattering through the t-channel with a Higgs boson

Figure 2.2: Feynman diagrams for the process $W^+W^- \to W^+W^-$ with a Higgs boson.

The key ingredient of the Brout-Englert-Higgs mechanism is a doublet scalar field ϕ (the Higgs field) that couples to all other particles. The Higgs potential in the SM is of the form $V(\phi) =$

$\frac{1}{2}\mu^2\phi^\dagger\phi+\frac{1}{4}\lambda(\phi^\dagger\phi)^2$, with μ^2 the mass term and λ the self-interaction term. The potential is invariant under transformations of the electroweak symmetry group $SU(2)_{\mathrm{L}}\times U(1)_{\mathrm{Y}}$ when $\mu^2 > 0$. Without loss of generality, ϕ can be chosen to be $\frac{1}{\sqrt{2}}(0\ \ \nu)$. In case $\mu^2 > 0$, the minimum of the potential occurs at $\nu = 0$ and the symmetry is unbroken. However, when $\mu^2 < 0$ the Higgs potential dramatically changes shape so that the minimum now occurs at $\nu = \sqrt{-\frac{\mu^2}{\lambda}}$. The symmetry is now broken to $U(1)_{\mathrm{EM}}$. Figure 2.3 shows the Higgs potential after the symmetry breaking. After electroweak symmetry breaking the weak bosons acquire mass, whereas the photon remains massless.

In its current form the SM contains a single Higgs boson. In principle, no limit exists on the number of Higgs bosons. In fact, many beyond the SM extensions implement an extended Higgs sector, such as the two-Higgs doublet model [80] and supersymmetric theories [81].

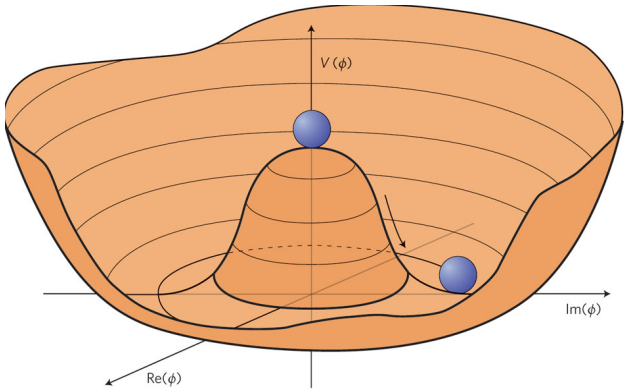

Figure 2.3: Quartic Higgs boson potential. Before EWSB, $\mu^2 > 0$, the potential has only a single minimum, at $\phi = 0$ which is invariant under $SU(2)_{\mathrm{L}} \times U(1)_{\mathrm{Y}}$ transformations. After EWSB, $\mu^2 < 0$, the Higgs potential has an infinite number of equivalent minima, which can be transformed into each other through $U(1)$ transformations. Reproduced from Ref. [82] with permission from the authors.

2.2 Intermezzo: The Standard Model Lagrangian

From a mathematical point of view the SM is a relativistic quantum field theory[1]. The behavior of particles and interactions is encoded in the Lagrangian (density) $\mathcal{L}_{\mathrm{SM}}$, a mathematical object, which is invariant under transformations of the gauge symmetry group $SU(3)_{\mathrm{C}} \times SU(2)_{\mathrm{L}} \times U(1)_{\mathrm{Y}}$ and the Poincaré group. Variation of the SM Lagrangian yields a set of Feynman rules that allow to derive measurable physical observables such as scattering cross sections and decay rates of particles. The Lagrangian has four components which describe (1) the dynamics of the gauge bosons, (2) the dynamics of the quarks and leptons, (3) the Higgs boson and SSB, and (4) how quarks and leptons acquire mass through the Higgs boson.

1. **The gauge term** contains the dynamic behavior of the spin-1 gauge bosons

$$\mathcal{L}_{\mathrm{Gauge}} = -\frac{1}{4} G^a_{\mu\nu} G^{\mu\nu}_a - \frac{1}{4} W^i_{\mu\nu} W^{\mu\nu}_i - \frac{1}{4} B_{\mu\nu} B^{\mu\nu}. \tag{2.1}$$

   In the expression above, $G^{\mu\nu}_a$ ($a = 1, \ldots, 8$), $W^{\mu\nu}_i$ ($i = 1, 2, 3$) and $B^{\mu\nu}$ are the field strength tensors associated with the symmetry groups $SU(3)_{\mathrm{C}}$, $SU(2)_{\mathrm{L}}$ and $U(1)_{\mathrm{Y}}$ before electroweak symmetry breaking. With each symmetry group corresponds a coupling g_i ($i = 1, 2, 3$): g_1 for $U(1)_{\mathrm{Y}}$, g_2 for $SU(2)_{\mathrm{L}}$ and g_3 for $SU(3)_{\mathrm{C}}$. The field strength tensors are defined as $G^a_{\mu\nu} = \partial_\mu G^a_\nu - \partial_\nu G^a_\mu - g_3 f_{abc} G^b_\mu G^c_\nu$, $W^i_{\mu\nu} = \partial_\mu W^i_\nu - \partial_\nu W^i_\mu - g_2 \varepsilon_{ijk} W^j_\mu W^k_\nu$, $B_{\mu\nu} = \partial_\mu B_\nu - \partial_\nu B_\mu$. As can be seen, G^μ_a and W^μ_i also couple to themselves through the structure constants f_{abc} and ε_{ijk}.

2. **The fermion term** encodes the spin-$\frac{1}{2}$ behavior of fermions and how they couple to the gauge bosons. The fermions are split up in left-handed doublets (Q^i_{L}, L^i_{L}) and right-handed singlets (u^i_{R}, d^i_{R}, e^i_{R}) with respect to the weak interaction: $\mathcal{L}_{\mathrm{Fermion}} = i\bar{Q}^i_{\mathrm{L}} \not{D} Q^i_{\mathrm{L}} + i\bar{u}^i_R \not{D} u^i_R + i\bar{d}^i_R \not{D} d^i_R + i\bar{L}^i_{\mathrm{L}} \not{D} L^i_{\mathrm{L}} + i\bar{e}^i_R \not{D} e^i_R$. The covariant derivative operator, $\not{D}$, contains the fermion-boson interactions:

$$\not{D} \equiv \not{\partial} + i g_3 \frac{\lambda^a}{2} \not{G}^a + i g_2 \frac{T^i}{2} \not{W}^i + i g_1 \frac{Y}{2} \not{B}. \tag{2.2}$$

[1] A thorough overview of the SM can be found in Ref. [83].

3. **The Higgs term** describes the spin-0 behavior of the Higgs boson and the Higgs potential $V(\phi) = \frac{1}{2}\mu^2\phi^\dagger\phi + \frac{1}{4}\lambda(\phi^\dagger\phi)^2$:

$$\mathcal{L}_{\text{Higgs}} = (D^\mu\phi)^\dagger(D_\mu\phi) - \frac{1}{2}\mu^2\phi^\dagger\phi - \frac{1}{4}\lambda(\phi^\dagger\phi)^2. \tag{2.3}$$

4. **The Yukawa term** connects the Higgs boson to the fermions and thus generates fermion mass $\mathcal{L}_{\text{Yukawa}} = -y_u^{ij}\bar{Q}_{\text{L}}^i\tilde{\phi}u_R^j - y_d^{ij}\bar{Q}_{\text{L}}^i\phi u_R^j - y_e^{ij}\bar{L}_{\text{L}}^i\phi e_R^j + h.c.$. The Yukawa couplings for the fermions are given by y_u^{ij}, y_d^{ij} and y_e^{ij}.

After electroweak symmetry breaking, the fields $W_{\mu\nu}^i$ and $B_{\mu\nu}$ transform into the weak boson fields $W_{\mu\nu}^+, W_{\mu\nu}^-, Z_{\mu\nu}$ and the photon field $A_{\mu\nu}$, and the fermion fields acquire mass through the Yukawa interaction.

2.3 Search for Higgs Boson and Discovery

Searches for the Higgs boson have started soon after the boson was postulated in 1964, and have accelerated after the discovery of the $W^\pm$ and Z boson by the UA1 and UA2 Collaborations at CERN. Searches for the Higgs boson have been carried out in the 1990s at the Large Electron Positron (LEP) Collider, at the Stanford Linear Collider and at the Tevatron. The combined results from indirect measurements at LEP have yielded a lower bound on the Higgs boson of $114.4\ \text{GeV}$ at 95% confidence level (CL) [84]. Searches at the Tevatron on the other hand have excluded the mass range $162 - 166\ \text{GeV}$ at 95% CL [85]. The upper limit on m_h has been improved to $152\ \text{GeV}$ from precision EW measurements [86].

The startup of the CERN LHC at $\sqrt{s} = 7\ \text{TeV}$ in the Spring of 2010 marked the beginning of a new era in particle physics. Searches for the Higgs boson by the ATLAS and CMS Collaborations have started following the first pp collisions. Data taking of pp collisions at $7\ \text{TeV}$ was continued in 2011. ATLAS and CMS each collected around $5\ \text{fb}^{-1}$. An additional $5\ \text{fb}^{-1}$ at $8\ \text{TeV}$ was collected in early 2012. The combination of the 2011 and 2012 datasets provided ATLAS and CMS with enough data to claim the discovery of the Higgs boson. On July 4, 2012, the ATLAS and CMS Collaborations made a joint announcement on the discovery of the long sought Higgs boson, which

is considered as one of the most important discoveries in fundamental physics [87,88]. A historical overview of the events leading up to the Higgs boson discovery can be found in Ref. [89]. The key Higgs boson discovery plots by CMS are shown in Fig. 2.4 [87]. Since its discovery, the Higgs boson decay has also been observed in $\tau^+\tau^-$ and $b\bar{b}$ final states.

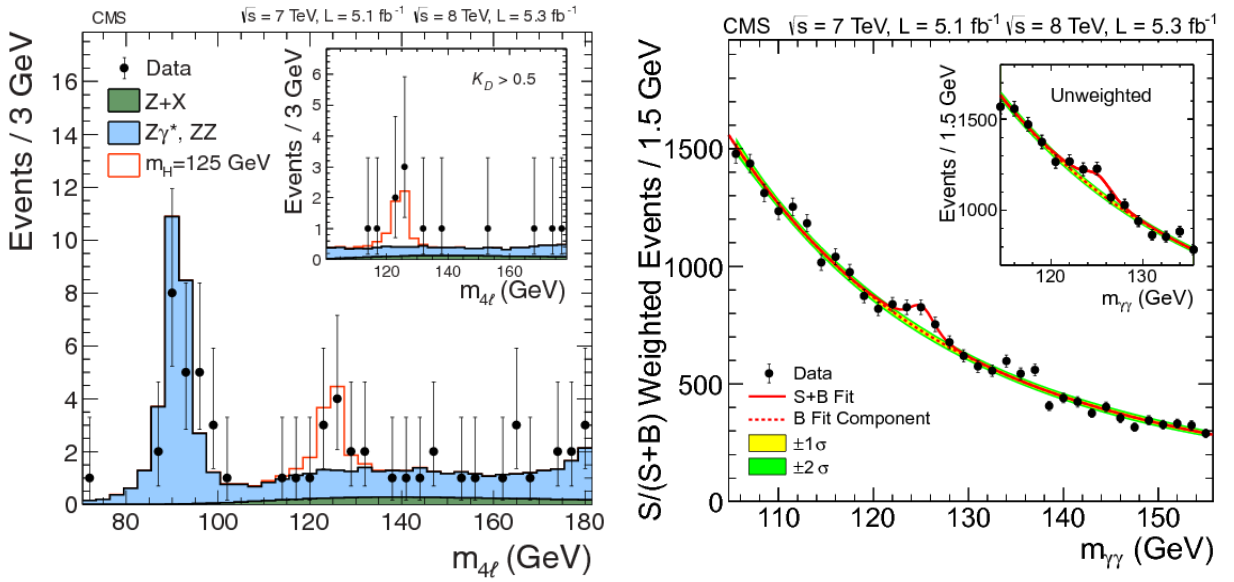

Figure 2.4: Higgs boson discovery plots by CMS. Left: distribution of the four-lepton reconstructed mass for the sum of the $4e$, 4μ, and $2e2\mu$ channels. Right: distribution of the diphoton invariant mass. Reproduced from Ref. [87]. Copyright 2012 CERN for the benefit of the CMS Collaboration.

2.4 Properties of the Higgs boson

The properties that determine the nature of the Higgs boson are its (1) mass, (2) spin-parity, (3) total decay width (the inverse of the particle lifetime), and (4) coupling strengths to fermions and gauge bosons. In this section we will briefly discuss the properties of the Higgs boson. Here, the Higgs boson may be denoted by either h or H.

The Higgs boson mass has been measured by the ATLAS and CMS Collaborations using different decay modes at 7, 8 and 13 TeV. The current world average is determined to be $m_h =$

125.18 ± 0.16 GeV [7]. Measurements of the spin and parity of the Higgs boson indicate that it is consistent with the $J^P = 0^+$ hypothesis, while all other spin-parity hypotheses are excluded above 97.8% [90]. The total decay width has been measured to be $\Gamma_h < 0.013$ GeV at 95% CL [7]. The coupling strengths have been measured to the level of $\sim 10\%$ and have been shown to be consistent with their SM expectations [91]. The measurements performed by the ATLAS and CMS Collaborations show that the observed particle is consistent with the SM Higgs boson hypothesis. However, decays of the Higgs boson to BSM particles are not entirely excluded. The beyond the SM (BSM) branching fraction of the Higgs boson, B_{BSM}, has been determined to be at most 34% at 95% CL by the ATLAS and CMS Collaborations using Run-1 data [91].

2.4.1 Production Mechanisms

Higgs bosons are produced through various mechanisms. At the LHC, the leading contributions are gluon-gluon fusion and vector boson fusion: 87 and 7% at $\sqrt{s} = 13$ TeV respectively. Smaller contributions come from associated Higgs boson production and top quark fusion. The dominant Feynman diagrams for each process are shown in Fig. 2.5. Figure 2.6a shows the Higgs boson production cross section for each channel versus Higgs boson mass at $\sqrt{s} = 13$ TeV.

2.4.2 Decay Modes

The SM Higgs boson couples to fermions and gauge bosons. The direct decays modes for 125 GeV Higgs boson are: $u\bar{u}$, $d\bar{d}$, $c\bar{c}$, $s\bar{s}$, $b\bar{b}$, e^+e^-, $\mu^+\mu^-$, $\tau^+\tau^-$, $W^{\pm}W^{\mp *}$ and ZZ^*. The Higgs boson can also indirectly decay into gg, $\gamma\gamma$ and $Z\gamma$ through virtual-particle loops. Rare Higgs decays, such as $\rho\gamma$, $\phi\gamma$ and $J/\psi\gamma$ allow to probe the coupling of the Higgs boson to light quarks. Decays into top quarks are kinematically forbidden since $m_h < m_t (\sim 173$ GeV). Decays into neutrinos are forbidden in the SM, but are allowed in certain BSM extensions, albeit with an negligible branching fraction. Figure 2.6b shows the branching fractions of various decay modes. In what follows we shall discuss these in more detail.

The most common decay mode of the 125 GeV Higgs boson is $h \to b\bar{b}$ with a branching ratio of $\approx 70\%$. Searches for Higgs bosons to b-quark pairs at the LHC are complicated by the large

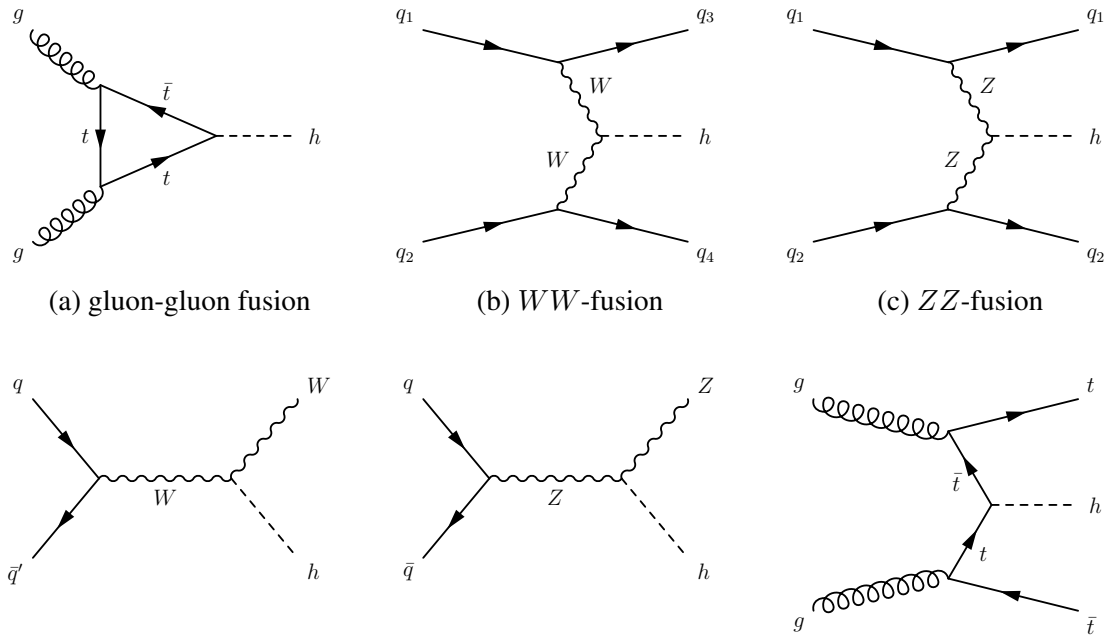

(a) gluon-gluon fusion (b) WW-fusion (c) ZZ-fusion

(d) Wh production (e) Zh production (f) top quark fusion

Figure 2.5: Feynman diagrams of Higgs production processes.

QCD multijet background. Additionally, the m_h resolution in b-quark pairs is poor which limits the handles to reduce the background. The next most common mode is $h \to W^{\pm}W^{\mp *}$ ($\approx 20\%$). Because the $W^{\pm}$ boson decay into hadrons in 68% of the cases, searches for $h \to W^{\pm}W^{\mp *}$ suffer from the same large QCD multijet background as $h \to b\bar{b}$ does. The signal over background ratio may be enhanced significantly in this channel by requiring one or more isolated leptons. The decay modes $h \to gg$ and $h \to c\bar{c}$ make up 9% and 3% respectively. However, the pure hadronic decay of the gluons and c quarks complicates searches in this channel at the LHC. The decay mode $h \to \tau^{+}\tau^{-}$ has a branching ratio of 6.3% for $m_h = 125$ GeV and has been recently discovered at the LHC. Decays into Z-boson pairs ($h \to ZZ^{*}$) are suppressed by a factor ten compared to W boson pairs. Searches using electrons and muons in the final state, $h \to ZZ^{*} \to 4e/4\mu/2e2\mu$, are especially interesting because of the excellent dilepton mass resolution in the ATLAS and CMS calorimeter and muon systems. Higgs boson decays into two photons are heavily suppressed compared to $h \to gg$ because of the small indirect coupling. Despite the small branching ratio

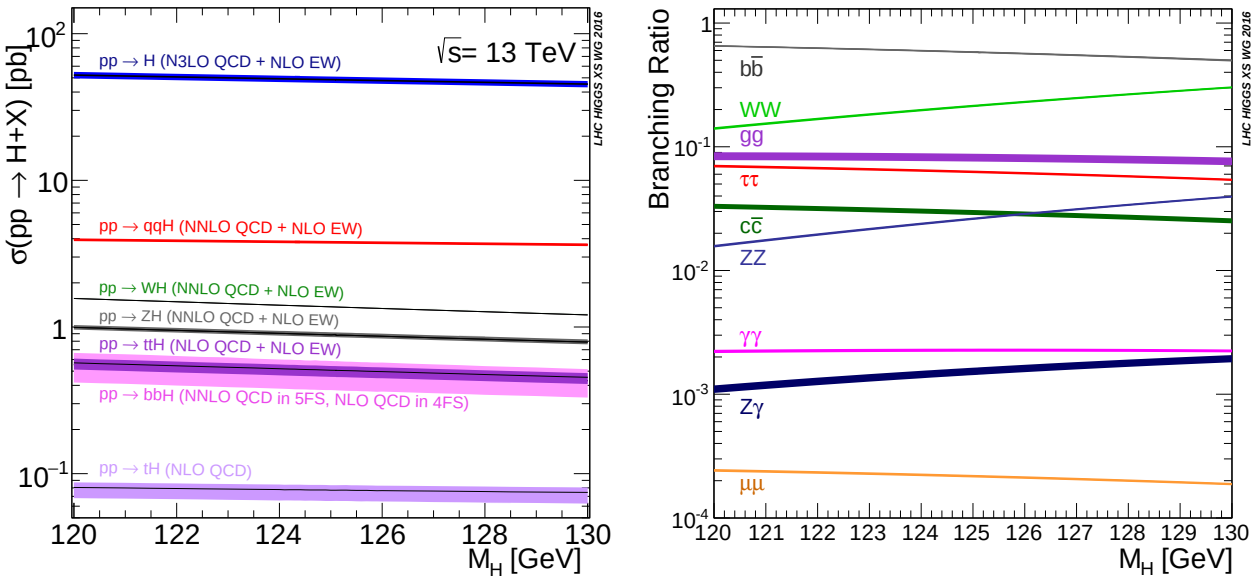

(a) (b)

Figure 2.6: Left: Cross sections for various Higgs boson production modes at $\sqrt{s} = 13$ TeV. Right: Higgs boson branching fraction to SM particles versus Higgs mass near 125 GeV. Branching fractions for Higgs decays into $u\bar{u}$, $d\bar{d}$, $s\bar{s}$, e^+e^- are too small to be shown. Decays into $t\bar{t}$ are also not shown because they are kinematically forbidden. Reproduced from Ref. [92]. Copyright 2017 CERN.

(0.2% at 125 GeV), the $h \to \gamma\gamma$ process is a discovery channel at the LHC due to the excellent diphoton mass resolution in the ATLAS and CMS calorimeter systems. The $h \to Z\gamma$ decay mode is similar to $h \to \gamma\gamma$, with a Z boson taking the place of one of the photons in the Feynman diagram. The most promising final state is $h \to Z\gamma \to \mu^+\mu^-\gamma$ which has a branching ratio of 5% of that of $h \to \gamma\gamma$, but should have a good m_h resolution. Finally, similarly to $h \to ZZ^* \to 4\mu$, Higgs boson decays into a pair of muons are expected to have an excellent mass resolution. However, because the branching ratio is only 2×10^{-4}, an observation of $h \to \mu^+\mu^-$ may require several thousand of fb^{-1} of LHC data.

2.5 Status of the SM

Precision measurements carried out at particle detectors around the world have consistently shown that the SM is an extremely accurate description of how particles interact at the subatomic

scale. Since the start of data taking in 2010, the ATLAS and CMS Collaboration have conducted hundreds of measurements at $\sqrt{s} = 7$, 8 and 13 TeV using pp and heavy ion collision data. A summary of the results obtained by CMS can be found in Ref. [93]. Figure 2.7 shows a summary of cross section measurements carried out by CMS at $\sqrt{s} = 7$ TeV (red), 8 TeV (blue) and 13 TeV (green) compared with the theoretical predictions.

Despite the successes of the SM, there is strong evidence that the SM does not provide a complete picture of physics at the quantum scale. As mentioned at the beginning of this chapter, the SM does not contain a quantum theory of gravity. Moreover, only 5% of the energy content of the Universe is described by the fermions and gauge bosons. The vast majority (95%) is made up of mysterious *dark energy* and *dark matter*. On top of that, the SM cannot account for the large excess of matter over antimatter in the Universe: $\approx 10^9$ to 1. Aside from these major problems, the SM also suffers from an unnatural amount of fine-tuning in the Higgs sector (hierarchy problem). Extensions beyond the SM attempt to address these problems in unique ways. Many models predict new particles to appear at the TeV energy scale, which is within reach of the CERN LHC.

2.6 Summary

In this chapter we have reviewed the basic ideas of the SM of particle physics. We have discussed the SM particles and their properties, the role of SSB and the Higgs boson, and have explained that the SM cannot be the ultimate theory of particle physics. The next chapter examines a few extensions beyond the SM and motivates a search for new physics.

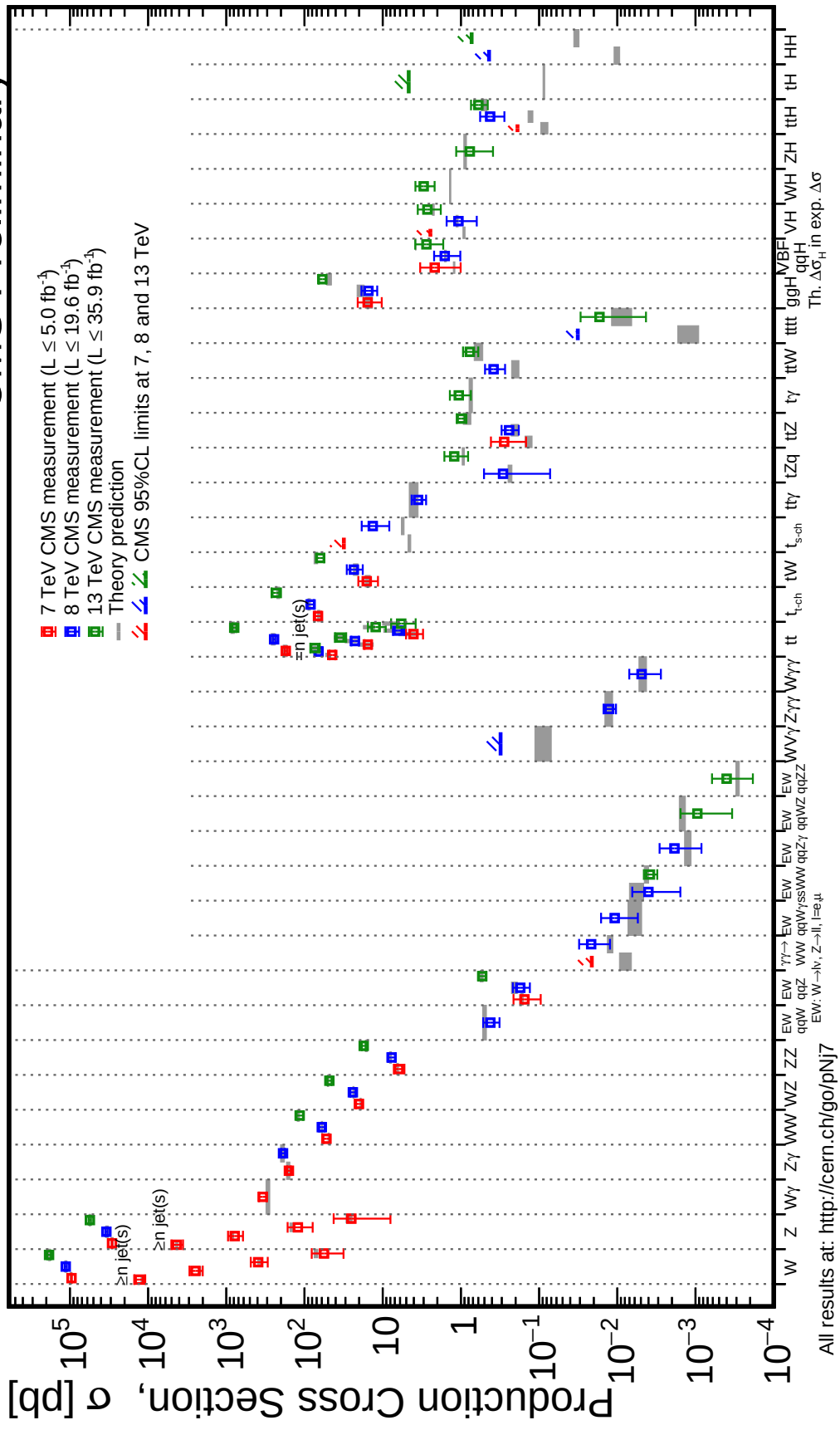

Figure 2.7: Summary of the cross section measurements of SM processes as measured by the CMS Collaboration at the LHC at center-of-mass energies $\sqrt{s} = 7, 8$ and $13\,\mathrm{TeV}$. Reproduced from Ref. [93]. Copyright 2018 CERN for the benefit of the CMS Collaboration.

3. PHYSICS BEYOND THE STANDARD MODEL

Measurements carried out during the last few decades at various high energy experiments around the world have shown that the SM is an accurate description of physics at the smallest distance scales. However, strong evidence indicates that the SM is not a complete theory. In this chapter we will review several models beyond the SM that attempt to address pressing problems. We will pay particular attention to models with extra scalar bosons. We end this chapter with a proposal to search for new light bosons in the context of two types of supersymmetric models.

3.1 Why Physics beyond the SM must exist

One of the critical problems is the energy content of the Universe. Astronomical observations indicate that the Universe contains less than 5% of its energy in the form of visible matter. The remaining 95% is made up of $\approx 70\%$ dark energy [94, 95] and $\approx 25\%$ dark matter which is not explained by the SM. Additionally, the SM cannot explain the matter-antimatter imbalance called baryon asymmetry. Charge-parity violating (CP-violation) effects of the weak interaction are too small to explain the large excess of matter over antimatter (10^9 to 1). Another key problem is the mass of the Higgs boson. The SM does not explain why the Higgs boson mass (≈ 125 GeV) is much smaller than the Planck mass ($\approx 10^{19}$ GeV), which is the natural cut-off scale for the SM. Quantum corrections to m_h^2 from fermion loops naturally inflate the Higgs boson mass, unless there is a large and unnatural amount of fine-tuning in the theory of the order of 10^{17}. This is also known as the *hierarchy problem*. Figure 3.1 shows the top quark loop as the leading contribution to m_h^2.

Furthermore, the SM does not provide a unified description of the strong and electroweak interaction. Because unification and SSB are such important concepts in the SM, a unified interaction is naturally expected at $\approx 10^{16}$ GeV (Grand Unified Theory scale). Such interaction may also include gravity at the Planck scale ($\approx 10^{19}$ GeV). However, these energy scales are far beyond the reach of the current technology. Finally, certain questions remain unanswered in the theory, such as the

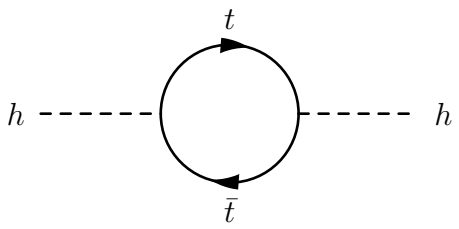

Figure 3.1: Top quark loop contribution to the Higgs mass squared.

origin of electric charge quantization, the number of fermion generations, and CP violation in the strong sector.

3.2 Extensions of the Standard Model

Many extensions of the SM of particle physics have been proposed to address the aforementioned problems with the SM. Generally, these extensions hypothesize the existence of additional symmetries, extra fundamental particles other than quarks and leptons or extra spatial dimensions. In this section we will have a brief look at a few general models - supersymmetry, string theory and hidden sector models - before turning to models with new light bosons.

3.2.1 Supersymmetric Models

Supersymmetry (SUSY) [81] attempts to address the problems in the SM by assigning a partner to each SM particle, a *superparticle*. Particles and their superparticles are combined in supermultiplets which share the same quantum numbers with respect to $SU(3)_{\rm C} \times SU(2)_{\rm L} \times U(1)_{\rm Y}$. The SUSY partners of quarks are *squarks* and of leptons are *sleptons*. The number of particles doubles also in the gauge sector and the Higgs sector. *Gluinos* are the SUSY partners of gluons, *winos* and *binos* are the SUSY partners of $W^{1,2,3}$ $(SU(2)_{\rm L})$ and B $(U(1)_{\rm Y})$ before EWSB, and *Higgsinos* are the superpartners of Higgs bosons. In the theory the winos, binos and Higgsinos mix among each other into a set of charged particles (*charginos*) and neutral particles (*neutralinos*).

Compelling arguments exist why doubling the particle spectrum is naturally interesting. First of all, SUSY particles provide negative contributions to m_h^2 through loop corrections, canceling the positive contributions due to SM particles. This solves the hierarchy problem. Secondly, many

SUSY models provide a cold dark matter candidate in the theory which could explain the 25% dark matter in the Universe. A third motivation comes from the converge of the SM couplings g_1, g_2 and g_3 at high energy, which naturally occurs in SUSY models. This suggests that the SM gauge group $SU(3)_{\mathrm{C}} \times SU(2)_{\mathrm{L}} \times U(1)_{\mathrm{Y}}$ may be unified into the larger $SU(5)$ or $SO(10)$ symmetry groups. Certain models also include gravity in a higher-dimensional supersymmetric space, called supergravity. Finally, some supersymmetric extensions introduce mechanisms that break baryon symmetry, thereby generating an excess of fermions over antifermions as is observed in the Universe. These arguments clearly motivate SUSY as a viable extension of the SM.

The smallest anomaly-free model is the Minimal Supersymmetric Standard Model (MSSM) which has a Higgs sector with two complex doublets. After electroweak symmetry breaking, five scalar bosons populate the Higgs sector: (1) two neutral CP-even states h^0, H^0, (2) one neutral CP-odd state A^0 and (3) two charged Higgs states H^+, H^-. However, The MSSM is not free from inconsistencies. A SUSY conserving parameter μ appears in the Higgs sector term $\mu H_u H_d$ of the MSSM superpotential which provides mass for the Higgsinos. The scale of μ is $\mathcal{O}(100)$ GeV, similar to the electroweak scale. The question why μ is much smaller than the natural SUSY cut-off scale $\mathcal{O}(10^{16})$ GeV is called the *μ-problem*. The Next-to-Minimal Supersymmetric SM (NMSSM) solves this problem by extending the theory with a singlet chiral supermultiplet S [67]. The modification in the Higgs sector ensures that the parameter μ remains at the EW scale. Moreover, it significantly reduces the number of parameters to be fine-tuned in the model. After EWSB, the Higgs sector consists of seven states: (1) three CP-even Higgs states $h_{1,2,3}$, (2) two CP-odd Higgs states $a_{1,2}$ and (3) two charged Higgs states H^+, H^-.

3.2.2 String Theory

String theory (see for example Ref. [96]) is a framework in theoretical physics that interprets particles in the SM as vibrating strings with a length of the order of the Plank length (10^{-33} m). String theory has been developed in the 1960s to reconcile the theory of general relativity with the principles of quantum mechanics. According to the theory, the properties of fundamental particles are determined by the harmonics of the oscillating strings. Moreover, interactions of fundamental

particles can be seen as a merging or splitting of strings. This is illustrated in Fig. 3.2.

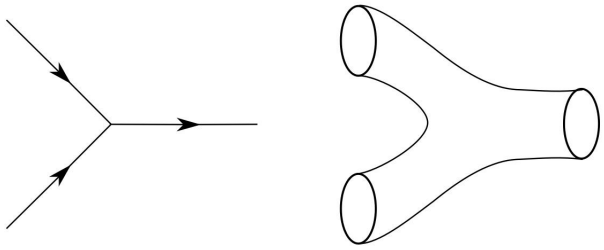

Figure 3.2: Two-particle interaction in quantum field theory (left) and string theory (right).

String theory has originally been developed purely for bosons (bosonic vibrations). The introduction to fermionic vibrations in addition to bosonic vibrations lead to supersymmetric string theories, or superstring theories. Superstring theory attempts to unify the four known forces in the Universe in a consistent quantum mechanical description. This includes a quantum description of gravity with spin-2 gravitons as gauge bosons. It has been shown that superstring theories require extra dimensions in addition to the $3 + 1$ space and time dimensions in nature to be mathematically consistent. A possible explanation why the extra dimensions are not observed is because they are compactified to extremely small dimensions. The known five variations of superstring theory (type-I, type-IIA, type-IIB, heterotic $SO(32)$ and heterotic $E_8 \times E_8$) in 10 spacetime dimensions have been shown to be limiting cases of a more general "M-theory" in 11 spacetime dimensions.

While superstring theory is an appealing solution for many of the problems in the SM, the framework currently has too many vacuum states for all practical purposes. The number of equivalent superstring solutions has been estimated to be around 10^{500}.

3.2.3 Hidden Sector Models

Certain extensions of the SM include sectors without SM gauge interactions at tree level. Such extensions are called *hidden sector*, *dark sector* or *hidden valley* models [97]. In the following we shall use both hidden sector and dark sector.

Quantum fields in hidden sectors do not transform under the SM gauge symmetry group $SU(3)_{\mathrm{C}} \times SU(2)_{\mathrm{L}} \times U(1)_{\mathrm{Y}}$. The corresponding hidden sector particles do not interact directly with SM particles. However, they can interact weakly through so-called *portals*. At least four possible portals have been identified, i.e. the vector portal [68–70], the axion portal [98], the neutrino portal [99] and the Higgs portal [100] (Fig. 3.3). For instance, in case of the vector portal model, kinetic mixing between SM photons and dark photons [101–103] allow dark photons to decay into SM fermions. In axion portals, SM photons mix with axions - hypothetical particles that have been postulated to solve the strong CP problem in QCD.

Figure 3.3: Interactions between the standard model and a hidden/dark sector can happen through mixing of SM particles and dark particles.

Hidden sectors are well motivated from cosmological and astrophysical observations, as well as from theoretical considerations:

- Certain analyses of the cosmic microwave background (CMB) and the large scale structure of the Universe indicate that, apart from the three known neutrino species, additional invisible particles are required to account for the total CMB radiation energy density [104]. Hidden sectors can provide such invisible particles in the form of dark photons for example.

- Models with hidden sectors could also explain the enhancement of the positron fraction in the primary cosmic ray flux seen by satellite experiments [105–108]. Dark matter particles could be annihilating to new light bosons which decay into into $e^{-}e^{+}$ pairs [109].

- In string theories, hidden sectors are required to compactify heterotic strings [110, 111].

- Finally, hidden sectors also naturally appear in Grand Unified Theories and SUSY models [112].

Models with hidden sectors suggest that heavy particles, such as the Higgs boson, could decay into hidden sector particles. Subsequently those hidden particles could decay (directly or through a cascade) to lighter SM or hidden particles.

3.2.4 Examples of Extensions with New Light Bosons

The theoretical frameworks mentioned earlier contain many models that predict the existence of new light bosons with a mass of a few GeV. In many SUSY models, light scalar bosons are present in extended Higgs sectors. In string theories dark photons appear naturally from large volume string compactifications [110, 113, 114]. M. Cicoli et al. (Ref. [113]) have suggested that searches for dark photons with a mass around $1\ \mathrm{GeV}$ can be conducted with collider detectors at the LHC and can provide insight into the existence of dark sectors (Fig. 3.4).

In this dissertation we will use two benchmark models in a search for new physics with light bosons decaying into pairs of muons. The first model is the NMSSM; the second is a MSSM with a $U(1)_{\mathrm{D}}$ dark sector [68–70], called hereafter called MSSMD.

- In the NMSSM, light scalar bosons a_1 appear from the necessity that the model is anomaly-free. The light bosons a_1 in the NMSSM model are short-lived, and they decay predominantly to light quarks and leptons when $m_{a_1} < m_h/2$. Decays of a_1 to pairs of opposite sign muons are favored when $2m_\mu < m_{a_1} < 2m_\tau$ (Fig. 3.5).

- MSSMD is a vector portal dark sector model where light vector bosons kinetically mix with SM photons. In the MSSMD, the dark vector boson field A^D_μ of $U(1)_{\mathrm{D}}$ and the hypercharge field B_μ of $U(1)_Y$ couple through a term in the Lagrangian $\mathcal{L}_{\text{gauge mix}} = \frac{1}{2}\varepsilon A^{\mu\nu}_{\mathrm{D}} B_{\mu\nu}$, with ε the kinetic mixing parameter. After EWSB, the dark vector bosons - called dark photons in this context - acquire a non-zero mass. Kinetic mixing with the SM photons allows them to

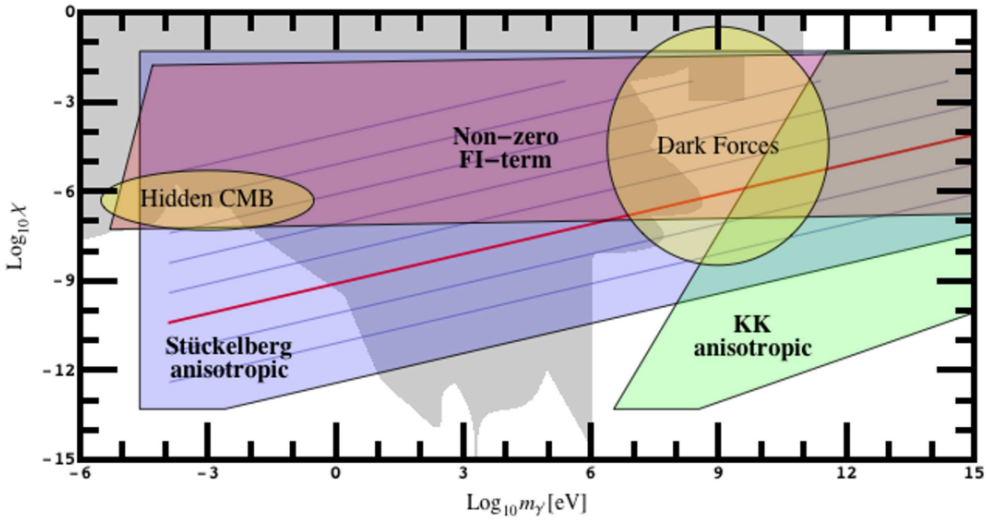

Figure 3.4: Predictions from anisotropic string compactifications in the 2D plane of kinetic mixing χ versus dark photon mass $m_{\gamma'}$. The areas shown in yellow are phenomenologically interesting in experimental searches. The range in kinetic mixing χ between 10^{-1} and 10^{-6}, and in dark photon mass $m_{\gamma'}$ between 10 MeV to 100 GeV is particularly interesting in the context of BSM models with dark sectors. Reproduced from Ref. [113] with permission from the authors.

decay into SM fermions. In particular, when ε is small, the dark photons can be long-lived, resulting in displaced fermionic final states.

In the case of NMSSM, pairs of muons are produced through the decay chain $h_{1,2} \to 2a_1 \to 4\mu$, with $h_{1,2}$ the lightest CP-even Higgs bosons, and a_1 the lightest CP-odd Higgs boson. In the case of MSSMD, dark photons $\gamma_{\rm D}$ decay into pairs of muons through $h \to 2n_1 \to 2n_{\rm D} + 2\gamma_{\rm D} \to 2n_{\rm D} + 4\mu$. Feynman diagrams of these processes are shown in Fig. 3.6 (left) and Fig. 3.6 (right) respectively.

3.3 Examples of Previous Searches for New Light Bosons

Searches for light bosons have been carried out since the 1980s at various experiments around the world. These include beam-dump experiments such as E774 [9]; E141 [10]; E137 [11]; SINDRUM [12]; WASA [13]; U70 [14]; KEK [15]; Orsay [16]; NOMAD and PS191 [17]; and CHARM [18], and fixed-target experiments such as APEX [19, 20] and A1 [21]. Limits on the dark boson mass and lifetime have been also obtained from precision measurements of the lep-

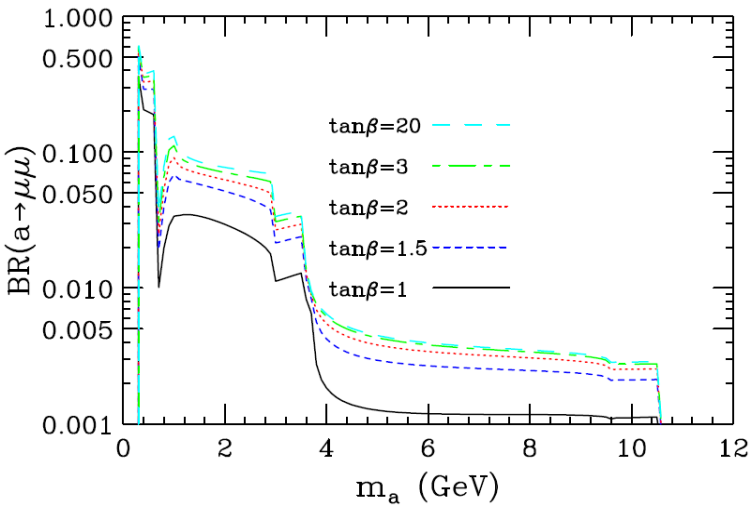

Figure 3.5: Branching ratio of $a \to \mu\mu$ as function of the light boson mass for several $\tan\beta$ values. Reproduced from Ref. [115] with permission from the authors.

ton anomalous magnetic moment [41–43] and from supernovae cooling [37–40]. Searches for light bosons in rare meson decay have been conducted at BaBar [32–36] at the Stanford Positron-Electron Project collider. Various studies have also been done at collider experiments such as HADES [22]; PHENIX [23] at the Relativistic Heavy Ion Collider; DØ [24] and CDF [24] at the Tevatron; CLEO [25] at the Cornell Electron Storage Ring; KLOE-II [26] at the DAPHNE collider; BESIII [27, 28] at the Beijing Electron-Positron Collider; and ALEPH, DELPHI, L3 and OPAL at the Large Electron Positron collider [29–31]. More recent results were published by CMS [44–54], ATLAS [55–64] and LHCb [65, 66] at the LHC. Many signatures have been investigated, including four-muon final states. An (incomplete) overview of previous searches for light bosons at the LHC is given in Tab. 3.1. A recent study by Abdullah et al. [116] suggests that dark photons can also be probed in coherent elastic neutrino-nucleus scattering. Finally, Bauer et al. [117] used experimental data from white dwarf cooling to apply new constraints on dark photons in various models.

3.4 Summary

In this chapter we have discussed the shortcomings of the SM. We have highlighted three extensions of the SM and how certain models address certain problems. We have paid particular

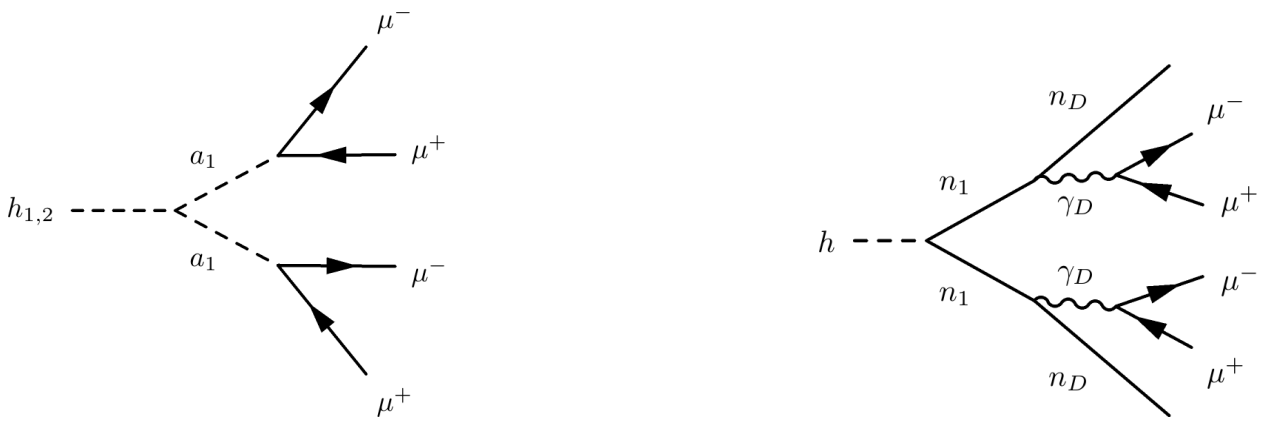

Figure 3.6: Left: Feynman diagram of the NMSSM process $h_{1,2} \to 2a_1 \to 4\mu$. Right: Feynman diagram of the MSSMD process $h \to 2n_1 \to 2n_{\mathrm{D}} + 2\gamma_{\mathrm{D}} \to 2n_{\mathrm{D}} + 4\mu$.

attention to the NMSSM and MSSMD as favorable extensions models with new light bosons. We will use these extensions as benchmark models in a search for new physics with light bosons decaying into muons. The next chapter discusses physics at the Large Hadron Collider.

Table 3.1: An (incomplete) overview of searches for new light bosons at the LHC. Most searches target direct decay of Higgs boson to light bosons, i.e. $h \to aa$.

Search	Experiment	$\sqrt{s}$ [TeV]	$\int \mathcal{L}$ [fb^{-1}]	Refs.
$pp \to a \to 4\mu$	ATLAS	7	0.036	[55]
$pp \to h \to aa \to 4\mu$	ATLAS	7	1.9	[56]
$pp \to h \to aa \to 4l/4\pi$	ATLAS	8	20.3	[57]
$pp \to h \to aa \to 4l$	ATLAS	13	3.4	[118]
$pp \to h \to aa \to 4l$	ATLAS	13	36.1	[58, 59]
$pp \to h \to aa \to 4b$	ATLAS	13	3.2	[60]
$pp \to h \to aa \to 4b$	ATLAS	13	36.1	[64]
$pp \to h \to aa \to 4\gamma$	ATLAS	7	4.9	[61]
$pp \to h \to aa \to 4\gamma$	ATLAS	8	20.3	[62]
$pp \to X \to aa \to 4\gamma$ [§]	ATLAS	13	36.7	[119]
$pp \to h \to aa \to 2\gamma$ 2jets	ATLAS	13	36.7	[63]
$pp \to a \to 2\mu$ [§]	CMS	7	1.3	[45]
$pp \to h \to aa \to 4\mu$	CMS	7	0.035	[44]
$pp \to h \to aa \to 4\mu$	CMS	7	5.3	[46]
$pp \to h \to aa \to 4\mu$	CMS	8	19.7	[47]
$pp \to h \to aa \to 4\mu$	CMS	13	2.8	[48]
$pp \to h \to aa \to 4\tau$	CMS	13	35.9	[49, 50]
$pp \to h \to aa \to 2b2\tau$	CMS	13	35.9	[51]
$pp \to h \to aa \to 2\tau 2\mu$	CMS	13	35.9	[52]
$pp \to h \to aa \to 2b2\mu$	CMS	8	19.7	[53]
$pp \to h \to aa \to 2b2\mu$	CMS	13	35.9	[120]
$pp \to h \to aa$ [¶]	CMS	8	19.7	[54]
$pp \to h \to aa$ [¶]	CMS	8, 13	$19.7 + 35.9$	[52]
$pp \to aa \to 4\mu$ [§]	LHCb	13	1.6	[65]
$pp \to h \to aa \to 6$ quarks	LHCb	7	0.62	[66]

[§]Search where the light boson is not produced in the decay of a Higgs boson.

[†]Includes final states $4c$, $4g$, 4τ, $2c2g$, $2g2\tau$ and $2c2\tau$.

[¶]Combined results from CMS including final states $2b2\tau$, 4τ, 4μ and $2\tau 2\mu$.

4. PHYSICS AT THE LARGE HADRON COLLIDER

In the previous chapters we have outlined the SM of particle physics and have distinguished several extensions beyond the SM. To make quantitative predictions about BSM physics hypotheses, precision scientific instruments are needed to study the interactions between fundamental particles. These fundamental particles may be produced in laboratory conditions or may have cosmic origins. The brute force approach to producing particles in a laboratory is by colliding two energetic particle beams head-on using accelerators. In particular, hadron synchrotrons can deliver the most energetic collisions. Currently, the CERN Large Hadron Collider (LHC) is the most powerful pp synchrotron in the world. Large detectors at the LHC register the pp collision fragments and reconstruct the collision events. The Compact Muon Solenoid (CMS) is such a state-of-the art detector at the LHC. Figure 4.1 shows a reconstruction of a pp collision at the CMS. In this and the following chapter we describe the main technologies and operating principles of the LHC and the CMS. Before we turn to the details of the LHC machine, we will have a brief look at the physics potential at the LHC.

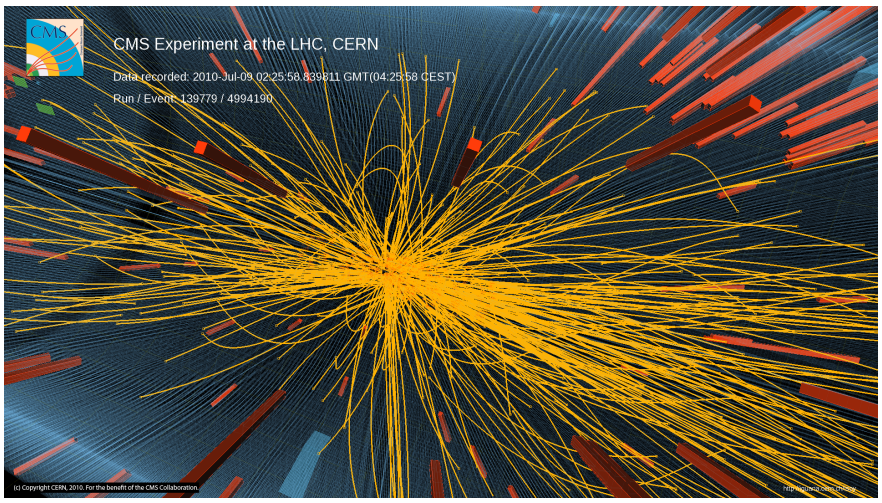

Figure 4.1: Reconstruction of an inelastic pp collision at CMS. Copyright 2010 CERN for the benefit of the CMS Collaboration.

4.1 Physics Potential at the LHC

The high luminosity and high center-of-mass energy of the LHC (see Sec. 4.4) allows to probe physics beyond the SM with direct searches and precision studies. One of the key points of interest is the properties of the Higgs boson, such as its coupling to second and third generation fermions and double Higgs boson production. Searches for BSM physics include models with extra W' and Z' bosons, supersymmetry, lepton flavor violation through $\tau \to 3\mu$ or $\tau \to \mu\gamma$, models with dark sectors etc. Analyses probing rare decays sensitive to BSM physics such as $B_s^0 \to \mu^+\mu^-$ can also be done at the LHC. Precision studies of heavy B-mesons - e.g. B_b, B_s and D - may find new sources of CP violation in nature to explain the matter-antimatter asymmetry. Finally, heavy ion runs at the LHC produce quark-gluon plasma what makes the study of QCD at extreme values of energy density possible.

4.2 What Happens when two Protons Collide Inelastically?

Protons are not point particles. Instead, they have a substructure that consists of quarks and gluons, which are commonly referred to as *partons*. These partons carry a fraction of the total proton energy. The number of partons in the proton increases rapidly with energy, so that ultra-relativistic protons at the LHC behave like diffuse clouds of partons. In inelastic pp collisions, the individual partons collide and produce other (fundamental) particles through strong and electroweak interactions. Figure 4.2 is a diagram showing the types of interactions that may occur during the collision.

The incoming protons are represented by three green lines and a green ellipse at the center of the diagram. The protons can radiate energy (*initial-state radiation*) even before the collision occurs, as shown by the blue straight and curly lines exiting the protons. Radiated partons can in turn radiate or hadronize, shown by the green arrows and green circles below the red circle. The most energetic partons collision is called the *hard-scatter* and is shown by the red circle. In this example, two gluons collide (red curly lines). The direct decay products are also part of the hard-scatter. Less energetic collisions happening at the same time form the *underlying event* (purple

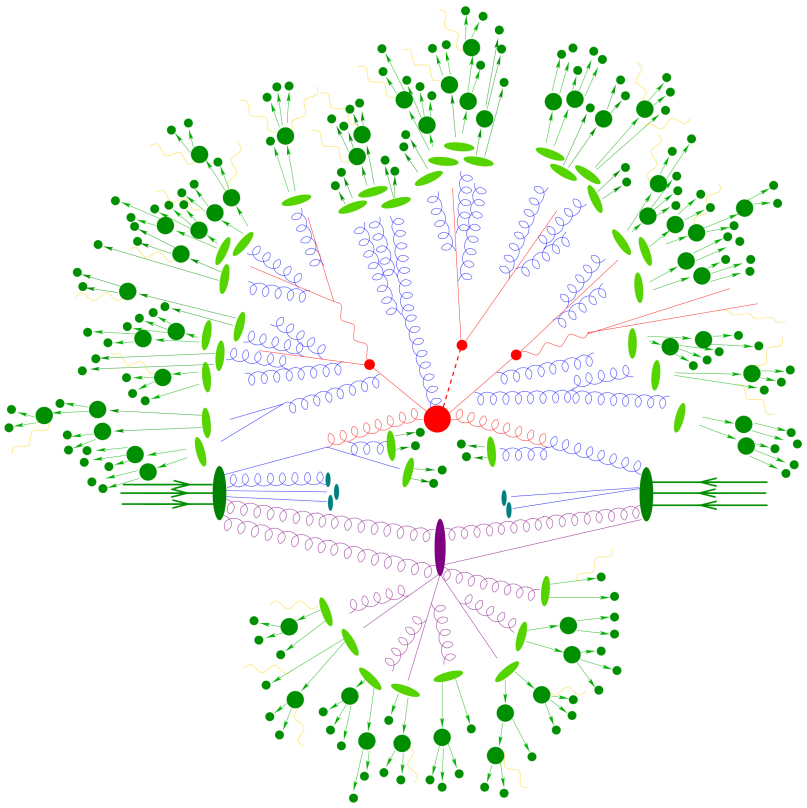

Figure 4.2: Diagram of a high-energy proton-proton collision. Two protons, shown by the dark green ellipses, collide head-on. In each proton, many partons can participate in the interaction. Copyright Frank Krauss. Reproduced with permission from the author.

curly and straight lines). The decay products of the hard-scatter can in turn radiate energy (*final-state radiation*) and can decay into other particles. This is shown by the curly and straight red lines leaving the diagram. Typical hadronic products in a pp collision are neutrons, pion and kaons. A cluster of hadrons ejected from the collision is also referred to as a hadronic jet. This is shown by the green arrows and circles on the outside of the diagram.

4.3 Simulating Proton-Proton Collisions

Testing new physics hypotheses or making precision measurements of SM observables at the LHC requires an accurate simulation of the previously mentioned processes in pp collisions. Because pp collisions are incredibly complicated, a computational approach is needed. The simulation of such processes is done with Monte Carlo (MC) event generators. Generally, not a single

MC event generator is equipped to accurately describe all aspects of a pp collision. In fact, a large number of generators have been developed for various experiments. While some have a very broad purpose, others are specific for a single type of particle. For example, MADGRAPH [121] and PYTHIA [122] are general-purpose MC generators, while TAUOLA [123] is specific for tau-lepton decays.

Simulating processes in pp collisions is more involved than for e^+e^- collisions, because the actual particles that collide at the LHC are the partons inside protons. The partons carry only a fraction of the total proton energy as mentioned before. The energy distribution for each type of parton is modeled with a Parton Distribution Function (PDF). These PDFs cannot be calculated using perturbative QCD, but are obtained from experimental measurements. MC event generators for pp collisions at the LHC rely on PDF sets, such as CTEQ [124] and NNPDF [125, 126].

4.4 The LHC Machine

The Large Hadron Collider (LHC) [8] is the largest particle accelerator in the world. The LHC produces pp or heavy-ion collisions at multi-TeV energies. It is located at CERN near Geneva, Switzerland, on the French-Swiss border. Figure 4.3 shows the CERN accelerator complex.

The LHC accelerates and collides hadrons in ultra-high vacuum tubes. Two counter-rotating hadron beams are kept on a circular trajectory using 1232 superconducting twin-bore dipole magnets operating at $8.33\ \mathrm{T}$. The LHC ring is actually not a perfect circle, but rather a polyhedron, divided into octants. Eight straight sections, each $528\ \mathrm{m}$ long, eight bending sections, and eight so-called points (P1,..., P8) make up the polyhedron. Four points, P1, P2, P5 and P8 are reserved for the experimental caverns of ATLAS, ALICE, CMS and LHCb respectively where the beams cross. P3 and P7 are operated as beam-cleaning points. The hadron beams are accelerated in radio-frequency accelerator cavities at P4. Finally, P6 is equipped with kicker magnets to dump the beam into a concrete block when the beam quality drops below a certain threshold and the remaining beam energy must be dissipated in a controlled manner.

The tunnel itself is located underground at a depth between 45 and $170\ \mathrm{m}$ and has a circumference of $26.7\ \mathrm{km}$. It has been constructed in the early 2000s after the decommissioning of the

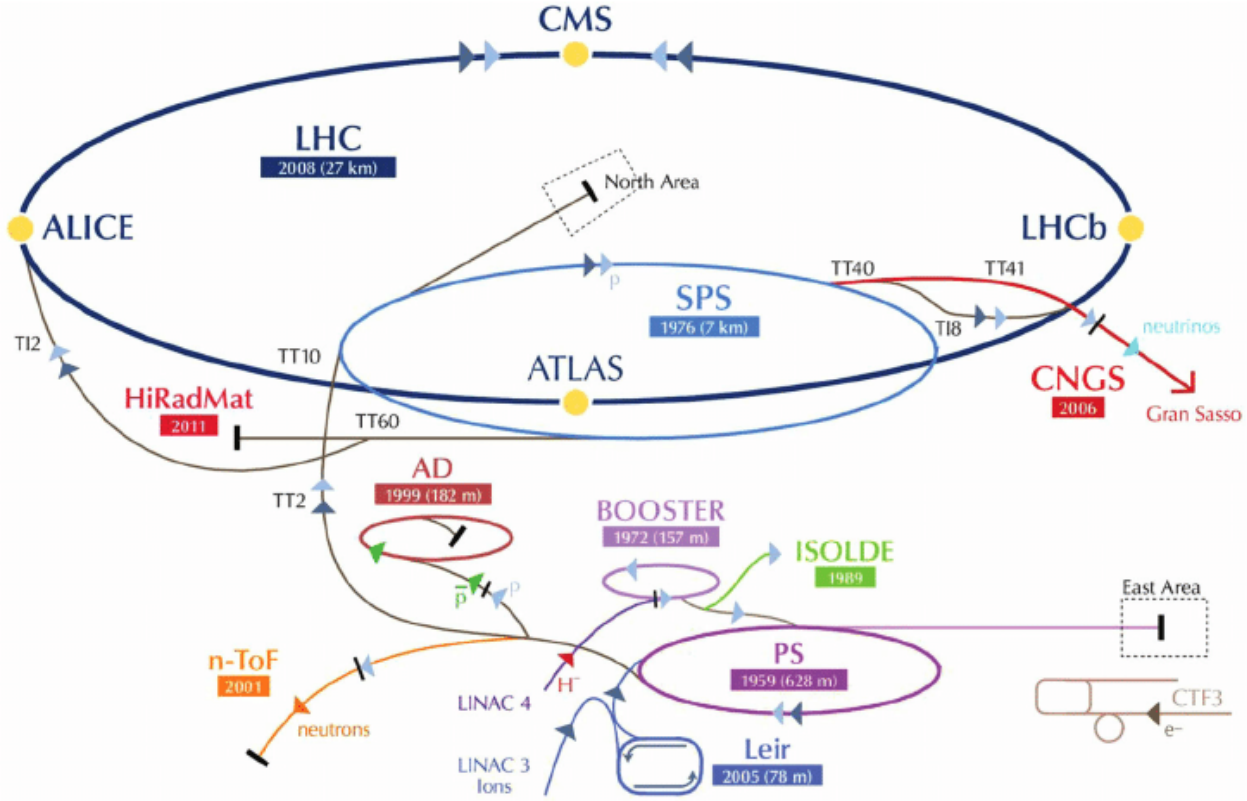

Figure 4.3: CERN accelerator complex showing the LHC, its pre-accelerators and various other accelerators and experiments. Copyright 2019 CERN. Reproduced with permission from CERN.

LEP collider in the same tunnel. Unlike LEP, the LHC has been designed for hadron collisions, in particular pp and heavy ions. Proton-proton collisions have been carried out at $\sqrt{s} = 7$, 8, and 13 TeV, and are planned at 14 TeV in the near future. Collisions with heavy ions have been carried out at a center-of-mass energy of $\sqrt{s_{NN}} = 2.76$ TeV. The design parameters for pp collisions, and the parameters used during data taking runs at $\sqrt{s} = 7$ TeV, 8 TeV and 13 TeV are shown in Tab. 4.1.

4.5 LHC Experiments

Four large LHC experiments are housed in points P1, P2, P5 and P8 along the beamline. These experiments are ATLAS [127], ALICE [128], CMS [129] and LHCb [130]. ATLAS (A Toroidal LHC ApparatuS) and CMS are general purpose detectors. The physics scope of the experiments is very broad and includes among others, the exploration of the EWSB mechanism, precision

Table 4.1: Design and operational LHC parameters for pp collisions.

Parameter	Design	7 TeV-Run	8 TeV-Run	13 TeV-Run
Beam energy [TeV]	7	3.5	4	6.5
Bunch crossing width [ns]	25	50	50	25/50
Peak luminosity [$10^{34}\mathrm{cm}^{-2}\mathrm{s}^{-1}$]	1	0.3	0.7	1.5
Average pileup	20	8	16	27

studies of the Higgs boson and searches for BSM physics. ALICE (A Large Ion Collider Experiment) has been designed to study the properties of the strong interaction at extremely high densities, i.e. quark-gluon plasma. LHCb (LHC-beauty) is an experiment designed for precision CP-violation measurements and searches for rare decays of neutral mesons. Two smaller experiments, TOTEM [131] and LHCf [132], are housed in the CMS and ATLAS caverns. TOTEM measures the total pp cross section, while LHCf studies the production of very forward hadrons.

4.6 Proton Accelerating Mechanism

The LHC is not a standalone hadron accelerator. Instead, several pre-accelerators gradually prepare the hadron beams for multi-TeV collisions. The proton accelerating mechanism is described next. The LEP electron-positron injection chain has been largely reused and optimized for protons. The first stage of the sequence is the extraction of the protons from hydrogen gas using an electric field. The protons are injected into the linear accelerator Linac-II where they are bunched to $25\ \mathrm{ns}$ bunch spacing and acquire an average energy of $50\ \mathrm{MeV}$. This is followed by the Proton Synchrotron Booster (PSB) and the Proton Synchrotron (PS) which ramp up the proton energy to $1.4\ \mathrm{GeV}$ and $25\ \mathrm{GeV}$ respectively. After the PS the protons are injected into the Super Proton Synchrotron (SPS). The SPS accelerates the proton bunches to $450\ \mathrm{GeV}$. Finally, the SPS injects the proton bunches into the LHC which accelerates them to $6.5\ \mathrm{TeV}$.

4.7 LHC Beam Luminosity

The task of the LHC is to deliver stable multi-TeV hadron beams with an intensity as high as possible for the ATLAS, ALICE, CMS and LHCb experiments. The beam intensity is character-

ized by the instantaneous luminosity $\mathcal{L}$ in accelerator physics. The instantaneous luminosity is a measure for the number of collisions per unit time. The instantaneous luminosity depends on a number of beam and magnet parameters and is given by the expression below:

$$\mathcal{L} = \frac{f N_{\mathrm{B}} N_p^2}{4\pi\sigma^2} R(\sigma_z, \theta) \tag{4.1}$$

Here, f is the beam revolution frequency, N_{B} the number of bunches per beam (2808 nominal) and N_p the number of protons per bunch (approximately 1.15×10^{11}). The design spacing between the bunches is 25 ns. Two geometric factors enter the equation: (1) the beamsize at the interaction point $\sigma^2 \approx 17\mu\mathrm{m} \times 2$ mm and (2) the geometrical luminosity loss factor $R(\sigma_z, \theta) \approx 0.8$ which depends on how the two beams cross.

The LHC design luminosity of 10^{34} $\mathrm{cm}^{-2}\mathrm{s}^{-1}$ has been surpassed during the 13 TeV run of 2016. In comparison with similar colliders, the Tevatron and LEP colliders operated at $\mathcal{L} = 3 - 4 \times 10^{32}$ $\mathrm{cm}^{-2}\mathrm{s}^{-1}$ and 10^{32} $\mathrm{cm}^{-2}\mathrm{s}^{-1}$ respectively.

The instantaneous luminosity of a particle collider is typically not fixed during data taking. Various processes such as (1) particle burn-off, (2) Coulomb intra-beam scattering, (3) synchrotron radiation and (4) beam-wall interactions cause the instantaneous luminosity to decrease over time.

From the instantaneous luminosity, one can calculate the number of times a particular physics process occurs during a certain data taking period. This is done by integrating the instantaneous luminosity over time and multiplying it with the cross section of the physics process:

$$N_{\mathrm{process}} = \sigma_{\mathrm{process}} \int \mathcal{L}\, dt. \tag{4.2}$$

Processes with a larger cross section are thus produced more frequently at the LHC.

4.8 LHC Performance during the 2016 Run

The LHC machine has performed excellently during the 2016 data taking run. The instantaneous luminosity has reached 1.5×10^{34} $\mathrm{cm}^{-2}\mathrm{s}^{-1}$. A total of 40.8 fb^{-1} *pp* collisions and 190 nb^{-1}

proton-lead collisions have been delivered to CMS. Figure 4.4 shows the cumulative luminosity for pp collisions delivered by the LHC to CMS during the data taking periods from 2010 to 2017. The LHC stable beam efficiency (58%) in 2016 nearly surpassed the maximum LEP stable beam efficiency (59% in 1994). These successes have been in part possible with the deployment of a new bunch-production scheme called Batch Compression Merging and Splitting during Summer 2016 which have delivered beams with a higher beam intensity [133].

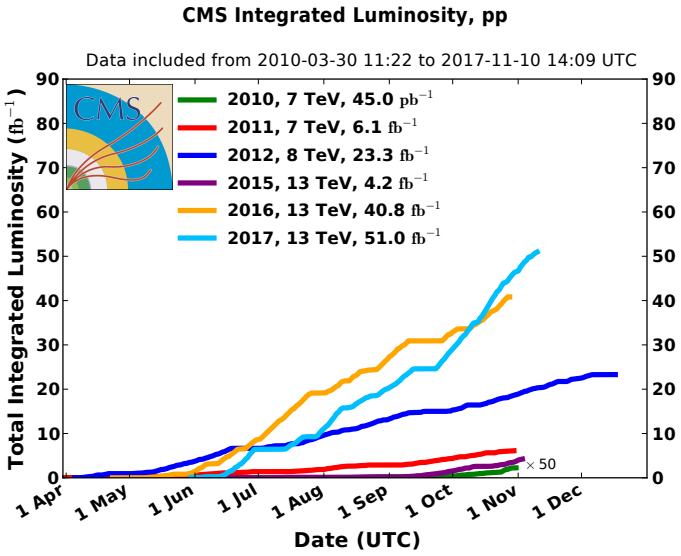

Figure 4.4: Cumulative luminosity delivered to CMS for pp collisions versus day during stable beams for data-taking periods between 2010 and 2017. Copyright 2017 CERN for the benefit of the CMS Collaboration.

4.9 Summary

In this chapter we have discussed in detail how the LHC delivers the pp collisions at $\sqrt{s} = 13$ TeV to the CMS detector. In the next chapter, we will examine how the detector registers and analyzes the collision fragments.

5. THE COMPACT MUON SOLENOID EXPERIMENT

The Compact Muon Solenoid (CMS) is one of the main scientific experiments associated with the CERN LHC. Over $4,000$ scientists and engineers from over 200 different institutes in 47 countries work on various aspects of CMS. The detector has been designed to support a vast experimental physics program which includes precision studies of electroweak processes, rare SM events and searches for BSM physics. In this chapter we will describe the CMS detector, distinguish the detector systems used in data taking, and highlight the computing tools used to analyze data.

5.1 What is the CMS Detector?

The CMS detector [129] is basically a huge digital camera that takes photos of particle collisions, 40 million times per second. The machine is an impressive feat of engineering that combines state-of-the-art technologies with a large detection volume. It has an overall length of $28.7\ \mathrm{m}$, a diameter of $15\ \mathrm{m}$, and weighs approximately $14,000$ metric tonnes.

The detector can be seen as an onion which covers almost 4π of the total solid angle around the beam interaction point. Each layer of the detector is constructed concentrically and registers specific types of particles. Figure 5.1 shows a quadrant of the Run-2 configuration with a detailed view of the subdetectors. The quadrant is mirror symmetric about the central plane and cylindrically symmetric around the z-axis. The cylindrical part is called the *barrel* and is closed by 2 *endcaps*, one on each end. The silicon tracker sits centrally and detects charged particles. It is composed of the pixel detector - close to the beamline - and the strip detector - further away. The electromagnetic calorimeter (ECAL) and hadronic calorimeter (HCAL) are installed outside the tracker volume and detect hadronic particles, such as the π^0 meson. The superconducting solenoid is the central component of the detector. It bends charged particles such that their momentum can be measured. The muon system is installed on the outside of CMS and combines three complementary muon detection technologies.

Systems for triggering, data acquisition and detector control are located outside the experi-

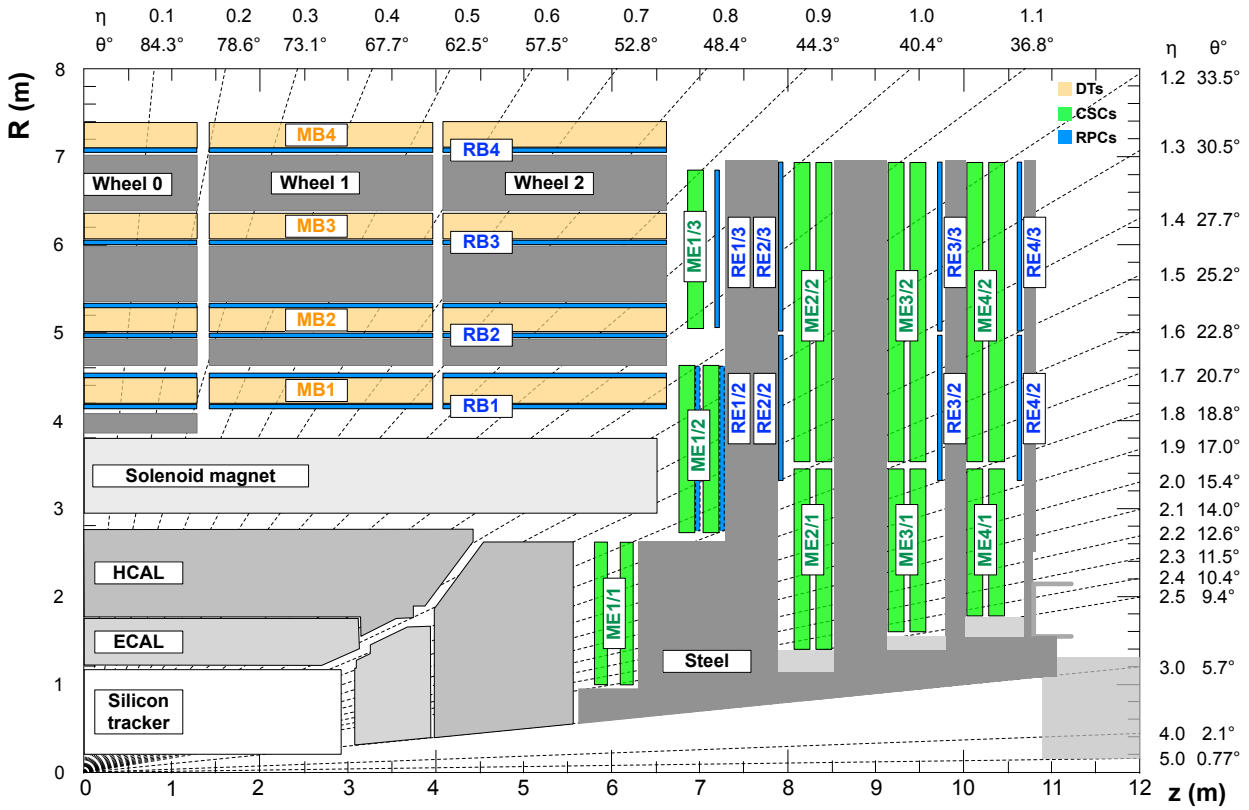

Figure 5.1: Quadrant of the CMS detector in the Run-2 configuration during the $2015 - 2016$ data taking period. The central component is the solenoid that surrounds the silicon tracker, the electromagnetic calorimeter (ECAL) and hadronic calorimeter (HCAL). Outside the solenoid sits the muon system. Drift tubes (DT), cathode strip chambers (CSC) and resistive plate chambers (RPC) are colored orange, green and blue respectively. Reproduced from Ref. [71]. Copyright 2018 CERN for the benefit of the CMS Collaboration.

mental cavern. Because of the large hadron collision rate, storing and analyzing each event is impractical. Instead, events are selected with a two-level trigger system, which filters events interesting to the physics program. The first step is a hardware-based level-one trigger (L1T) which reduces the event rate from 40 MHz to about 100 kHz. The second step is a software-based high level trigger (HLT) that further trim the event rate to 1 kHz.

The detector is designed such that each component can be accessed for inspection, repair or replacement. This feature is especially important because the experiment is expected to last several decades. During the course of its lifetime, many of its hardware components will have to be replaced due to the exposure to intense radiation. Others may need to be upgraded in order to

run more sophisticated particle reconstruction algorithms or to cope with the increasingly hostile radiation environment. For example, the silicon pixel detector has been replaced during the Year-End Technical Stop of $2016 - 2017$. The Phase-2 upgrade of CMS, foreseen in $2020 - 2023$, includes a complete overhaul of the L1T system.

The following sections discuss each system in more detail. Extensive information can be found in Ref. [129].

5.2 CMS Coordinate System

The CMS detector uses a right-handed Cartesian coordinate system $(O; x, y, z)$ (Fig. 5.2). The center, O, sits at the nominal collision point. The x-axis points to the center of the LHC ring. The y-axis runs vertically upward and the z-axis runs along the beamline in the anti-clockwise direction. A cylindrical coordinate system is defined on the same center, with the azimuth angle, ϕ, measured from the x-axis in the xy-plane. The radius r is the distance to the z-axis. The polar angle, θ, is measured from the positive z-axis in the rz-plane. For ultra-relativistic particles the pseudorapidity, $\eta = -\ln(\tan\theta/2)$, is used instead of θ. The energy of particles is given in terms of transverse momentum p_{T} or transverse energy E_{T}. The transverse momentum is the component of the momentum in the xy-plane, $p_{\mathrm{T}} = p\sin\theta$, and is typically used for charged particles. Particles detected by CMS are characterized by the triplet $(p_{\mathrm{T}}, \eta, \phi)$. The imbalance of energy in the xy-plane is called *missing transverse momentum* and denoted as $\not{E}_{\mathrm{T}}$. The distance between two points in the (η, ϕ) coordinate system is given by the $\Delta R(1,2) = \sqrt{(\eta_1 - \eta_2)^2 + (\phi_1 - \phi_2)^2}$. The displacement of a particle can be characterized in terms of its transverse displacement with respect to the beamline, L_{xy}, or the displacement with respect to the beamspot vector, Δ_{xy}. In terms of the beamspot $\vec{B}$, these quantities are defined as $\Delta_{xy} = -(v_x - B_x)\sin\phi + (v_y - B_y)\cos\phi = \left(-(v_x - B_x)p_{\mathrm{y}} + (v_y - B_y)p_{\mathrm{x}}\right)/p_{\mathrm{T}}$ and $L_{xy} = \sqrt{(v_x - B_x)^2 + (v_y - B_y)^2}$.

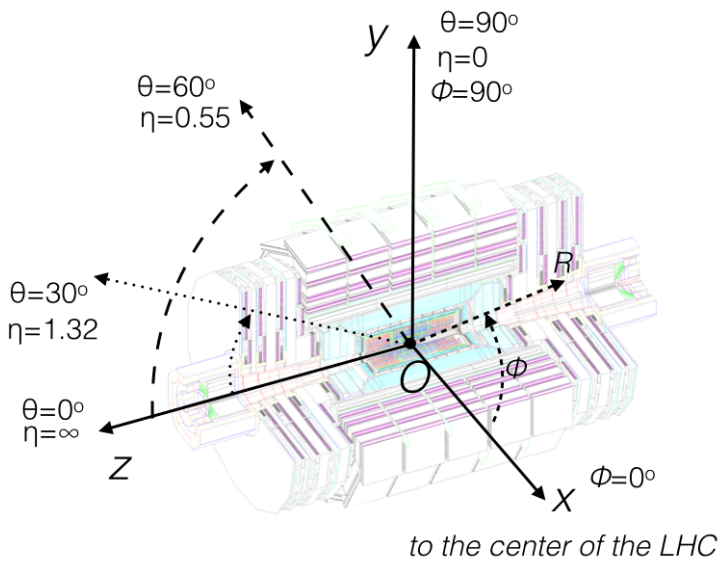

Figure 5.2: Coordinate system used by CMS. Figure adapted from [129]. Copyright 2008 CERN for the benefit of the CMS Collaboration.

5.3 Detector Systems

5.3.1 Silicon Tracker

The purpose of the silicon tracker is to reconstruct vertices (points in 4D Lorentz-space where particles interact) and tracks in the central part of CMS. It is composed of a pixel-based detector that reconstructs the primary and secondary vertices, and a strip-based detector that fits the trajectories of charged particles in the magnetic field. The tracker has a total length of 5.8 m and diameter of 2.5 m. The tracker is radiation hardened so that it can operate in the extreme environment close to the interaction point. The tracker has been provided with high-granularity components which allow to distinguish trajectories from different interactions in the same beam crossing. The original tracker has been designed without a trigger system, meaning that its information is not used in the L1T decision. It is however used in the full event reconstruction of charged particle trajectories.

The original pixel detector had with 3 barrel layers (with radii $R_{B1} = 4.0$-4.4 cm, $R_{B2} = 6.9$-7.3 cm and $R_{B3} = 9.8$-10.2 cm) and 2 endcap disks (at distances $z_{E1} = \pm 34.5$ cm and $z_{E2} = \pm 46.5$ cm) that covered ~ 1 m^2 active surface. This is shown in Fig. 5.3 (left). It took data from

2008 to 2016. The original pixel detector has been replaced during the Year-End Technical Stop of 2016-2017 by the Phase-1 pixel detector. It has 4 barrel layers and 3 endcap disks that cover an active surface of 2.7 m^2 [134]. Figure 5.3 (right) compares the position and size of the pixel barrel layers.

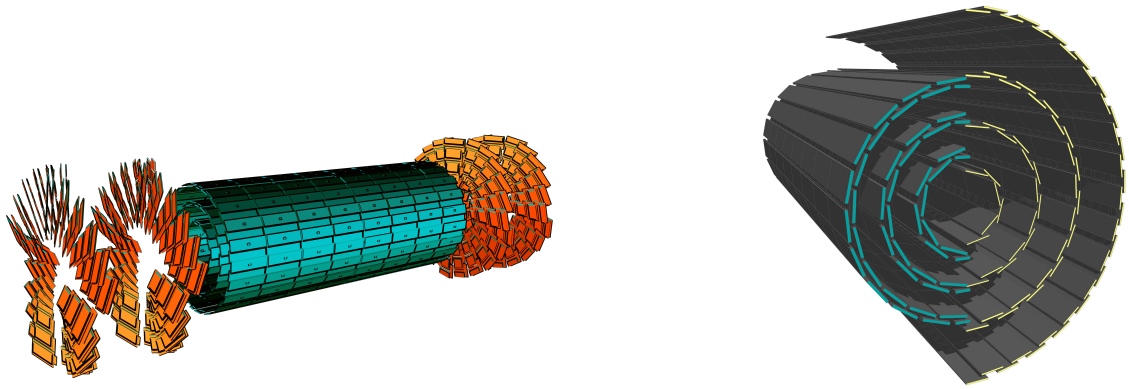

Figure 5.3: Left: the original pixel detector has been installed in 2008 and took data until 2016. Right: comparison of the pixel barrel layers between the original (blue) and present pixel detector (yellow). Reproduced from Refs. [129, 134]. Copyright 2008-2012 CERN for the benefit of the CMS Collaboration.

The strip detector has several components, see Fig. 5.4. The barrel consists of the Tracker Inner Barrel (TIB), Track Outer Barrel (TOB) and Tracker Inner Disk (TID). Two Tracker EndCaps are installed, one on each side of the barrel (TEC+, TEC-). Multiple silicon strip layers allow for an accurate reconstruction of the trajectories coming from particles with $p_{\mathrm{T}} > 1$ GeV and $|\eta| < 2.5$.

The tracker system will be upgraded for the HL-LHC (Phase-2) era. Instantaneous luminosities are expected to increase to from 2×10^{34} $\mathrm{cm}^{-2}\mathrm{s}^{-1}$ to 5×10^{34} $\mathrm{cm}^{-2}\mathrm{s}^{-1}$ (nominal) and 7.5×10^{34} $\mathrm{cm}^{-2}\mathrm{s}^{-1}$ (maximal), which correspond to an average pileup between 140 and 200. The Phase-1 tracker system would severely degrade under these conditions: (1) the outer tracker would suffer from thermal runaway and (2) the pixel resolution would degrade after collecting 500 fb^{-1} [135]. To maintain physics performance under the HL-LHC regime, the entire Phase-1 tracker detector will be replaced by the Phase-2 tracker during the third long shutdown (LS3).

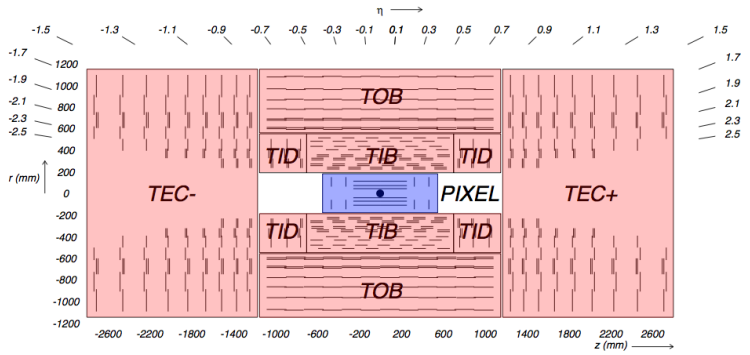

Figure 5.4: Schematic overview of the silicon tracker components. Reproduced from Ref. [129]. Copyright 2008 CERN for the benefit of the CMS Collaboration.

The inner Phase-2 pixel detector will have a significantly larger active surface, $4\ \mathrm{m}^2$ compared to $2.7\ \mathrm{m}^2$. In addition, it will be designed to be radiation tolerant up to $3000\ \mathrm{fb}^{-1}$ in the HL-LHC radiation environment. Unlike the Phase-1 predecessor, the Phase-2 version will have a L1T system where strip information will be used online to reconstruct vertices and trajectories. This will not only improve the performance of existing trigger algorithms, such as the single muon trigger, but it may also allow to deploy new triggers. For example, dedicated triggers for b jets or displaced muons.

5.3.2 Electromagnetic Calorimeter

The electromagnetic calorimeter (ECAL) is located around the tracker and detects electrons and photons. The ECAL is made up of radiation-hard lead tungstate ($\mathrm{PbWO_4}$) crystals in large homogeneous modules in the barrel (EB) and two endcaps (EE). The EB covers the region $|\eta| < 1.479$ with $61,200$ crystals. Each EE contains $7,324$ crystals and covers $1.479 < |\eta| < 3.0$ in pseudorapidity. The EE has an endcap preshower (ES) detector which is installed in between the EE and the hadronic endcap. Each $\mathrm{PbWO_4}$ crystal is $23\ \mathrm{cm}$ long, which corresponds to 25.8 radiation lengths X_0. The area of the front side of each crystal is $2.2 \times 2.2\ \mathrm{cm}^2$, or 10 Mollière radii squared. The crystals generate light when energetic particles deposit energy. The scintillating light is then detected by avalanche photodiodes (APDs) in the barrel and vacuum phototriodes (VPTs) in the endcaps. The granularity of a single ECAL crystal, $\Delta\eta \times \Delta\phi = 0.0174 \times 0.0174$,

has been chosen such that 5×5 ECAL crystals match a single HCAL scintillating tile, $\Delta\eta \times \Delta\phi = 0.087 \times 0.087$.

The Higgs boson discovery channel $h \to \gamma\gamma$ has been key to the design of the ECAL. While the diphoton branching ratio is very small, its signature is clean: a clear resonance over the Drell-Yan background. The ECAL is also important for the channels $h \to ZZ^* \to 4e$ and $h \to WW^* \to e^+\nu_e e^-\bar{\nu}_e$.

The front-end of the ECAL is equipped with fast algorithms for the online reconstruction of photons and electrons. The energy resolution of electrons in ECAL has been measured in beam tests [136]. It is characterized by contributions from the stochastic term, the noise term and the constant term:

$$\frac{\sigma_E}{E} = \frac{2.8\%}{\sqrt{E[\mathrm{GeV}]}} \oplus \frac{12\%}{E[\mathrm{GeV}]} \oplus 0.3\% \tag{5.1}$$

Figure 5.5 shows a crystal (left) and a so-called EE *Dee* (right).

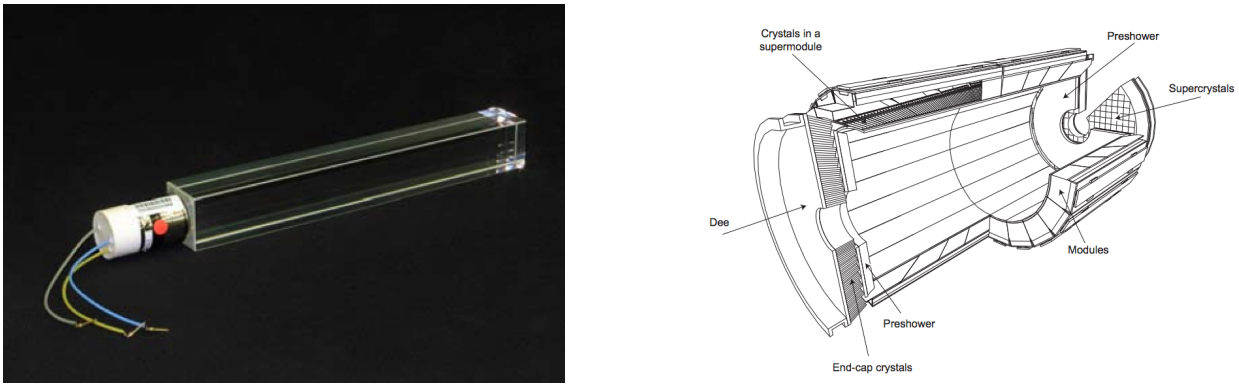

Figure 5.5: Left: a lead tungstate $\mathrm{PbWO_4}$ crystal equipped with a VPT. Right: overview of the ECAL system. The EE *Dees* are located on the outside of the ECAL. Reproduced from Ref. [129]. Copyright 2008 CERN for the benefit of the CMS Collaboration.

The lead tungstate crystals are expected to perform well in the radiation environment at the HL-LHC. The APDs will continue to operate as expected up to $3000\ \mathrm{fb}^{-1}$, but the radiation-induced dark currents will slightly increase the electronic noise [137]. The main driver of the upgrade of

the Phase-2 ECAL is the requirement to handle the increasing trigger rate at the HL-LHC [138]. The front-end electronics will be replaced with high-speed optical links which will transmit the single-crystal readout data at $40\ \mathrm{MHz}$ to upgraded off-detector processors. This will eliminate the need for on-chamber data preprocessing.

5.3.3 Hadronic Calorimeter

The accurate reconstruction of a jet (collimated cluster of hadronic particles) and its substructure is critical to the CMS physics program. The QCD multijet events stem from a variety of processes in hadronic collisions and compose the largest background in most physics analyses. For this reason, the CMS HCAL has been designed to detect and reconstruct hadronic jets. The HCAL relies on a combination of absorber material that slow down the particles and scintillators to detect the fragments. Four complimentary subsystems are combined into an almost hermetic HCAL: the hadron barrel (HB), the hadron endcap (HE), the hadron outer (HO) and the hadron forward calorimeter (HF). The total coverage is 2π in the azimuth angle and $0 < |\eta| < 5.2$ in pseudorapidity. The radiation length of the HCAL varies with η between $7 - 11\lambda_I$ and between $10-15\lambda_I$ with the HO included. The locations of the calorimeter subsystems are shown in Fig. 5.6.

The HB and HE lie within the superconducting magnet and provide coverage in the regions $|\eta| < 1.3$ and $1.3 < |\eta| < 3$ respectively. They are sampling detectors with layers of absorber material and plastic scintillating tiles. While HB uses brass as an absorber, HE uses the non-magnetic material C26000 cartridge brass. The HB extends radially from the outer layers of the ECAL at $R = 1.77\ \mathrm{m}$ to the inner extent of the solenoid at $R = 2.95\ \mathrm{m}$. There are 18 sectors in ϕ, subdivided in four subsectors, and 16 sectors in η, resulting in a segmentation $\Delta\eta \times \Delta\phi = 0.087 \times 0.087$. The HCAL segmentation matches the ECAL segmentation allowing precision calculations of the hadronic quantities, such as jet energy and $\not\!\!E_{\mathrm{T}}$.

The HO - also called *tail-catcher* - reconstructs showers that extend beyond the radiation length of the HB. It covers up to $|\eta| < 1.3$ and is located between the solenoid and the barrel muon system. The solenoid coil acts as the absorber material and two layers of scintillating tiles on either side of the coil measure the energy depositions.

The very forward section of CMS is instrumented with the HF, at $11.2\ \mathrm{m}$ from the interaction point along the beamline. It detects hadronic showers in the region $3 < |\eta| < 5.2$. Because of its proximity to the beamline, particle rates are the highest across CMS. Therefore, HF uses radiation-hard Cherenkov light detection technology. The light is collected with wavelength-shifting quartz fibers and photomultipliers. The segmentation of HF largely follows that of HB, but the granularity is four times coarser: $\Delta\eta \times \Delta\phi = 0.175 \times 0.175$.

The harsh radiation darkens the scintillating tiles in the HCAL. This causes significant losses in the performance after long operating times. To mitigate these losses, two upgrades are foreseen. The first one, the Phase-1 upgrade, aims to replace the barrel and endcap photosensors with silicon PMTs. The endcap sections have been upgraded during the Year-End Technical Stop of $2016 - 2017$. The barrel sections will be upgraded during the second long shutdown (LS2) of the LHC in 2019. Even after the Phase-1 upgrade the HE will likely not survive the high particle rate expected in the HL-LHC regime. Therefore, the EE and HE detectors will be replaced by a high-granularity calorimeter during the third long shutdown (LS3) in 2023 as part of the Phase-2 upgrade of the CMS detector [139].

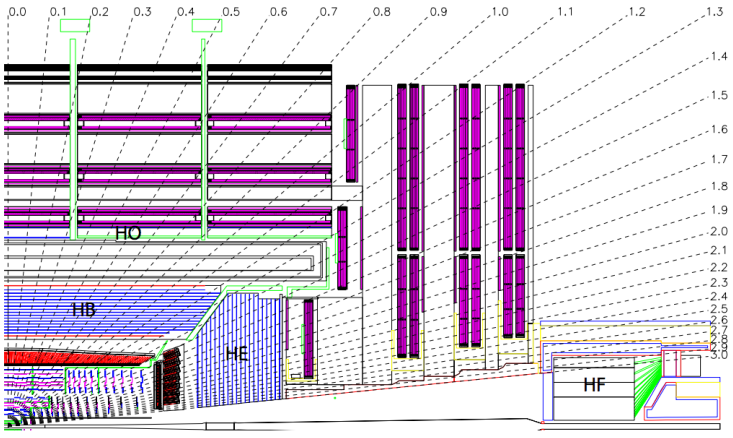

Figure 5.6: The present HCAL system consists of a hadron barrel (HB), hadron endcap (HE), outer hadron (HO) and hadron forward (HF) calorimeter. Reproduced from Ref. [129]. Copyright 2008 CERN for the benefit of the CMS Collaboration.

5.3.4 Superconducting Solenoid

The central component of CMS is the superconducting solenoid which operates at a temperature of 4.5 K. The magnetic field provides a direct measurement of the momentum of charged particles through the expression $p_{\mathrm{T}} = 0.3B[\mathrm{T}]\rho[\mathrm{m}]$, with ρ the curvature of the charged particle's trajectory. The magnet has a cold mass of 220 t, diameter of 6.3 m and a length of 12.5 m that provides a homogeneous magnetic field of 3.8 T over the active volume of the silicon tracker. The magnetic field is generated by a ≈ 20 kA superconducting current flowing in a four-strip NbTi reinforced conductor. A $10,000$ t steel return yoke closes the magnetic field in five barrel wheels and eight endcap disks. This is shown in Fig. 5.7.

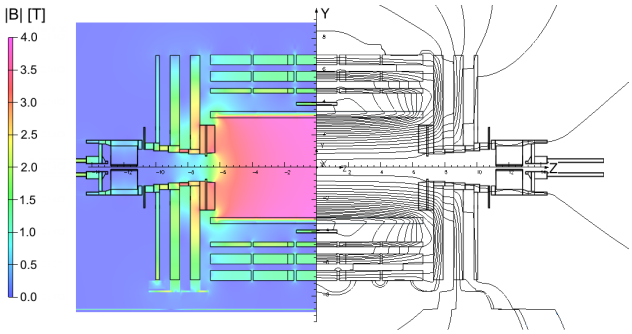

Figure 5.7: Magnetic field strength (left) and field lines (right) in the CMS detector. Adapted from Ref. [140]. Copyright 2009 CERN for the benefit of the CMS Collaboration.

5.3.5 Muon System

The muon system has been essential to confirm the observation of the Higgs boson with CMS detector in the four-lepton channel, $h \to ZZ^* \to 4l$. This channel - also called the *golden channel* - comprises $h \to ZZ^* \to 4\mu$, $h \to ZZ^* \to 2\mu 2e$ and $h \to ZZ^* \to 4e$. The golden channel is rare - only 0.012% of the total branching fraction contains electrons or muons - but it provides a clean signature with excellent Higgs boson mass resolution [87]. The mass resolution in the four-muon channel is even better $(1 - 2\%)$ than the mixed or the four-electron channel, because

muons are generally less affected by radiative effects in CMS than electrons. Muons are also frequently present in the signatures of electroweak processes (e.g. $W^- \to \mu\bar{\nu}_\mu$), rare SM events (e.g. $B_s \to \mu^+\mu^-$), and are often used in searches for BSM physics.

Muons are detected with the inner tracking system and the outer muon system. The muon system is embedded in the steel return yoke and uses three complementary technologies to detect muons and measure their properties with excellent precision [141]. Drift Tubes (DTs) are instrumented in the barrel region (up to $|\eta| < 1.2$), supplemented with Cathode Strip Chambers (CSCs) in the endcap region (starting from $|\eta| > 0.9$). Fast triggering Resistive Plate Chambers (RPCs) instrumented in the barrel and endcap in complement the DTs and CSCs up to $|\eta| < 1.8$. The region $1.8 < |\eta| < 2.4$ is presently only instrumented with CSCs. This is shown in Fig. 5.1.

Each technology relies on the same basic operating principle. The muon detection chambers are filled with a gas mixture in which a high voltage is placed over two electrodes. An incoming muon ionizes the surrounding gas molecules as it travels through the gas mixture. The primary electrons and ions drift towards the cathode and anode respectively. The static electric field accelerates the primary electrons which induce further ionization. The collection of electrons grows into an electronic avalanche. The accumulation of electric charge onto the electrodes generates an electronic pulse which signals the passage of a muon. In what follows we will discuss each technology in more detail.

5.3.5.1 DT

The DT system divides 250 chambers over five barrel wheels, numbered MB-2, MB-1, MB0, MB+1 and MB+2. Each wheel has 12 sectors, instrumented with 4 DT rectangular chambers per sector. This is shown in Fig. 5.8. The chamber configuration has been chosen such the coverage is continuous in ϕ and goes up to $|\eta| < 1.2$ in pseudorapidity.

The DT chambers are segmented into drift cells with a transverse size of $4.2\ \mathrm{cm} \times 1.3\ \mathrm{cm}$. Each drift cell contains a fiducial volume filled with a 85% Ar/15% CO_2 gas mixture and a high-voltage anode wire operated at $3.6\,\mathrm{kV}$. Muons that pass through the cell ionize neighboring Ar/CO_2 molecules. The electrons drift towards the anode wire with a constant drift velocity of $\approx 54\ \mu\mathrm{m/ns}$.

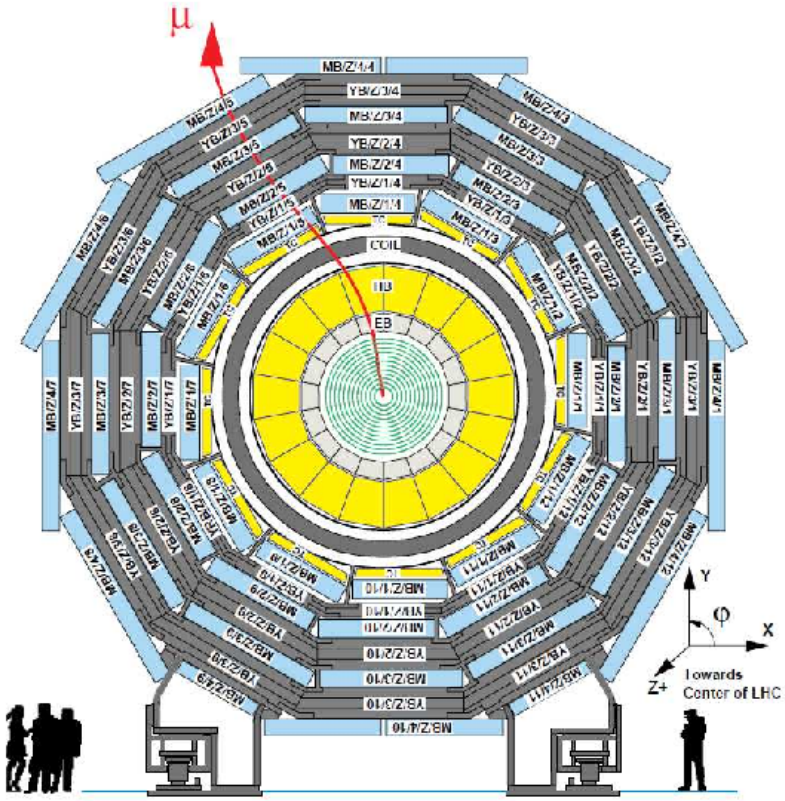

Figure 5.8: Layout of the CMS muon barrel system. Reproduced from Ref. [129]. Copyright 2008 CERN for the benefit of the CMS Collaboration.

The typical spatial resolution of a single cell is $\approx 250\ \mu\mathrm{m}$. The drift cells are organized in layers perpendicular to the beam or parallel with the beam, measuring $r-\phi$ or $r-z$ respectively. DT cells are staggered by a half-cell between two layers. Four layers make up a superlayer. The innermost chambers (in stations $1-3$) have three superlayers, whereas the outermost chambers (in station 4) only have two superlayers. Figure 5.9 shows the layout of a DT cell and a DT chamber. Track segments are reconstructed in each 30° sector from hits in the superlayers. During data taking, the DT chambers deliver track segments to the L1T which provide position and timing (bunch crossing) information to the track-finders. Segments are also reconstructed offline with a spatial resolution of $\approx 100\ \mu\mathrm{m}$ in $r-\phi$ and time resolution of $\approx 2\ \mathrm{ns}$.

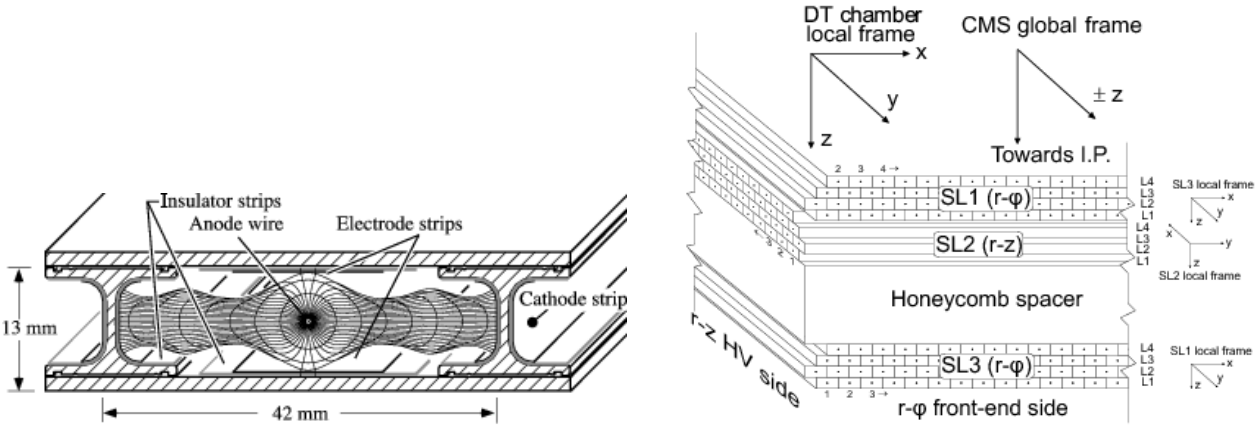

Figure 5.9: Left: drawing of a DT cell showing electric field lines and isochrones in the fiducial volume. Right: drawing of a DT chamber with 3 superlayers. Reproduced from Ref. [142]. Copyright 2009 CERN for the benefit of the CMS Collaboration.

5.3.5.2 CSC

The muon endcap is instrumented with four stations of CSCs, a type of multiwire proportional chamber. The first station has three concentric rings of chambers, numbered ME$1/1$, ME$1/2$ and ME$1/3$. Each chamber spans 10 degrees. Disks $2, 3, 4$ have similar configurations. The inner chambers span 20 degrees, while the outer chambers span 10 degrees each. A total of 540 chambers participate in the data taking.

Each CSC is trapezoidally shaped and has six layers (Fig. 5.10a). Each chamber has a 2D readout system, with anode wires spanning the width along the azimuth direction, and cathode strips spanning the length of the chamber. The wires are bundled into wiregroups of 10 to 15 wires. The wiregroups measure the polar angle θ, or pseudorapidity η, while the strips measure the azimuth angle ϕ. The fiducial volume is filled with a gas mixture of 50% CO_2, 40% Ar and 10% CF_4. The anode wires are operated at a high voltage between 2.9 kV and 3.6 kV. CSCs have different sizes depending on the station and ring number. ME$1/3$ chambers are the smallest, while ME$4/2$ chambers are the largest. Large chambers have mechanical spacers in the gas volume where the high voltage drops and sensitivity to muons is reduced.

Figure 5.10b shows the operating principle of a CSC. A muon that passes through a CSC ion-

izes the surrounding molecules. The electrons drift towards the anode wire, while the positive ions move towards the cathode strips. The charge deposits generate electronic pulses. The pulses are registered in specific wires and strips of the 2D electronic readout. Track segments are reconstructed by combining wire and strip information from each of the six layers. The L1T provides track segments with a resolution of about 2 mm in $r-\phi$. The offline spatial resolution is remarkably better, between 50 μm and 150 μm depending on the chamber.

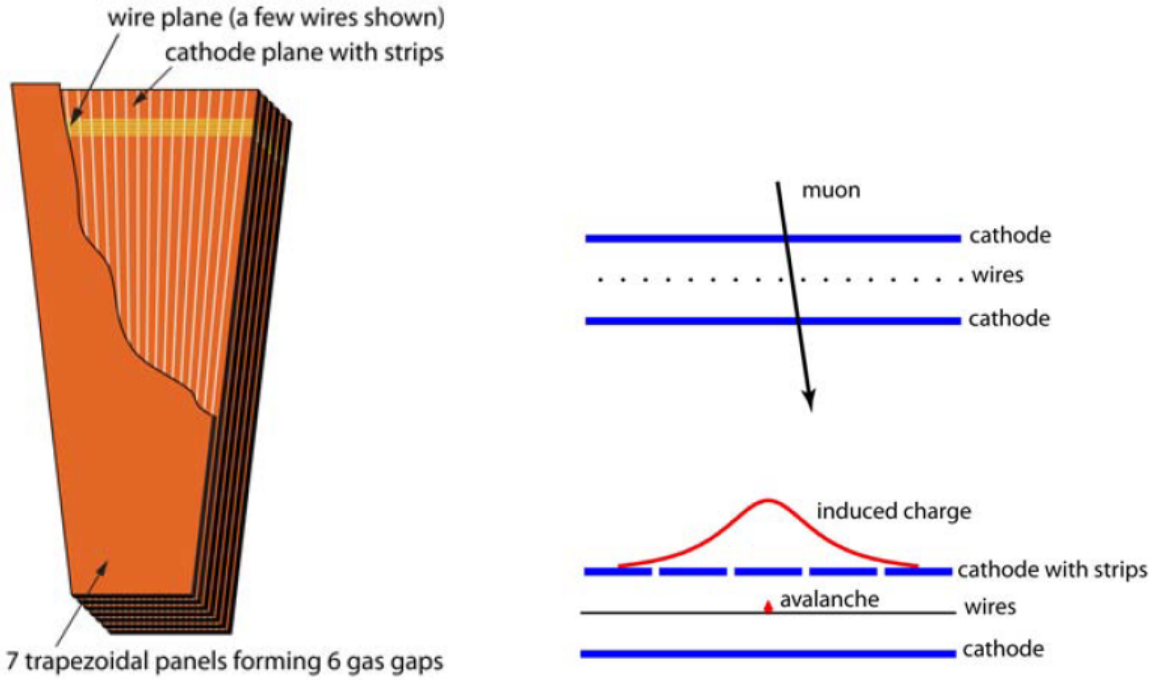

(a) (b)

Figure 5.10: Left: layout of a CSC. Right: operating principle of a CSC. Reproduced from Ref. [129]. Copyright 2008 CERN for the benefit of the CMS Collaboration.

The innermost CSC chambers (ME$1/1$) are located closest to the interaction point. Because ME$1/1$ chambers experience a large magnetic field, they are an essential to measure momentum in the region $1.55 < |\eta| < 2.4$. The wires are slanted by 29 degrees to account for the Lorentz effect. Furthermore, ME$1/1$ chambers are divided into two sections: a top half further away from

the beamline (ME1/b) and a bottom half closer to the beamline (ME1/a). The wire readout is continuous across ME1/1, whereas the strip readout is separated into sections of 32 strips for ME1/a and 48 strips for ME1/b.

The initial commissioning of CMS did not include the ME4/2 station. During the first long shutdown (LS1) of CMS, ME4/2 has been installed and the ME1/1 on-chamber electronics has been upgraded.

In order to perform optimally in HL-LHC conditions, the forward CSCs (ME2/1, ME3/1 and ME4/1) will be equipped with faster on- and off-detector electronics [143].

5.3.5.3 RPC

Double gap resistive plate chambers (RPCs) are instrumented both in the barrel and the endcap of CMS. The coverage is continuous in ϕ and spans up to $|\eta| < 1.8$ in pseudorapidity. RPCs are used for triggering purposes in the muon system. Figure 5.11 shows the layout of a double gap CMS RPC. Each RPC consists of two gaps in which a gas volume composed of 96.2% $C_2H_2F_4$, 3.5% C_4H_{10} and 0.3% SF_6 is placed under a high voltage. Electrons generated from the passage of a muon through the chamber drift towards the readout strip between the gaps under influence of the high voltage. The readout strip captures the charge deposition and registers a pulse which is processed by the on-chamber electronics.

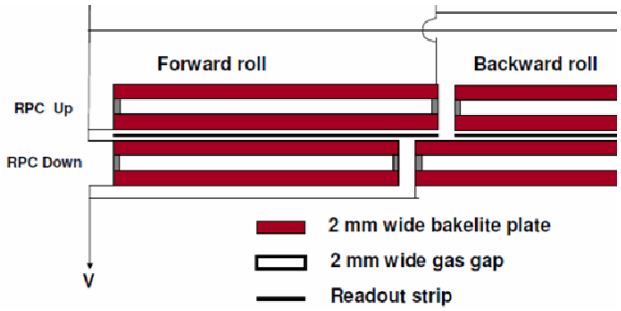

Figure 5.11: Layout of a double gap CMS RPC. Reproduced from Ref. [144]. Copyright 2014 CERN for the benefit of the CMS Collaboration.

RPCs are operated in avalanche mode and tolerate particle rates up to $\approx 1\ \mathrm{kHz/cm^2}$. They have a relatively poor spatial resolution ($\approx 1\ \mathrm{cm}$ in $r - \phi$), but excellent hit timing resolution ($\approx 2\ \mathrm{ns}$).

The chamber geometry follows the DT/CSC geometry: barrel RPCs are rectangular, while endcap RPCs are trapezoidal. A total of 480 barrel and 576 endcap chambers are presently installed. The innermost regions of the endcap are not instrumented with RPCs.

The RPC system has been upgraded during LS1 with the installation of RE$4/2$. Additional RPCs are planned for installation in the innermost rings RE$3/1$ and RE$4/1$ during LS3. Moreover, the on-chamber electronics of all RPCs will be upgraded which will improve the spatial resolution to $\approx 1\ \mathrm{mm}$ [143].

5.3.6 Luminosity Measurement

An accurate measurement of the luminosity is needed as it enters the cross section measurement through Eq. 4.2. The luminosity is measured in CMS with a number of instruments. Five detectors participate in the measurement: the silicon pixel detector, the DT, the HF, the fast beam conditions monitor and the pixel luminosity telescope [145]. Dedicated trigger rate algorithms use hit information from these detectors to measure the luminosity. The participating detectors are calibrated with Van der Meer scans using a special LHC machine configuration.

5.3.7 Trigger and Data Acquisition

The LHC produces hadron collision events at a rate of $40\ \mathrm{MHz}$. The typical size of a reconstructed event is of the order of $1\ \mathrm{Mb}$. Selecting all events (including uninteresting ones) would require storing about $60\ \mathrm{TB}$ of data per second - an impractical task. Therefore, events interesting to the CMS physics program are selected using the two-tiered CMS Trigger system [146]. The first level is a hardware-based L1 trigger (L1T). The second level is a software-based high level trigger (HLT). Events not selected are permanently lost.

The L1T does a crude event reconstruction using information from the calorimeter and muon systems on fast, programmable hardware applications. In less than $4\ \mu\mathrm{s}$ events are reconstructed and selected so that the event rate reduces from $40\ \mathrm{MHz}$ to about $100\ \mathrm{kHz}$. Figure 5.12 is a

schematic view of the L1T. As can be seen, the Global Trigger takes a decision based on the combined information from the Calorimeter Trigger and the Muon trigger. However, an upgrade of the L1T system is planned for the HL-LHC that would include Tracker information [147].

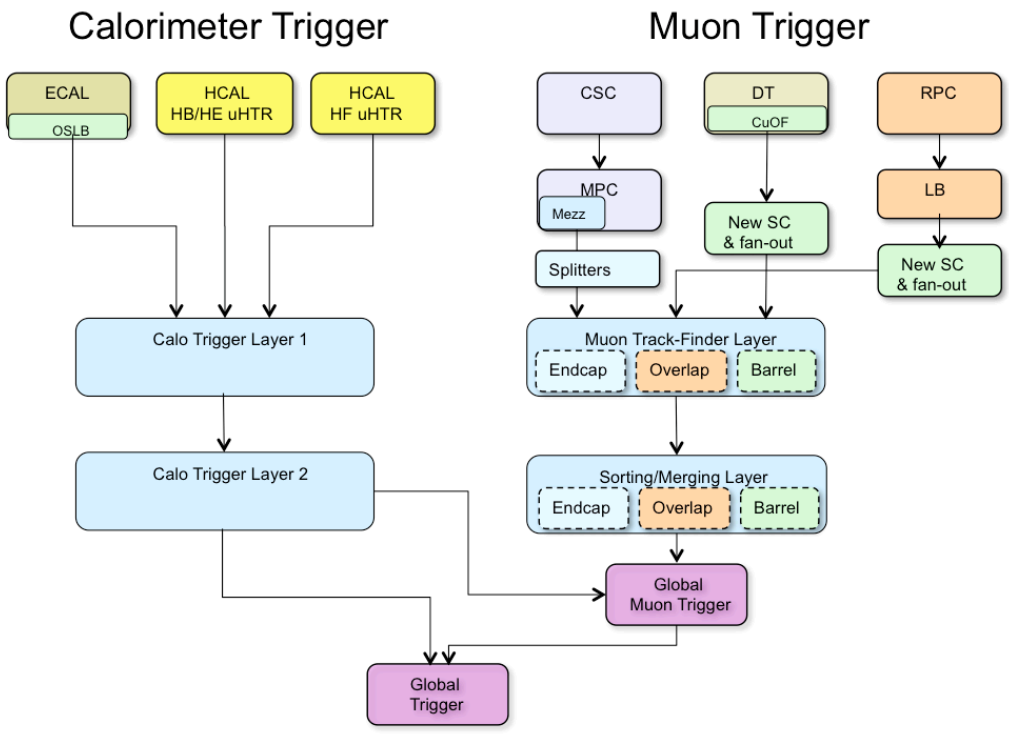

Figure 5.12: Schematic view of the L1T system. Reproduced from Ref. [148]. Copyright 2013 CERN for the benefit of the CMS Collaboration.

Following the L1T, the HLT does the full event reconstruction and selection on a processor farm at CERN. The HLT consists of several hundred software algorithms running on thousands of CPUs. Each algorithm is designed to select events with a specific signature in the detector. Events selected by at least one such algorithm are in turn selected by the HLT and permanently stored. Thus the event rate reduces from about 100 kHz to about 1 kHz. Stored events are reprocessed later to include global detector effects such as detector misalignment.

5.4 Simulation and Computing Tools

The CMS Collaboration uses state-of-the-art computing tools and algorithms to reconstruct, simulate and analyze collision data. These simulation and reconstruction software are maintained within the CMS software package (CMSSW). A highly detailed model of the CMS detector based on GEANT4 [149] is implemented in CMSSW that ensures an accurate simulation of the detector response to SM and new physics processes.

The detector simulation is done in a number of steps. The first step predicts the location and intensity of energy depositions from fundamental particles in the different subdetectors. The second step, digitization, converts the simulated hits into digital pulses in each system. In the next step, the L1 trigger, the digitized pulses are combined into trigger objects which play a key role in the trigger decision. The final step, data acquisition, emulates how front-end detector elements read out and store raw collision data.

Simulated and real data are processed using a large-scale redundant computing system called the Worldwide LHC Computing Grid [150]. The data are archived using the CMS Data Aggregation System [151] and made accessible through the CMS Remote Analysis Builder [152].

5.5 Summary

This chapter we have provided a broad overview of the CMS and how it detects particles. In the next chapter we will discuss how individual objects and events are reconstructed with the particle-flow algorithm.

6. EVENT RECONSTRUCTION

Before real LHC data or Monte Carlo simulated data can be used in physics analyses, the individual objects in the data must be reconstructed. These objects may represent real particles, such as muons, but can also represent more abstract quantities, such as missing transverse energy. The CMS offline software contains algorithms to reconstruct these objects. The object reconstruction is done in a series of steps of increasing complexity. For example, charge depositions on several CSC wires and strips may combine into a three dimensional track segment in that chamber. Multiple track segments can be fit to form a muon track. Once each object has been assembled, all information is combined into a global fit called the *Particle-Flow* (PF) algorithm [153]. From these objects, the PF algorithm reconstructs the following particles: electrons, muons, photons, charged hadrons (e.g. $\pi^{\pm}$) and neutral hadrons (e.g. neutrons). In turn, these particles are used to recreate jets and missing transverse energy, identify tau leptons etc.

In this chapter, largely based on Ref. [153], we will describe the steps to reconstruct the individual particles with the PF algorithm. In particular, we will focus on muon reconstruction because muons dominate the event signature in this search.

6.1 What is the Particle-Flow Algorithm?

The PF algorithm reconstructs electrons, muons, photons, charged hadrons and neutral hadrons. Figure 6.1 shows how each of these particles interact with CMS subdetectors. From this set of particles, heavier decaying ones can be identified, such as b quarks or W bosons.

The PF reconstruction has been developed and commissioned in 2009 prior to the start of the LHC data taking. It has been extremely successful: the results of nearly every CMS physics analysis have been obtained with the PF algorithm.

The PF algorithm is particularly suitable for CMS. The large magnetic field separates charged from neutral particles in jets and allows to measure transverse momentum. The tracker has a fine resolution to efficiently reconstruct trajectories in jets up to $1\ \mathrm{TeV}$. The ECAL is highly segmented

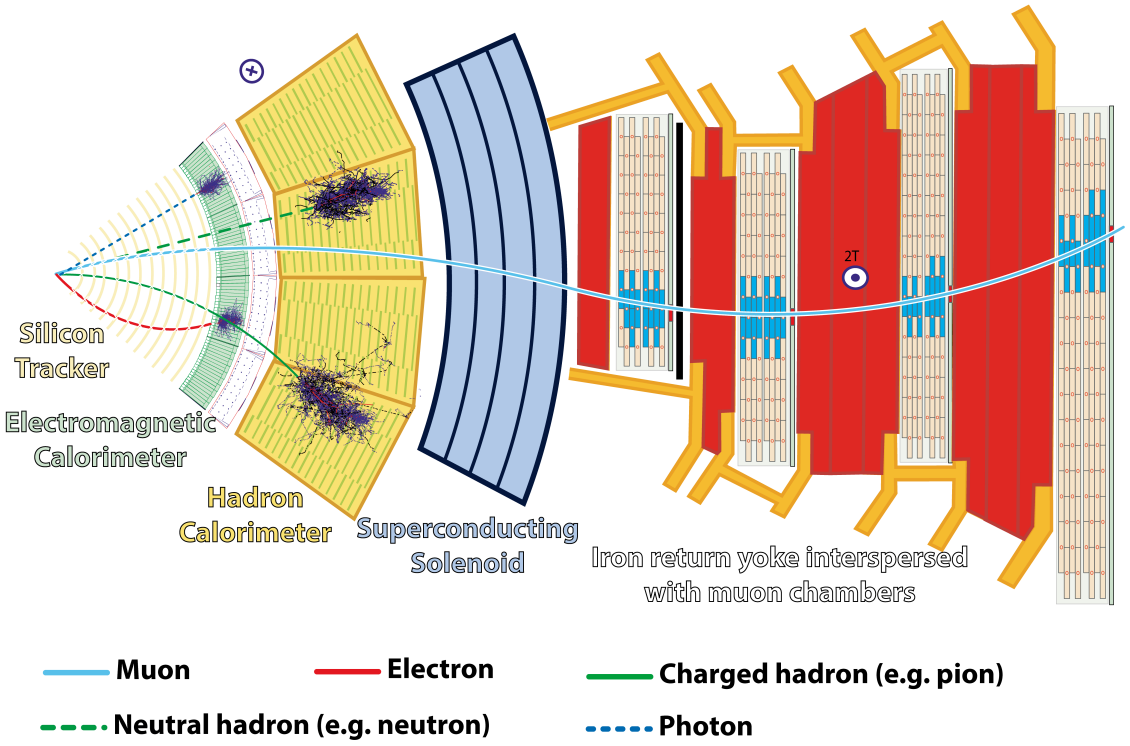

Figure 6.1: A slice of CMS showing the different subdetectors and which particles interact with them. Reproduced from Ref. [154]. Copyright 2016 CERN for the benefit of the CMS Collaboration.

so that it can distinguish clusters of energy depositions coming from particles in jets and identify photons. The HCAL is hermetic around the beam axis and separates charged from neutral hadronic energy depositions. Finally, the muon system has an excellent resolution in (η, ϕ) and provides a clean muon identification.

The following sections treat the object and PF event reconstruction in more detail. Tau lepton identification is not discussed.

6.2 Reconstruction of Individual Objects

6.2.1 Tracks and Vertices

Tracks and vertices are reconstructed in the silicon tracker with a Kalman Filter (KF). The algorithm reconstructs electrons, muons, hadronic tau leptons and tag b-quark jets. The KF algorithm starts off by generating trajectory seeds from a few hits. The trajectory is then built by

matching hits in the tracker layers. Once the hits are collected, the track is fitted and the particle properties such as transverse momentum and direction are determined. A vertex is fitted to the location where two or more tracks intersect. Dedicated vertex reconstruction algorithms have been developed for the purpose of reconstruction heavy b-quark decays. The reconstruction efficiency for charged pions with $p_{\mathrm{T}} > 1$ GeV is 70-80%. Isolated muons have near perfect reconstruction efficiency (99%).

6.2.1.1 Electrons

Electrons radiate a signification fraction of their energy while traversing the tracker volume, known as *bremsstrahlung*. This complicates the electron reconstruction in the tracker. Reconstruction algorithms for well-isolated electrons have been developed using only calorimeter information. A crystal with the largest energy deposition in its neighborhood is chosen as the center. All energy associated to bremsstrahlung coming from electrons, positrons and photons is collected into an ECAL supercluster. The supercluster energy provides accurate position information which is used to reconstruct the electron in the tracker.

6.2.1.2 Muons

Muons are reconstructed in a number of steps [71]. The first step is the *local muon reconstruction*. A muon hit in the RPC, CSC or DT system is reconstructed from charge depositions onto a readout wire or strip. In the CSC and DT chambers single hits are combined into multilayer segments. However, such segments are not built for the single layer RPCs. Hits and segments are subsequently used in one or more muon reconstruction algorithms.

Standalone Muon A first algorithm reconstructs the track only in the muon system starting from reconstruction seeds. Those seeds are generated from the DT/CSC segments. They have a position vector, direction vector, and an initial transverse momentum estimate. Standalone muons are reconstructed by fitting a track in the muon system (*muon track*) to at least two DT/CSC segments using the KF technique. Any number of RPC rechits can also participate. The track-fit provides an updated estimate of the muon p_{T}.

Global Muon Standalone muons matched to tracks reconstructed in the inner tracker system (*tracker track*) are called global muons. The track is refitted using the combined information and the muon p_{T} is updated. The result of this fit is an improvement of the transverse momentum resolution.

Tracker Muon Tracker muons are complementary to global muons. They are reconstructed by matching tracker tracks to CSC/DT segments. Low p_{T} signatures which do not have a sufficient number of associated muon hits to be reconstructed as global muons can still be reconstructed as tracker muons. The transverse momentum resolution of each of these objects versus p_{T} is shown in Fig. 6.2. Tracker muons have a good p_{T} resolution ($< 1 - 2\%$) up to $200\ \mathrm{GeV}$. The complementary muon system helps to keep the p_{T} resolution down to $5 - 10\%$ for very energetic muons ($200\ \mathrm{GeV} - 1\ \mathrm{TeV}$).

Displaced Muon Prior to the start of Run-2, algorithms specific for displaced muons have been deployed in the standard muon reconstruction sequence [155, 156]. The algorithms release the constraint that muons must come from the beamspot and produce *displaced standalone muons*, *displaced global muons* and *displaced tracker muons*. Figure 6.3 compares the performance of prompt and displaced muon reconstruction in the decay of heavy, long-lived particles. Displaced muon algorithms are better able to identify muons with large production radius than prompt muon algorithms. However, the loss of the beamspot constraint negatively affects the p_{T} resolution. Displaced global muons and displaced tracker muons have a similar resolution as prompt global muons (around $2 - 4\%$). Displaced standalone muons, on the other hand, do not have hits in the tracker, so the p_{T} resolution is much poorer (between 20 and 50%).

6.2.2 Calorimeter Clusters

Calorimeter clusters are reconstructed separately in the ECAL and HCAL systems. The clustering algorithm is multifunctional by design. First, it measures energy depositions coming from stable neutral particles (photons and neutral hadrons). Second, it distinguishes energy deposits

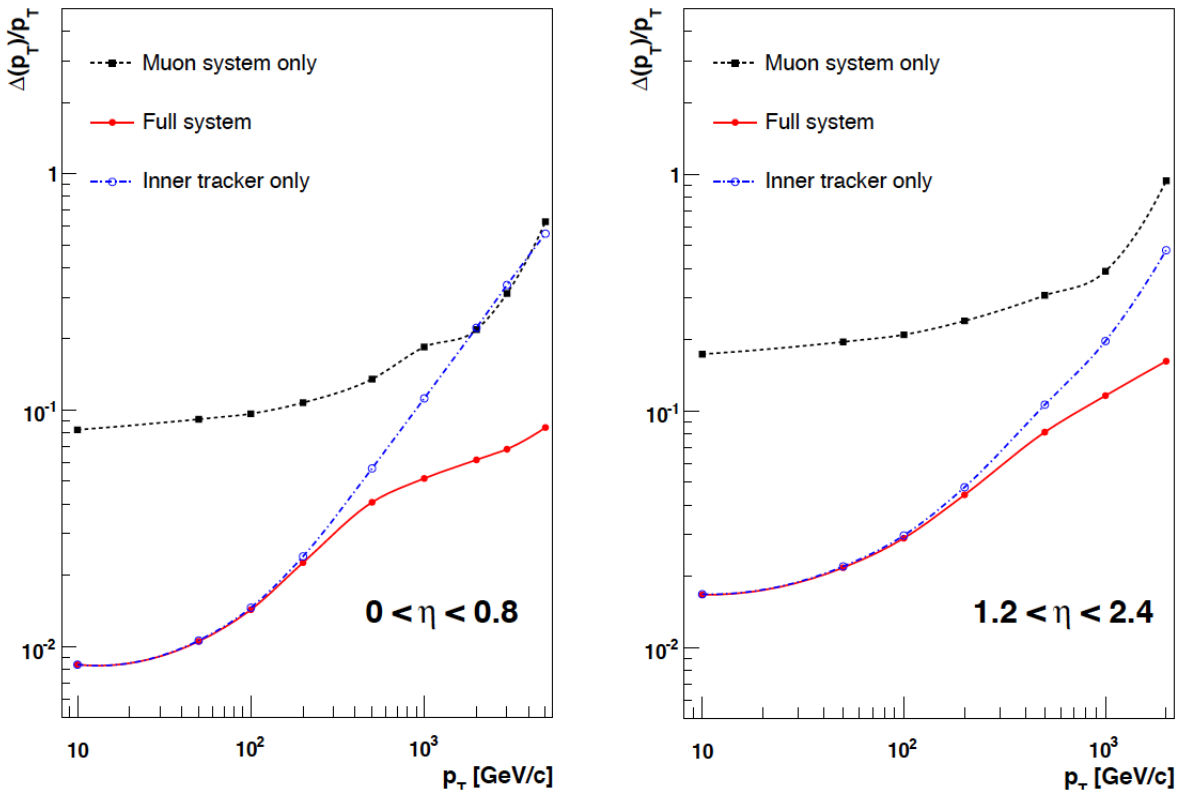

Figure 6.2: Muon p_{T} for prompt standalone (black), tracker (blue) and global muons (red) in the region $|\eta| < 0.8$ (left) and $1.2 < |\eta| < 2.4$ (right). Reproduced from Ref. [129]. Copyright 2008 CERN for the benefit of the CMS Collaboration.

from neutral and charged hadrons. In addition, it reconstructs the electrons and radiated photons. Finally, the algorithm measures the energy of charged hadrons for which the trajectories could not be identified precisely - typically low-quality or high-momentum tracks.

6.3 Particle Flow Event Reconstruction

Once the individual elements of the PF algorithm are reconstructed in the different subdetectors, they are linked together. This linking is limited by the (η, ϕ) resolution of the subdetectors and by the number of particles each subdetector can reconstruct. Only the closest pairs in (η, ϕ) are considered in the linking process.

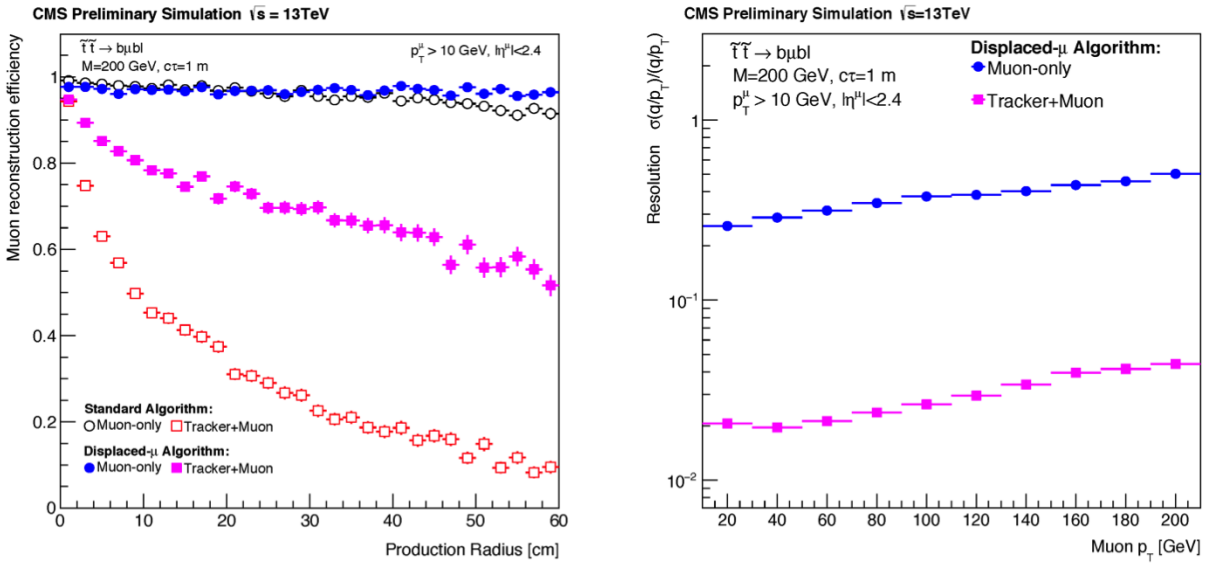

Figure 6.3: Left: Muon reconstruction efficiency as a function of the production radius. The standard muon and global algorithms are compared to the new algorithms specific for displaced muons. Right: q/p_{T} resolution as a function of muon p_{T}. Reproduced from Ref. [156]. Copyright 2015 CERN for the benefit of the CMS Collaboration.

6.3.1 Muons

6.3.1.1 Identification

The PF algorithm identifies three types of muons for CMS analyses based working points. The *loose muon* is defined as a PF muon reconstructed by the global or tracker algorithm. Loose muons are designed to be very efficient. The reconstruction efficiency for muons with $p_{\mathrm{T}} > 20$ GeV is $> 99\%$ and $> 95\%$ in simulation and 13 TeV data respectively [157]. The *medium muon* identifies as a loose muon with additional selections on the track and muon quality. The *tight muon* is a global muon with additional constraints on the muon quality to suppress muons from (1) hadronic punch-through, (2) cosmic radiation, (3) decays-in-flight and (4) pileup. The identification of loose, medium and tight muons is $\approx 100\%$, $> 99\%$ and $\approx 98\%$ respectively efficient for prompt muons [153].

6.3.1.2 *Isolation*

The CMS Muon Physics Object Group (POG) recommends two types of muon isolation, namely *PF-based isolation* and *tracker-based isolation*. The PF-based isolation is calculated from the contributions of charged and neutral hadrons and photons

$$Iso^{\mathrm{PF}} = \frac{1}{p_{\mathrm{T}}^{\mu}} \sum p_{\mathrm{T}}^{\text{ch. had.,PU}} + \frac{1}{p_{\mathrm{T}}^{\mu}} \max\left(0, \sum p_{\mathrm{T}}^{\text{neut. had.}} + \sum p_{\mathrm{T}}^{\text{photon}} - \frac{1}{2} \sum p_{\mathrm{T}}^{\text{ch. had.,PV}}\right), \tag{6.1}$$

while the tracker-based isolation is calculated from the contributions of the charged tracks from the primary vertex

$$Iso^{\mathrm{Tracker}} = \frac{1}{p_{\mathrm{T}}^{\mu}} \left(\sum p_{\mathrm{T}}^{\text{charged track,PV}}\right). \tag{6.2}$$

These isolation variables are suited for individual muons, but are inappropriate for close-by (i.e. almost parallel) muons. Such muons could come from the decay of light bosons with a very low mass $m_a \approx 2m_\mu$. As a result, application of the PF-based isolation or the tracker-based isolation in the event selection could eliminate pairs of close-by muons. This could degrade the selection efficiency for events with such pairs. However, this analysis does not make use of either isolation variables. A more appropriate isolation variable is introduced in Chap. 7.

6.3.2 Electrons and Isolated Photons

The PF algorithm reconstructs electrons using a Gaussian Sum Filter (GSF) in lieu of a KF, because the electronic energy losses cause the electron trajectory to deviate substantially from a helix. The track is propagated to the ECAL where it is linked to an ECAL cluster to form a tracker-based electron. The final decision in the electron track fit is made by a Boosted Decision Tree that uses several variables such as the track χ^2, potential energy losses and the distance between the propagated track and the nearest ECAL cluster. Isolated photons are similar to electrons, except that they are not seeded by GSF tracks.

6.3.3 Hadrons and Nonisolated Photons

The LHC produces an abundant number of charged and neutral hadrons, and photons in each collision. Charged hadrons include protons, charged pions and kaons, while neutral hadrons are mostly π^0 and neutrons. Hadrons and photons are common byproducts of pp collisions. Charged hadrons are reconstructed as tracker tracks linked to ECAL and HCAL clusters. ECAL and HCAL clusters not linked to tracks are reconstructed as photons and neutral hadrons.

6.4 Jet and MET Reconstruction

Hadronic jets are among the most common objects in collisions at the LHC. The anti-k_{T} jet-clustering algorithm [158], with a distance parameter of $R = 0.4$, has been adopted by CMS to reconstruct jets in the detector. Depending on the basic constituents, different types of jets can be reconstructed. These include PF jets from PF objects, and calorimeter jets from energy deposits in the calorimeter towers.

Noninteracting particles, such as neutrinos and certain BSM particles, generate an imbalance in the transverse momentum sum. This imbalance is referred to as missing transverse momentum p_T^{miss} or missing transverse energy ($\not\!\!E_T$ or MET). The missing transverse momentum is calculated as $p_{\mathrm{T}}^{\mathrm{miss}} = -\sum_{i=1}^{N} p_{\mathrm{T},i}$.

6.5 Summary

In this chapter we have discussed the event reconstruction with the PF algorithm. We have paid particular attention to the various muon reconstruction algorithms relevant to the physics search which will be described in the next chapter.

7. SEARCH FOR NEW PHYSICS WITH LIGHT BOSONS DECAYING INTO MUONS

7.1 Analysis Strategy

The strategy of this analysis[1] is based on the selection of events in pp collision data in which two well-identified muon pairs are present. We require that each of the muon pairs corresponds to having originated from the decay of a light boson. Muons are paired when they satisfy the following requirements: (1) they are oppositely charged, (2) each muon has a transverse momentum of at least 8 GeV, (3) the invariant mass of the muon pair is within the search window ($0.25 < m_{\mu\mu} < 8.5\ \mathrm{GeV}$), and (4) the two muon trajectories are consistent with having originated from the same vertex. The data in this search have been collected with a multimuon trigger and correspond to $35.9\ \mathrm{fb}^{-1}$ of pp collision data. The trigger selects events with at least three muons, one of which has $p_{\mathrm{T}} > 15\ \mathrm{GeV}$ and the other two have $p_{\mathrm{T}} > 5\ \mathrm{GeV}$. To match the event topology of pair production of light bosons, events are selected to have exactly two muon pairs. However, no restriction is set on the number of extra unpaired muons, called *orphan muons*. The event selection is further optimized to enhance the sensitivity to muon pairs that are consistent to have originated from long-lived bosons. The search is limited to new light bosons of the same type and the same mass. Muon pairs are therefore required to have invariant masses consistent within 5σ of the core mass width. This mass requirement defines a narrow search region in the dimuon-dimuon mass spectrum $(m_{(\mu\mu)_1}, m_{(\mu\mu)_2})$.

The event selection is fine-tuned such that the analysis is nearly background-free. Still, few SM background events that mimic the signal can pass the event selection. The SM backgrounds relevant for this search are double b quark production, prompt double J/ψ meson production, and electroweak production of four muons. In the dominant background, double b quark production, muon pairs are produced in semileptonic decays or in decays with light SM resonances. Suppression of this background is achieved by requiring that the muon pairs are sufficiently isolated from other

[1]Part of this section has been reprinted from "A search for pair production of new light bosons decaying into muons in proton-proton collisions at 13 TeV" by CMS Collaboration, 2018 [159, 160]. Submitted to Physics Letters B. Copyright 2018 CERN for the benefit of the CMS Collaboration.

particles in the event. In prompt double J/ψ meson production, each J/ψ meson decays directly to a muon pair, $J/\psi \to \mu^+\mu^-$. This background is only relevant in the region where two dimuon invariant masses are close to the J/ψ mass, $m_{(\mu\mu)_1} \approx m_{(\mu\mu)_2} \approx m_{J/\psi}$. The electroweak contribution to the background, consisting of low mass Drell-Yan production and $pp \to Z/\gamma^* \to 4\mu$ production, is heavily suppressed by the requirement of additional muons and by the requirement that the dimuon invariant masses are small and consistent.

In case of a signal, an enhancement in the data would be observed in a distinct point along the main diagonal of the dimuon-dimuon mass spectrum. This is shown in Fig. 7.1. The analysis has been designed to also be sensitive to new physics models with multiple light bosons, in which case multiple enhancements may be observed along the main diagonal. Events with at least one dimuon coming from a SM resonance may appear as enhancements along horizontal and vertical lines near known SM particle masses.

To quantify the significance of the excess - if observed - a binned likelihood fit of the signal and background model is performed using the CL_s method [161] in the diagonal search region. In absence of an excess, the fit determines the confidence level limits on the production rate of a pair of light bosons decaying into muons pairs. The results may then be interpreted in models with the same event signature. Interpretations in this search are made for the NMSSM and MSSMD benchmark models.

7.2 Monte Carlo Event Generation

Proton-proton collision events producing light bosons in the NMSSM and MSSMD benchmark models have been simulated using Monte Carlo event generators. The parton energy inside the proton is modeled with the leading order Neural Network PDFs NNPDF2.3LO with $\alpha_S(M_Z) = 0.119$ [125,126]. Effects from underlying event activity and jet fragmentation at the LHC at $13\ \mathrm{TeV}$ are modeled with the event generator PYTHIA 8.2 using the "CUETP8M1" tune [122, 162, 163]. Events are generated in which two gluons inside the colliding protons interact head-on. Only Higgs boson production through gluon-gluon fusion is considered, which corresponds to 87% of the total production cross section at $\sqrt{s} = 13\ \mathrm{TeV}$ if the Higgs boson were SM-like. The Higgs

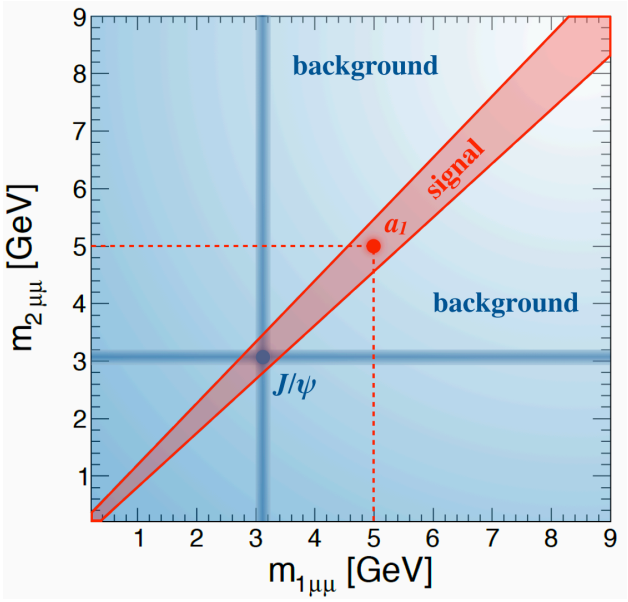

Figure 7.1: Two dimensional dimuon mass spectrum in a search for new light bosons decaying into muons. The blue shaded area notes the background region, whereas the red shaded area along the main diagonal shows the signal region. If an observation is made, the signal will appear as an enhancement somewhere in the signal region. In this schematic, an enhancement is shown at $m_a = 5$ GeV.

boson decays into a pair of a_1 bosons in the case of NMSSM or dark photons γ_D in the case of MSSMD. More details on the model specific event generation mechanism is provided in the following sections.

7.2.1 NMSSM

NMSSM samples are generated and processed for hadronization with PYTHIA 8.212 [122]. The two-Higgs-doublet BSM states are initialized where the Higgs boson is produced only through gluon-gluon fusion with contributions primarily from top quark loops. All SM decay modes are turned off. Instead, the Higgs boson is forced to decay into a pair of light bosons, $h_{1,2} \to 2a_1$. The mass $m_{h_{1,2}}$ varies between 90 and 150 GeV. The light boson mass m_{a_1} is chosen to vary between 0.25 and 3.55 GeV (between approximately $2m_\mu$ and $2m_\tau$) where $a_1 \to \mu^+\mu^-$ decays are expected to be dominant. Finally, new light bosons are forced to decay into muon pairs $a_1 \to \mu^+\mu^-$ 100% of the time. The light bosons in the NMSSM sample are always short-lived, meaning that they

decay at the interaction point (IP). A Feynman diagram of the $h_{1,2} \to 2a_1 \to 4\mu$ process is shown in Fig. 7.2. Table A.1 lists the parameters for and number of events in each NMSSM sample.

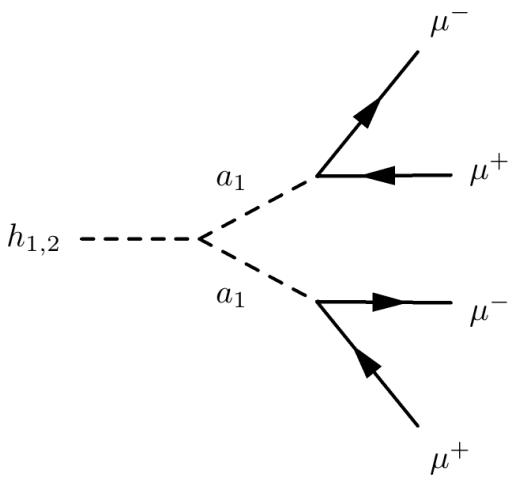

Figure 7.2: Feynman diagram of the NMSSM process $h_{1,2} \to 2a_1 \to 4\mu$.

7.2.2 MSSMD

MSSMD events are generated using MADGRAPH 4.5.2 [164]. A Higgs effective field theory is defined in which Higgs bosons are solely produced through gluon-gluon fusion. Particle decay is modeled with the BRIDGE program [165]. The *narrow width approximation* is applied in all decays. The width of the Higgs boson and the dark photon is set to the small value of 10^{-3} GeV. A physics model is then implemented in which all SM Higgs boson decays are turned off. Instead, the Higgs boson is forced to undergo a BSM decay into a pair of SUSY neutralinos n_1, $h \to 2n_1$. The neutralino with mass m_{n_1} is forced to decay into a dark photon γ_{D} and a dark neutralino n_{D} according to $n_1 \to \gamma_{\mathrm{D}} + n_{\mathrm{D}}$. The dark neutralino escapes CMS without being detected. Finally, the dark photon is forced to decay into a pair of muons $\gamma_{\mathrm{D}} \to \mu^+\mu^-$. A Feynman diagram of the process $h \to 2n_1 \to 2n_{\mathrm{D}} + 2\gamma_{\mathrm{D}} \to 2n_{\mathrm{D}} + 4\mu$ is shown in Fig. 7.3.

The dark photon mass is varied between 0.25 GeV ($\approx 2m_\mu$) and 8.5 GeV. The upper limit is chosen so that any observed peak will be fully below 9 GeV. Above this limit contributions from

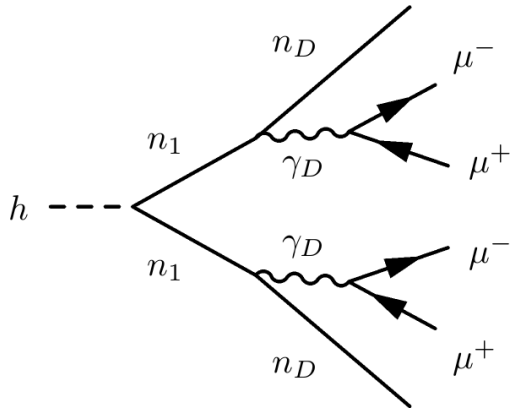

Figure 7.3: Feynman diagram of the MSSMD process $h \to 2n_1 \to 2n_{\mathrm{D}} + 2\gamma_{\mathrm{D}} \to 2n_{\mathrm{D}} + 4\mu$.

Υ-meson (9460) and Z-boson decays complicate the b-quark pair background estimation. Below this limit, Υ-meson and Z-boson contributions are negligible.

The Higgs boson is chosen to be SM-like, with a mass of $125\ \mathrm{GeV}$. The dark neutralino mass is fixed to the arbitrarily small value of $1\ \mathrm{GeV}$. The SUSY neutralino mass is fixed to $10\ \mathrm{GeV}$ to allow for decays into a dark neutralino and a dark photon. The BRIDGE program produces a list of MSSMD events in the *Les Houches Event* (LHE) data format [166]. Each LHE file contains up to $80,000$ events and is processed for hadronization using PYTHIA 8.205.

Nonnegligible dark photon lifetime is simulated by sampling the coordinates of the dark photon decay vertices according to exponential distribution $\exp(-r/c\tau)$. A dark photon with a long lifetime corresponds to a small kinetic mixing parameter ε and will decay into a pair of displaced muons. In contrast, a short-lived dark photon will decay into a pair of prompt muons. Table A.5 lists the samples, their parameters and the number of events.

7.3 Design and Performance of the Trigger Algorithm

7.3.1 Design Criteria

Several aspects of the signal topology have been taken into account in selecting a good trigger for this analysis: (1) multiple close-by muons degrade the L1T efficiency, (2) muon tracks from dark photon decays do not perfectly point back to the beamspot and may not have the same vertex

z position with increasing mass or increasing lifetime, (3) the muon p_{T} thresholds should be kept low as the acceptance falls fast for leading muon p_{T} above $15 - 20$ GeV, and (4) isolation cannot be applied reliably per muon. In addition, the trigger should be unprescaled: it accepts all events to maintain maximum sensitivity.

In previous iterations of this search the data have been collected with an unprescaled, inclusive, nonisolated double muon trigger `HLT_Double_Mu17_Mu8`. This trigger requires the presence of two muons with $p_{\mathrm{T}} > 17$ GeV and $p_{\mathrm{T}} > 8$ GeV in the event. While this trigger has been suitable during Run-1, prior to the start of Run-2 `HLT_Double_Mu17_Mu8` was replaced with a different set of triggers, each of which would have affected the model independence of the analysis. The available triggers (1) required ≥ 3 L1T muons, (2) placed cuts on the impact parameter Δ_{xy} or the longitudinal distance of the muon vertex to the IP d_z, (3) significantly increased the p_{T} cuts thus affecting the acceptance, (4) applied track-based isolation on the muons, or (5) were heavily prescaled for Run-2 data taking.

New muon reconstruction algorithms optimized for displacement have been implemented during LS1. These algorithms release the beamspot constraint on the momentum fit and allow the implementation of trigger paths sensitive to signatures with displaced muons. However, a trigger with two displaced muons and with transverse momentum cuts $p_{\mathrm{T}} > 17$ GeV and $p_{\mathrm{T}} > 8$ GeV would have to be prescaled.

Therefore, an additional muon would be needed to keep the trigger rate sufficiently low. However, since the addition of an extra muon at the L1T step would violate criterion (1), the third muon would have to be reconstructed at a later stage. The two displaced global muons are reconstructed in the first stage and then later used as seeds for the displaced tracker muon reconstruction.

With the requirement of three displaced tracker muons the trigger satisfies criteria (1-4), has sufficiently low trigger rate and has high trigger efficiency.

7.3.2 Implementation

An inclusive nonisolated triple muon trigger (`HLT_TrkMu15_DoubleTrkMu5NoFilters-NoVtx`) has been implemented in the trigger menu for data taking. It requires three muons, two

muons with $p_{\mathrm{T}} > 5$ GeV and one muon with $p_{\mathrm{T}} > 15$ GeV. The steps in the implementation of the trigger are shown in Tab. 7.1.

Table 7.1: Implementation of the trigger path.

Step	Explanation
1	Require two L1T muons with $p_{\mathrm{T}} > 12$ GeV and $p_{\mathrm{T}} > 5$ GeV or $p_{\mathrm{T}} > 10$ GeV and $p_{\mathrm{T}} > 3.5$ GeV
2	Reconstruct the L2 muons using algorithms optimized for displacement
3	Require two L2 muons, one of which has $p_{\mathrm{T}} > 10$ GeV
4	Reconstruct the L3 muons from the L2 muons using algorithms optimized for displacement
5	Require two L3 muons, one with $p_{\mathrm{T}} > 5$ GeV and one with $p_{\mathrm{T}} > 15$ GeV
6	Reconstruct the tracker muons from the L3 muons using algorithms optimized for displacement
7	Require three tracker muons: two with $p_{\mathrm{T}} > 5$ GeV and one with $p_{\mathrm{T}} > 15$ GeV

During the 2016 data taking period, the instantaneous luminosity of the machine gradually increased from 0.7×10^{34} cm^{-2}s^{-1} to 1.4×10^{34} cm^{-2}s^{-1}. The transverse momentum cuts on the muons in the L1T paths have been modified two times to cope with the increasing rate. `L1_DoubleMu_10_3p5` was replaced by `L1_DoubleMu_11_4` soon after the start of data taking. `L1_DoubleMu_12_6` has been added later as a backup trigger in the later stages of data taking. Table 7.2 lists the L1T selection and HLT versions used to take LHC data.

Table 7.2: List of triggers used to collect LHC data. All triggers are unprescaled during the entire 2016 data taking period.

L1T selection	**HLT version**	Run range
`L1_DoubleMu_10_3p5` OR `L1_DoubleMu_12_5`	`HLT_TrkMu15_DoubleTrkMu5NoFiltersNoVtx_v2`	272760 - 274443
`L1_DoubleMu_11_4` OR `L1_DoubleMu_12_5`	`HLT_TrkMu15_DoubleTrkMu5NoFiltersNoVtx_v3` `HLT_TrkMu15_DoubleTrkMu5NoFiltersNoVtx_v4`	274954 - 276244 276282 - 280385
`L1_DoubleMu_11_4` OR `L1_DoubleMu_12_5` OR `L1_DoubleMu_13_6`	`HLT_TrkMu15_DoubleTrkMu5NoFiltersNoVtx_v6`	281613 - 284044

7.3.3 Performance

7.3.3.1 Trigger Rate

The requirement of three muons in the trigger path ensures that the trigger rate remains low (≈ 1 Hz), despite the absence of a beamspot constraint on each of the muons. Figure 7.4 shows the rate of the signal and backup HLT path versus time during run 283270 (late 2016). Data is taken at a rate of about 1 Hz, i.e. only one in $40,000,000$ collision events is selected for the analysis. The corresponding L1T rates in that run are shown in Fig. 7.5. The rate curves typically decrease versus time after startup as protons are lost during the run and the proton bunches empty.

7.3.3.2 Trigger Efficiency

As mentioned before, the three muon legs ensure that the trigger is highly efficient for multi-muon signatures. This is illustrated below for MC and data events that match the signal topology. The efficiency has been calculated on events which have at least four reconstructed muons with $p_{\mathrm{T}} > 8$ GeV, of which one has $p_{\mathrm{T}} > 17$ GeV (see Sec. 7.4.2.3). The trigger efficiency is then the fraction of the selected events that pass the trigger. Figures 7.6 and 7.7 show the trigger efficiency as function of the leading muon p_{T}, η and ϕ for NMSSM and MSSMD MC events respectively. Figure 7.8 shows the efficiency on data events. It can be seen that the trigger efficiency drops beyond $|\eta| \sim 1$. This drop is a due to a well-known feature in the CMS muon endcap trigger system and will be discussed in Sec. 7.4.2.3. While these plots provide a rough quality indicator, the trigger efficiency on MC and data will be estimated in a more thorough way in Sec. 7.6.2.5.

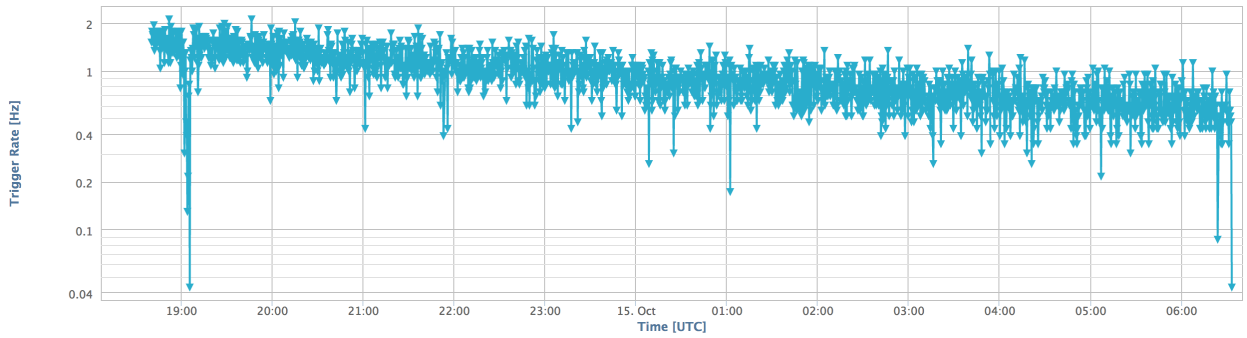

Figure 7.4: Trigger rate of the trigger path during run 283270, fill 5413 (October 14-15, 2016). The average trigger rate is about 1 Hz. Rate plots are obtained from CMS Web Based Monitoring (WBM) [167].

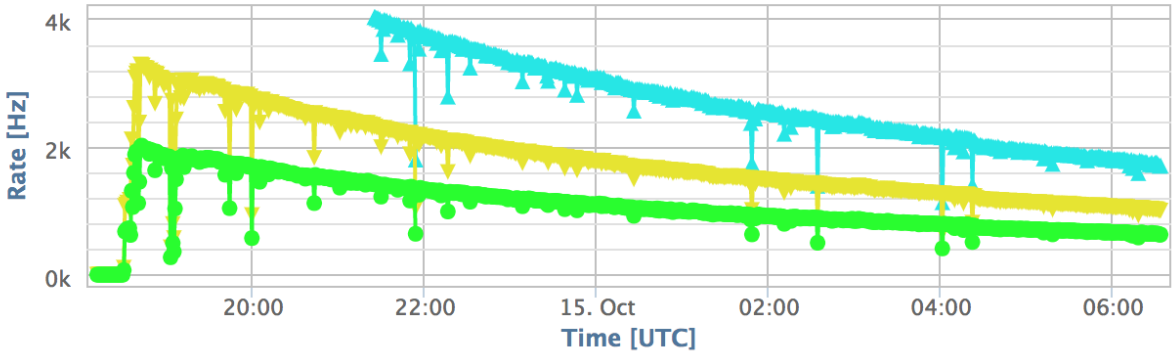

Figure 7.5: Rate of the L1T paths `L1_DoubleMu_11_4` (cyan), `L1_DoubleMu_12_5` (gold) and `L1_DoubleMu_13_6` (green) during run 283270, fill 5413 (October 14-15, 2016). The trigger `L1_DoubleMu_11_4` is turned off beyond a trigger rate of 4 kHz. Rate plots are obtained from CMS WBM.

7.4 Analysis Selections

In this section we describe in detail the event selection procedure.

7.4.1 Data Selection

This analysis is based on the full data sample recorded in 2016 by the CMS detector in pp collisions with 25 ns bunch spacing at a center-of-mass energy of $\sqrt{s} = 13$ TeV. The data only include runs when the LHC provided stable beams at 3.8 T and when the tracker, calorimeter and muon system participated in the data taking. Figure 7.9 shows the cumulative day-by-day

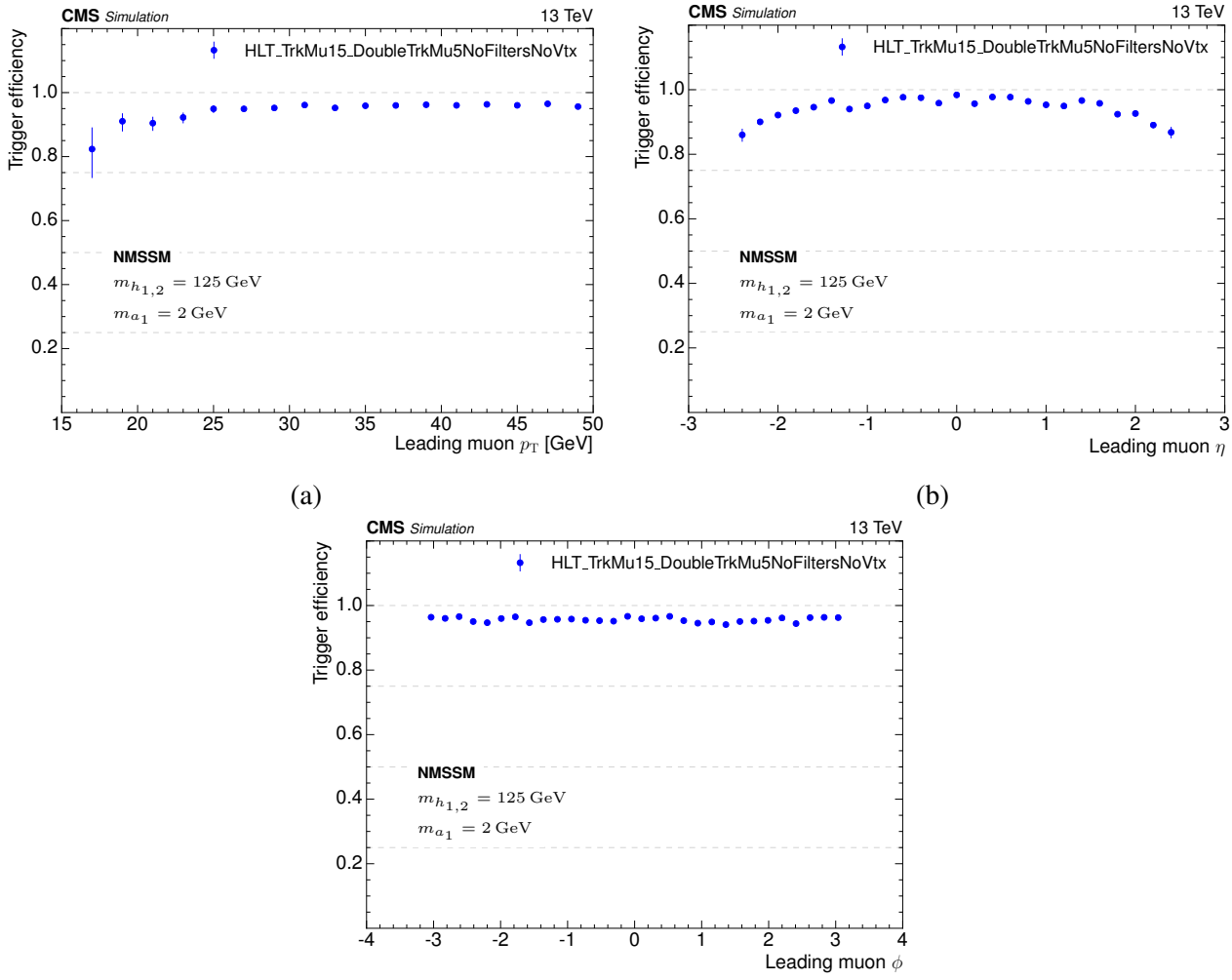

Figure 7.6: Trigger efficiency on MC simulated events in a NMSSM benchmark model with $m_{h_{1,2}} = 125$ GeV and $m_{a_1} = 2$ GeV. The efficiency is calculated for events with at least four reconstructed muons with $p_T > 8$ GeV, of which one has $p_T > 17$ GeV and is plotted as a function of the leading muon p_T, η and ϕ.

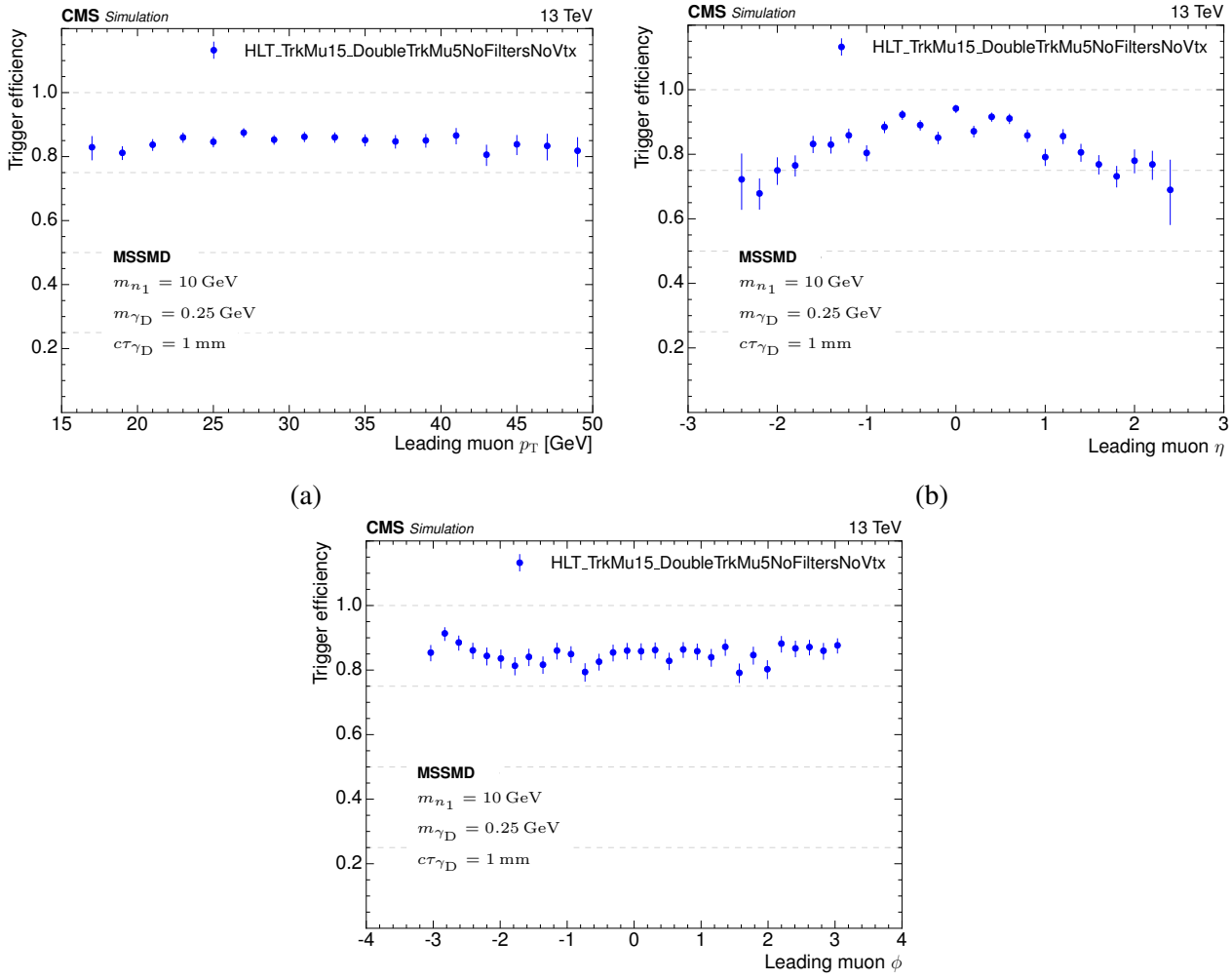

Figure 7.7: Trigger efficiency on MC simulated events in a MSSMD benchmark model with $m_{\gamma_D} = 0.25\,\text{GeV}$ and $c\tau_{\gamma_D} = 1\,\text{mm}$. The efficiency is calculated for events with at least four reconstructed muons with $p_T > 8\,\text{GeV}$, of which one has $p_T > 17\,\text{GeV}$, and is plotted as a function of the leading muon p_T, η and ϕ.

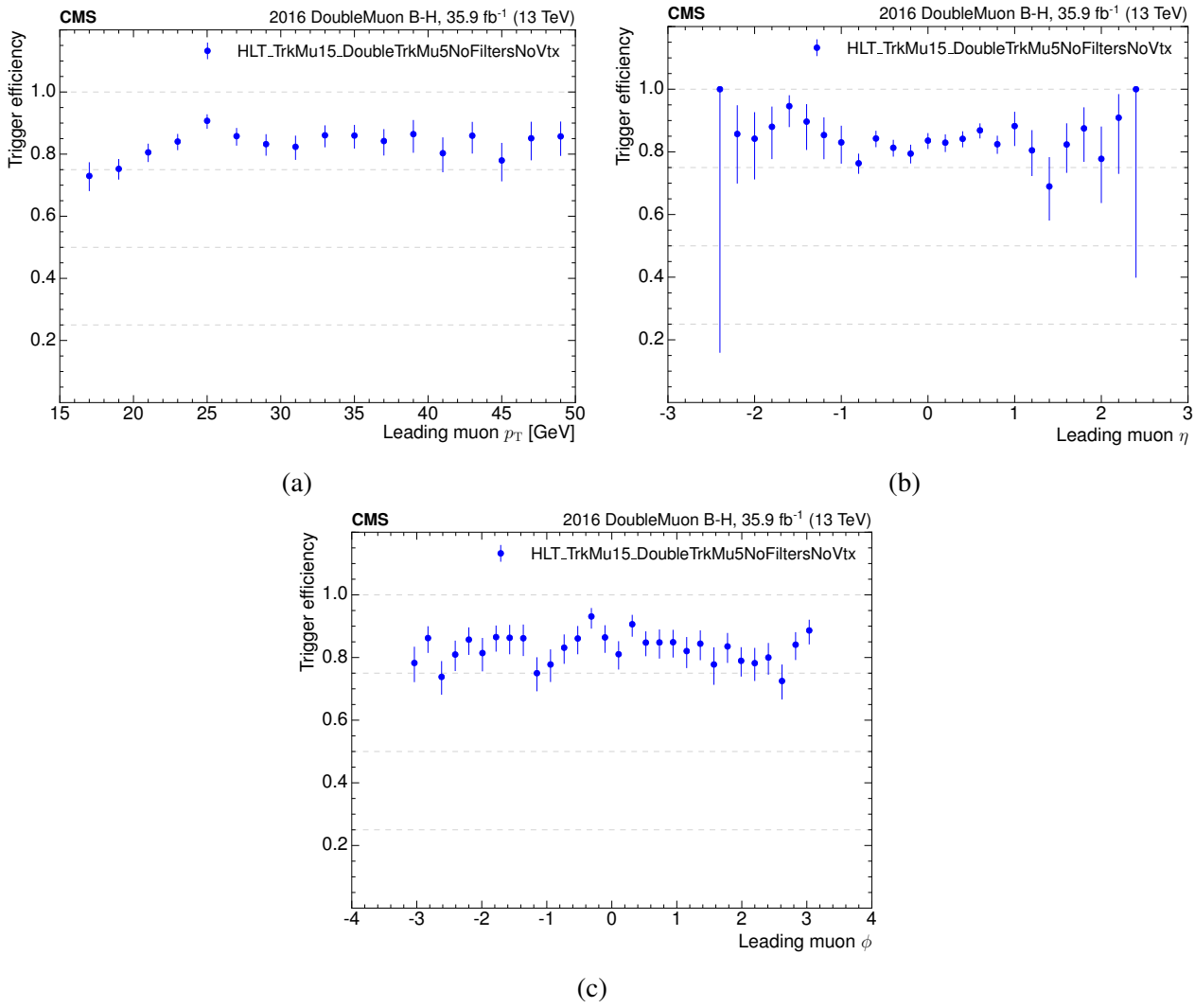

Figure 7.8: Trigger efficiency on data events in the DoubleMuon dataset. The efficiency is calculated for events with at least four reconstructed muons with $p_{\mathrm{T}} > 8$ GeV, of which one has $p_{\mathrm{T}} > 17$ GeV, and is plotted as a function of the leading muon p_{T}, η and ϕ.

integrated luminosity during the 2016 data taking period. CMS recorded $\int \mathcal{L}\, dt = 37.76\ \mathrm{fb}^{-1}$, of which $\int \mathcal{L}\, dt = 35.922\ \mathrm{fb}^{-1}$ has been certified by CMS for physics analyses.[2] This is equivalent to about 2.5×10^{15} collisions at $\sqrt{s} = 13\ \mathrm{TeV}$.

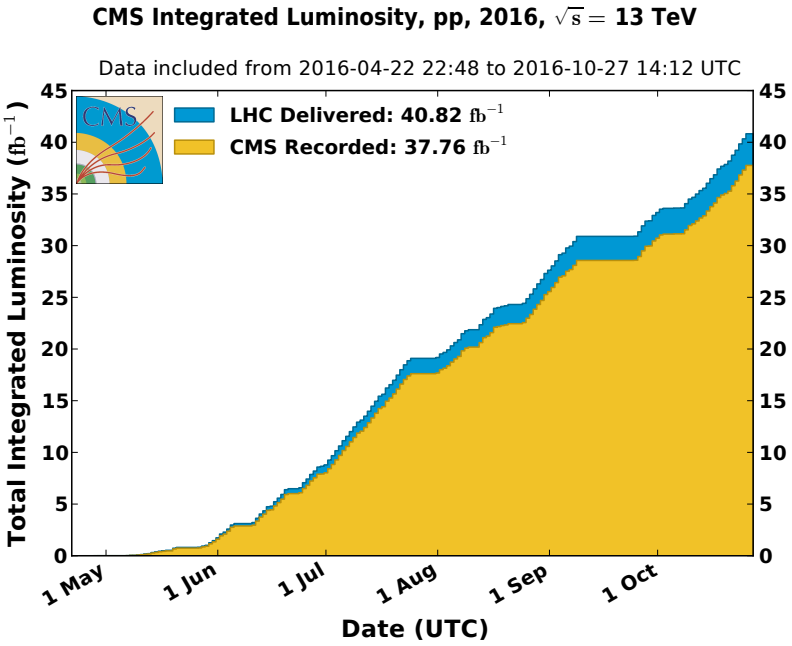

Figure 7.9: Integrated luminosity delivered by LHC (blue) and recorded by CMS (orange) versus day at $\sqrt{s} = 13\ \mathrm{TeV}$ center-of-mass energy in 2016. Copyright 2018 CERN for the benefit of the CMS Collaboration.

The DoubleMuon datasets are used in this search, which contain events with at least two L1T muons. Table 7.3 lists the names, run range and size of the datasets as published in CMSDAS.

7.4.2 Optimization of the Event Selection

In this section we will describe the selection procedure for real data and MC events.

[2]The certified runs, in range $[271036, 284044]$, are collected in the JSON file `Cert_271036-284044-_13TeV_PromptReco_Collisions16_JSON.txt`.

Table 7.3: Data samples in the DoubleMuon dataset. Multi-volume samples have their volume numbers in brackets.

Dataset name	Run range	Number of events
/DoubleMuon/Run2016B-07Aug17_ver[1,2]-v1/AOD	272760-275371	86,735,473
/DoubleMuon/Run2016C-07Aug17-v1/AOD	275656-276283	27,934,629
/DoubleMuon/Run2016D-07Aug17-v1/AOD	276315-276811	33,861,745
/DoubleMuon/Run2016E-07Aug17-v1/AOD	276831-277420	28,246,946
/DoubleMuon/Run2016F-07Aug17-v1/AOD	277932-278808	20,329,921
/DoubleMuon/Run2016G-07Aug17-v1/AOD	278820-280385	45,235,604
/DoubleMuon/Run2016H-07Aug17-v1/AOD	281085-284068	49,316,548
Total	272760-284068	291,660,866

7.4.2.1 Primary Vertex Selection

We require at least one well-reconstructed primary vertex in the event, which satisfies the quality requirements: (1) the vertex is "valid" and not "fake", (2) it has at least four associated tracks and (3) the global z coordinate of the primary vertex must be within $24\ \mathrm{cm}$ of the nominal CMS IP. The primary vertex reconstruction efficiency is nearly 100% in MC.

7.4.2.2 Muon Selection

In this search, the muon candidates are reconstructed with the PF algorithm and identified as *PF loose* muons. This means that the muons must also be reconstructed with either the *Tracker* or *Global* reconstruction algorithms. Each muon is required to pass a set of geometric and kinematic requirements: (1) pseudorapidity $|\eta| < 2.4$ and (2) transverse momentum $p_{\mathrm{T}} > 8\ \mathrm{GeV}$. The geometric requirement ensures that muons are reconstructed within the acceptance of the muon system. The kinematic requirement ensures that the event selection is not affected by turn-on effects at the trigger thresholds.

7.4.2.3 Baseline Event Selection

The baseline event selection derives from the signal event topology. At least four PF loose muons are required with kinematic and geometric cuts described in the previous section. One of these muons is required to have transverse momentum $p_{\mathrm{T}} > 17\ \mathrm{GeV}$. As mentioned in Sec. 7.3.3.2, the trigger efficiency drops in the forward region $|\eta| > 0.9$. This is due to a negative interference

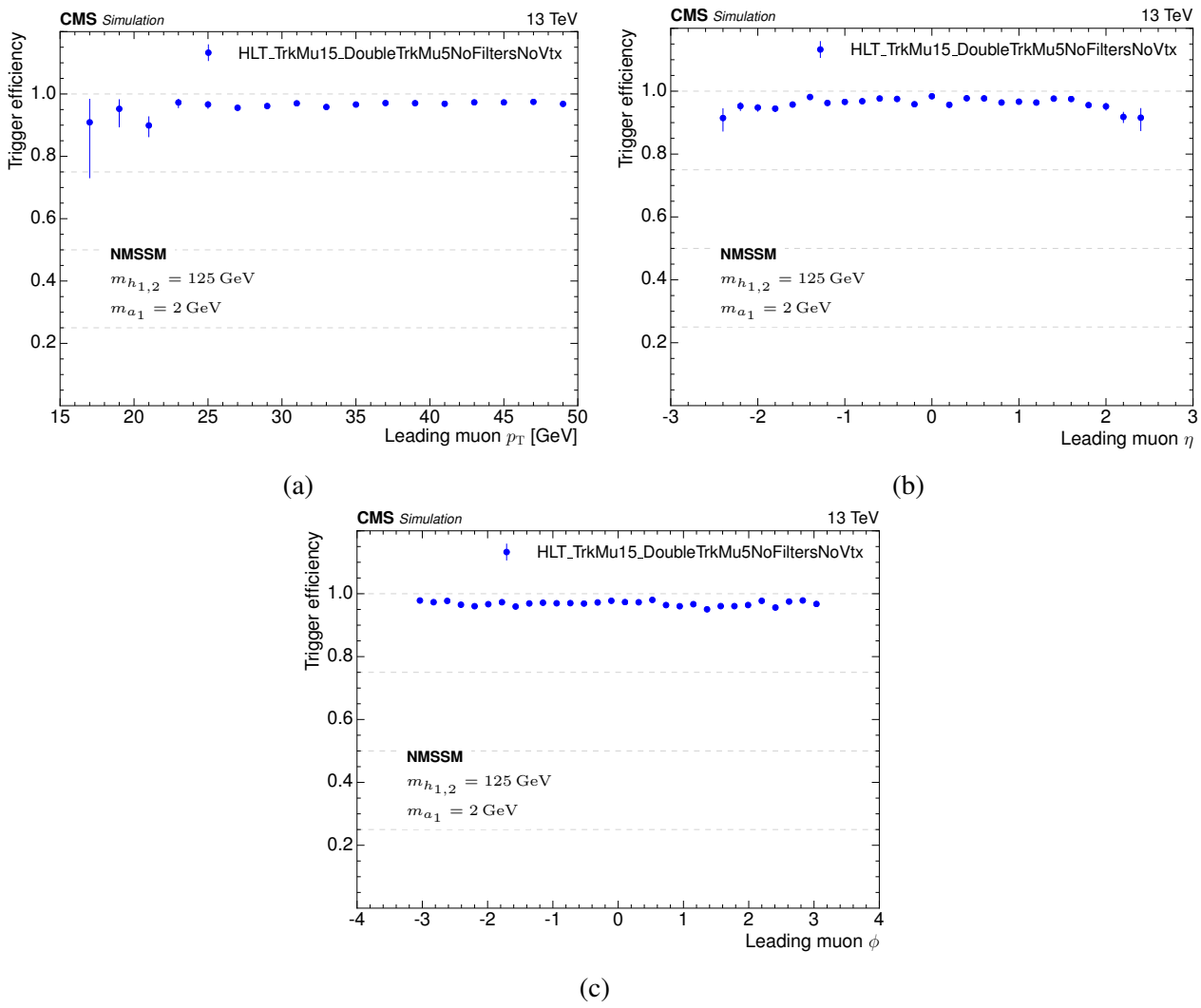

Figure 7.10: Trigger efficiency on MC simulated events in a NMSSM benchmark model with $m_{h_{1,2}} = 125$ GeV and $m_{a_1} = 2$ GeV. The efficiency is calculated for events with at least four reconstructed muons with $p_T > 8$ GeV, of which one has $p_T > 17$ GeV and is required to be in the barrel region, and is plotted as a function of the leading muon p_T, η and ϕ.

of multiple close-by muons in the endcap region, resulting in a reduction of muon reconstruction efficiency. These effects have also been studied in Ref. [168]. To enhance the model independence of the results, we require at least one muon with $p_T > 17$ GeV and $|\eta| < 0.9$ in the event. The effect is a much flatter trigger efficiency versus leading muon η. This is shown in Figs. 7.10 and 7.11 for the NMSSM and MSSMD benchmark scenarios. The additional selection on η reduces the signal acceptance by about $10 - 20\%$ in MC. Figure 7.12 shows the trigger efficiency in data.

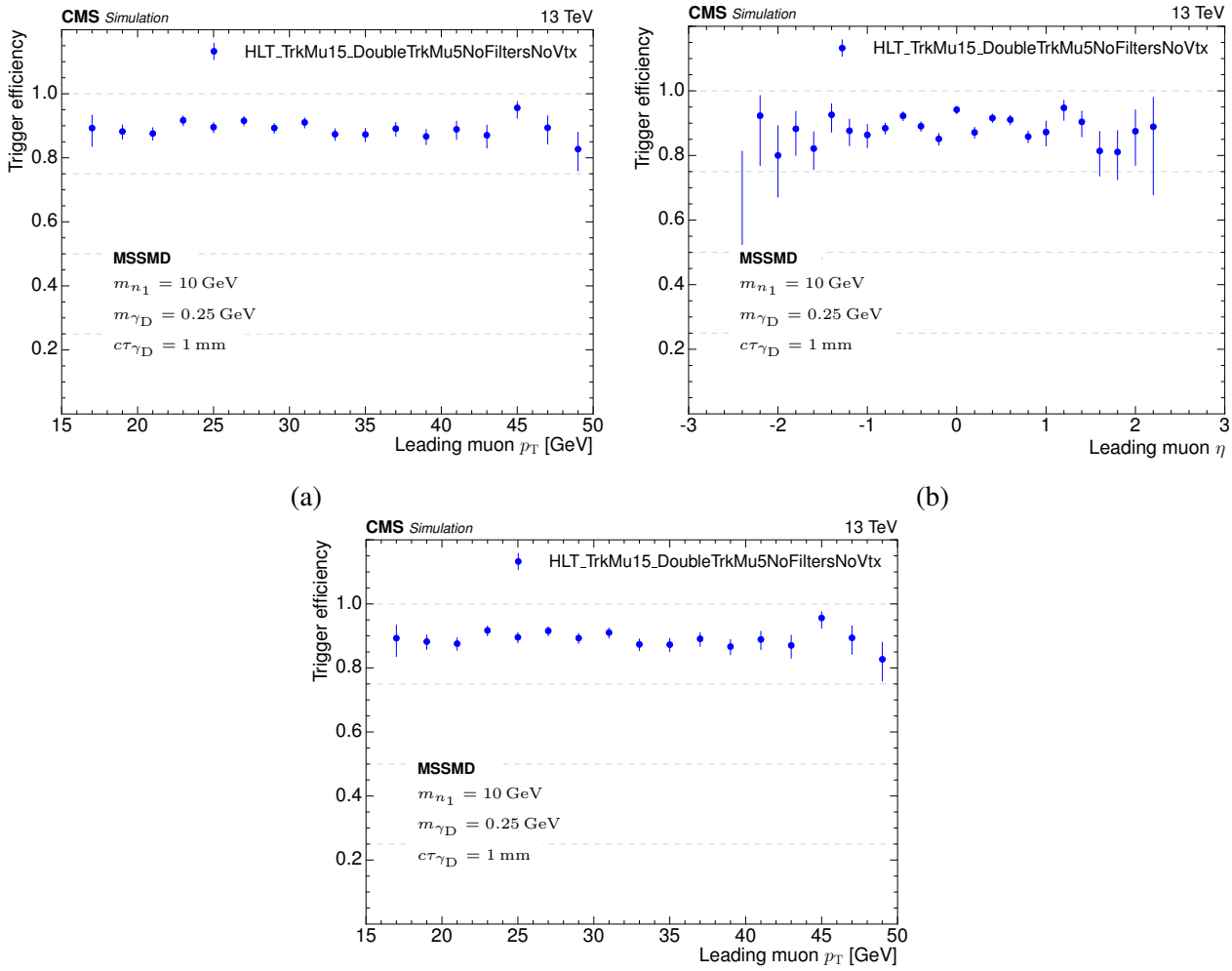

Figure 7.11: Trigger efficiency on MC simulated events in a MSSMD benchmark model with $m_{\gamma_D} = 0.25$ GeV and $c\tau_{\gamma_D} = 1$ mm. The efficiency is calculated for events with at least four reconstructed muons with $p_T > 8$ GeV, of which one has $p_T > 17$ GeV and is required to be in the barrel region, and is plotted as a function of the leading muon p_T, η and ϕ.

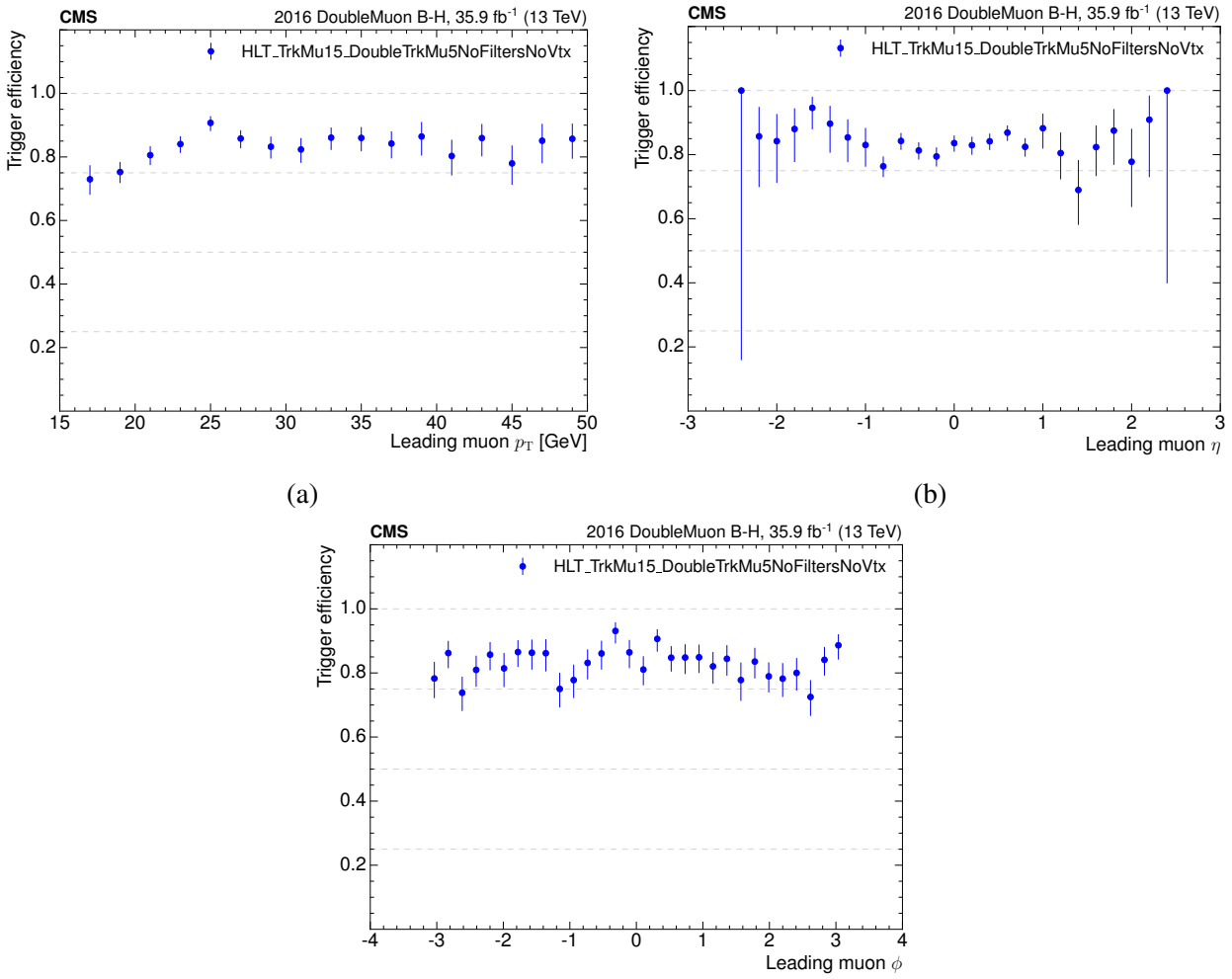

Figure 7.12: Trigger efficiency on data events in the DoubleMuon dataset. The efficiency is calculated for events with at least four reconstructed muons with $p_{\mathrm{T}} > 8$ GeV, of which one has $p_{\mathrm{T}} > 17$ GeV and is required to be in the barrel region, and is plotted as a function of the leading muon p_{T}, η and ϕ.

7.4.2.4 Muon Clustering

Since the muons must be consistent with having originated from the decay of a light boson, the muons are clustered into dimuons in three steps:

1. Construct a muon pair from two muons. Nearby muons are clustered into muon pairs if their invariant mass is less than $9\ \mathrm{GeV}$. This selection ensures that there is no contribution from Υ-meson or Z-boson decays. The mass cut is slightly higher than the $8.5\ \mathrm{GeV}$ mass point so that the clustering is not affected by resolution effects near the mass resonance. In addition, the muon pairs must satisfy at least one of the following requirements. Either the muon pair vertex from the KF has a vertex probability $P_{\mathrm{vertex}}(\mu^+\mu^-) > 1\%$ or the two muons are within $\Delta R(\mu^+\mu^-) < 0.01$. The latter compensates for the reduced efficiency of the vertex probability when the two muons are spatially close together (such as the case of boosted muons). Note that at this stage a muon can be associated to more than one pair. To prevent misidentification of the primary vertex the vertex of any muon pair is not required to be associated to any primary vertex in the event and multiple muon pairs are not required to share a common vertex.

2. Construct a muon jet from muon pairs. Multiple muon pairs are clustered into a muon jets if they share a common muon. No limit is set on the number muons in a muon jet.

3. Muon jets with exactly two muons are reconstructed as dimuons.

Finally, events with exactly two dimuons are selected. No limit is set on the number of unpaired (orphan) muons.

7.4.2.5 Fiducial Search Region

As mentioned in Sec. 7.2.2, the MSSMD benchmark model allows for light bosons that decay into a pair of displaced muons. The displacement of the muon negatively affects the performance of the muon reconstruction algorithms. If a muon is produced too far perpendicular from the beamline, too few tracker layers remain in which a hit can be recorded. On the other hand, if a

muon trajectory does not point back to the IP the transverse momentum measurement worsens. Both effects can introduce inefficiencies in the reconstruction algorithms, which can influence the model independence of the search. These effects are mitigated in the trigger by requiring the muons to be reconstructed with the tracker algorithm optimized for displaced muons.

It is instructive to investigate the dark photon reconstruction efficiency by looking at the performance of the dimuon reconstruction efficiency versus L_{xy} and $|L_z|$. This is shown in Fig. 7.13 and Fig. 7.14. The dimuon reconstruction efficiency as function of L_{xy} and $|L_z|$ can also be plotted.

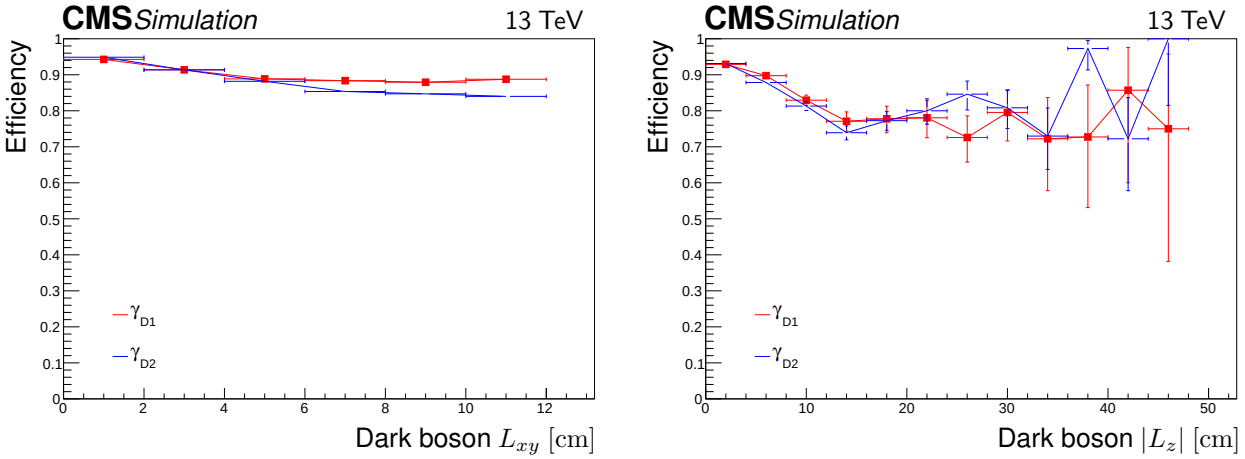

Figure 7.13: Reconstruction efficiency per dimuon as a function of L_{xy} (left) and $|L_z|$ (right) for the MSSMD MC samples $m_{\gamma_D} = 0.25$ GeV for all dark photon lifetimes $c\tau_{\gamma_D}$ combined. The blue dashed lines correspond to the layers of the pixel detector; barrel in L_{xy}, endcap in $|L_z|$. The dimuon that contains the leading p_T barrel muon is denoted as γ_{D1}. The other dimuon is denoted as γ_{D2}.

Fig. 7.15 shows the dimuon reconstruction efficiency as function of L_{xy} and $|L_z|$ for a dark photon mass of 0.25 GeV including all lifetimes. As can be seen, the dimuon reconstruction efficiency is high for small displacements, $L_{xy} < 9.8$ cm and $|L_z| < 46.5$ cm. The dimuon efficiency decreases with L_{xy} and $|L_z|$ as fewer hits are reconstructed in the pixel detector that participate in the track fit. To mitigate such reconstruction inefficiencies, a fiducial region - a cylinder - is constructed around the IP. We require that each dimuon must have at least one muon with at least one hit in the

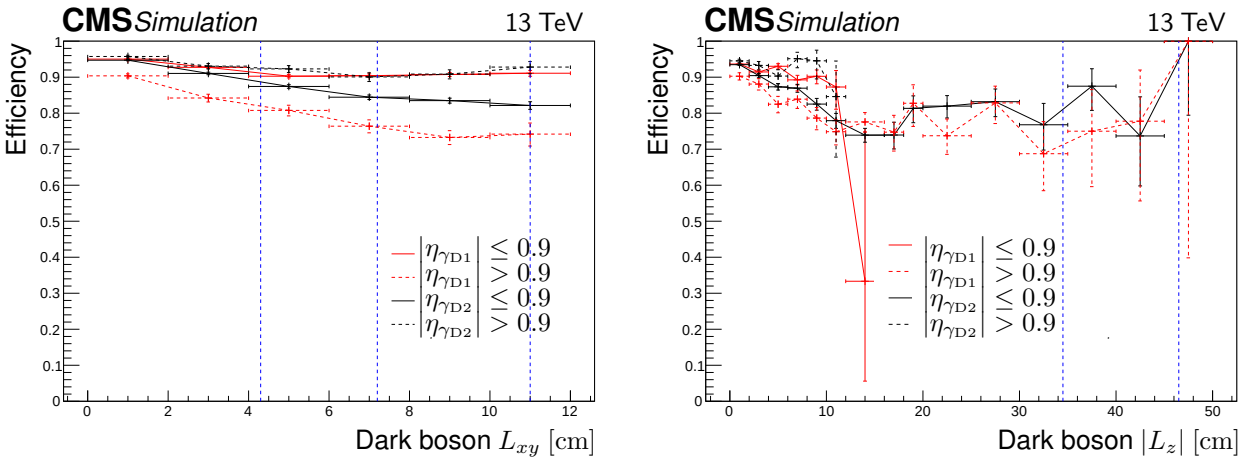

Figure 7.14: Reconstruction efficiency per dimuon as a function of L_{xy} (left) and $|L_z|$ (right) for the MSSMD MC samples $m_{\gamma_D} = 0.25$ GeV for all dark photon lifetimes $c\tau_{\gamma_D}$ combined, separated by η regions corresponding to the CMS detector geometry. The blue dashed lines correspond to the layers of the pixel detector; barrel in L_{xy}, endcap in $|L_z|$. The dimuon that contains the leading p_T barrel muon is denoted as γ_{D1}. The other dimuon is denoted as γ_{D2}.

pixel detector system. This corresponds to a maximum radial distance between the dimuon vertex and the nominal IP L_{xy} of 9.8 cm (third pixel barrel layer), and a maximum distance along the z-axis between the dimuon vertex and the nominal IP $|L_z|$ of 46.5 cm (second pixel endcap layer). The fiducial region is outlined as a gray dashed line in Fig. 7.15.

7.4.2.6 Dimuon Vertex Selection

In this search the two dimuons are produced in the decay chain of the same heavy parent particle. For both benchmark models the parent particle is a BSM Higgs boson with a mass between 90 and 150 GeV. The Higgs boson is much heavier and has a negligible lifetime, so that it decays at the beamline. We assume that the light bosons are produced sufficiently close the beamline. The light bosons production vertices should therefore also be close to the beamline and consistent with each other within the detector resolution.

To this end the z-position of the light boson "production vertex" $z_{\mu\mu}$ is calculated by extrapolating the dimuon production vertex in a straight line along the direction of the dimuon momentum to the beamline. The extrapolated dimuon vertex position is denoted as $z_{(\mu\mu)_1}$ for the first and

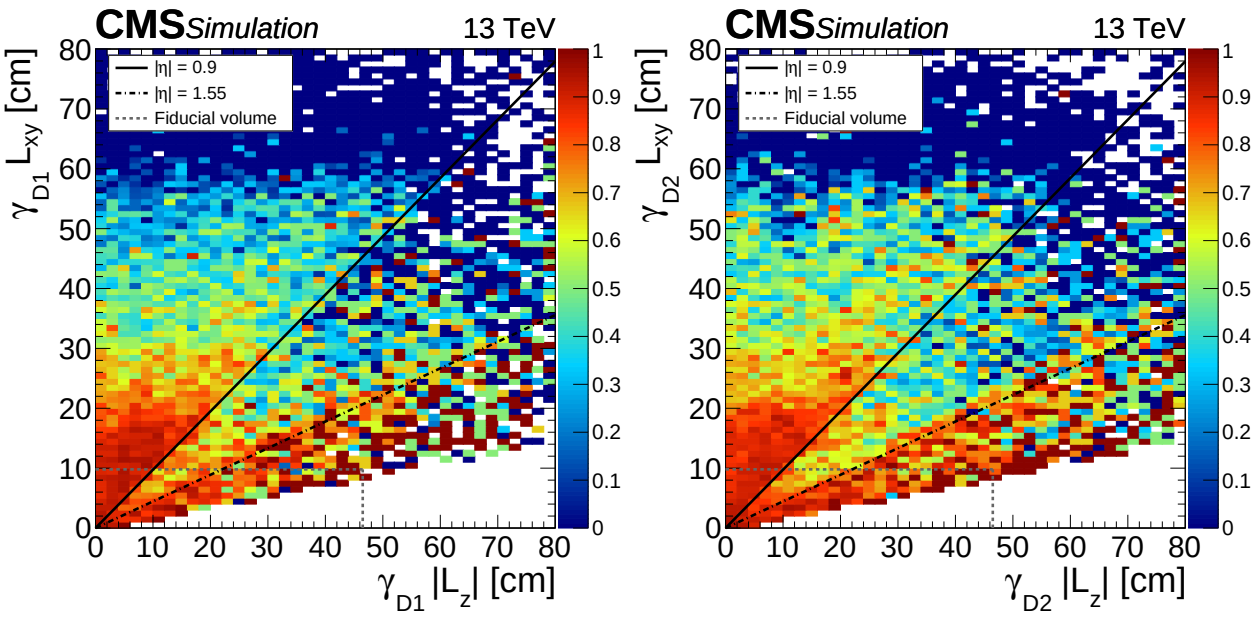

Figure 7.15: Dimuon reconstruction efficiency as function of L_{xy} and $|L_z|$ for a dark photon mass of 0.25 GeV including all lifetimes.

$z_{(\mu\mu)_2}$ for the second dimuon. The extrapolated $z_{(\mu\mu)_1}$ and $z_{(\mu\mu)_2}$ should then be consistent within the detector resolution along the beamline. Figure 7.16 shows $|z_{(\mu\mu)_1} - z_{(\mu\mu)_2}| = \Delta z$ for two representative mass points (including all lifetimes) in the MSSMD benchmark models. Also shown is the corresponding Δz distribution for the b-quark pair background dominated data sample with exactly three muons, for which Δz is calculated as the difference between $z_{\mu\mu}$ of the dimuon and z_{μ} of the orphan muon. As can be seen, the Δz distribution of the b-quark pair background is much wider than for the MC signal distribution. The topology of b-quark pair background events is very different than the signal topology. Neither the dimuon nor the orphan muon are capturing the direction of the original b quarks correctly, due to the unaccounted b-jet constituents in the muon and dimuon momentum. A requirement that $|z_{(\mu\mu)_1} - z_{(\mu\mu)_2}| < 0.1$ cm is sufficiently loose so that the selection is highly efficient for all signal samples. It is important to note that this requirement allows for a nonnegligible lifetime of the light boson to accommodate for signatures with long-lived particles, such in the case for the MSSMD benchmark model.

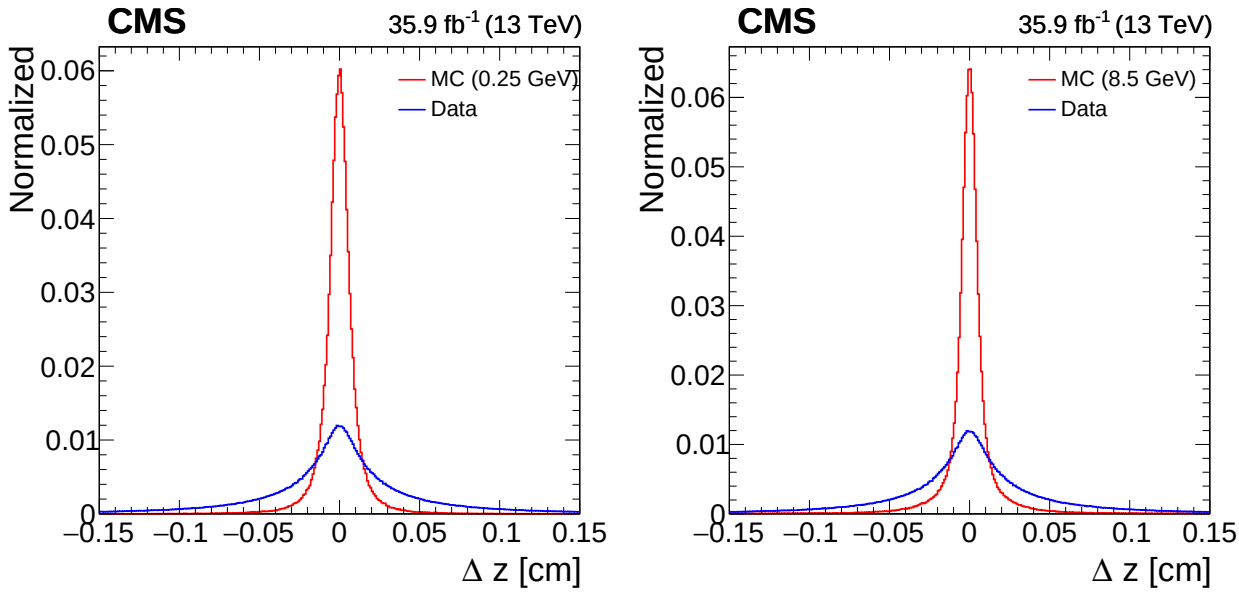

Figure 7.16: Distance between vertices measured for two dimuons $\Delta z = z_{(\mu\mu)_1} - z_{(\mu\mu)_1}$ in the MSSMD simulated sample with $m_h = 125$ GeV and $m_{\gamma_D} = 0.25$ GeV, and for dimuon and orphan muon ($\Delta z = z_{\mu\mu} - z$) in events from the b-quark pair background enriched part of the DoubleMuon data sample.

7.4.2.7 Dimuon Isolation

As mentioned in Sec. 7.1, the leading background in this analysis constitutes multimuon events where the muons have been produced in double b-quark events, where the b quarks decay semileptonically or through light mesonic resonances such as $\rho(770)$, $\omega(782)$, $\phi(1020)$, $J/\psi(3097)$ and $\psi(2S)(3686)$. The muons in these decays are typically produced in the vicinity of other particles such as light hadrons. By applying isolation around the muons, we can significantly reduce this background. The relative isolation introduced in Sec. 6.3.1.2 could affect the model independent interpretation of the results. Therefore, an absolute isolation value is calculated instead. Tracks with $p_T > 0.5$ GeV within $\Delta R(\text{track} - \mu\mu) < 0.4$ and $\Delta z(\text{track} - \mu\mu) < 0.1$ cm are selected. Tracks forming the dimuon are excluded.

$$\text{Iso}_{\mu\mu} = \sum_{\text{tracks} \notin \mu\mu} p_T(\text{track}) < 2 \text{ GeV}. \tag{7.1}$$

Tracks from nearby pileup collisions do not contribute to the isolation as the position between two interactions in the same bunch crossing is significantly larger than 0.1 cm. As such, the dimuon isolation definition is insensitive to pileup with as much as 30 interactions. Figure 7.17 shows the dimuon isolation for a MSSMD signal sample and the b-quark pair background. We require the total isolation to be less than 2 GeV. This selection reduces the signal acceptance by about 20%, but trims the background by a factor of 30.

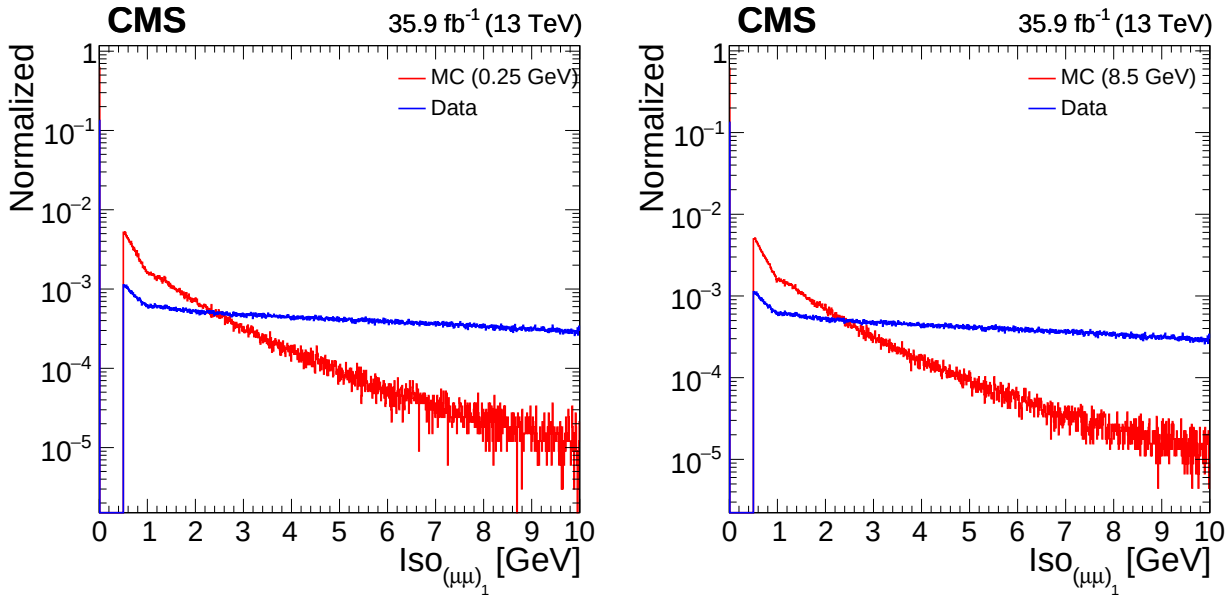

Figure 7.17: Dimuon isolation for a MSSMD simulated sample with $m_h = 125$ GeV and $m_{\gamma_D} = 0.25$ GeV, and for a b-quark pair background enriched data sample.

7.4.2.8 Dimuon Mass

The dimuons are expected to be produced in the decay of same type of new light boson. Therefore, the invariant masses of two dimuons in the event should be the same. Because the light boson interacts only weakly with SM particles, the width of the mass peak is driven by detector resolution. The width of the dimuon mass in CMS has been studied with light SM resonances in Ref. [168]. The core width is given by $\sigma(m_{\mu\mu}) = 0.026$ GeV $+ 0.013\ m_{\mu\mu}$. We require that the

dimuon masses are consistent within five times the core width of the mass distribution.

$$\left|m_{(\mu\mu)_1} - m_{(\mu\mu)_2}\right| < 0.13 \text{ GeV} + 0.065 \times \frac{m_{(\mu\mu)_1} + m_{(\mu\mu)_2}}{2} \tag{7.2}$$

This criterion carves out a diagonal corridor in the two dimensional dimuon-dimuon invariant mass plane, in which the mass difference between the two dimuons is less than five times the core width. Figure 7.18 is a two dimensional distribution of $m_{(\mu\mu)_1}$ versus $m_{(\mu\mu)_2}$ for the simulated MSSMD samples (using all lifetimes).

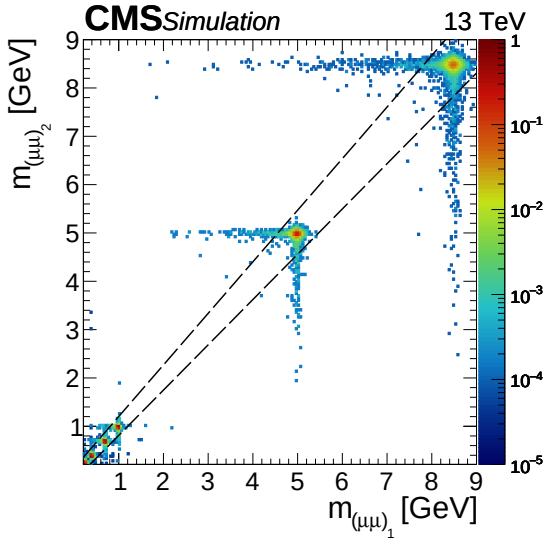

Figure 7.18: Distribution of $m_{(\mu\mu)_1}$ versus $m_{(\mu\mu)_2}$ for the simulated MSSMD samples (using all lifetimes). The signal region is enclosed by the dashed lines and is described by Eq. 7.2.

7.4.3 Summary of the Selection Efficiencies

The data event selection procedure is summarized in Tab. 7.4. The tables in Appendices F and G list the event selection efficiencies at each step for several representative points for the NMSSM and MSSMD benchmark models using fully-reconstructed simulated events. As a reference, two cumulative efficiencies are also listed for events, the acceptance α_{gen} and the full reconstruction efficiency ϵ_{full}.

Table 7.4: Summary of the event selection

Step	Selection
	Online selection
1	Trigger
	Basic Reco level selections
2	Good primary vertex
3	$p_{\mathrm{T}_1} > 17$ GeV, $\lvert\eta_1\rvert < 0.9$
4	$p_{\mathrm{T}_2} > 8$ GeV, $\lvert\eta_2\rvert < 2.4$
5	$p_{\mathrm{T}_3} > 8$ GeV, $\lvert\eta_3\rvert < 2.4$
6	$p_{\mathrm{T}_4} > 8$ GeV, $\lvert\eta_4\rvert < 2.4$
	Extra Reco level selections
7	Two muon jets
8	Two dimuons
9	Pixel hit requirement
10	$\lvert z_{(\mu\mu)_1} - z_{(\mu\mu)_2}\rvert < 0.1$ cm
11	$\mathrm{Iso}_{(\mu\mu)_{1,2}} < 2$ GeV
12	$m_{(\mu\mu)_1} \approx m_{(\mu\mu)_2}$

The acceptance facilitates a future reinterpretation of the results of this analysis into models with the same final state. It is calculated using generator level information only, as in the case of a perfect Monte Carlo simulation. It is defined as the fraction of generated Monte Carlo events that pass the selections at the generator level, i.e. $\alpha_{\mathrm{gen}} = N_{\mathrm{gen,sel}}/N_{\mathrm{gen}}$. The generator level selection requires at least four muons with $|\eta| < 2.4$ and $p_{\mathrm{T}} > 8$ GeV, of which at least one muon with $|\eta| < 0.9$ and $p_{\mathrm{T}} > 17$ GeV, and a maximum displacement of $L_{xy} < 9.8$ cm and $|L_z| < 46.5$ cm for the light bosons.

The obtained acceptance of the analysis selection requirements with respect to m_{γ_D} and $c\tau_{\gamma_D}$ is shown in Fig. 7.19, where the solid bullets represent points for the simulated MSSMD MC samples.

The full selection efficiency ϵ_{full} is defined as the fraction of generated MC events that pass the full analysis selection summarized in Table 7.4, i.e. $\epsilon_{\mathrm{full}} = N_{\mathrm{reco,sel}}/N_{\mathrm{reco}}$.

Values for ϵ_{full}, α_{gen} and $\epsilon_{\mathrm{full}}/\alpha_{\mathrm{gen}}$ are provided for the NMSSM and MSSMD benchmark models in Appendices F and G. The results for a few representative NMSSM and MSSMD signal models are also shown in Tab. 7.5 and Tab. 7.6. The values of $\epsilon_{\mathrm{full}}/\alpha_{\mathrm{gen}}$ for all benchmark models are

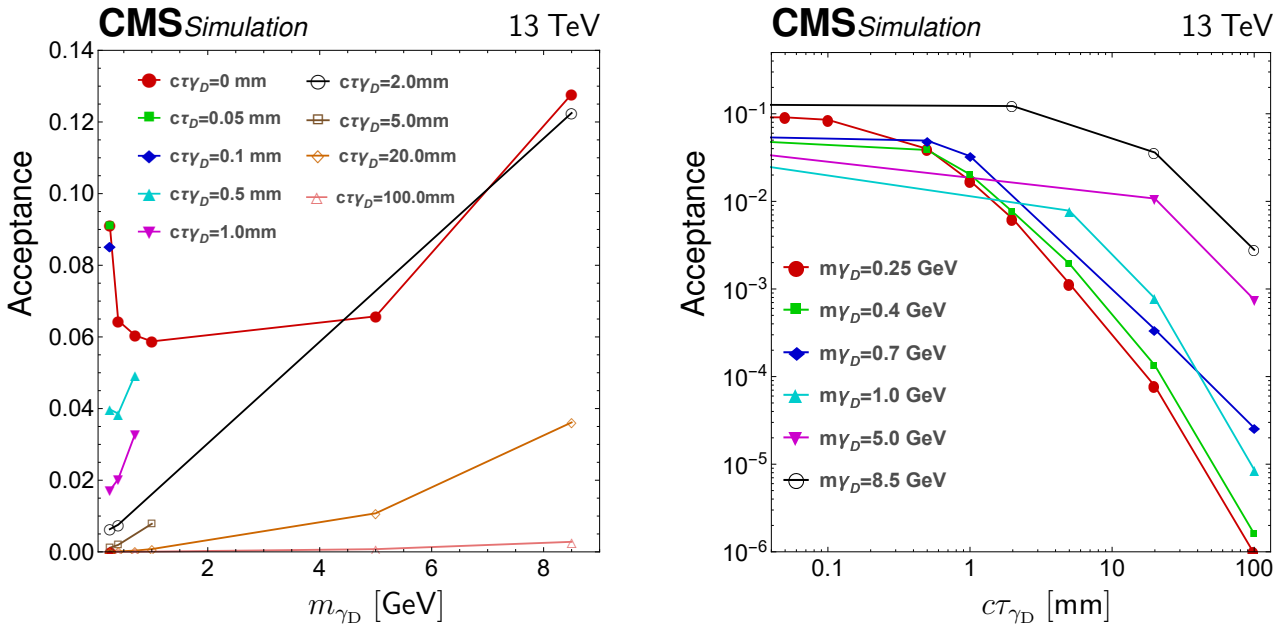

Figure 7.19: Acceptance of the analysis selection requirements evaluated using the simulated MC samples for several sets of m_{γ_D} and $c\tau_{\gamma_D}$ (solid bullets). For these plots the bullet points at which the efficiency is evaluated are connected by a simple line to guide the eye.

plotted in Fig. 7.20. It can be seen that $\epsilon_{\text{full}}/\alpha_{\text{gen}}$ is quasi independent of m_a and m_h in the case of NMSSM. In the case of MSSMD, the $\epsilon_{\text{full}}/\alpha_{\text{gen}}$ distributions are quasi independent of $c\tau_{\gamma_D}$. For models with large displacements $c\tau_{\gamma_D} = 100$ mm, few events pass the full event selection, resulting in large uncertainties on $\epsilon_{\text{full}}/\alpha_{\text{gen}}$. The model independence is important so that the results can be reinterpreted in the context of similar new physics models. Excluding these points, the weighted average ratio is calculated to be $\epsilon_{\text{full}}/\alpha_{\text{gen}} = 0.61 \pm 0.06$. The error is taken as the largest spread of the values $\epsilon_{\text{full}}/\alpha_{\text{gen}}$.

Table 7.5: Signal acceptance over the full reconstruction efficiency $\epsilon_{\text{full}}/\alpha_{\text{gen}}$ for several representative signal NMSSM benchmark models.

m_{h_1}[GeV]	90	100	110	125	150
m_{a_1}[GeV]	2	0.5	3	1	0.75
ϵ_{full}[%]	8.85 ± 0.06	13.23 ± 0.08	11.96 ± 0.07	14.68 ± 0.08	18.48 ± 0.09
α_{gen}[%]	13.93 ± 0.08	20.47 ± 0.09	19.24 ± 0.09	23.59 ± 0.10	29.93 ± 0.10
$\epsilon_{\text{full}}/\alpha_{\text{gen}}$[%]	63.52 ± 0.29	64.62 ± 0.24	62.19 ± 0.25	62.23 ± 0.22	61.73 ± 0.20

Table 7.6: Signal acceptance over the full reconstruction efficiency $\epsilon_{\text{full}}/\alpha_{\text{gen}}$ for several representative signal MSSMD benchmark models.

m_{γ_D}[GeV]	0.25			8.5		
$c\tau_{\gamma_D}$[mm]	0	1	5	0	2	20
ϵ_{full}[%]	9.12 ± 0.21	1.72 ± 0.06	0.12 ± 0.01	12.78 ± 0.12	12.25 ± 0.06	3.61 ± 0.02
α_{gen}[%]	13.52 ± 0.25	2.85 ± 0.07	0.20 ± 0.01	20.49 ± 0.14	20.05 ± 0.08	6.16 ± 0.03
$\epsilon_{\text{full}}/\alpha_{\text{gen}}$[%]	67.47 ± 0.91	60.24 ± 1.27	58.39 ± 2.04	62.36 ± 0.38	61.10 ± 0.21	58.70 ± 0.24

7.4.4 Modeling of the Signal Shape

We now turn to the modeling of the signal shape in the dimuon mass spectrum. Good knowledge of the signal shape is important since both signal and background shapes are used in the final fit to data, and thus in the interpretation of the results. The new light bosons are expected to interact weakly with SM fermions. Therefore, the width of the dimuon invariant mass (signaling the light boson decay) is determined solely by the detector resolution, which is driven by the intrinsic spatial resolution of the tracker, CSC and DT system. Radiative losses in the detector and momentum mismeasurement causes the invariant mass peak to broaden. While radiative losses only affect the low-mass tail, momentum mismeasurement may affect both tails of the distribution. The momentum resolution for prompt (or almost prompt) muons in this analysis is $< 1 - 2\%$ (Sec. 6.2.1.2), so acceptance losses due to the dimuon mass constraint are driven by the description of radiative losses in the simulation.

SM particles such as the light neutral hadronic states ω, ϕ, J/ψ, and $\psi(2S)$ exhibit a similar behavior as the new light bosons. The width of the invariant mass spectrum of these dimuon resonances has been studied in Ref. [168] where the shapes are modeled with a Crystal Ball function with four parameters $m_0, \sigma, \alpha\ (> 0)$ and $n\ (> 0)$:

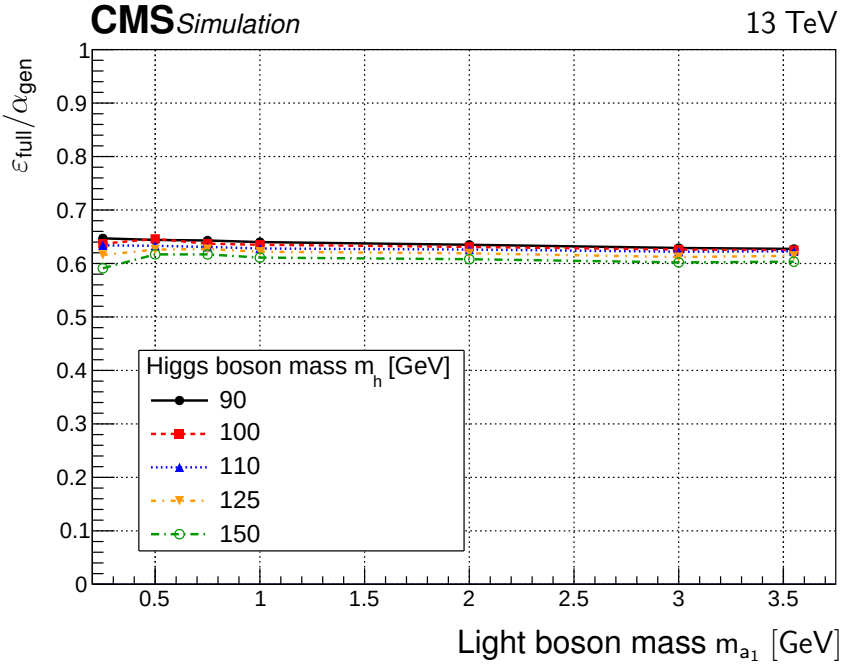

(a)

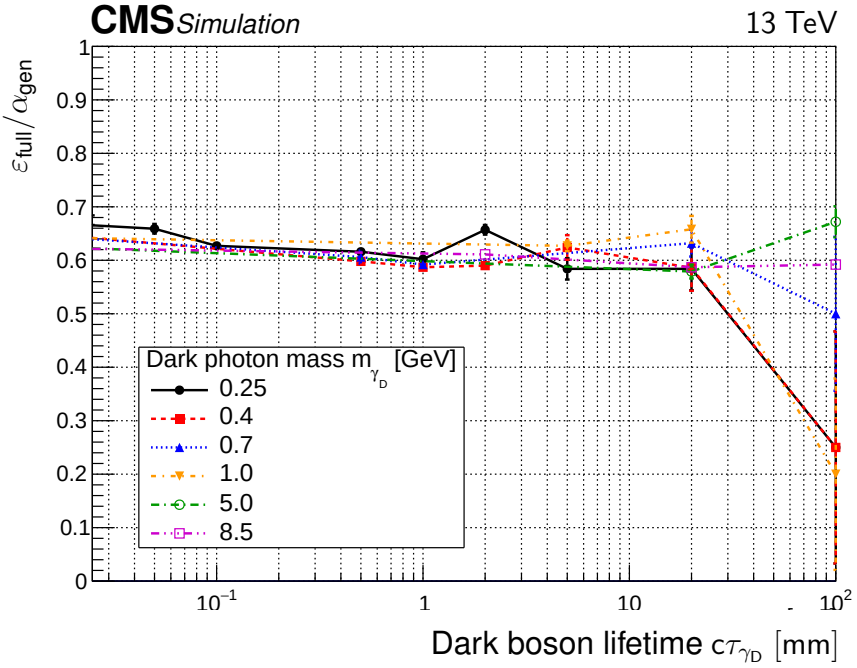

(b)

Figure 7.20: Summary of the values $\epsilon_{\text{full}}/\alpha_{\text{gen}}$ for each mass point in the NMSSM (top) and MSSMD (bottom) benchmark models.

$$CB(m; m_0, \sigma, \alpha, n)$$
$$= N \times \begin{cases} \exp(-\frac{(m-m_0)^2}{2\sigma^2}), & \text{for } \frac{m-m_0}{\sigma} > -\alpha \\ \left(\frac{n}{|\alpha|}\right)^n \exp\left(-\frac{|\alpha|^2}{2}\right) \left(\frac{n}{|\alpha|} - |\alpha| - \frac{m-m_0}{\sigma}\right)^{-n}, & \text{for } \frac{m-m_0}{\sigma} \leqslant -\alpha \end{cases} . \quad (7.3)$$

The parameters m_0, σ, are the same as for a Gaussian, whereas α and n generate the tails. The Crystal Ball function is asymmetric and can have a long tail towards $m < m_0$, depending on n. The signal shapes for a few mass points are shown in Fig. 7.21. The influence of the Crystal Ball function as the signal shape on the acceptance has been studied in Ref. [168] and used in this dissertation. The uncertainty on the acceptance due to the signal shape is 1.5% and is quoted as a systematic uncertainty.

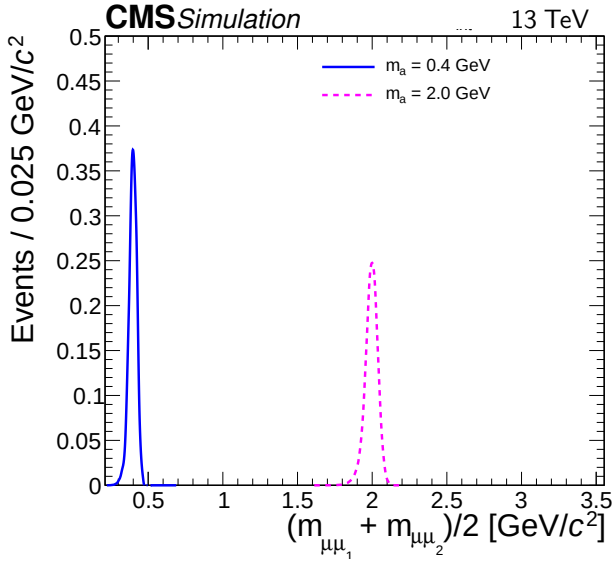

Figure 7.21: Crystal Ball templates for signal samples projected on the diagonal line $m_{(\mu\mu)_1} = m_{(\mu\mu)_2}$ for two masses.

7.5 Background Estimation

We considered three backgrounds that can mimic the signal shape: (1) b-quark pair production (Sec. 7.5.1), (2) prompt double J/ψ production (Sec. 7.5.2) and (3) higher-order electroweak processes (Sec. 7.5.3). In this chapter we shall discuss each background in detail and estimate its contribution in the signal region.

7.5.1 B-quark Pair Production

7.5.1.1 Description of the Background

A first source of background is b-quark pair production. Such processes can emulate signal if both b quarks decay into a muon pair via double semileptonic decay of the b quarks and the daughter c quarks, or via light meson resonances such as $\rho(770)$, $\omega(782)$, $\phi(1020)$, $J/\psi(3097)$ and $\psi(2S)(3686)$. The predominant contribution is from J/ψ which has an enhanced branching fraction $\Gamma(J/\psi \to \mu^+\mu^-)$. The lighter ρ and ω decay primarily to pions, whereas ϕ decays into kaons. J/ψ mesons produced in the decay of b quark are typically displaced with respect to the IP due to the large b-quark lifetime. Muons from light mesons are correctly identified as PF muons with 90% efficiency at a track $p_{\mathrm{T}} \sim 10$ GeV. This identification efficiency decreases with increasing track p_{T} [153]. Figure 7.22 shows a diagram in which two b quarks decay double semileptonically into a total of four muons.

In addition to the b-quark decay modes with four real muons mentioned above, a small fraction of events can contribute to this background if one or more charged tracks is misidentified as a real muon. This happens when a charged track from b-quark decay is incorrectly matched to a nearby real muon segment, resulting in two muon candidates. The misidentification efficiency of a light meson as a muon is around $1-2\%$ at $p_{\mathrm{T}} > 10$ GeV [153]. The fraction of events with one or more misidentified tracks decreases with increasing muon momentum.

It is important to note that the dimuon isolation requirement guarantees that the two dimuons originate from two well-separated b jets.

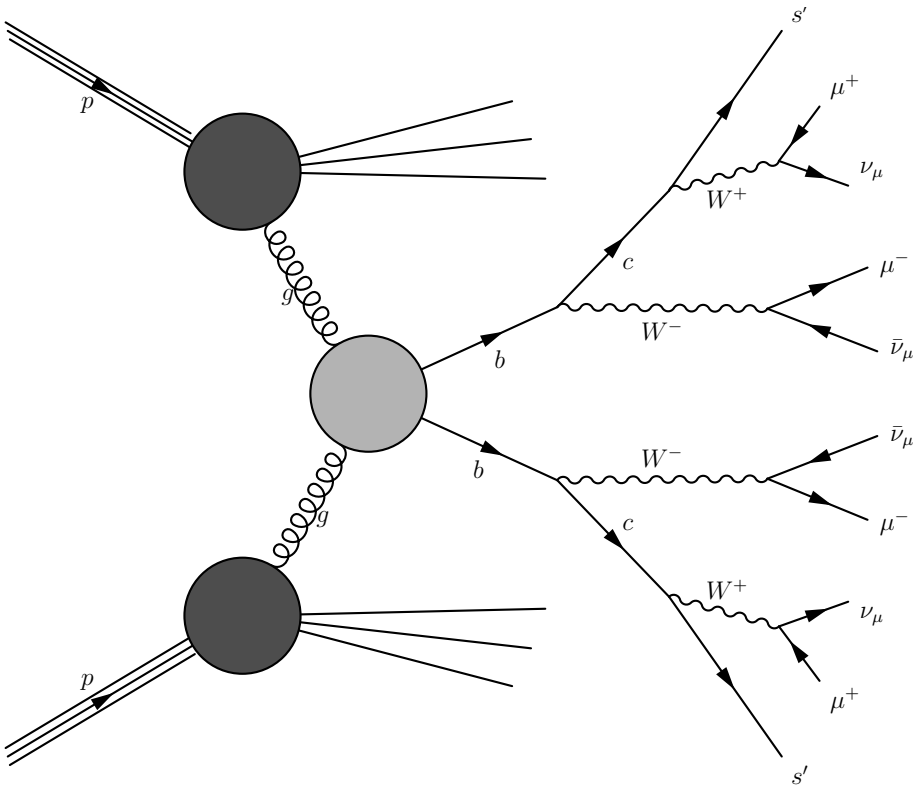

Figure 7.22: Example diagram of a four-muon event through b-quark pair production in which both b quarks decay double semileptonically. Note that in this diagram the W bosons are all off-shell.

7.5.1.2 Overview of the Method

A data-driven approach is chosen to study this background for three reasons: (1) events with multiple muons in the decay of b or c quarks are not well understood in MC simulation, (2) events with multiple muons are rare so a large dataset would be required for an accurate background estimation and (3) b quarks are produced abundantly at the LHC.

The contribution is estimated in the following sections. A template is first constructed in a control region (Sec. 7.5.1.3). Events are selected using the procedure in Sec. 7.5.1.4. The template is parameterized using analytical functions in Sec. 7.5.1.5. Normalization of the template done in Sec. 7.5.1.6 yields the estimate in the signal region. Finally, the result is cross-checked in Sec. 7.5.1.7.

7.5.1.3 Construction of the Template

This section describes the construction of a 2D template in the $(m_{(\mu\mu)_1}, m_{(\mu\mu)_2})$ plane for $0.25 < m_{(\mu\mu)_1} < 9$ GeV and $0.25 < m_{(\mu\mu)_2} < 9$ GeV covering both the diagonal and off-diagonal part.

Considering the fact that the two b quarks decay independently of each other, we expect two components, each contributing differently to the total 2D mass template. The 2D mass template will therefore be a Cartesian product of two unique 1D templates: one for the b quark decaying in the exclusively in the barrel region and one for the other b-quark decaying in the barrel or endcap region. The kinematic requirements for the two dimuons are therefore slightly different. One dimuon is required to contain at least one high-p_{T} muon ($p_{\mathrm{T}} > 17$ GeV) in the barrel region ($|\eta| < 0.9$), while the other dimuon requires only muons with $p_{\mathrm{T}} > 8$ GeV in the barrel or endcap region ($|\eta| < 2.4$). Because of these reasons, the two 1D templates will have different shapes and therefore need to be constructed independently.

We denote the dimuon that contains at least high-p_{T} muon as a "high-p_{T}" dimuon. A dimuon that does not contain such muon is denoted as a "low-p_{T}" dimuon. Taking this into account, two cases of b-quark background events need to be considered: (1) events with two high-p_{T} dimuons (of which at least one muon in the barrel region) and (2) events with a high-p_{T} dimuon in the barrel region and low-p_{T} dimuon.

Let $S_{17}(m_{\mu\mu})$ be the 1D mass template associated to the high-p_{T} dimuon and $S_8(m_{\mu\mu})$ be the 1D mass template associated to the low-p_{T} dimuon. The 2D mass template associated to case (1) is then $S_1(m_{(\mu\mu)_1}, m_{(\mu\mu)_2}) = S_{17}(m_{(\mu\mu)_1}) \times S_{17}(m_{(\mu\mu)_2})$ and to case (2) is $S_2(m_{(\mu\mu)_1}, m_{(\mu\mu)_2}) = S_{17}(m_{(\mu\mu)_1}) \times S_8(m_{(\mu\mu)_2})$. Let $N_{17,17}$ and $N_{17,8}$ be the event count associated to case (1) and case (2) respectively, the resulting normalized 2D template can then be written as:

$$S(m_1, m_2) = \frac{N_{17,17}}{N_{17,17} + N_{17,8}} \left(S_{17}(m_1) \times S_{17}(m_2)\right) + \frac{N_{17,8}}{N_{17,17} + N_{17,8}} \left(S_{17}(m_1) \times S_8(m_2)\right), \quad (7.4)$$

with $m_1 \equiv m_{(\mu\mu)_1}$ and $m_2 \equiv m_{(\mu\mu)_2}$. This 2D template can be factorized as follows:

$$S(m_1, m_2) = S_{17}(m_1) \times \left(\frac{N_{17,8}}{N_{17,8} + N_{17,17}} S_8(m_2) + \frac{N_{17,17}}{N_{17,8} + N_{17,17}} S_{17}(m_2) \right) \tag{7.5}$$

or as $S(m_1, m_2) = S_{17}(m_1) \times S_{mix}(m_2)$, with

$$S_{mix}(m_2) = \frac{N_{17,8}}{N_{17,8} + N_{17,17}} S_8(m_2) + \frac{N_{17,17}}{N_{17,8} + N_{17,17}} S_{17}(m_2). \tag{7.6}$$

It is clear that the 2D template is a Cartesian product of the 1D template S_{17} (for high-p_{T} dimuons) and the 1D template S_{mix} (which is a mix of high-p_{T} and low-p_{T} dimuons).

7.5.1.4 b-quark Background Event Selection

A background-enriched sample is used to obtain the background templates S_{17} and S_{mix}. Events are collected from the DoubleMuon dataset and with the same trigger as for the signal selection. Exactly three muons are required in each event: two muons forming a dimuon and one orphan muon (see Sec. 7.4.2.4). One muon is required to have $p_{\mathrm{T}} > 17$ GeV within $|\eta| < 0.9$, while the other two muons are only required to have $p_{\mathrm{T}} > 8$ GeV. In addition, we require in each event: (1) a good primary vertex, (2) exactly one dimuon with a reconstructed secondary vertex, (3) the distance between the dimuon vertex and the orphan vertex, $\Delta z(\mu\mu, \mu_{\mathrm{orphan}})$, is less than 0.1 cm, (4) the dimuon has a hit in barrel pixel layers $1-3$ or endcap pixel layers 1 or 2, and (5) the dimuon has a maximum isolation of 2 GeV.

With the selections above, the sample is heavily dominated by b-quark pair events, while the kinematics are nearly identical to those of the sample for the signal selection.

The S_{17} 1D template is obtained using only events with a high-p_{T} dimuon. Figure 7.23a shows the resulting 1D high-p_{T} distribution. The S_{mix} 1D template uses events with both high-p_{T} and low-p_{T} dimuons. Note that when the dimuon is low-p_{T}, the orphan muon needs to have $p_{\mathrm{T}} > 17$ GeV within $|\eta| < 0.9$. Figure 7.23b shows the resulting 1D low-p_{T} distribution.

As can be seen, both distributions look similar. However, S_{mix} has an enhanced bulk component

and slightly broader resonances. This is clearly the case for J/ψ, but is less prominent for other light meson resonances. Dimuons in $S_{\rm mix}$ are on average less energetic and a fraction of them fall in the muon endcap region, which has a poorer $p_{\rm T}$ resolution.

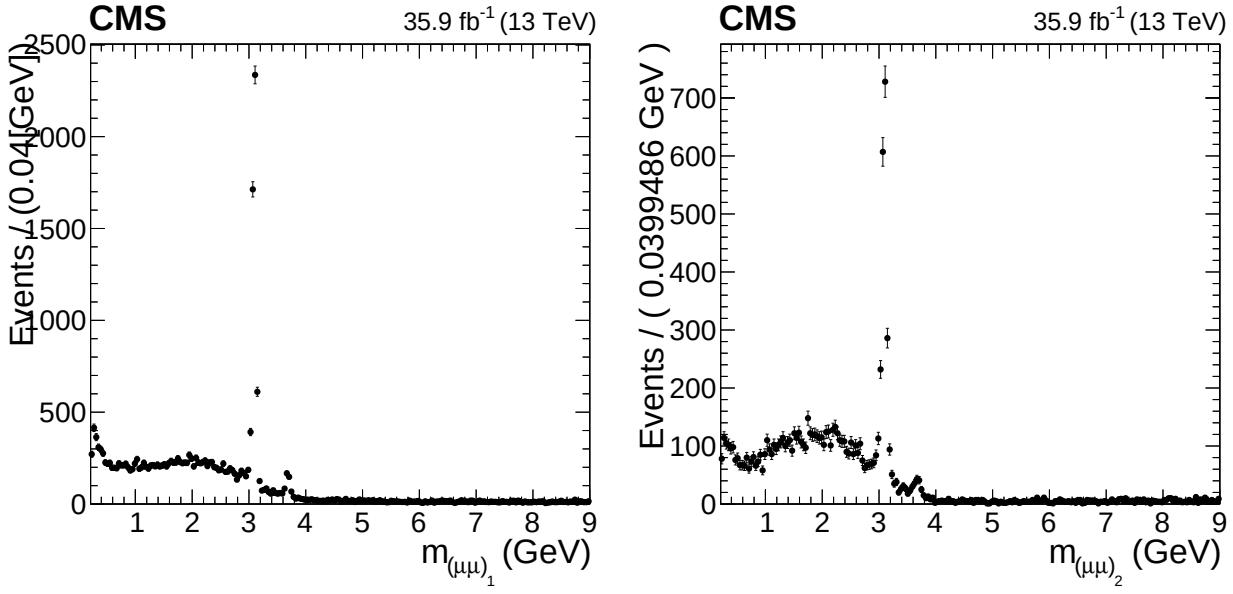

(a) S_{17} (b) $S_{\rm mix}$

Figure 7.23: The S_{17} (left) and $S_{\rm mix}$ (right) distributions for dimuons obtained with background-enriched data samples.

7.5.1.5 Parameterization of the Template

The 1D templates acquired in the previous section are fit with an analytic parametric function in the region $0.25 < m < 9$ GeV. The parametric description is convenient to build the final 2D template. The inputs to the parametric function are Gaussian distributions, $G(m; m_0, \sigma)$, for each of the low mass mesons: $\eta(548), \omega(782), \phi(1019)$ and $\psi(3686)$. For each Gaussian the average mass, m_0, is fixed to the PDG mass (Ref. [7]) and the width, σ, is fixed to the detector resolution (see Tab. 7.7). The J/ψ peak is modeled with a Crystal Ball function, $CB(m; m_{J/\psi}, \sigma_{J/\psi}, \alpha_{J/\psi}, n_{J/\psi})$. $\sigma_{J/\psi}$, $\alpha_{J/\psi}$, $n_{J/\psi}$ are obtained in Sec. 7.4.4, $\sigma_{J/\psi}$ is allowed to float in the fits. A Bernstein polynomial of order six, $B(m; p_{06}, ..., p_{66})$, is used to model the electroweak continuum. Note that

Bernstein polynomials are positive-definite in their domain, which is a necessary element to have a well-behaving distribution. A Gaussian complemented with a decaying exponential is added in the low mass region to model the kinematic behavior for mass values smaller than $0.5\ \mathrm{GeV}$.

Table 7.7: Mass and detector resolution of each light meson used in the template fit. The light meson masses are the world average ones obtained from Ref. [7].

Light meson	m_0 [GeV]	Detector resolution σ [GeV]
η	0.548	0.030
ω	0.782	0.031
ϕ	1.019	0.033
J/ψ	3.095	0.040
ψ	3.686	0.050

The 1D parametric description of each 1D template is thus of the form

$$\begin{aligned}
&BG(m;p_\eta, p_\omega, p_\phi, p_{J/\psi}, \alpha_{J/\psi}, \sigma_{J/\psi}, p_\psi, p_B, p_{06}, ..., p_{66}) \\
&\quad = p_\eta G(m; m_{0,\eta}, \sigma_\eta) + p_\omega G(m; m_{0,\omega}, \sigma_\omega) \\
&\quad + p_\phi G(m; m_{0,\phi}, \sigma_\phi) + p_\psi G(m; m_{0,\psi}, \sigma_\psi) \\
&\quad + p_{J/\psi} CB(m; m_{J/\psi}, \sigma_{J/\psi}, \alpha_{J/\psi}, n_{J/\psi}) \\
&\quad + p_B B(m; p_{06}, ..., p_{66}) \\
&\quad + p_{AH} G(m; m_{0,AH}, \sigma_{AH}) \\
&\quad + p_{E0} \left[\left(\frac{p_{E0}}{m} \right)^2 - 1 \right]^{p_{E1}} \times \exp \left[-p_{E2} \left[\left(\frac{p_{E0}}{m} \right)^2 - 1 \right] \right]
\end{aligned} \tag{7.7}$$

where p_η, p_ω, p_ϕ, $p_{J/\psi}$, p_ψ and p_B are normalization factors for the resonances and bulk component respectively obtained from the fit.

The fitted templates for S_{17} and S_{mix} are shown in Fig. 7.24a and in Fig. 7.24b respectively as solid red lines. The 2D template, constructed from $S_{17} \times S_{\mathrm{mix}}$, is shown in Fig. 7.25. The fitted parameter uncertainties and their correlations are taken into account in the final fit to data.

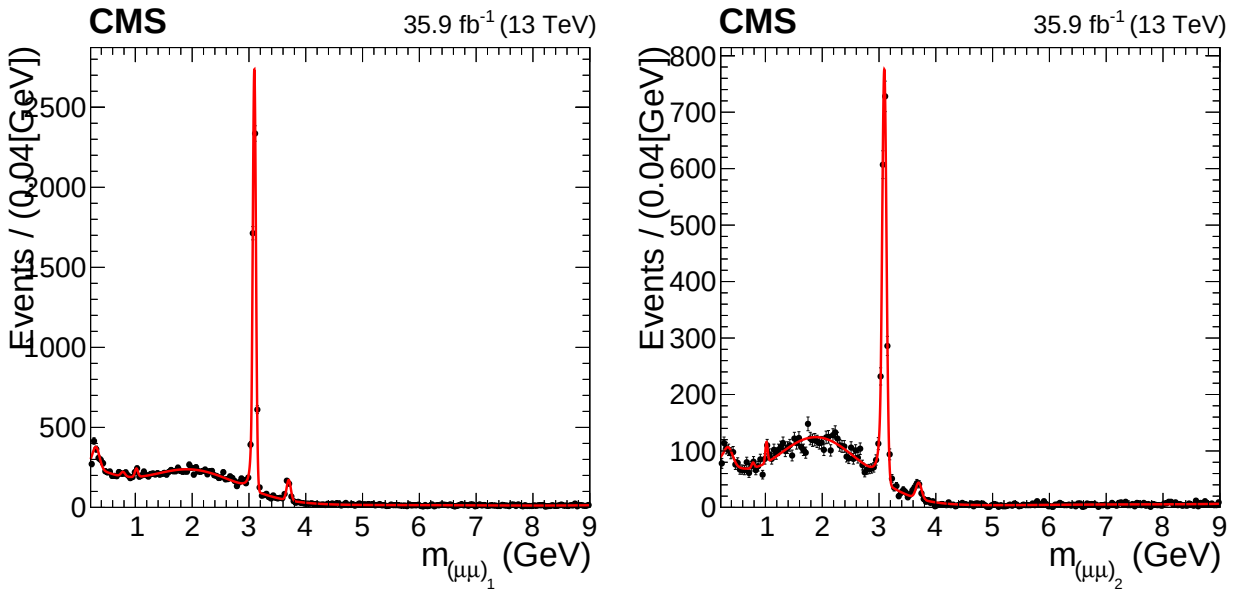

(a) S_{17} (b) S_{mix}

Figure 7.24: The S_{17} (left) and S_{mix} (right) fitted templates (solid lines) for dimuons obtained with background-enriched data (solid circles) samples.

7.5.1.6 Normalization of the Template

The 2D template is normalized in the region 0.25 to 9 GeV, i.e.

$$\int_{0.25}^{9} dm_{(\mu\mu)_1} \int_{0.25}^{9} dm_{(\mu\mu)_2}\, S_{17}(m_{(\mu\mu)_1}) \times S_{\mathrm{mix}}(m_{(\mu\mu)_2}) = 1. \tag{7.8}$$

To estimate the background contribution in the signal region, we calculated the ratio R of the template integral in the diagonal region over the off-diagonal region:

$$R = \frac{\int dm_{(\mu\mu)_1} \int dm_{(\mu\mu)_2}\, S_{17}(m_{(\mu\mu)_1}) \times S_{\mathrm{mix}}(m_{(\mu\mu)_2}) \theta(|m_{(\mu\mu)_1} - m_{(\mu\mu)_2}| < 5\sigma(m_{\mu\mu}))}{\int dm_{(\mu\mu)_1} \int dm_{(\mu\mu)_2}\, S_{17}(m_{(\mu\mu)_1}) \times S_{\mathrm{mix}}(m_{(\mu\mu)_2}) \theta\left(|m_{(\mu\mu)_1} - m_{(\mu\mu)_2}| > 5\sigma(m_{\mu\mu})\right)}, \tag{7.9}$$

where the integrals run from 0.25 to 9 GeV. The function $\theta\left(|m_{(\mu\mu)_1} - m_{(\mu\mu)_2}| < 5\sigma(m_{\mu\mu})\right)$ restricts the 2D integral to the diagonal region and $\theta\left(|m_{(\mu\mu)_1} - m_{(\mu\mu)_2}| > 5\sigma(m_{\mu\mu})\right)$ to the off-diagonal region. This ratio has been found to be $R = 0.1444/0.8566$.

A total of 43 events are observed in the off-diagonal region passing the signal selection. We es-

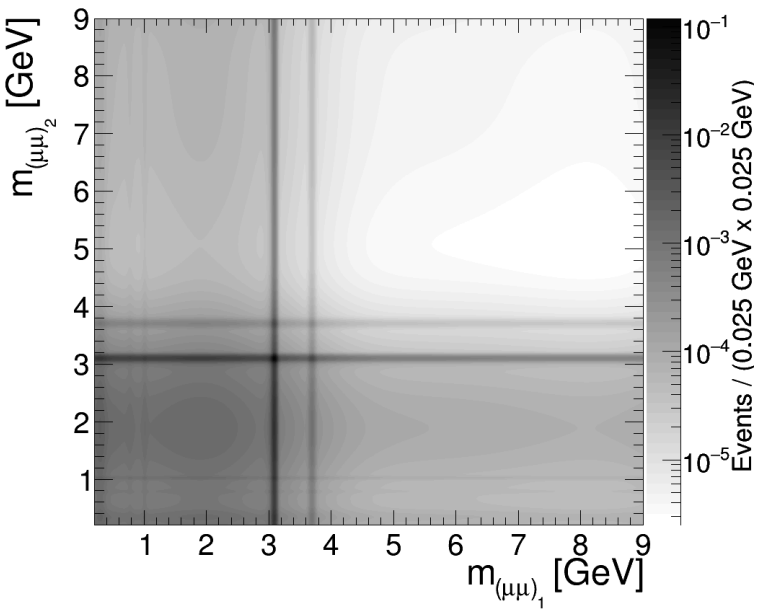

Figure 7.25: The 2D analytical template for distribution of the dimuon masses obtained using background-enriched data sample.

timate the background yield in the diagonal region as $N_{b\bar{b},\text{ signal region}} = (43 \pm \sqrt{43}) \times 0.1444/0.8566 = 7.26 \pm 1.11$ events. Figure 7.26 shows the background events in the off-diagonal sideband region overlaid on top of the 2D template.

7.5.1.7 Validation of the Template

The technique is validated in two different ways which are discussed below.

7.5.1.7.1 Template Fit to Nonisolated Data with Two Dimuons

A first check is the stability of the template method in absence of a cut on the dimuon isolation. A high statistics b-quark pair background-enriched sample is obtained using the selections in Sec. 7.4.2, but without the dimuon isolation requirement. Events in the signal region are excluded to avoid accidental unblinding in case a large signal is present in the data. Hence, only the off-diagonal part of the dimuon-dimuon mass space is examined.

The 1D S_{17} and S_{mix} templates are overlaid on the $m_{(\mu\mu)_1}$ and $m_{(\mu\mu)_2}$ distributions respectively in the b-quark pair background-enriched data. The results are shown in Fig. 7.27a and

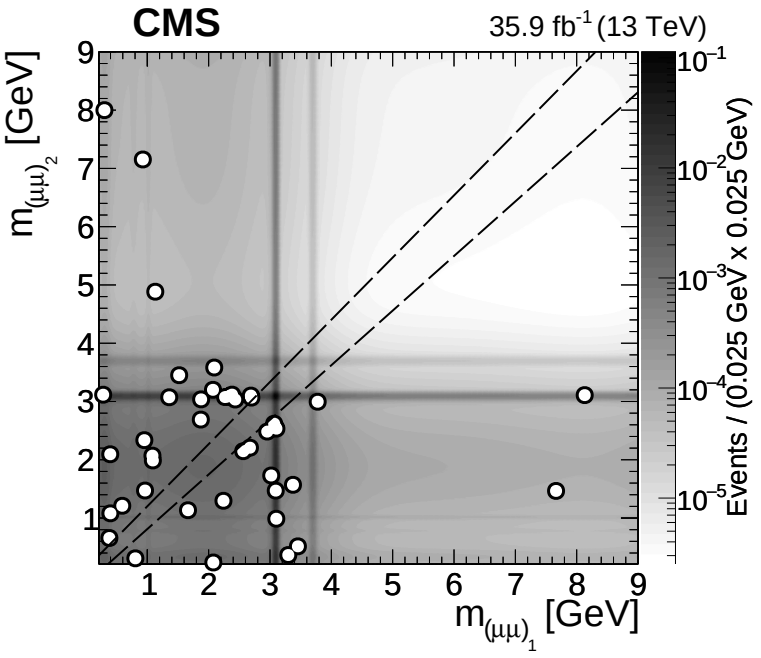

Figure 7.26: Distribution of the invariant masses $m_{(\mu\mu)_1}$ vs. $m_{(\mu\mu)_2}$ for the 43 events in the data (shown as empty circles) surviving all selections but failing the dimuon mass consistency requirement, $|m_{(\mu\mu)_1} - m_{(\mu\mu)_2}| < 5\sigma(m_{\mu\mu})$. The diagonal signal region (outlined with dashed lines) remains blind.

Fig. 7.27b. The combined 1D template $S_{17}+S_{\rm mix}$ is also overlaid to the distribution $m_{(\mu\mu)_1}+m_{(\mu\mu)_2}$ (Fig. 7.27c) as a cross-check. Figure 7.27d is a zoom of near the J/ψ resonance. All 1D templates used in the fits are normalized to the number of selected data events. The results in Fig. 7.27 demonstrate that the analytic templates, obtained with b-quark pair enriched data, provide a good description of the dimuon mass distributions in data with two dimuons.

7.5.1.7.2 Relaxing the Dimuon Isolation

A second check is the stability of the event yield in the signal region with respect to the different dimuon isolation values. The procedure above is repeated for dimuon isolation values 5, 10, and 50 GeV. With each dimuon isolation a new template is constructed and the yield in the signal region is re-evaluated. The results are shown in Tab. 7.8. The event yields are consistent within their uncertainty. A conservative systematic uncertainty of 20% is quoted on the number of b-quark pair events in the signal region.

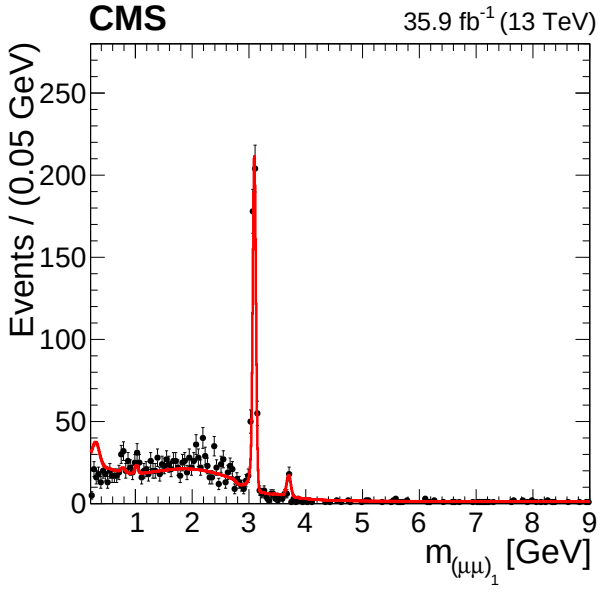

(a) S_{17}

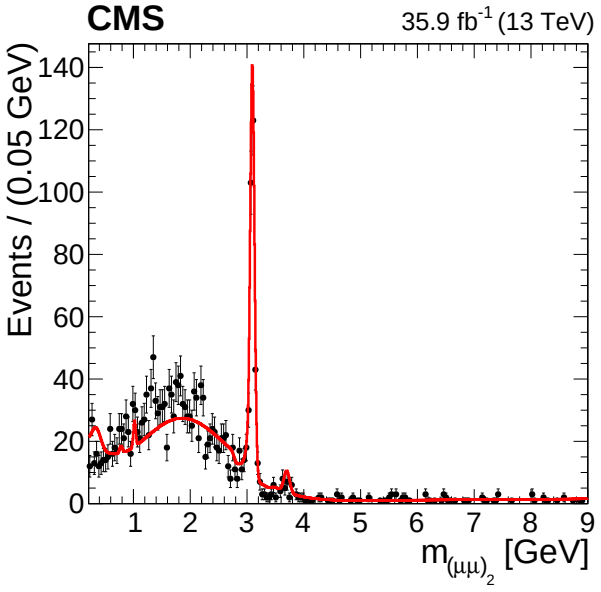

(b) S_{mix}

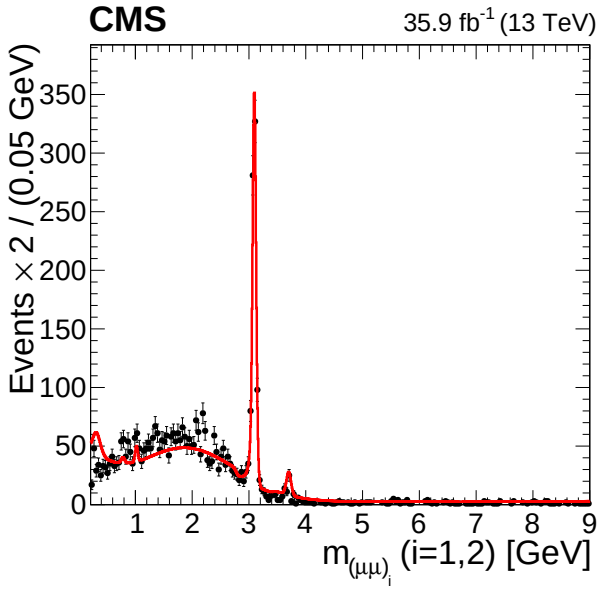

(c) $S_{17} + S_{\mathrm{mix}}$

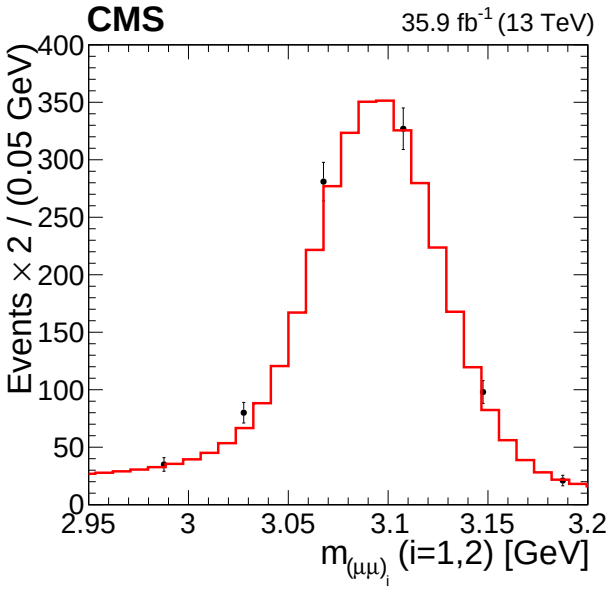

(d) $S_{17} + S_{\mathrm{mix}}$ near the J/ψ resonance.

Figure 7.27: Comparison of the templates (red line) with the data passing the signal event selection in absence of the dimuon isolation requirement that fail $|m_{(\mu\mu)_1} - m_{(\mu\mu)_2}| < 5\sigma(m_{\mu\mu})$ (black dots). The templates S_{17} and S_{mix} are scaled to the entries in data.

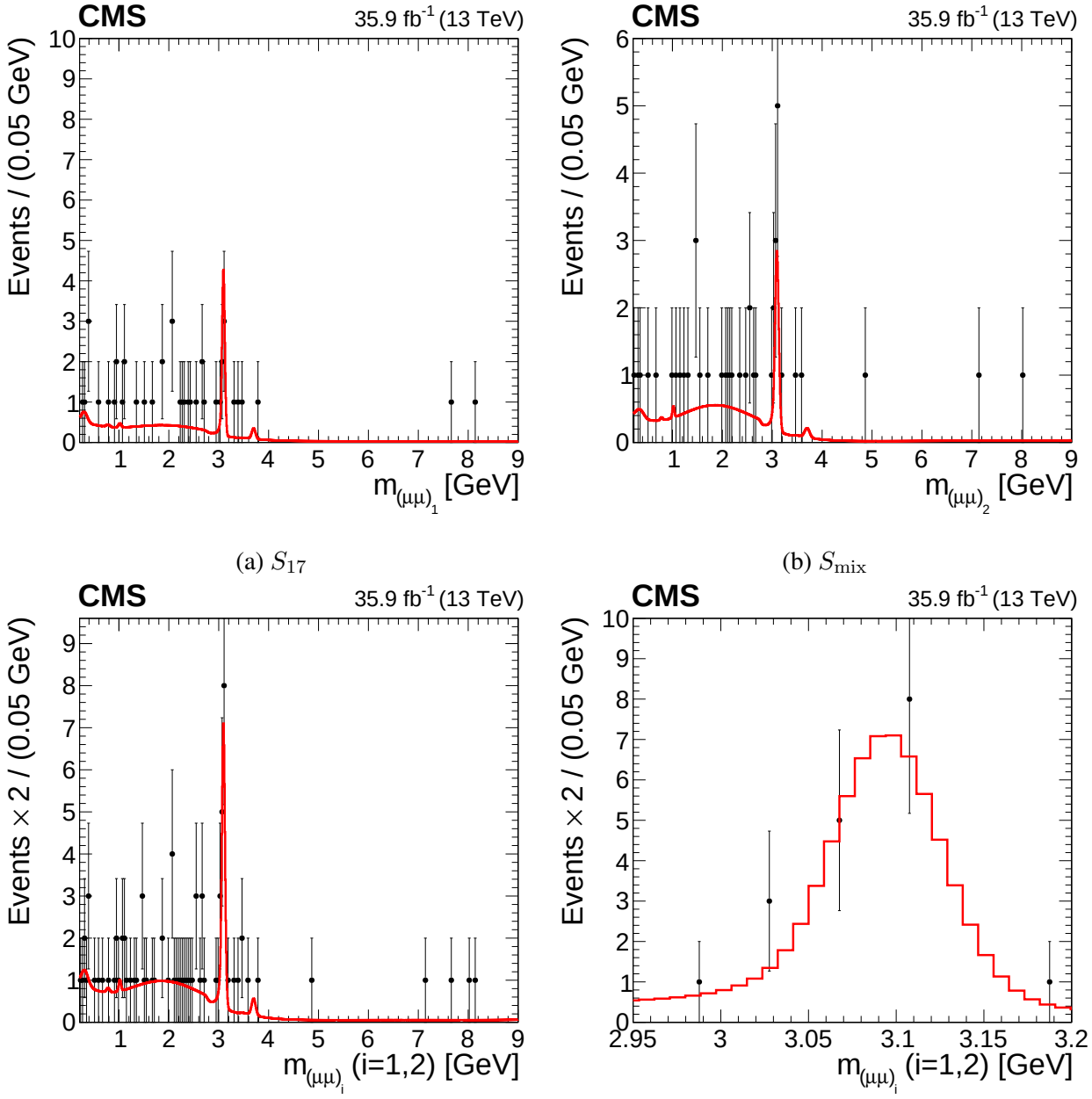

(a) S_{17}

(b) S_{mix}

(c) $S_{17} + S_{\mathrm{mix}}$

(d) $S_{17} + S_{\mathrm{mix}}$ near the J/ψ resonance.

Figure 7.28: Comparison of the templates (red line) with the data passing the signal event selection that fail $|m_{(\mu\mu)_1} - m_{(\mu\mu)_2}| < 5\sigma(m_{\mu\mu})$ (black dots). The templates S_{17} and S_{mix} are scaled to the entries in data.

Table 7.8: Isolation cut in control region and expected b-quark pair event yield in signal region

Isolation cut (GeV)	R-value	b-quark pair event yield
2	$\frac{0.1444}{0.8556}$	7.26 ± 1.11
5	$\frac{0.1436}{0.8564}$	7.21 ± 1.10
10	$\frac{0.1384}{0.8616}$	6.90 ± 1.05
50	$\frac{0.1267}{0.8733}$	6.24 ± 0.95

7.5.1.8 Conclusions

The b-quark pair background contribution is estimated to be 7.26 ± 1.11 events in the signal region. A systematic uncertainty of 20% on the background event yield is quoted.

7.5.2 Prompt Double J/ψ Production

7.5.2.1 Description of the Background

A second source of four-muon background events is prompt double J/ψ production. Double J/ψ's produced in b-quark pair production (see Sec. 7.5.1.1) are typically displaced (i.e. non-prompt). Two prompt J/ψ mesons can be produced through *single parton scattering* (SPS) or *double parton scattering* (DPS). Prompt double J/ψ production can mimic the signal when both J/ψ mesons decay into a muon pair. Figure 7.29 shows an example SPS process. Two partons are radiated from colliding protons and fuse into two J/ψ mesons which decay into two muon pairs. Figure 7.30 shows an example DPS process. Each proton radiates two partons which fuse into two J/ψ mesons.

7.5.2.2 Overview of the Method

The contribution of prompt double J/ψ production is estimated with a data-driven method based on Ref. [169]. First, a double J/ψ control sample is obtained from data (Sec. 7.5.2.3). Second, possible separation methods are investigated in Sec. 7.5.2.4. Next, the control sample is further cleaned (Sec. 7.5.2.5) and then separated into a prompt and nonprompt component (Sec. 7.5.2.6). This is followed by the separation of the SPS from the DPS contribution in the

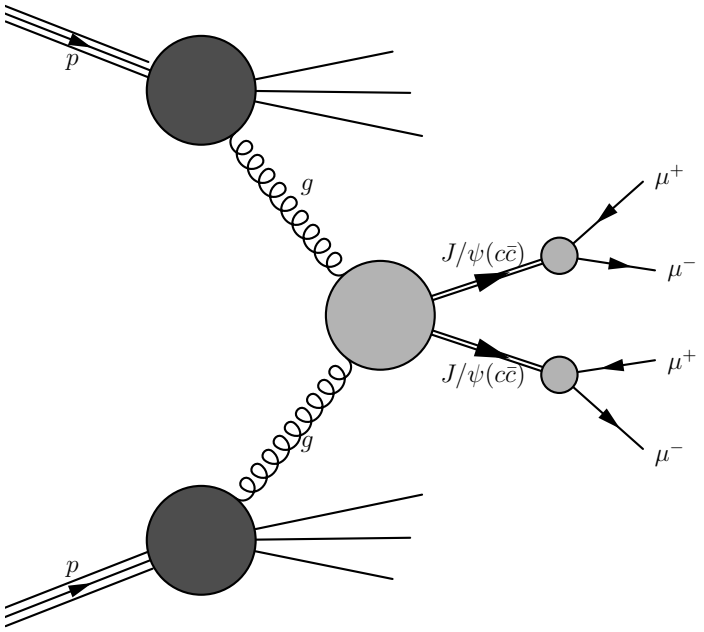

Figure 7.29: Diagram of prompt double J/ψ production to four muons through SPS.

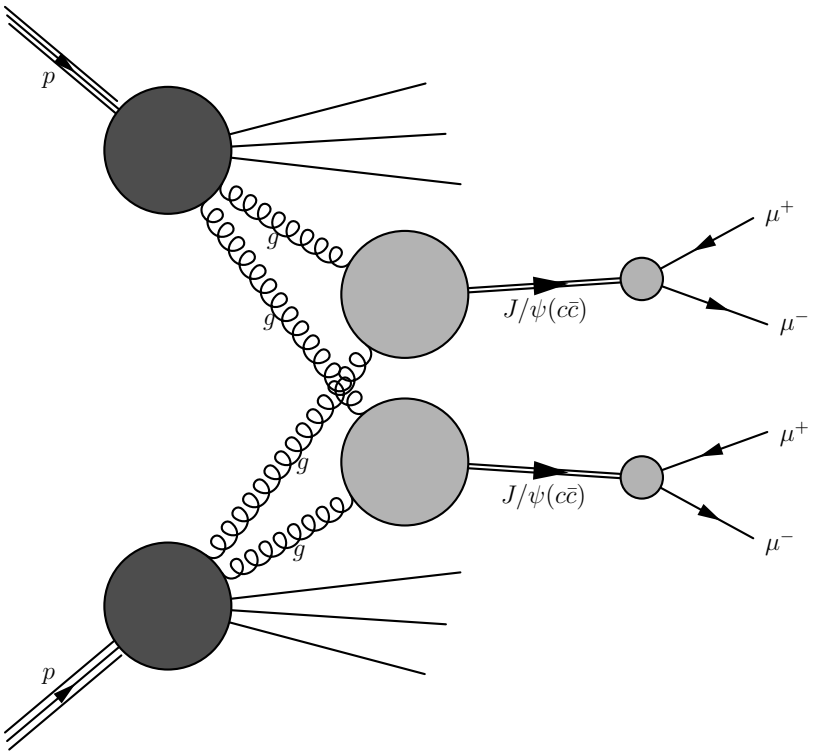

Figure 7.30: Diagram of prompt double J/ψ production to four muons through DPS.

prompt data sample (Sec. 7.5.2.7). Finally, the SPS and DPS contributions are extrapolated to the signal region (Sec. 7.5.2.9).

7.5.2.3 Double J/ψ Control Data Sample

A control data sample is obtained with a object and event selection, similar to the signal event selection, but optimized for double J/ψ events.

Events are taken from the MuOnia dataset (see app. A), which is a sample obtained with triggers optimized for b-physics studies. Events are selected with the trigger `HLT_Dimuon0_Jpsi_Muon` that requires each event to have at least three muons, of which two have a common vertex and an invariant mass consistent with the J/ψ meson. Muons are reconstructed and identified with the PF algorithm. Four muons within $|\eta| < 2.4$ are required. However, the muon transverse momentum cut is relaxed to $p_{\mathrm{T}} > 3.5\ \mathrm{GeV}$. A high-$p_{\mathrm{T}}$ barrel muon is not required for the control sample. The high-p_{T} label is meaningless in the control sample and dimuons are thus assigned random labels, $(\mu\mu)_1$ or $(\mu\mu)_2$. A random label also prevents the introduction of a bias in the SPS and DPS kinematic distributions, such as the dimuon isolation. The dimuon isolation follows the same definition as for the signal sample. However, no cut on the dimuon isolation is set at this point, since the dimuon isolation distribution will be used to separate the prompt from the nonprompt J/ψ's in the control sample.

7.5.2.4 Separation of SPS and DPS in MC

The kinematic properties of SPS and DPS are studied using MC simulation. Prompt double J/ψ events through DPS are simulated purely with PYTHIA 8.2 [122]. HERWIG [170] 2.7.1 interfaced with PYTHIA 8.2 for hadronization is used to produce the SPS sample. Events are preselected with a generator level filter requiring

1. exactly two decaying J/ψ particles with $p_{\mathrm{T}} > 10\ \mathrm{GeV}$ within $|\eta| < 2.5$
2. at least four muons $p_{\mathrm{T}} > 3\ \mathrm{GeV}$ within $|\eta| < 2.5$

The SPS and DPS generator level filters have a filter efficiency of approximately 10^{-4}. The

SPS and DPS samples are run through the full detector simulation. The object and event selections described in Sec. 7.5.2.3 are subsequently applied to the SPS and DPS samples.

The SPS and DPS contributions to the prompt double J/ψ background can be separated with a single kinematic variable. The distributions of several kinematic variables are shown in Fig. 7.31 and Fig. 7.32. As can be seen, the difference in rapidity between the two dimuons ($|Y_{(\mu\mu)_1} - Y_{(\mu\mu)_2}|$) has the most discrimination power and will be used in the next sections. Note that in Fig. 7.31c and Fig. 7.31d the "corrected L_{xy}" is shown. The corrected L_{xy} is defined as

$$L_{xy} = \frac{(v_x - B_x)p_{\mathrm{x}} + (v_y - B_y)p_{\mathrm{y}}}{p_{\mathrm{T}}}, \tag{7.10}$$

where B_x and B_y denote the position of the beamspot in data along the x and y-axis respectively.

7.5.2.5 Additional Cleaning of the Control Sample

The sample obtained in Sec. 7.5.2.3 contains a mixture of prompt and nonprompt double J/ψ's and nonresonant muon pairs coming from the semileptonic decay of b quarks. The latter two contributions are already contained in the background estimation in Sec. 7.5.1. The fraction of events with two resonant muon pairs corresponding to J/ψ's can be enhanced with an appropriate cut on the dimuon invariant mass. Figure 7.33a shows the 2D invariant mass distribution of $(\mu\mu)_1$ and $(\mu\mu)_2$ in the data control sample before the dimuon mass cut. Clearly, both $(\mu\mu)_1$ and $(\mu\mu)_2$ dimuon mass distributions have long tails. A window of 0.5 GeV wide around the J/ψ mass (between 2.8 and 3.3 GeV) is chosen to remove the events with nonresonant muon pairs.

The dimuon isolation distribution, after application of the dimuon mass cut, is shown in Fig. 7.33b. The data control sample now contains a mixture of prompt and nonprompt J/ψ's. The prompt J/ψ mesons typically have a smaller absolute isolation than that of nonprompt J/ψ's. Therefore, the largest contribution of prompt J/ψ's is expected in the signal region, i.e. $\mathrm{Iso}_{(\mu\mu)_1} < 2$ GeV and $\mathrm{Iso}_{(\mu\mu)_2} < 2$ GeV. The largest contribution of nonprompt J/ψ's has been found in the region $\mathrm{Iso}_{(\mu\mu)_1} > 2$ GeV or $\mathrm{Iso}_{(\mu\mu)_2} < 2$ GeV. However, a nonnegligible fraction of nonprompt J/ψ's still enters the signal region.

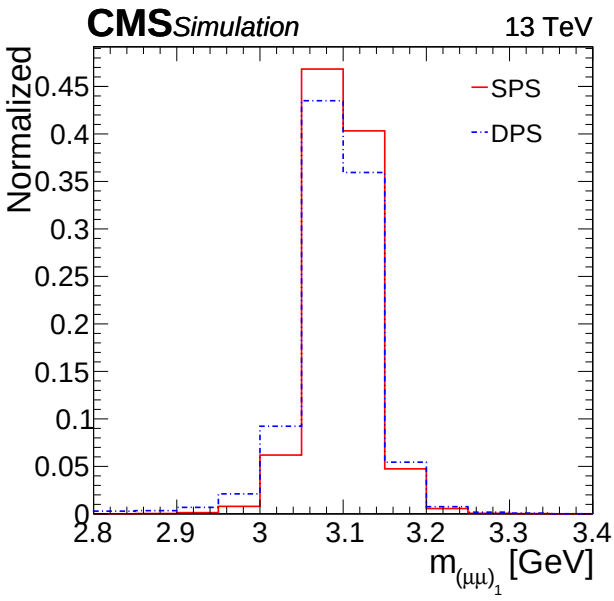

(a) $(\mu\mu)_1$ mass

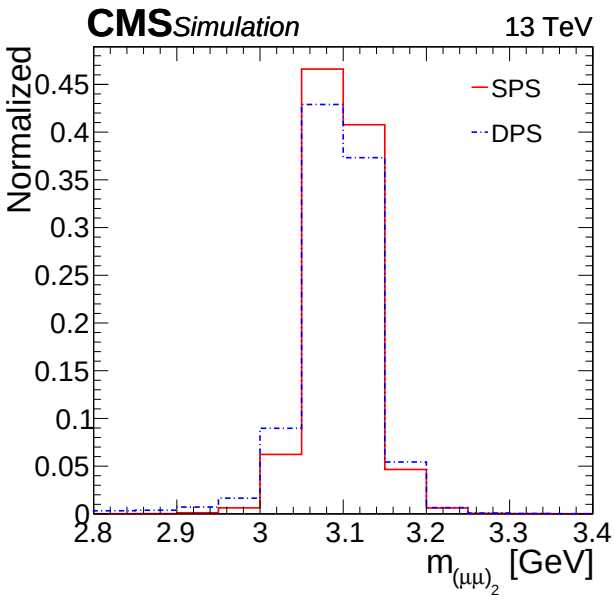

(b) $(\mu\mu)_2$ mass

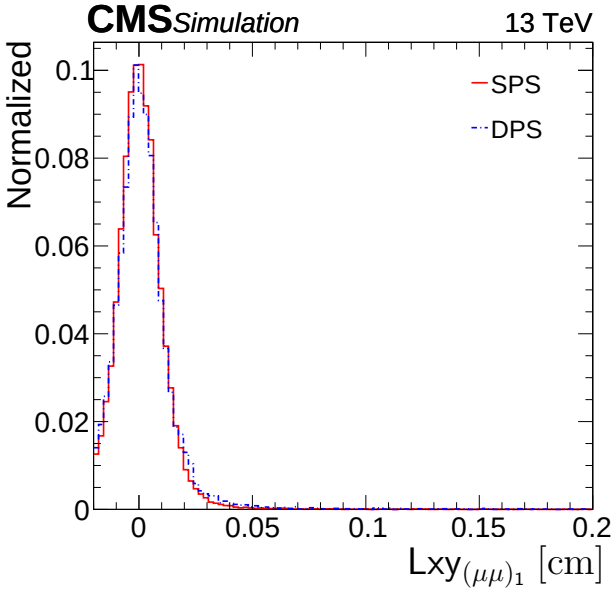

(c) Corrected $(\mu\mu)_1$ displacement L_{xy}

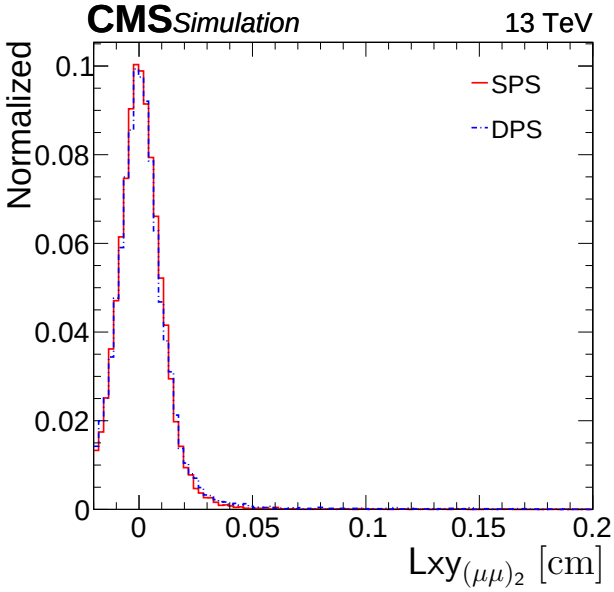

(d) Corrected $(\mu\mu)_2$ displacement L_{xy}

Figure 7.31: Comparison of the $m_{(\mu\mu)_1}$ and $(\mu\mu)_2$ invariant mass and transverse displacement for the SPS and DPS MC samples.

The nonprompt double J/ψ contribution is already estimated in Sec. 7.5.1 using a different method. Only the prompt component is of interest in this study, which is obtained by subtracting the nonprompt contribution from the data. This is done with the so-called "ABCD" method [171]

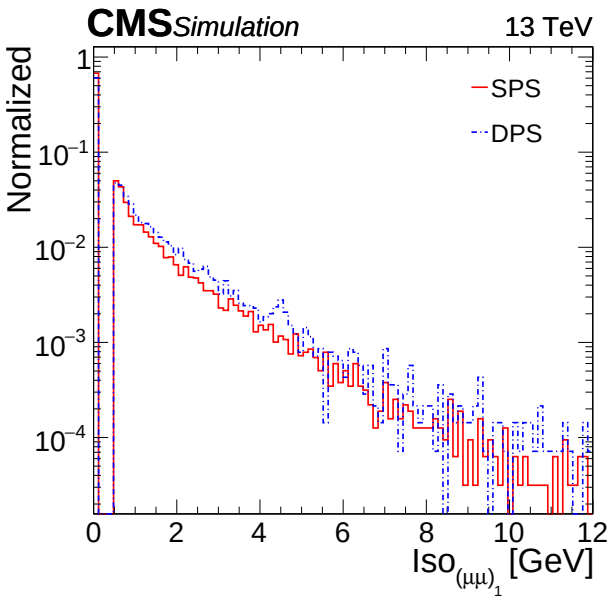

(a) $(\mu\mu)_1$ isolation

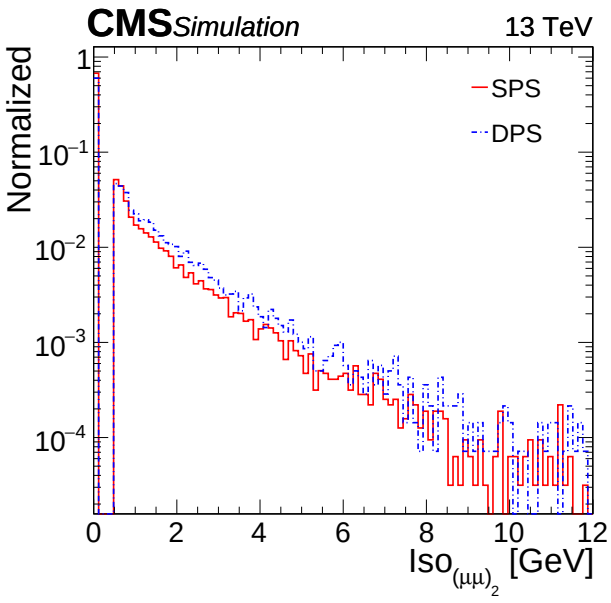

(b) $(\mu\mu)_2$ isolation

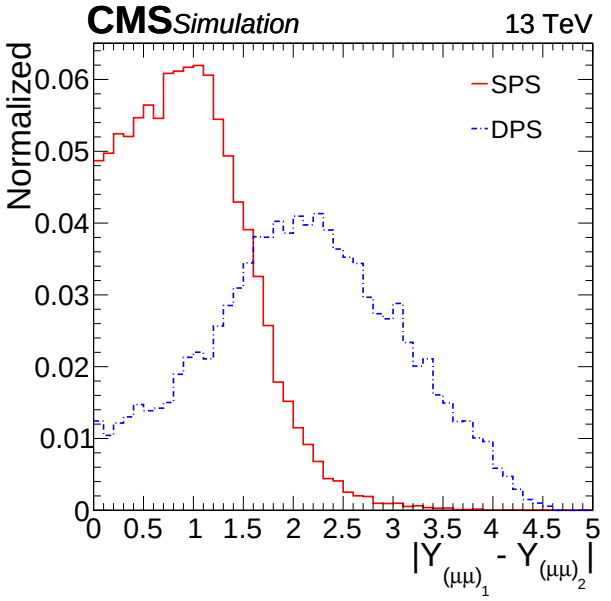

(c) $|Y_{(\mu\mu)_1} - Y_{(\mu\mu)_2}|$

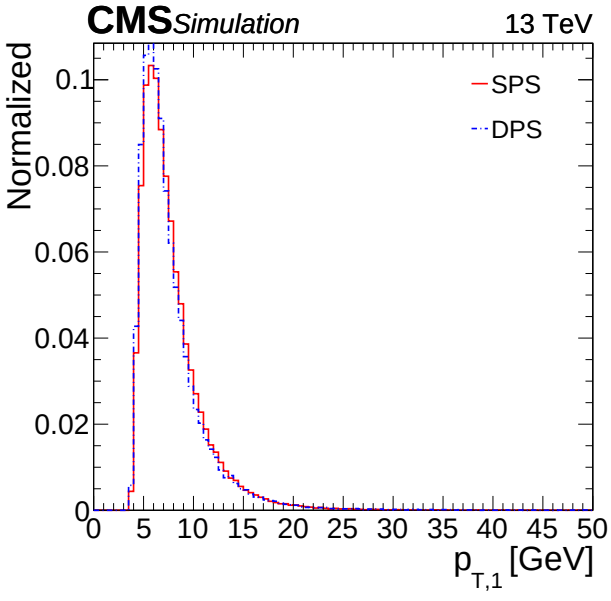

(d) Leading muon p_{T}

Figure 7.32: Comparison of the $m_{(\mu\mu)_1}$ and $(\mu\mu)_2$ isolation, difference in absolute rapidity and leading muon p_{T} for the SPS and DPS MC samples.

and is explained in the next section.

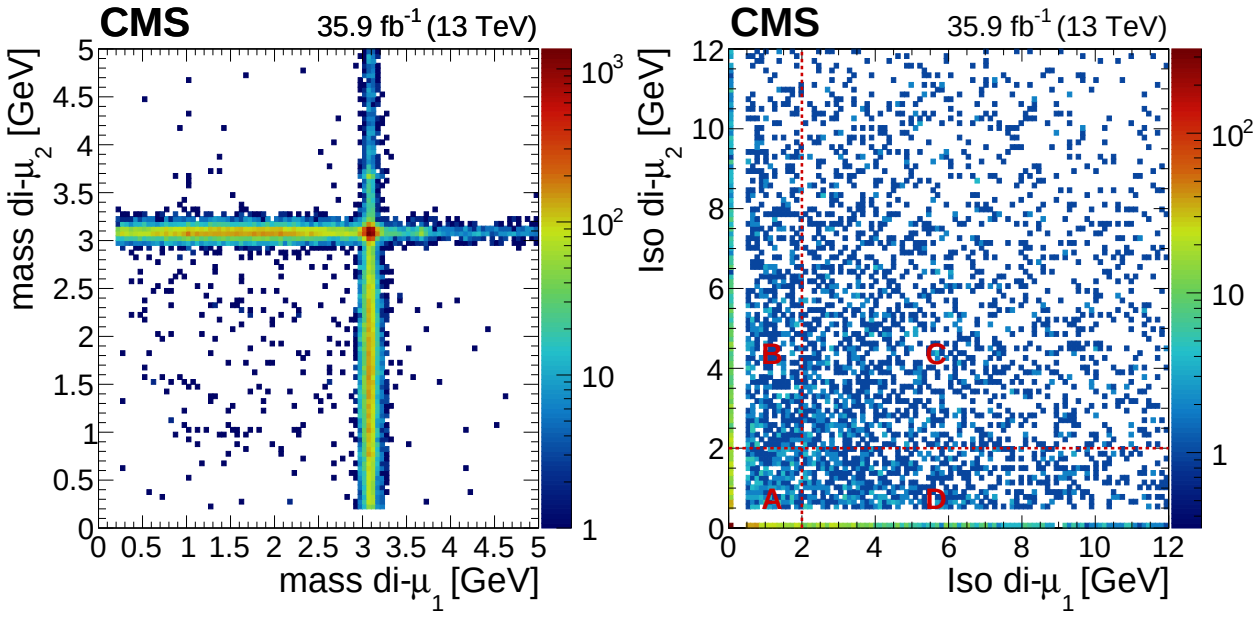

(a) (b)

Figure 7.33: Left: Invariant mass distributions for $(\mu\mu)_1$ and $(\mu\mu)_2$ in data after applying the control sample cuts. The long tails correspond to nonprompt double J/ψ's and nonresonant muon pairs coming from the semileptonic decay of b-quarks. Right: Isolation distribution for $(\mu\mu)_1$ and $(\mu\mu)_2$ after applying the control sample selection cuts and the J/ψ invariant mass constraint, i.e. $2.8 < m_{(\mu\mu)_1} < 3.3$ GeV and $2.8 < m_{(\mu\mu)_2} < 3.3$ GeV. The events are divided into four independent regions. The majority of the events are located in region A.

7.5.2.6 Separation of the Prompt and nonprompt Double J/ψ Contributions using the ABCD Method

The ABCD method makes use of two uncorrelated (or nearly uncorrelated) variables that discriminate between two processes.

The $(\mu\mu)_1$ and $(\mu\mu)_2$ isolation are chosen as uncorrelated variables because they provide a clear discrimination between prompt and nonprompt contributions. The correlation between $(\mu\mu)_1$ and $(\mu\mu)_2$ has been found to be 0.12. This weak correlation is sufficient to proceed with the ABCD method.

Four independent regions A, B, C and D are defined based on the $(\mu\mu)_1$ and $(\mu\mu)_2$ isolation values. This is shown in Fig. 7.33b. Region A is in the lower-left part of the 2D plot and is bounded by the isolation cut in the signal region: $\text{Iso}_{(\mu\mu)_1} < 2$ GeV and $\text{Iso}_{(\mu\mu)_2} < 2$ GeV. The

three remaining regions - B, C, and D - are nonisolated sidebands ($\text{Iso}_{(\mu\mu)_1} > 2$ GeV or $\text{Iso}_{(\mu\mu)_2} > 2$ GeV). They are used to extrapolate the nonprompt contribution into region A. To avoid effects from highly nonisolated dimuons, a maximum isolation value is imposed, $\text{Iso}_{(\mu\mu)_{1,2}} < 12$ GeV.

Figure 7.34a and Fig. 7.34b shows the dimuon-dimuon isolation for events in the SPS and DPS prompt double J/ψ MC samples. Clearly, most events are located in the isolated region A. Events in the sideband regions are mostly composed of J/ψ's from b-quark decays.

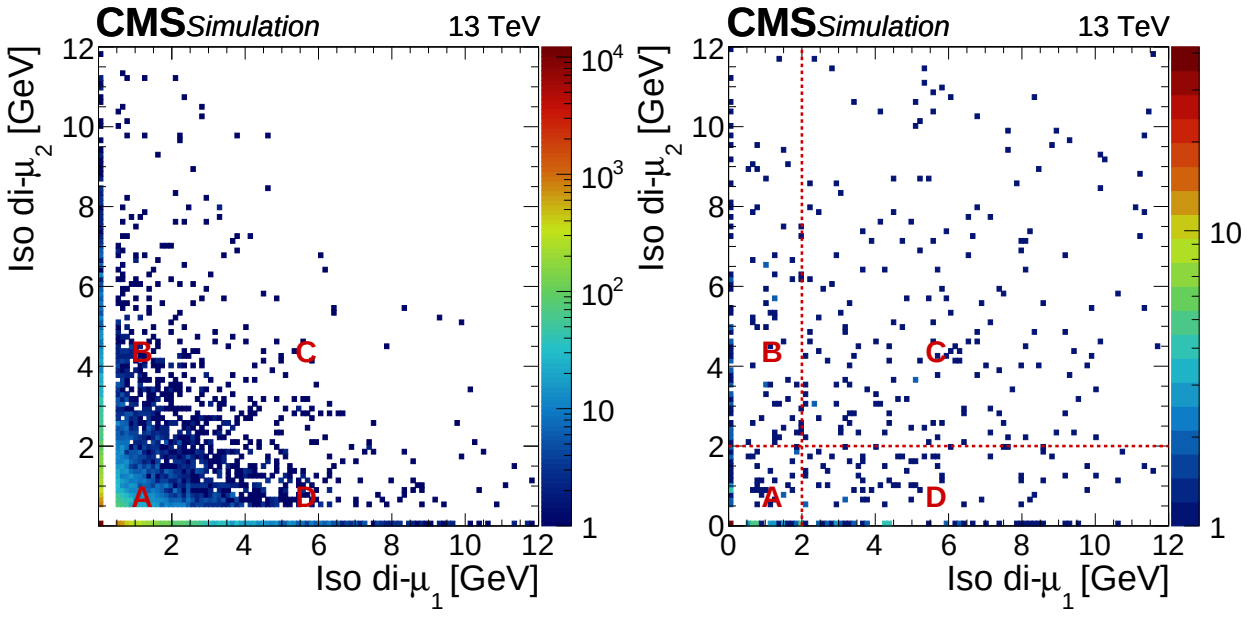

(a) (b)

Figure 7.34: Isolation distributions for $\mu\mu_1$ and $\mu\mu_2$ in the SPS MC sample (left) and DPS MC sample (right).

The number of data events in each region (N_A, N_B, N_C and N_D) is shown in Tab. 7.9. Let $N_{A,\text{nonprompt}}$ the number of data events with nonprompt J/ψ's in region A and $N_{A,\text{prompt}}$ the num-

ber of data events with prompt J/ψ's in region A, then the following expressions must hold:

$$N_{A,\mathrm{nonprompt}}/N_B \sim N_D/N_C \tag{7.11}$$

$$N_{A,\mathrm{prompt}} = N_A - N_{A,\mathrm{nonprompt}} \tag{7.12}$$

$$= N_A - N_B N_D/N_C. \tag{7.13}$$

With this expression, the prompt and nonprompt contribution in region A can be estimated. The results are shown in Tab. 7.10. The statistical uncertainties are obtained through error propagation of Eq. 7.13. The resulting prompt and nonprompt fractions in A can be determined from $f_{\mathrm{A,prompt}} = N_{A,\mathrm{prompt}}/N_A$ and $f_{\mathrm{A,nonprompt}} = N_{A,\mathrm{nonprompt}}/N_A$, and have been found to be $f_{\mathrm{A,prompt}} = 0.34 \pm 0.06)$ and $f_{\mathrm{A,nonprompt}} = 0.66 \pm 0.06$. The systematic uncertainty on the prompt contribution is derived by varying the maximum isolation value in the nonisolated sideband region from $12\ \mathrm{GeV}$ to $6\ \mathrm{GeV}$ in steps of $2\ \mathrm{GeV}$ and is quoted as the maximum difference between the largest and smallest contribution, and is quoted as 15%.

Table 7.9: Data events in regions A,B,C, and D where the regions are defined as in Fig. 7.33b.

N_A	N_B	N_C	N_D
1219	1232	1999	1313

Table 7.10: Estimation of the prompt and nonprompt contribution in region A. The first uncertainty is the statistical uncertainty after error propagation, the second is the systematic uncertainty. The systematic uncertainty on $N_{A,\mathrm{nonprompt}}$ is not derived.

$N_{A,\mathrm{prompt}}$	$N_{A,\mathrm{nonprompt}}$
$409.79 \pm 50.76\ (\mathrm{stat.}) \pm 61.79\ (\mathrm{syst.})$	$809.21 \pm 36.85\ (\mathrm{stat.})$

7.5.2.7 Separation of SPS and DPS in Data

Following the separation of the prompt and nonprompt contribution to double J/ψ events in data, the prompt SPS can be separated from the prompt DPS in data. This is done by fitting the template SPS and DPS rapidity distributions in MC to the rapidity distribution in the data. Figure 7.35 compares the MC SPS and DPS rapidity distributions to the one in data. Note that the SPS and DPS distributions are normalized to the number of entries in data. A combined rapidity template is constructed for the fit to data: $y_{\mathrm{prompt,MC}} = f_{\mathrm{SPS}}\, y_{\mathrm{prompt,SPS}} + f_{\mathrm{DPS}}\, y_{\mathrm{prompt,DPS}}$, with f_{SPS} and f_{DPS} the contribution of SPS and DPS to the prompt double J/ψ events and $f_{\mathrm{SPS}} = 1 - f_{\mathrm{DPS}}$. The fit to data is shown in Fig. 7.35b and has a goodness of $\chi^2/\mathrm{ndf} = 1.39$. The resulting SPS and DPS contributions have been found to be $f_{\mathrm{SPS}} = 0.60 \pm 0.03$ and $f_{\mathrm{DPS}} = 0.40 \pm 0.03$ respectively.

7.5.2.8 Separation of SPS and DPS with the L_{xy} Variable.

An alternative method to separate the prompt and nonprompt double J/ψ's relies on the dimuon lifetime. We assume that promptly produced double J/ψ typically have a smaller lifetime than those from b-quark decay. In that case, the "corrected L_{xy}" variable can discriminate between the prompt and nonprompt contributions.

Region A has both prompt ($f_{A,\mathrm{prompt}}$) and nonprompt ($f_{A,\mathrm{nonprompt}}$) double J/ψ events. The L_{xy} is denoted as $L_{xy,\mathrm{Data}\ A}$. The prompt template, $L_{xy,\mathrm{MC}}$, is obtained from a double J/ψ MC sample. Here, either SPS or DPS can be used since they have similar lifetimes (see Fig. 7.31c and Fig. 7.31d). Events in the nonisolated sideband region C determine the nonprompt L_{xy} template, $L_{xy,\ \mathrm{Data}\ C}$. The distributions of $L_{xy,\mathrm{Data}\ A}$, $L_{xy,\mathrm{MC}}$ and $L_{xy,\ \mathrm{Data}\ C}$ are shown in Fig. 7.36a. The fit of the combined template $f_{\mathrm{A,\ prompt}} L_{xy,\mathrm{MC}} + f_{A,\mathrm{nonprompt}} L_{xy,\ \mathrm{Data}\ C}$ to $L_{xy,\mathrm{Data}\ A}$ yields the fraction of each contribution. The fit is shown in Fig. 7.36b.Figure 7.36b is the same fit, but shown with logarithmic scale on the y-axis. The contributions are $f_{\mathrm{A,prompt}} = 0.27 \pm 0.02$ and $f_{\mathrm{A,nonprompt}} = 0.73 \pm 0.03$. These results are consistent with those obtained using the ABCD method, i.e. $f^{ABCD}_{\mathrm{A,prompt}} = 0.33 \pm 0.06$ and $f^{ABCD}_{\mathrm{A,nonprompt}} = 0.66 \pm 0.06$.

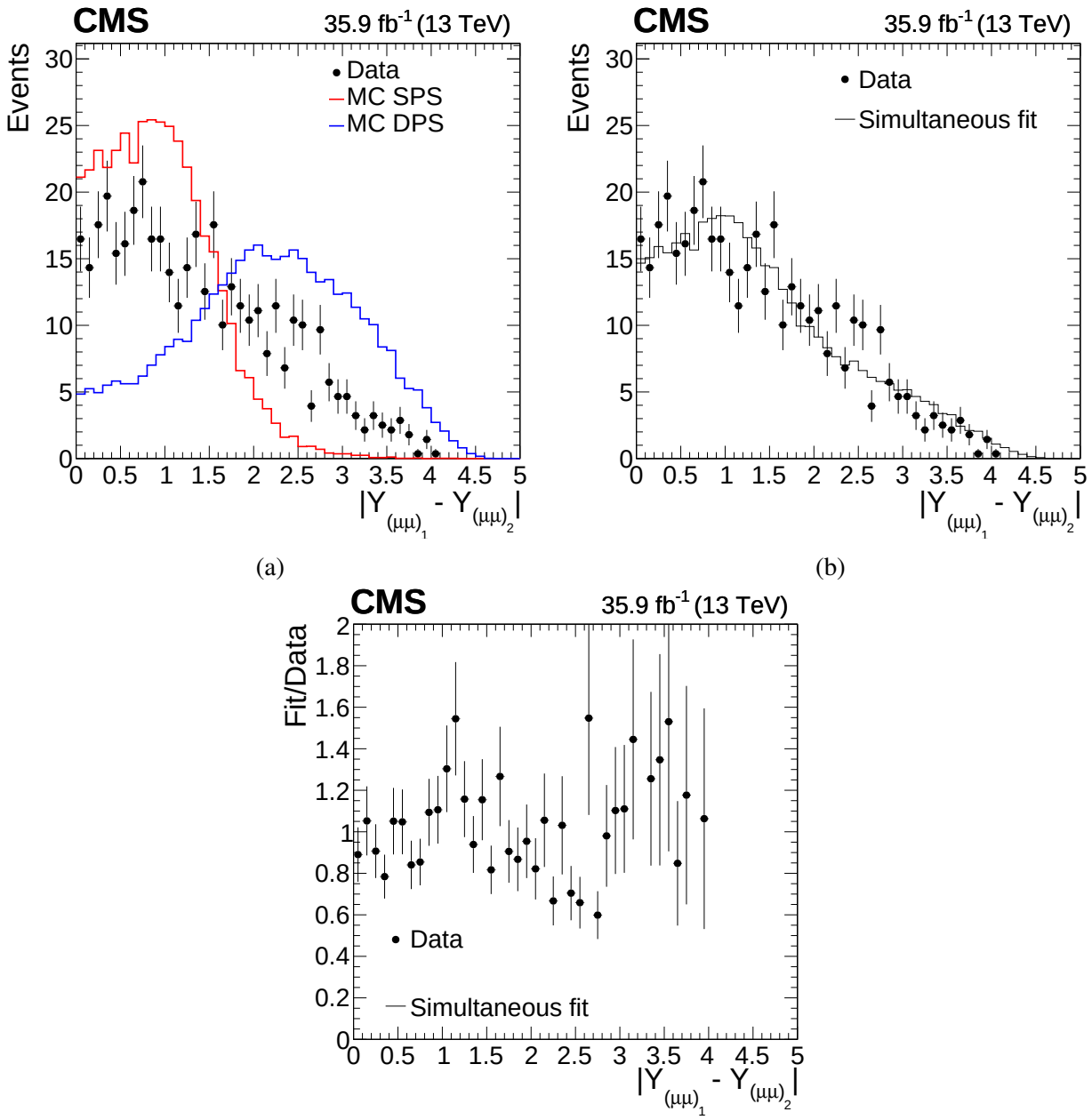

Figure 7.35: Top left: Rapidity distribution for SPS and DPS prompt double J/ψ (normalized to the number of entries in data) compared to data. Top right: Combined fit of SPS and DPS to data to obtain the relative contribution of each process. Bottom: distribution of the ratio between fit and data.

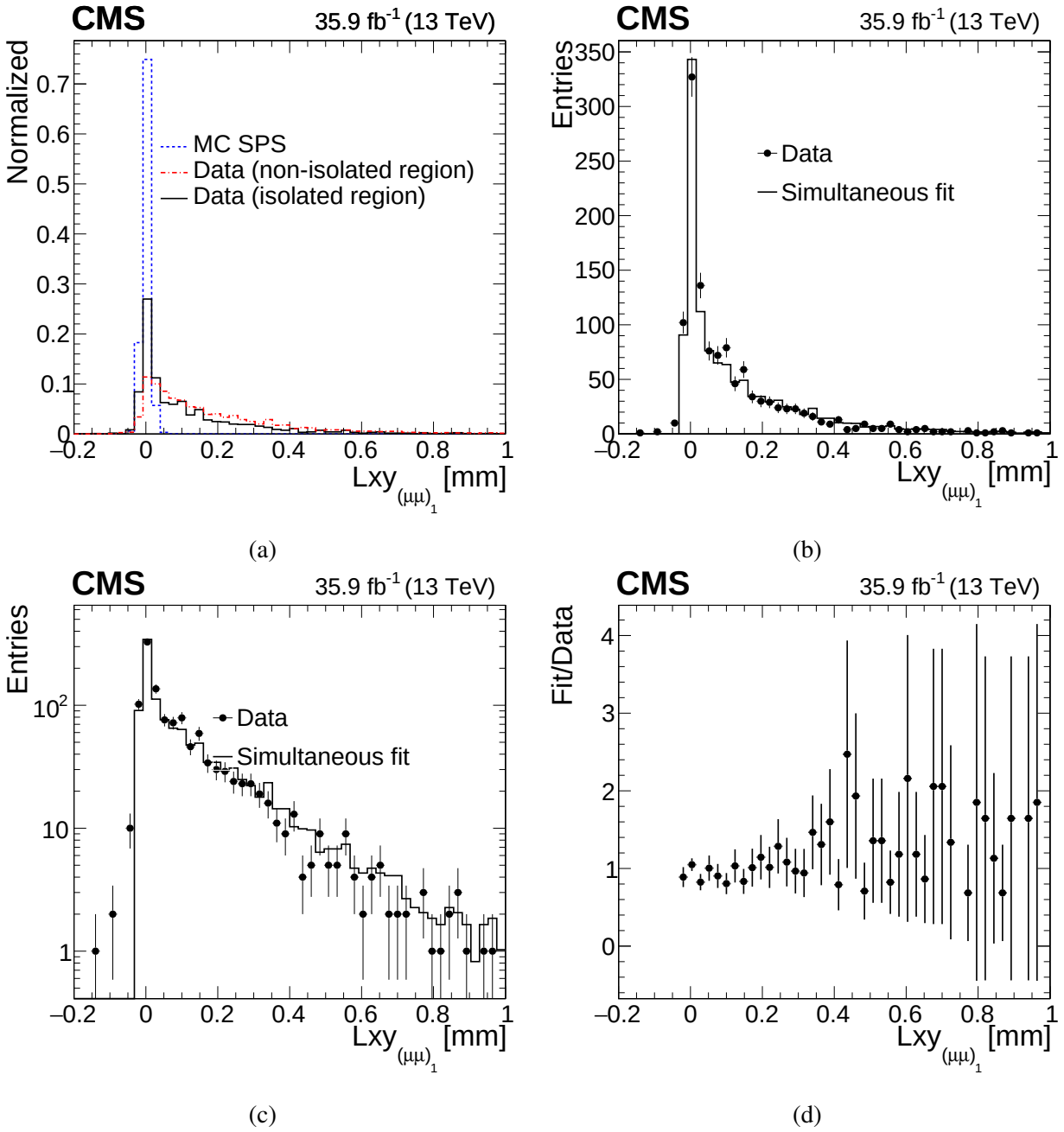

Figure 7.36: Top left: L_{xy} distributions for SPS MC simulation, nonprompt double J/ψ events from a nonisolated distribution in data and prompt double J/ψ events in data. Top right: fit of the combined L_{xy} template, from MC simulation and the nonprompt using a nonisolated distribution in data, to the L_{xy} distribution for double J/ψ events in data. Bottom left: same as top right, but with logarithmic scale on the y-axis. Bottom right: distribution of the ratio between fit and data.

7.5.2.9 *Extrapolation of Double J/ψ Events from Control Region to Signal Region*

Finally, the prompt double J/ψ contribution in the signal region (events passing the signal selection) can be estimated by extrapolating the data from the control region.

We denote $N_{\mathrm{MC,SPS}}(SR)$ ($N_{\mathrm{MC,DPS}}(SR)$) the number of SPS (DPS) MC events passing signal region selections, $N_{\mathrm{MC,SPS}}(CR)$ ($N_{\mathrm{MC,DPS}}(CR)$) the number of SPS (DPS) MC events passing control region selections and $N_{\mathrm{Data}}(CR)$ the estimated number of prompt double J/ψ events the control data region. The number of SPS and DPS events in the signal data region is estimated as follows:

$$N_{\mathrm{data,SPS}}(SR) = N_{\mathrm{MC,SPS}}(SR) \times f_{\mathrm{SPS}} \times \frac{N_{\mathrm{Data}}(CR)}{N_{\mathrm{MC,SPS}}(CR)} \tag{7.14}$$

$$N_{\mathrm{data,DPS}}(SR) = N_{\mathrm{MC,DPS}}(SR) \times f_{\mathrm{DPS}} \times \frac{N_{\mathrm{Data}}(CR)}{N_{\mathrm{MC,DPS}}(CR)}. \tag{7.15}$$

The results for each process are shown in Tab. 7.11.

Table 7.11: Summary table showing the estimate of SPS and DPS double J/ψ events in the signal region.

Process	$N_{\mathrm{MC}}(SR)$	$N_{\mathrm{Data}}/N_{\mathrm{MC}}(CR)$	f	$N_{\mathrm{Data}}(SR)$
SPS	27 ± 5.2	0.019 ± 0.003	0.60 ± 0.03	0.31 ± 0.08
DPS	5 ± 2.2	0.010 ± 0.002	0.40 ± 0.03	0.02 ± 0.01

7.5.2.10 *Conclusions*

The yield of prompt double J/ψ production in the signal region is estimated to be 0.33 ± 0.08 events.

7.5.3 Electroweak Production of Four Muons

7.5.3.1 Description of the Background

A third source of background is the production of four muons in the collision of two protons through second-order electroweak processes ($pp \rightarrow ZZ^* \rightarrow 4\mu$). Two channels are expected to contribute to the electroweak background, namely electroweak SPS and DPS. Example Feynman diagrams are shown in Fig. 7.37. In the first case, two partons fuse into a neutral boson (γ, Z, h) which decays into a muon pair. A second muon pair is produced via neutral boson radiation. In the second case, two partons fuse into two neutral bosons, with each decaying into a muon pair. Only diagrams with γ or Z are considered. Other electroweak processes involving Higgs bosons are heavily suppressed. Examples of such diagrams with Higgs bosons are shown in Fig. 7.38.

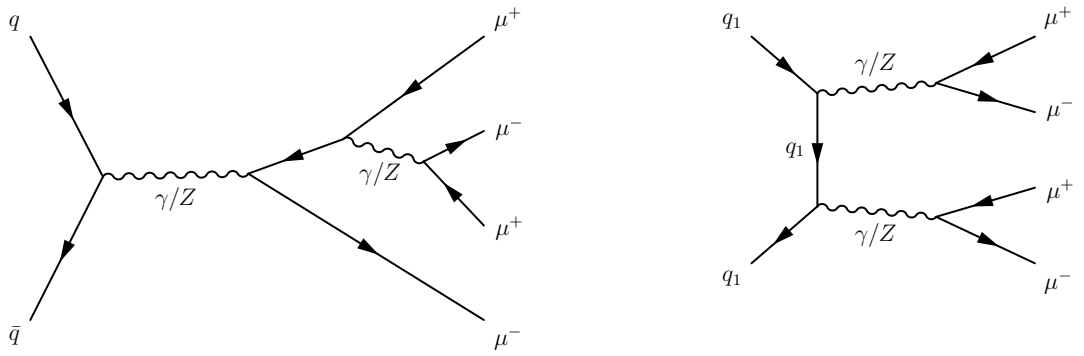

(a) (b)

Figure 7.37: Feynman diagrams of electroweak production of four muon events through SPS (a) and DPS (b) considered in the electroweak background.

7.5.3.2 Overview of the method

This contribution is estimated using MC simulation. A sample $pp \rightarrow ZZ^* \rightarrow 4\mu$ has been generated, processed for full detector simulation and run through the event selection procedure.

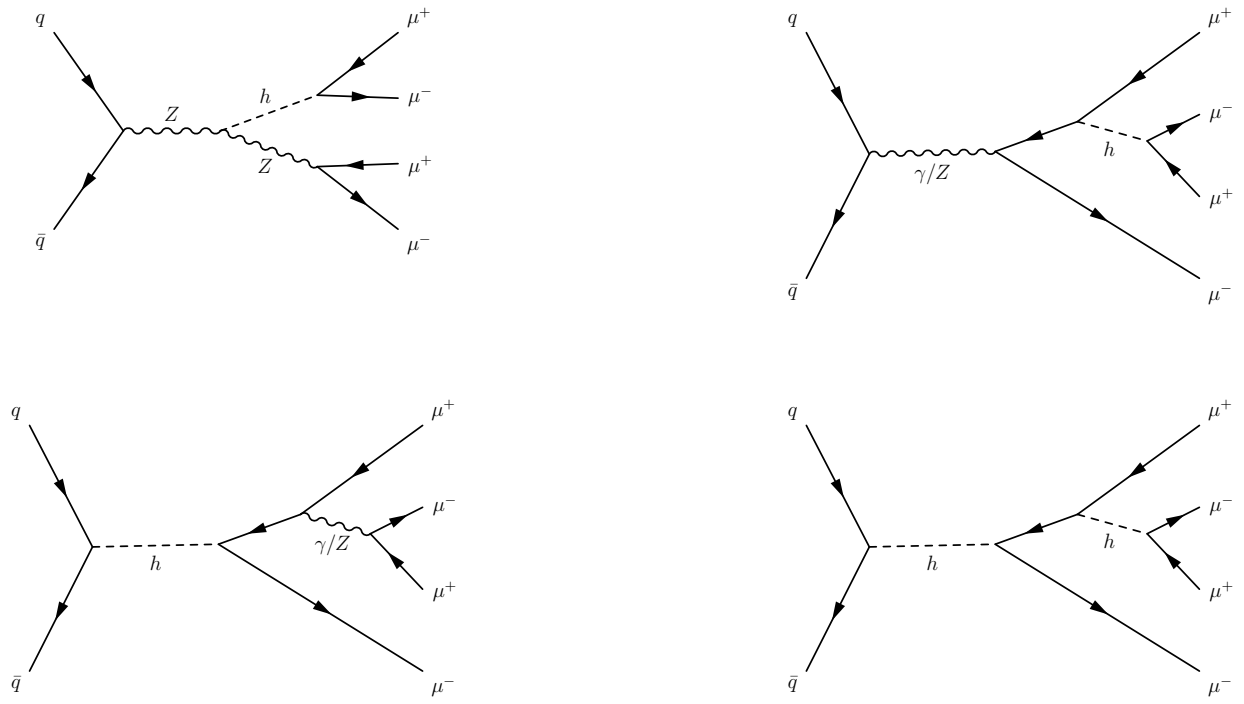

Figure 7.38: Examples of Feynman diagrams of electroweak production of four muon events through SPS with Higgs bosons not considered in the electroweak background.

The knowledge of the process cross section and event yield in MC provides an estimate of the event yield in data in the signal region.

7.5.3.3 Monte Carlo Background Estimation

A sample of $100,000$ $pp \rightarrow ZZ^* \rightarrow 4\mu$ events is generated using the Monte Carlo event generator CALCHEP 3.6.5 [172], interfaced with PYTHIA 8.2 [162] for the hadronization (see App. A. Events are preselected at the generator level to enhance the fraction of events passing the full analysis selection. Each event is required to have exactly four muons with $|\eta| < 2.5$ and $p_{\mathrm{T}} > 5$ GeV. The leading muon is required to have $p_{\mathrm{T}} > 15$ GeV. The production cross section is calculated to be 55.884 fb.

The transverse momentum p_{T} and pseudorapidity η of the muons in the process $pp \rightarrow ZZ^* \rightarrow 4\mu$ are shown in Fig. 7.39. As can be seen, the shapes of the muon pseudorapidity distributions are

similar. However, the shapes of the muon transverse momentum distributions are very different. Moreover, they peak at different momenta, namely 40 GeV (1st muon), 20 GeV (2nd muon), 10 GeV (3rd muon) and 5 GeV (fourth muon) respectively. The combination of the small cross section and the soft fourth muon suppresses the electroweak background contribution.

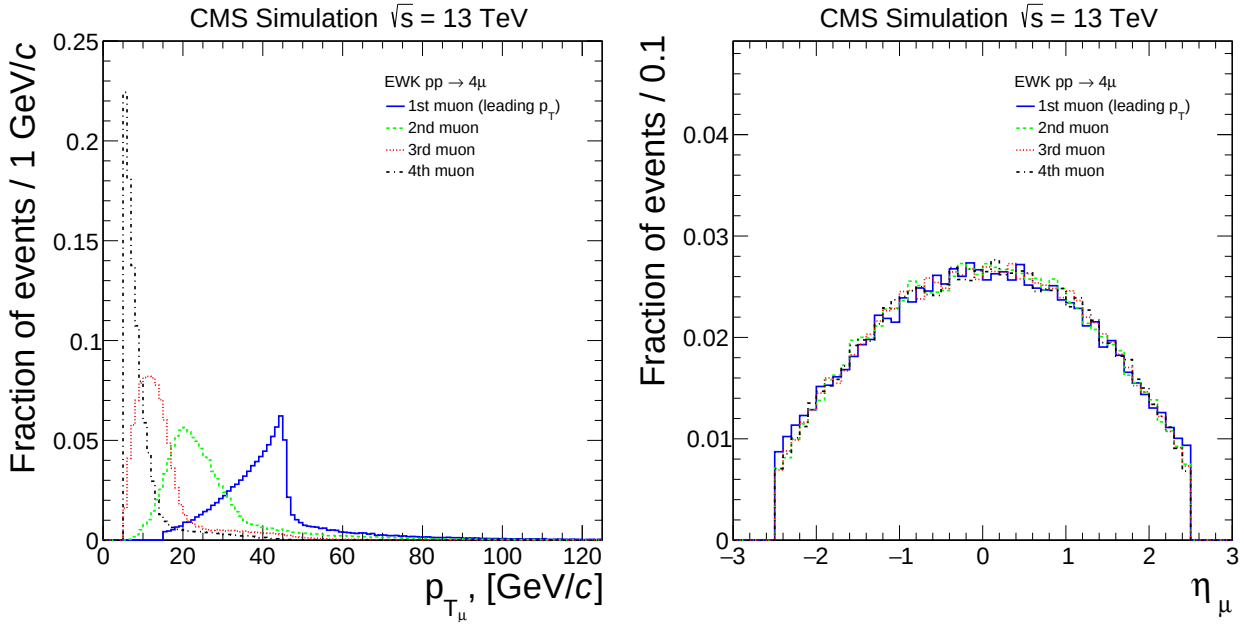

Figure 7.39: Transverse momentum distribution (left) and pseudorapidity distribution (right) of each of the four muons in the simulated electroweak $pp \to ZZ^* \to 2\mu^+2\mu^-$.

Generated events are run through the detector simulation and full event selection. Table 7.12 shows the event yield after each step in the selection procedure. Based on the surviving events, the electroweak contribution is calculated to be $(18 \pm \sqrt{18}) \times 55.884$ fb $\times\, 35.9$ fb$^{-1}/100,000 = 0.36 \pm 0.09$ events.

7.5.3.4 Conclusions

The contribution of electroweak production of four muons is estimated to be 0.36 ± 0.09 events in the signal region.

Table 7.12: Event yield in the electroweak sample after each step in the selection procedure. The filter efficiency of each step is shown in the third column.

Sample	$pp \to ZZ^* \to 4\mu$		
Selection	Events	Total efficiency	Relative efficiency
All events	100000	1.0000 ± 0.0000	1.0000 ± 0.0000
Online selection			
Trigger	76166	0.7617 ± 0.0013	0.7617 ± 0.0013
Basic Reco level selections			
Good primary vertex	76165	0.7617 ± 0.0013	1.0000 ± 0.0000
$p_{\mathrm{T}_1} > 17$ GeV, $\lvert\eta_1\rvert < 0.9$	53333	0.5333 ± 0.0016	0.7002 ± 0.0017
$p_{\mathrm{T}_2} > 8$ GeV, $\lvert\eta_2\rvert < 2.4$	53326	0.5333 ± 0.0016	0.9999 ± 0.0000
$p_{\mathrm{T}_3} > 8$ GeV, $\lvert\eta_3\rvert < 2.4$	52402	0.5240 ± 0.0016	0.9827 ± 0.0006
$p_{\mathrm{T}_4} > 8$ GeV, $\lvert\eta_4\rvert < 2.4$	30731	0.3073 ± 0.0015	0.5864 ± 0.0022
Extra Reco level selections			
Two muon-jets	353	0.0035 ± 0.0002	0.0115 ± 0.0006
Two dimuons	353	0.0035 ± 0.0002	1.0000 ± 0.0000
Pixel hit requirement	353	0.0035 ± 0.0002	1.0000 ± 0.0000
$\lvert z_{(\mu\mu)_1} - z_{(\mu\mu)_2}\rvert < 0.1$ cm	351	0.0035 ± 0.0002	0.9943 ± 0.0040
$\mathrm{Iso}_{(\mu\mu)_{1,2}} < 2$ GeV	283	0.0028 ± 0.0002	0.8063 ± 0.0211
$m_{(\mu\mu)_1} \approx m_{(\mu\mu)_2}$	18	0.0002 ± 0.0001	0.0636 ± 0.0145

7.5.4 Summary of the Background Estimation

In this section we have investigated the most prominent background contributions to this analysis, namely b-quark pair production, and prompt double J/ψ production and electroweak production of four muons. The expected event yield of each background contribution and the expected total yield in the signal region for 35.9 fb^{-1} of data is shown in Tab. 7.5.4. The dominant contribution is b-quark pair production, while the other two backgrounds contribute equally. Note that, unlike b-quark pair production and prompt double J/ψ production, the electroweak background contribution is not resonant, i.e. it is spread across the entire signal region. The total number of background events has been estimated to be 7.95 ± 1.83 in the signal region.

7.6 Systematic Uncertainties

Before turning to the results and interpretation we investigate the systematic uncertainties relevant to this analysis. Two main classes of systematic uncertainties will be discussed, theoretical

Table 7.13: Event yield for each background contribution in the signal region.

Contribution	Event yield in signal region
b-quark pair production	$7.26 \pm 1.11\ (\text{stat.}) \pm 1.45\ (\text{syst.})$
Prompt double J/ψ production	$0.33 \pm 0.08\ (\text{stat.}) \pm 0.05\ (\text{syst.})$
Electroweak production of four muons	$0.36 \pm 0.09\ (\text{stat.})$
Total	7.95 ± 1.83

uncertainties in Sec. 7.6.1 and experimental uncertainties in Sec. 7.6.2. These systematic uncertainties are (1) obtained from new studies in the context of this dissertation, (2) taken over from previous iterations of this analysis, or (3) derived from studies conducted by other groups in the HEP community. The uncertainties are summarized in Sec. 7.6.3.

7.6.1 Theoretical Uncertainties

7.6.1.1 NNLO Higgs p_{T} Reweighting

The MC samples in this analysis are generated at next-to-leading order (NLO). Resummation of Feynman diagrams in the Higgs boson production may affect the shape of the Higgs boson p_{T} distribution and thus $\epsilon_{\text{full}}/\alpha_{\text{gen}}$. A study conducted in Ref. [47] investigated the effect of next-to-next-to-leading order (NNLO) reweighting functions on the Higgs boson p_{T}. The effect on $\epsilon_{\text{full}}/\alpha_{\text{gen}}$ has been evaluated, which is mostly negligible. Therefore a conservative systematic of 2% is set.

7.6.1.2 PDFs, α_s and QCD Scales

Systematic uncertainties on the parton distribution functions (PDFs, the strong coupling α_s or the QCD renormalization μ_R and factorization scales μ_F can affect the signal acceptance. Uncertainties due to the PDFs and α_s are evaluated in Ref. [173] by following the PDF4LHC recommendations in Refs. [174–177]. The systematic uncertainty due to μ_R and μ_F has been found using MCFM (MC for FeMtobarn processes) in Ref. [178]. The μ_R and μ_F scales are varied by a factor of two up and down. Last, the uncertainty due to the choice of the PDF is evaluated by (1) investigating alternative parameterizations within NNPDF2.3 and by (2) investigating alternative

PDFs. When treated as uncorrelated and added in quadrature, the combined systematic uncertainty due to PDFs, α_s and QCD scales has been found to be 8%.

7.6.1.3 Higgs Boson Cross Section and Branching Fraction

Uncertainties in the Higgs boson production cross section $\sigma(pp \to h)$ and branching fraction $B(h \to 2a \to 4\mu)$ might yield more or fewer expected signal events. The systematic uncertainties have been found to be 3.2% and 2% and are obtained from Refs. [92, 179]. Both are assumed to be independent of the Higgs boson mass.

7.6.2 Experimental Uncertainties

7.6.2.1 Luminosity

The systematic uncertainty on the luminosity measurement is determined by the CMS Luminosity POG and has been estimated to be 2.5% [145].

7.6.2.2 Muon Tracking

The uncertainty on the muon tracking efficiency is determined by the CMS Tracking POG on 2016 data using the Tag-and-Probe (T&P) method (Ref. [180]) and has been found to be negligible.

7.6.2.3 Muon Identification

The muon identification (ID) scale factor is extracted with the Tag-and-Probe (T&P) method following instructions recommended by the muon POG. The scale factors are derived as function of the muon p_{T} and η. Simulated events are taken from a MC Drell-Yan + jets sample (Tab. A.3). The data are taken from the DoubleMuon dataset and obtained with the `HLT_Mu17_Mu8` trigger. A loose selection is applied on MC simulated and real data events, namely both muons are required to have $p_{\mathrm{T}} > 8$ GeV. The *tag muon* is required to have PF tight ID and *probe muon* is required to have PF loose ID. The efficiency is calculated to have a probe muon present in double muon events with a tag muon. The efficiencies are plotted versus p_{T} in several η slices. The results are shown in Fig. 7.40 and summarized in Tab. 7.14. The scale factors in the low-p_{T} spectrum are cross-checked with a MC J/ψ sample (Tab. A.4) and a Charmonium dataset (Tab. B.2) using the

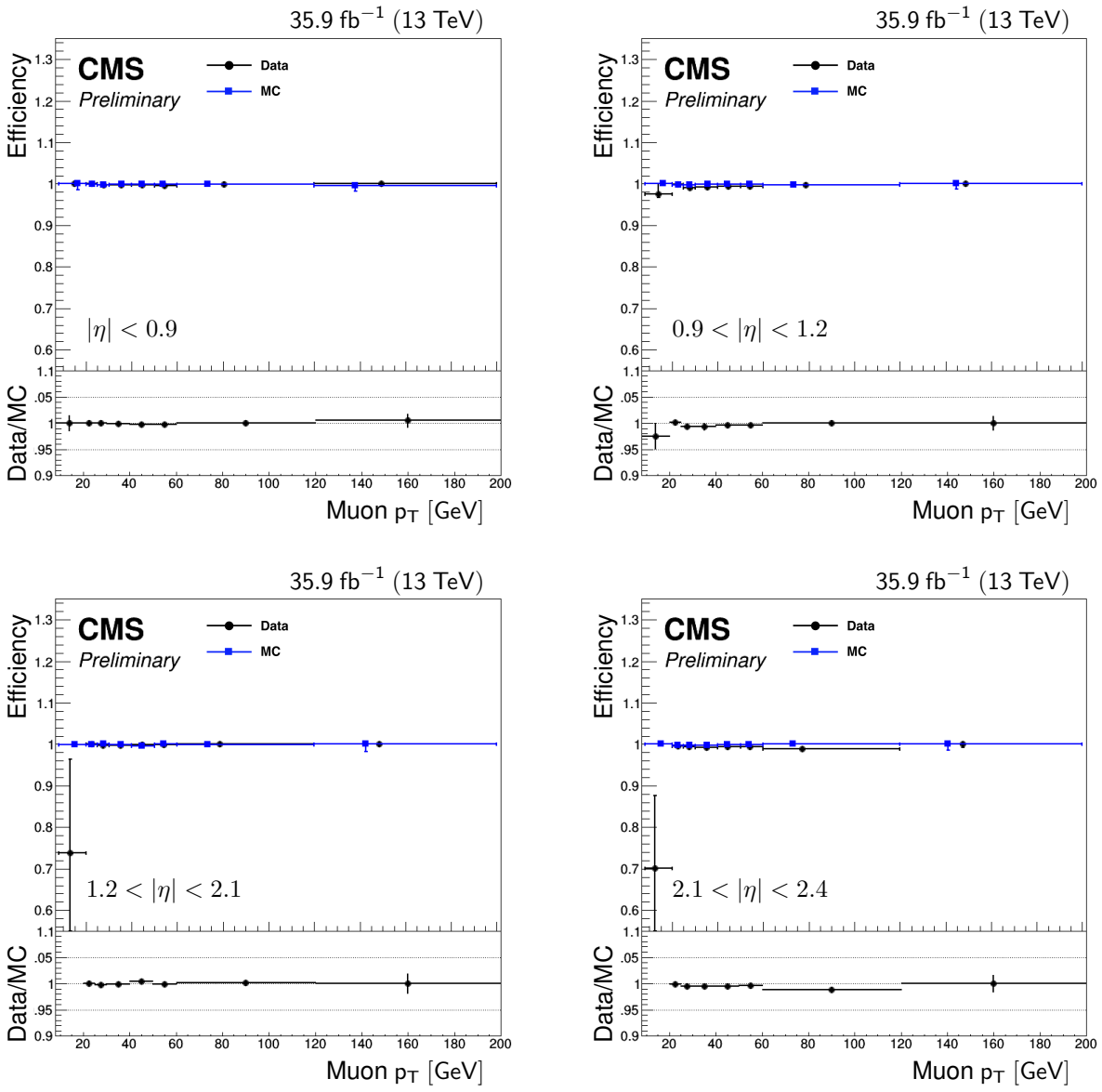

Figure 7.40: Scale factor plots for the muon ID extracted with the T&P method using the Charmonium dataset and a Drell-Yan MC sample with $p_{\mathrm{T}} > 8$ GeV.

`HLT_Dimuon6_Jpsi_NoVertex` trigger. The results are shown in Fig. 7.41. A systematic uncertainty on the muon ID scale factor of 0.6% has been assigned per muon.

7.6.2.4 Muon Isolation

The muon isolation scale factor is also extracted with the T&P method as in Sec. 7.6.2.3. The scale factors are derived with the MC Drell-Yan + jets sample and DoubleMuon data. Tag

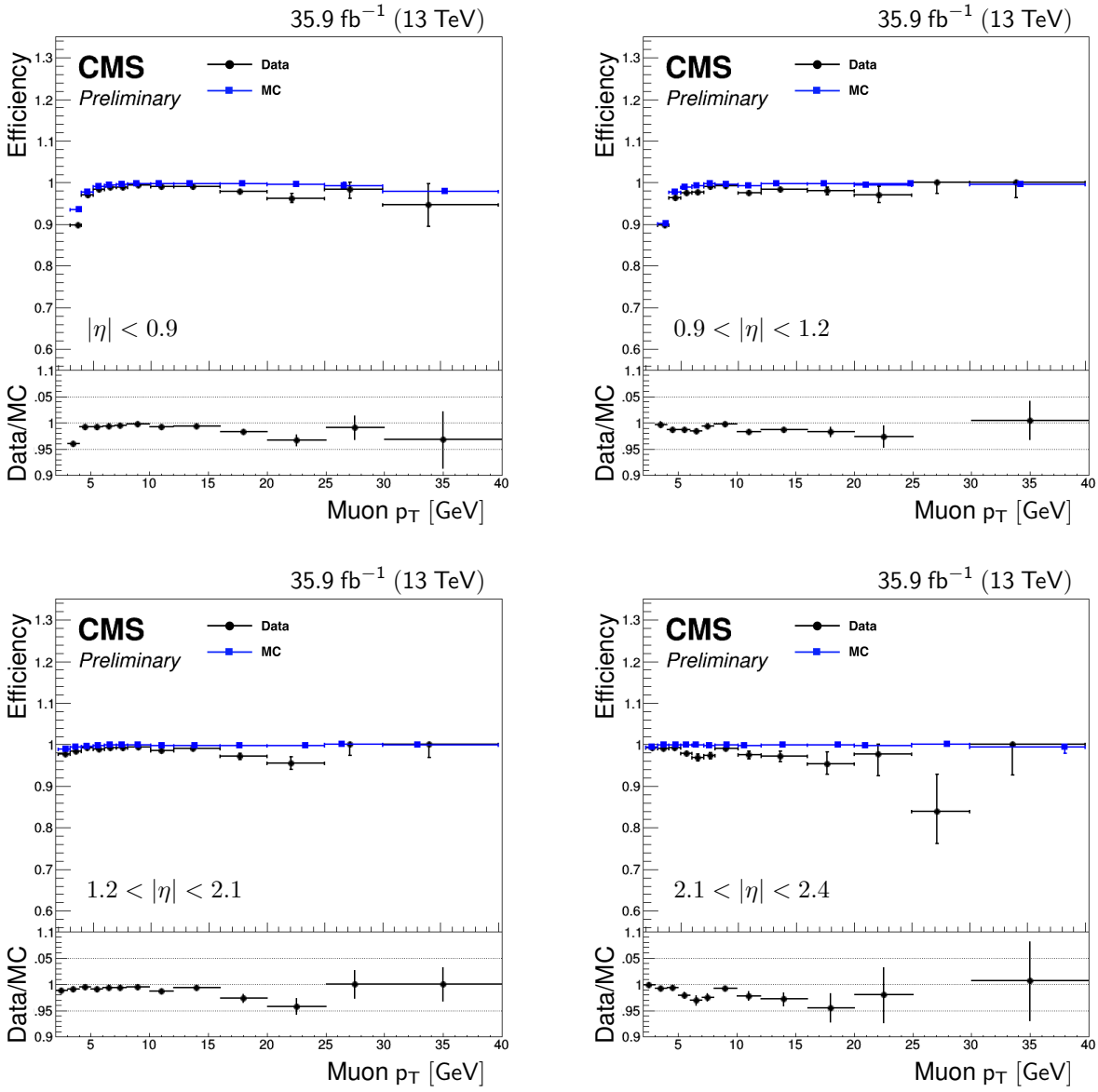

Figure 7.41: Scale factor plots for the muon ID extracted with the T&P method using the Charmonium dataset and a J/ψ MC sample with $p_{\mathrm{T}} > 2$ GeV.

Table 7.14: Summary of the scale factors for muon ID. Scale factors given by weighted averages in several η regions. The relative uncertainty is given in %.

η region	SF	Rel. Uncert. %
$0 - 0.9$	0.99842	0.6
$0.9 - 1.2$	0.99593	0.3
$1.2 - 2.1$	1.00110	0.4
$2.1 - 2.4$	0.99514	0.2
$0 - 2.4$	0.99765	0.6

muons have $p_{\mathrm{T}} > 8$ GeV, $\mathrm{Iso}_{\mu} < 2$ GeV and a PF tight ID. Passing probes are required to have $p_{\mathrm{T}} > 8$ GeV, $\mathrm{Iso}_{\mu} < 2$ GeV, a PF tracker ID and are matched to a muon in the `HLT_Mu17_Mu8` trigger. The efficiencies are plotted versus p_{T} in several η slices. The results are shown in Figs. 7.42 and summarized in Tab. 7.15. A systematic uncertainty on the muon isolation scale factor of 0.1% has been assigned per dimuon.

Table 7.15: Summary of the scale factors for dimuon isolation. Scale factors given by weighted averages in several η regions. The relative uncertainty is given in %.

η region	SF	Rel. Uncert. %
$0 - 0.9$	0.98910	0.02
$0.9 - 1.2$	0.99570	0.1
$1.2 - 2.1$	0.99667	0.1
$2.1 - 2.4$	0.99871	0.1
$0 - 2.4$	0.99505	0.1

7.6.2.5 Trigger

The trigger scale factor of the triple-muon trigger has been estimated with the orthogonal method using three-muon events emulating WZ events. The orthogonal method assumes that such events are mainly triggered by the substantial MET in the event topology, and therefore independent of muons selection criteria. This should yield an unbiased estimation of the trigger efficiency.

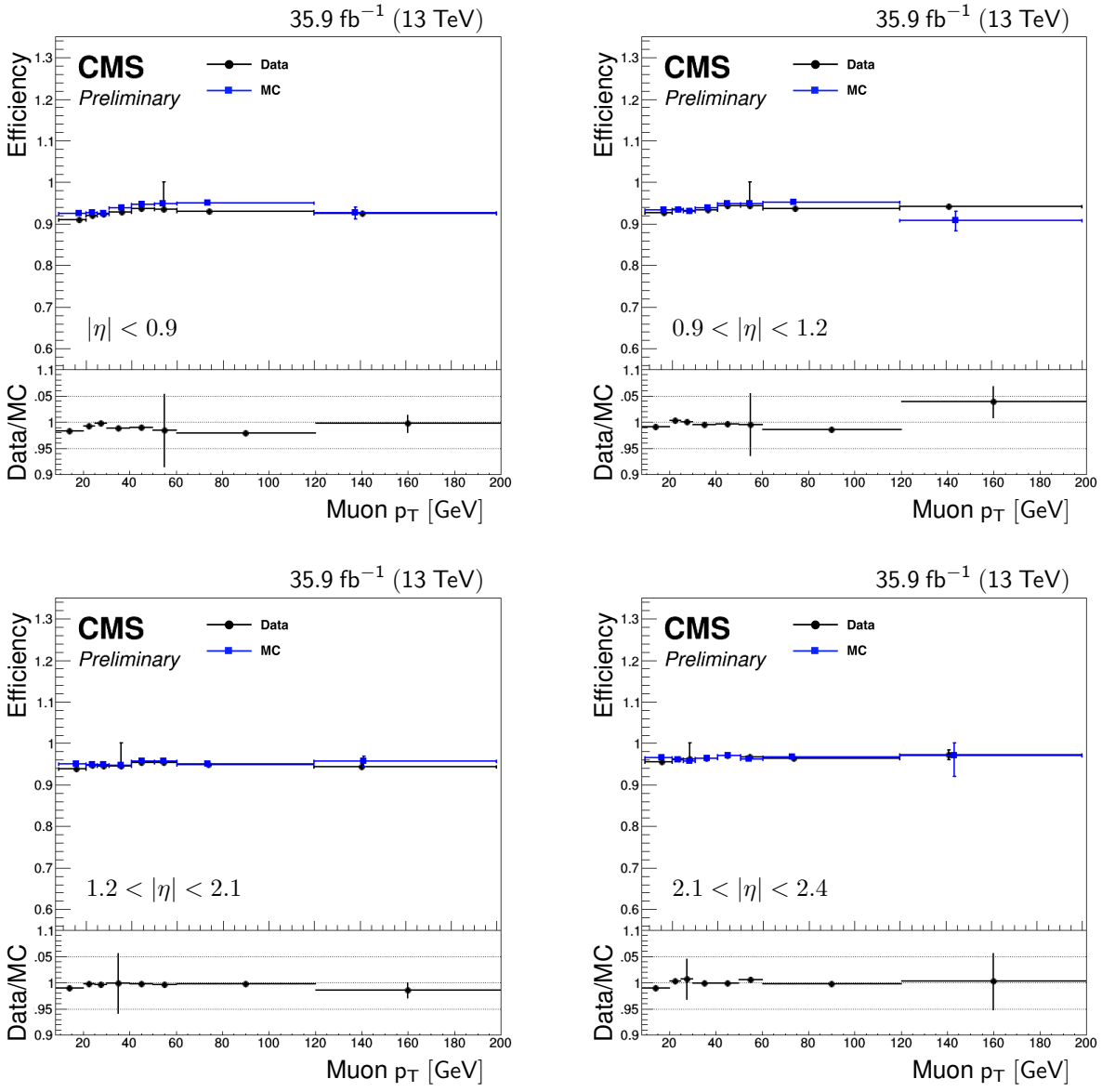

Figure 7.42: Scale factor plots for the muon isolation extracted with the T&P method using the Charmonium dataset and a Drell-Yan MC sample with $p_{\mathrm{T}} > 8$ GeV.

The efficiency of the triple-muon trigger is determined on events passing a set of selection criteria optimized to select WZ events. This is done both on data and on MC simulated events. The data are selected using a set of pure MET triggers in the MET dataset. MET triggers with one or more muons in the selection are ignored. MC events are simulated for the processes (1) $pp \to ZZ$, (2) $pp \to WZ$, (3) $pp \to t\bar{t}Z$ and (4) $pp \to t\bar{t}W$.

The data and MC samples are cleaned by selecting high-quality muons to obtain a set of well-reconstructed WZ-like events. The selection criteria are derived from Ref. [181]. Events are required to pass at least one pure MET trigger (see Tab. 7.16). Each of these trigger applies a cut of at least 100 GeV on the missing transverse energy in the trigger. In addition, events must have exactly three muons with $|\eta| < 2.4$ and with transverse momenta thresholds $40 : 40 : 10$ GeV. The thresholds have been chosen to reduce the nonprompt contribution. Two muons must have the same charge and one muon have the oppositely charge. Two event categories can thus be identified: $\mu^+\mu^+\mu^-$ and $\mu^+\mu^-\mu^-$. The muons must be prompt, i.e. $\Delta_{xy} < 0.01$ cm and $d_z < 0.1$ cm, and must pass the tight ID and tight PF isolation requirement. These selections significantly reduce decays-in-flight. Two muons with opposite charge and with an invariant mass compatible with the Z mass ($|m_{(\mu\mu)} - m_Z| < 15$ GeV) are paired. At least one pair is required in each event. Finally, events with at least one b jet with $p_{\mathrm{T}} > 20$ GeV are vetoed.

The requirement of having three muons and large missing transverse energy eliminates contributions from $pp \to ZZ$ and from Drell-Yan + jets. The requirement of having at least one muon pair compatible the Z boson further eliminates the $pp \to t\bar{t}W$ contribution. Several distributions comparing data with MC after all selection cuts are shown in Fig. 7.43. As expected, only the $pp \to WZ$ and $pp \to t\bar{t}Z$ process contribute to the background. A reasonable agreement between data and MC can be seen.

The trigger efficiency versus leading muon p_{T} and η on the MC and real MET data samples is shown in Fig. 7.44. Additional plots related to this study can be found in App. H. The weighted average trigger efficiency on MC has been calculated to be 95.5%. The trigger efficiency on real MET data is 89.2%. The trigger scale factor has been estimated to be $93.4 \pm 6\%(\mathrm{stat.})$. A sys-

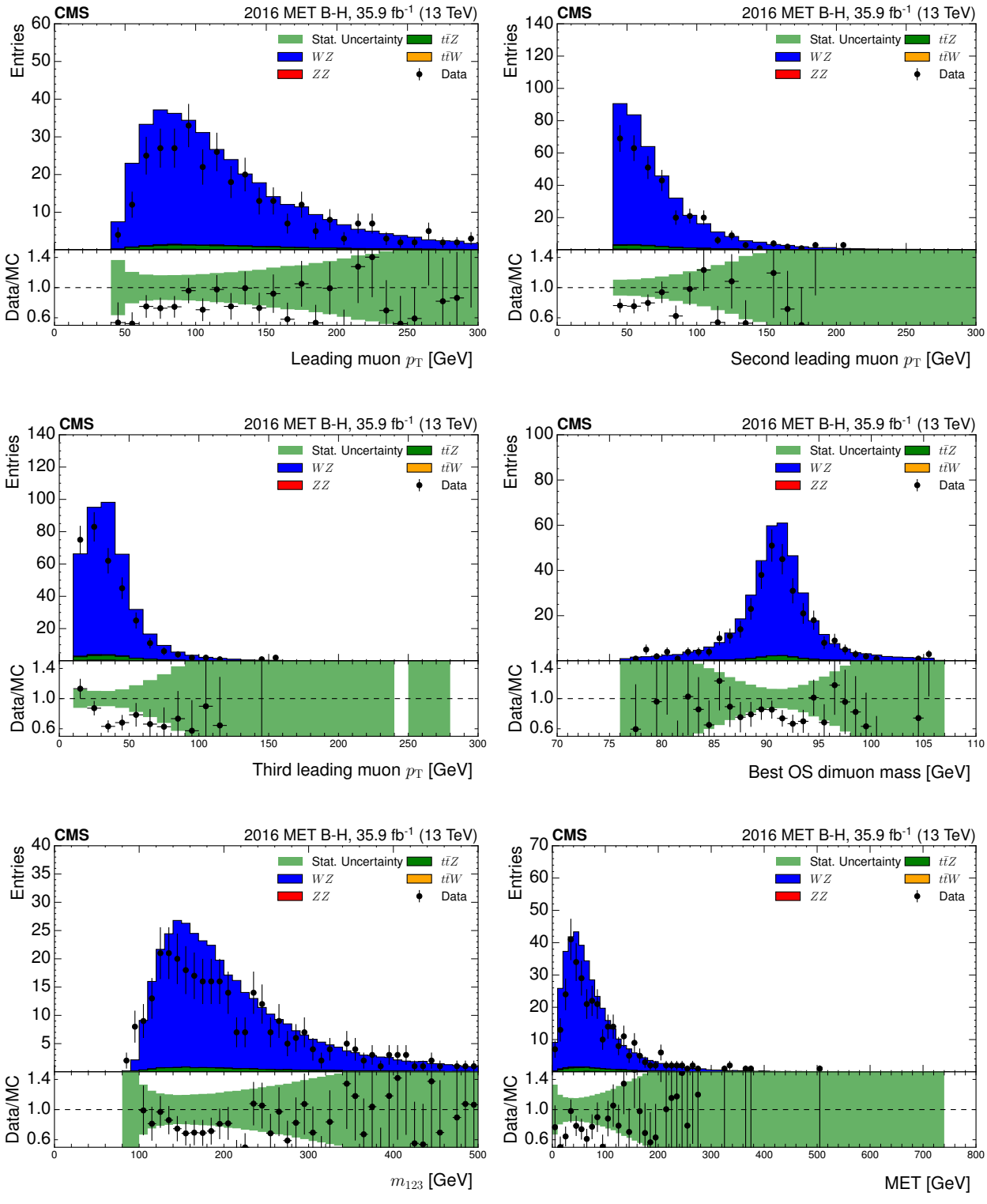

Figure 7.43: Data vs MC comparison of the WZ-like events.

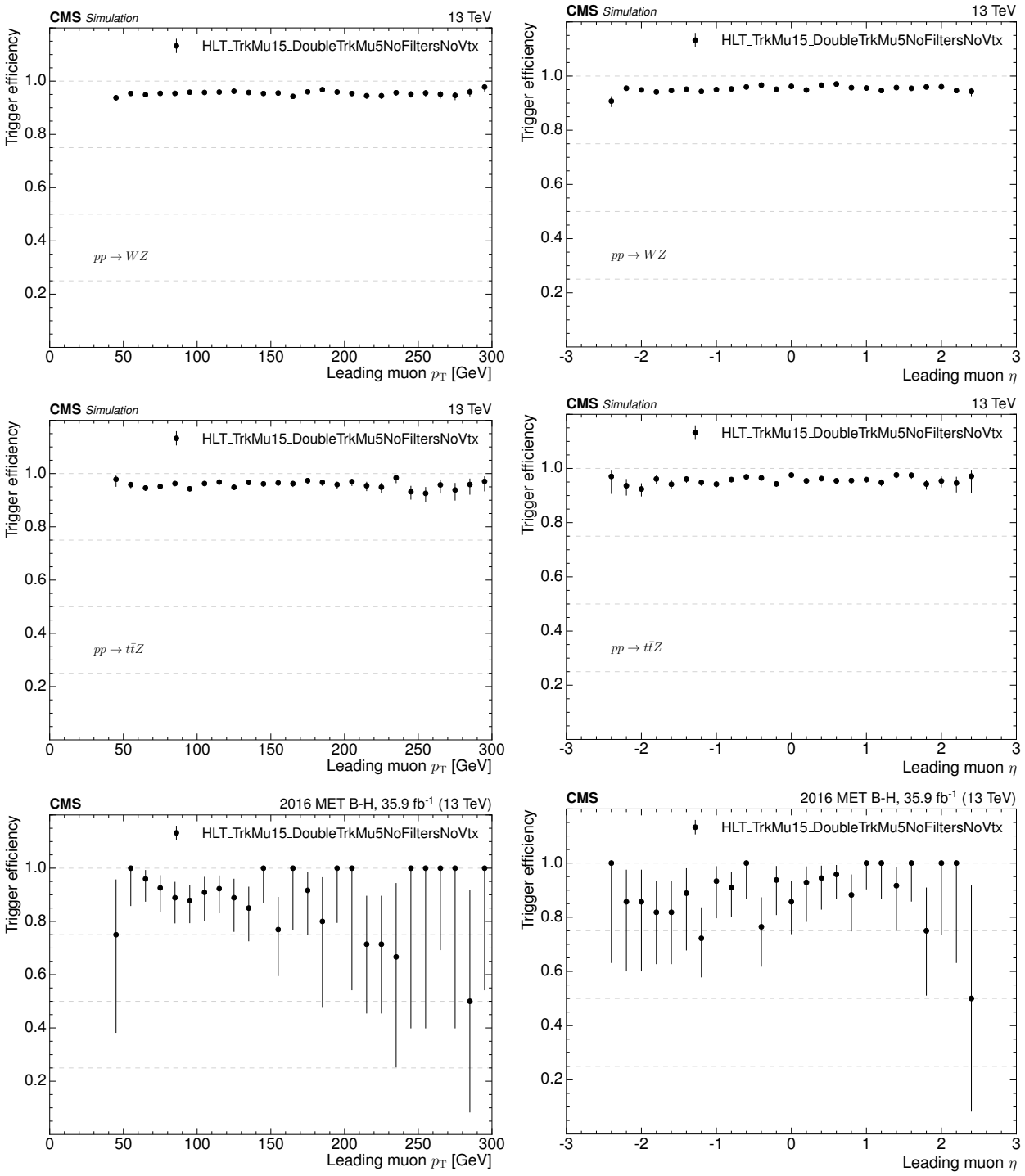

Figure 7.44: Trigger efficiency versus leading muon p_{T} and η on $pp \to WZ$ MC (top), $pp \to t\bar{t}Z$ MC (middle) and MET data (bottom).

Table 7.16: List of pure MET triggers in the 2016 HLT menu used to determine the trigger scale factor.

Trigger Path
HLT_MET100_v*
HLT_MET150_v*
HLT_MET200_v*
HLT_MET250_v*
HLT_MET300_v*
HLT_MET600_v*
HLT_MET700_v*
HLT_PFMET110_PFMHT110_IDTight_v*
HLT_PFMET120_PFMHT120_IDTight_v*
HLT_PFMET170_BeamHaloCleaned_v*
HLT_PFMET170_HBHECleaned_v*
HLT_PFMET170_HBHE_BeamHaloCleaned_v*
HLT_PFMET170_JetIdCleaned_v*
HLT_PFMET170_NoiseCleaned_v*
HLT_PFMET170_NotCleaned_v*
HLT_PFMET300_v*
HLT_PFMET400_v*
HLT_PFMET500_v*
HLT_PFMET600_v*
HLT_PFMETTypeOne190_HBHE_BeamHaloCleaned_v*

tematic uncertainty of 15% has been obtained by calculating the difference in the normalization between the Monte Carlo and the data and then dividing by the normalization in data.

Lowering the transverse momentum thresholds from $40 : 40 : 10$ GeV to $30 : 30 : 10$ GeV lowers the trigger efficiency on data by about 0.5%. The trigger scale factor also drops by about 0.5%. However, relaxing the p_{T} cuts too much introduces a nonprompt contribution in the data. Unfortunately, no available MC simulation sample adequately describes this contribution. The authors in Ref. [181] employed a data-driven method using dijet events enriched with nonprompt leptons. However, such study is beyond the scope of this analysis. The incomplete description of the background using MC simulation would bias the estimation of the trigger scale factor. Therefore, the p_{T} thresholds have been set to $40 : 40 : 10$ GeV to reduce the nonprompt contribution and to minimize the bias in the estimation of the trigger scale factor.

7.6.2.6 Muon p_{T} Scale

Scaling the transverse momentum of the muons up and down by a certain amount has no influence on the sensitivity in this analysis. Points in the 2D dimuon-dimuon mass space corresponding to events passing the full event selection would collectively scale up or down along the diagonal in case of a signal.

7.6.2.7 Muon p_{T} Resolution due to Displacement

The muons in this analysis are reconstructed both in the tracker and the muon system and have limited displacement ($L_{xy} < 9.8$ cm). The p_{T} resolution for such displaced muons is similar to prompt muons and is $\lesssim 2\%$ (see Sec. 6.2.1.2). The effect of displacement on the p_{T} resolution is therefore neglected in this study.

7.6.2.8 Dimuon Overlap in Tracker and Muon System

The effect of reconstructing dimuons from overlapping muons in tracker and muon system has been studied extensively in Ref. [168]. Conservative uncertainties are set for these effects which have been found to be 1.3% (tracker system) and 1.2% (muon system) per dimuon and per event.

7.6.2.9 Dimuon Mass Consistency

A systematic uncertainty of 1.5% on the acceptance is set, as mentioned in Sec. 7.4.4.

7.6.2.10 Pileup

The systematic uncertainty due to mischaracterization of the pileup distribution in MC is evaluated using a luminosity-based pileup estimation method. First, per-bunch luminosities are obtained from pixel detector information. Next, the delivered and recorded luminosity is calculated in each lumisection (which is about 23 seconds of data taking with CMS). The number of expected pileup interactions is then obtained from the per-bunch luminosities, the information in each lumisection and the pp total inelastic cross section. The pileup distribution is derived for the nominal case with $\sigma(pp)_{\mathrm{nom}} = 69.2$ mb. Similar pileup distributions are derived for data with a 5% shifted up cross section $\sigma(pp)_{\mathrm{up}} = 72.3$ mb and 5% shifted down cross section $\sigma(pp)_{\mathrm{down}} = 65.8$ mb. These

pileup distributions are shown in Fig. 7.45(left). The three pileup distributions in data have been normalized to unity and divided by the pileup distribution in MC (see Fig. 7.45(right)). The effect on $\epsilon_{\text{full}}/\alpha_{\text{gen}}$ for a representative MC sample is calculated for each of the three cases ($0\%, +5\%$, and -5%). The greatest absolute difference by magnitude in $\epsilon_{\text{full}}/\alpha_{\text{gen}}$ is taken as the uncertainty. Using this method, the systematic uncertainty has been measured to be 0.17%.

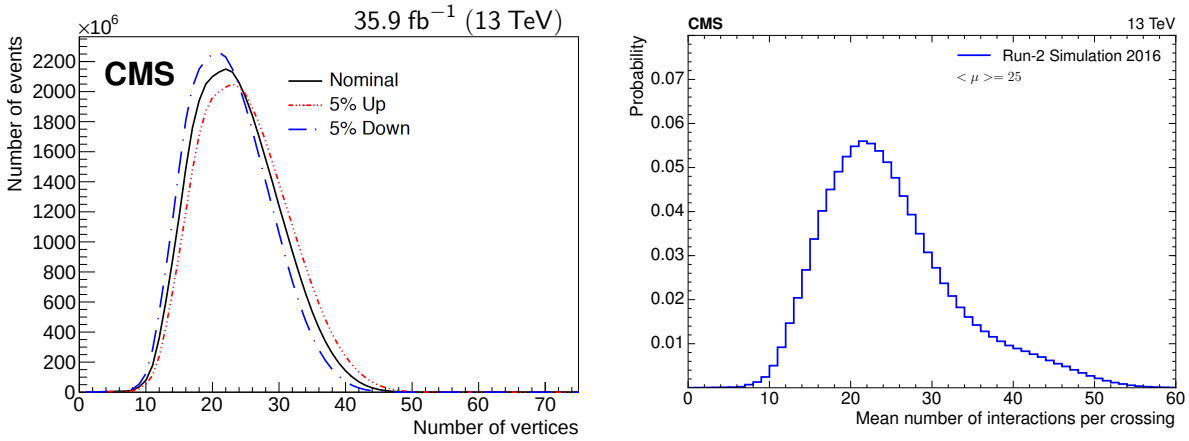

Figure 7.45: Left: Mean number of interactions per bunch crossing for the 2016 pp run at 13 TeV. The nominal case (black), 5% shifted up (red) and 5% shifted down (blue) are shown. Right: Probability distribution of the mean number of interactions per crossing in the 2016 CMS simulation.

7.6.3 Summary

The systematic uncertainties are summarized in Tab. 7.17. The total systematic uncertainty on the $\epsilon_{\text{full}}/\alpha_{\text{gen}}$ is obtained by adding the individual contributions in quadrature and has been estimated to be 12.1%.

Table 7.17: Summary of systematic uncertainties on $\epsilon_{\text{full}}/\alpha_{\text{gen}}$.

Source of uncertainty	Relative magnitude
Theoretical	
NNLO Higgs p_{T} reweighting	2.0%
PDF+α_s+QCD scales	8.0%
Higgs boson cross section	3.2%
Higgs boson branching fraction	2%
Experimental	
Integrated luminosity	2.5%
Muon ID	$4 \times 0.6\%$
Dimuon isolation	$2 \times 0.1\%$
Muon HLT	6%
Overlapping muons in tracker system	$2 \times 1.2\%$
Overlapping muons in muon system	$2 \times 1.3\%$
Dimuons mass consistency	1.5%
Pileup	0.17%
Total	12.1%

7.7 Results and Interpretation

In this section we unblind the signal region and examine the data that passes the full event selection. The unblinding is done in Sec. 7.7.1. The model-independent results are given in Sec. 7.7.2, and the interpretation for each of the two benchmark models NMSSM and MSSMD is discussed in Sec. 7.7.3 and Sec. 7.7.4. Conclusions and outlook are given in Sec. 7.7.5.

7.7.1 Unblinding of the Signal Region

The event selection criteria in Sec. 7.4 are applied to the DoubleMuon data sample. The signal region is populated with nine events passing the selection criteria including the $m_{(\mu\mu)_1} \simeq m_{(\mu\mu)_2}$ requirement. The data agrees with the 7.95 ± 1.83 background events predicted in Sec. 7.5.4. Table 7.18 shows some of the main parameters of the nine data events. These events are also shown in Fig. 7.46 as yellow triangles in the diagonal signal region in the $(m_{(\mu\mu)_1}, m_{(\mu\mu)_2})$ plane. The first event in the table is displayed in Fig. 7.47. The two isolated dimuons are clearly visible.

Table 7.18: Parameters of the 9 events in data that pass all selection criteria. Note: LS stands for "luminosity section"

Row	Run	LS	Event	$m_{(\mu\mu)_1}$ [GeV]	$m_{(\mu\mu)_2}$ [GeV]	Iso$_{(\mu\mu)_1}$ [GeV]	Iso$_{(\mu\mu)_2}$ [GeV]
1	275847	1705	2106699737	2.860	3.002	0	0.530
2	276437	1025	1853260264	3.073	3.054	1.745	0.564
3	278273	83	40062290	2.825	2.650	0.838	0
4	278769	83	26539721	3.152	2.855	1.238	0.944
5	279760	154	174402676	1.254	1.152	0	1.084
6	281707	695	1065646434	1.354	1.483	1.451	1.055
7	282814	1028	1890506418	2.386	2.358	0.657	1.966
8	283306	151	277427894	3.064	3.097	1.708	0
9	283453	122	100162832	1.940	1.820	0	0

7.7.2 Model Independent Limit

Since no excess is seen in the signal region, model independent upper limits can be set on $\sigma(pp \to 2a) \times B^2(a \to 2\mu) \times \alpha_{\text{gen}}$.

$$\sigma(pp \to 2a) \times B^2(a \to 2\mu) < \frac{N(m_{\mu\mu})}{\mathcal{L} \times \bar{r} \times \alpha_{\text{gen}}}, \tag{7.16}$$

where $\mathcal{L} = 35.9\ \text{fb}^{-1}$ the integrated luminosity in data and $\bar{r} = 0.56 \pm 0.06$ is the average of the ratio

$$r = \frac{\epsilon_{\text{full}}}{\alpha_{\text{gen}}} = \frac{\epsilon_{\text{full}}}{\epsilon_{\text{full}}^{\text{MC}}} \frac{\epsilon_{\text{full}}^{\text{MC}}}{\alpha_{\text{gen}}}. \tag{7.17}$$

The first term $\epsilon_{\text{full}}/\epsilon_{\text{full}}^{\text{MC}}$ is the product of the muon scale factors in Sec. 7.6: $\epsilon_{\text{full}}/\epsilon_{\text{full}}^{\text{MC}} = \text{SF}_{\text{ID}} \times \text{SF}_{\text{Iso}} \times \text{SF}_{\text{Trigger}} = 0.92 \pm 0.05$. The second term $\epsilon_{\text{full}}^{\text{MC}}/\alpha_{\text{gen}}$ is the ratio of the full reconstruction efficiency to the generator level acceptance. This ratio is averaged over all used benchmark points and has the value 0.61 ± 0.06.

The upper limits are set using the modified frequentist method [182, 183] according to recommendations set by the ATLAS-CMS LHC Higgs Combination Group [184–186]. This is the so-called CL_s method using test statistic $\text{CL}_s = \frac{p_{s+b}}{1-p_b}$ with p_{s+b} the p-value of the signal plus background hypothesis and p_b the p-value of the background-only hypothesis. Systematic uncertainties are incorporated in the analysis via nuisance parameters that are treated according to the frequentist

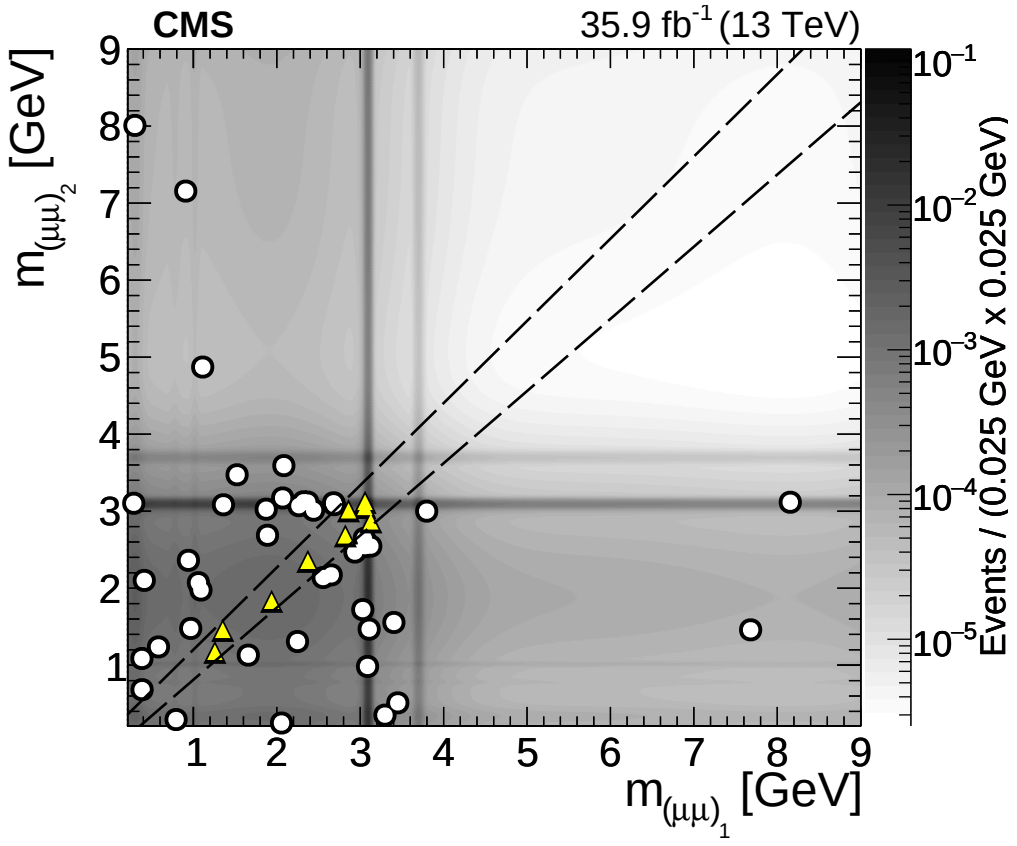

Figure 7.46: Distribution of the events in the $(m_{(\mu\mu)_1}, m_{(\mu\mu)_2})$ plane. The unblinded diagonal signal region is outlined with dashed lines. The white bullets depict the 43 events surviving all selections except the $m_{(\mu\mu)_1} \simeq m_{(\mu\mu)_2}$ requirement. The yellow triangles represent the nine events observed in data passing all selections. The gray scale indicates the expected SM background.

paradigm. Uncertainties on the signal yield are taken from Tab. 7.17, while uncertainties on the background yield are taken to be 20% (b-quark pair) and 15% (double J/ψ).

The limit-setting tool requires knowledge of the signal and background template in the parameter space of $\left(m_{(\mu\mu)_1}, m_{(\mu\mu)_2}\right)$. The signal template is a single 2D Crystal Ball function. We use the background templates derived in Sec. 7.5 for resonant backgrounds b-quark pair and double J/ψ production. The negligible nonresonant electroweak background is not used in the limit setting. With this information we test each mass point in the parameter space for how signal- or background-like it is. Per mass point 30 times $10,000$ pseudo-experiments are analyzed. The outputs of the tests are 90% and 95% CL limits on $N(m_{\mu\mu})$ in the mass range $0.25 - 8.5$ GeV, shown

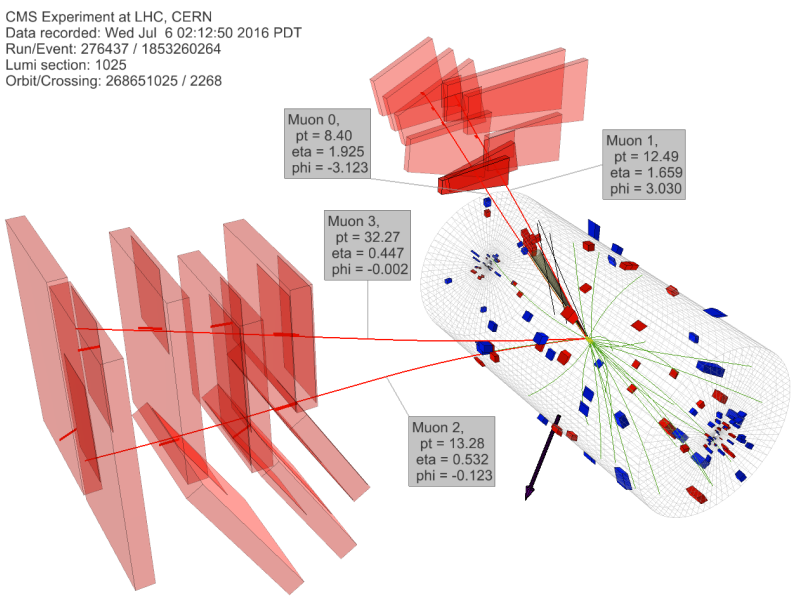

(a) 3D view

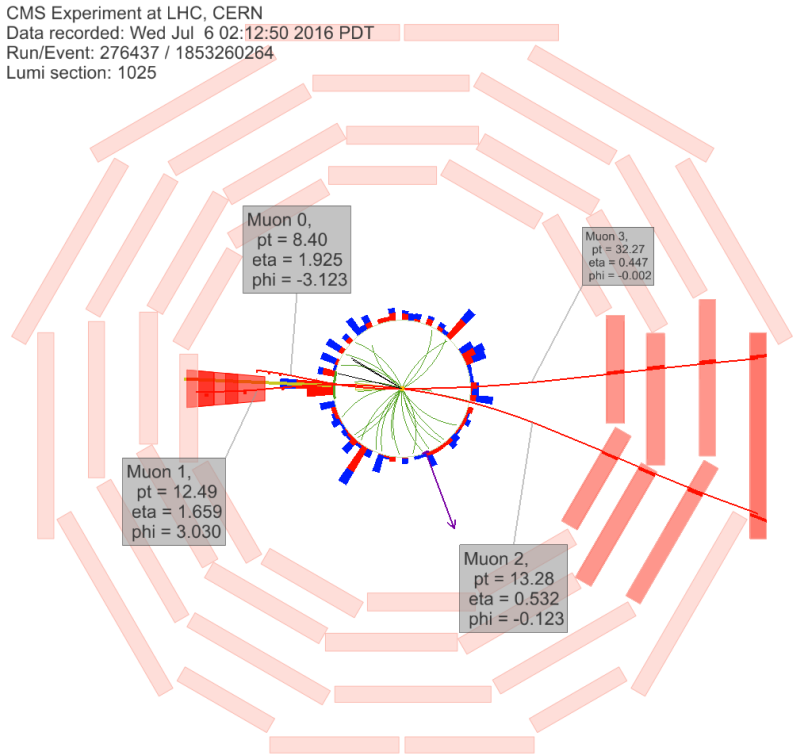

(b) $\rho - \phi$ view

Figure 7.47: Display of an event in data that passed all selection requirements. Muons are shown as red curves with kinematic parameters labeled. Muon chambers with hits are shown as red shapes. The inner silicon tracker is outlined with charged tracks shown as green curves. Top left: 3D view. Bottom: $\rho - \phi$ view.

as black dots in Fig. 7.48. The limits are fitted in the mass spectrum using a series of Gaussian distributions on top of a flat line. The resulting approximations as function of the light boson mass are shown by the solid red lines in Fig. 7.48 and take the form:

$$\begin{aligned}\lim(m_a; 0.90) = 2.34 &+ 0.49 \times \mathcal{G}(m_a, 1.2, 0.016) + 1.75 \times \mathcal{G}(m_a, 1.38, 0.036) \\ &+ 0.47 \times \mathcal{G}(m_a, 1.89, 0.062) + 1.2 \times \mathcal{G}(m_a, 2.37, 0.052) \\ &+ 2.05 \times \mathcal{G}(m_a, 2.84, 0.07) + 4.48 \times \mathcal{G}(m_a, 3.06, 0.07)\end{aligned} \tag{7.18}$$

$$\begin{aligned}\lim(m_a; 0.95) = 3 &+ 0.76 \times \mathcal{G}(m_a, 1.21, 0.04) + 1.81 \times \mathcal{G}(m_a, 1.41, 0.05) \\ &+ 0.58 \times \mathcal{G}(m_a, 1.90, 0.065) + 1.46 \times \mathcal{G}(m_a, 2.38, 0.059) \\ &+ 1.85 \times \mathcal{G}(m_a, 2.8, 0.07) + 4.89 \times \mathcal{G}(m_a, 3.05, 0.09)\end{aligned} \tag{7.19}$$

Where $\mathcal{G}$ is the nonnormalized Gaussian distribution

$$\mathcal{G}(x, \mu, \sigma) = \exp\left[-\frac{1}{2}\frac{(x-\mu)^2}{\sigma^2}\right] \tag{7.20}$$

Model independent limits are then calculated from $\sigma(pp \rightarrow 2a + X) \times B^2(a \rightarrow 2\mu) \times \alpha_{\text{gen}} \leq \lim(m_a)$. These limits are shown in Fig. 7.49. As can be seen, the limits vary between $0.11 - 0.34(90\%)$ and $0.15 - 0.39(95\%)$ in the mass range $0.25 - 8.5$ GeV. These results can be interpreted in the context of a given benchmark model with a similar final state. In these models, the light bosons must have masses between 0.25 and 8.5 GeV and the dimuons must be sufficiently isolated and spatially separated. Since the analysis is designed to be model independent, the limit calculation is a simple procedure and requires only the model-specific acceptance. This can be obtained from generator level information and does not require the full simulation of the detector response or the reconstruction software.

7.7.3 Interpretation in the Context of NMSSM

The model independent limit can be interpreted as a 95% CL upper limit on $\sigma\left(pp \rightarrow h_{1,2}\right) \times B\left(h_{1,2} \rightarrow 2a_1\right) \times B^2(a_1 \rightarrow 2\mu)$ as a function of m_{a_1} in the context of the NMSSM benchmark

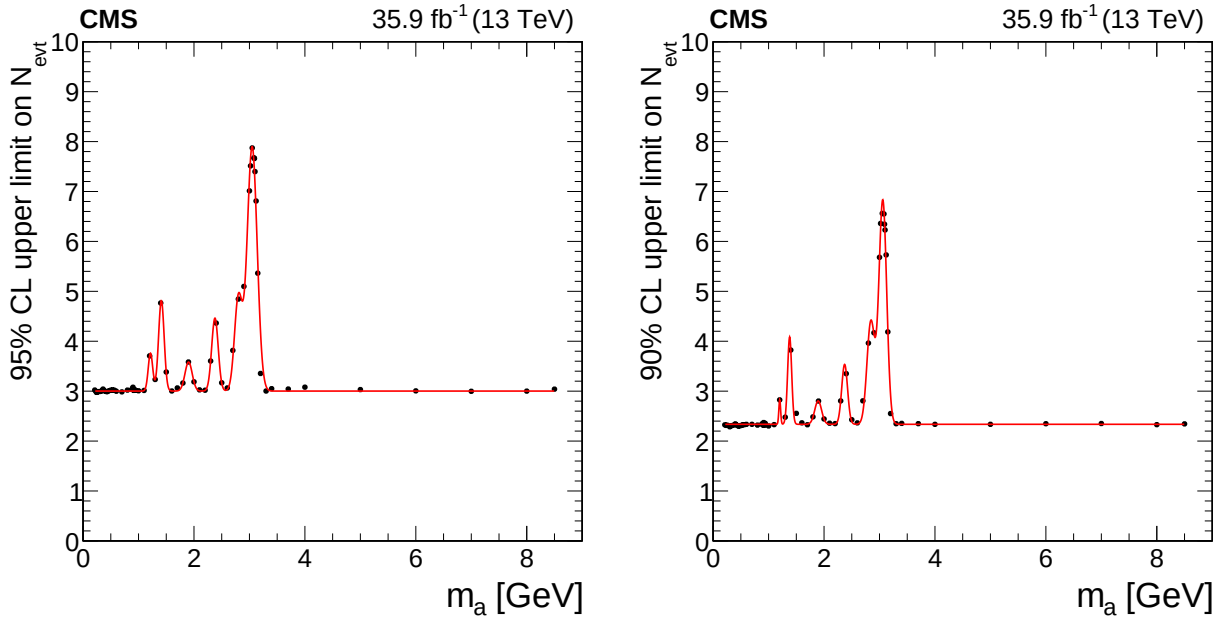

(a) (b)

Figure 7.48: The 90% CL (left) and 95% CL (right) upper limits on $N_{\mu\mu}$ versus light boson mass. Limits are calculated for a set of mass points (black dots). The limits is approximated with a smooth curve (solid red line).

model. This is done using the inequality

$$\sigma\left(pp \to h_{1,2}\right) \times B(h_{1,2} \to 2a_1) \times B^2(a_1 \to 2\mu) < \frac{N(m_{\mu\mu})}{\mathcal{L} \times \bar{r} \times \alpha_{\text{gen}}}. \tag{7.21}$$

The 95% CL upper limit curves are shown in Fig. 7.50 for three choices of m_{h_1}.

Conservative limits can also be obtained as function of $m_{h_{1,2}}$ for several values of m_{a_1}. This is done below. Recall that NMSSM has three CP-even Higgs bosons. One Higgs boson h_3 is typically very heavy, while $h_{1,2}$ are relatively light. One of the Higgs bosons is SM-like, with a large branching fraction to SM particles, but small couplings to new light bosons $B(h_i \to 2a_1)$. The other Higgs boson is BSM-like and has a large branching fraction to light bosons. With this information we can factorize the phase space of $m_{h_{1,2}}$ in three categories of which two can be probed by this analysis.

A first category involves h_1 being a BSM-like Higgs boson and lighter than the 125 GeV SM-

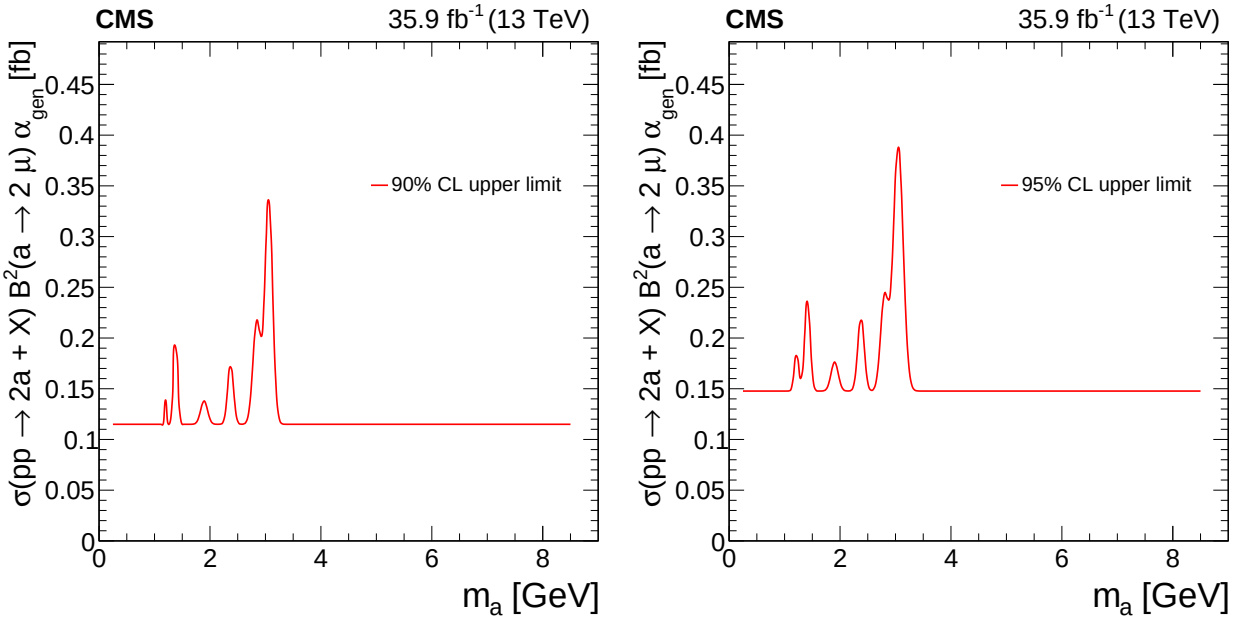

(a) (b)

Figure 7.49: Model independent 90% CL (left) and 95% CL (right) upper limits on $\sigma(pp \to 2a) \times B^2(a \to 2\mu) \times \alpha_{\text{gen}}$.

like Higgs boson h_2. Its production cross section is reduced compared to the SM-like Higgs boson, $\sigma(pp \to h_1) < \sigma(pp \to h_2)$, while the branching fraction to light bosons $B(h_1 \to 2a_1)$ is large.

A second category involves h_2 being a BSM-like Higgs boson and heavier than the 125 GeV SM-like Higgs boson h_1. Its production cross section is reduced compared to the SM-like Higgs boson, $\sigma(pp \to h_2) < \sigma(pp \to h_1)$, while the branching fraction to light bosons $B(h_2 \to 2a_1)$ is large.

In the third category, the BSM-like Higgs boson (lighter or heavier than 125 GeV) has a large branching fraction to light bosons, but has such a small production cross section, that it would be produced in too few numbers to be observed at CMS.

To set limits on each category, we use the following notation: $(\sigma \times B)_{\text{h}_1} \equiv \sigma(pp \to h_1) \times B(h_1 \to 2a_1) \times B^2(a_1 \to 2\mu) \times \alpha(m_{h_1})$.

In the first category we have $(\sigma \times B)_{\text{h}_1} \leq (\sigma \times B)_{\text{h}_1} + (\sigma \times B)_{\text{h}_2} \leq X$, with X the limit set by this analysis. Assuming that the SM-like contribution $(\sigma \times B)_{\text{h}_2}$ is negligible, the limit is exact.

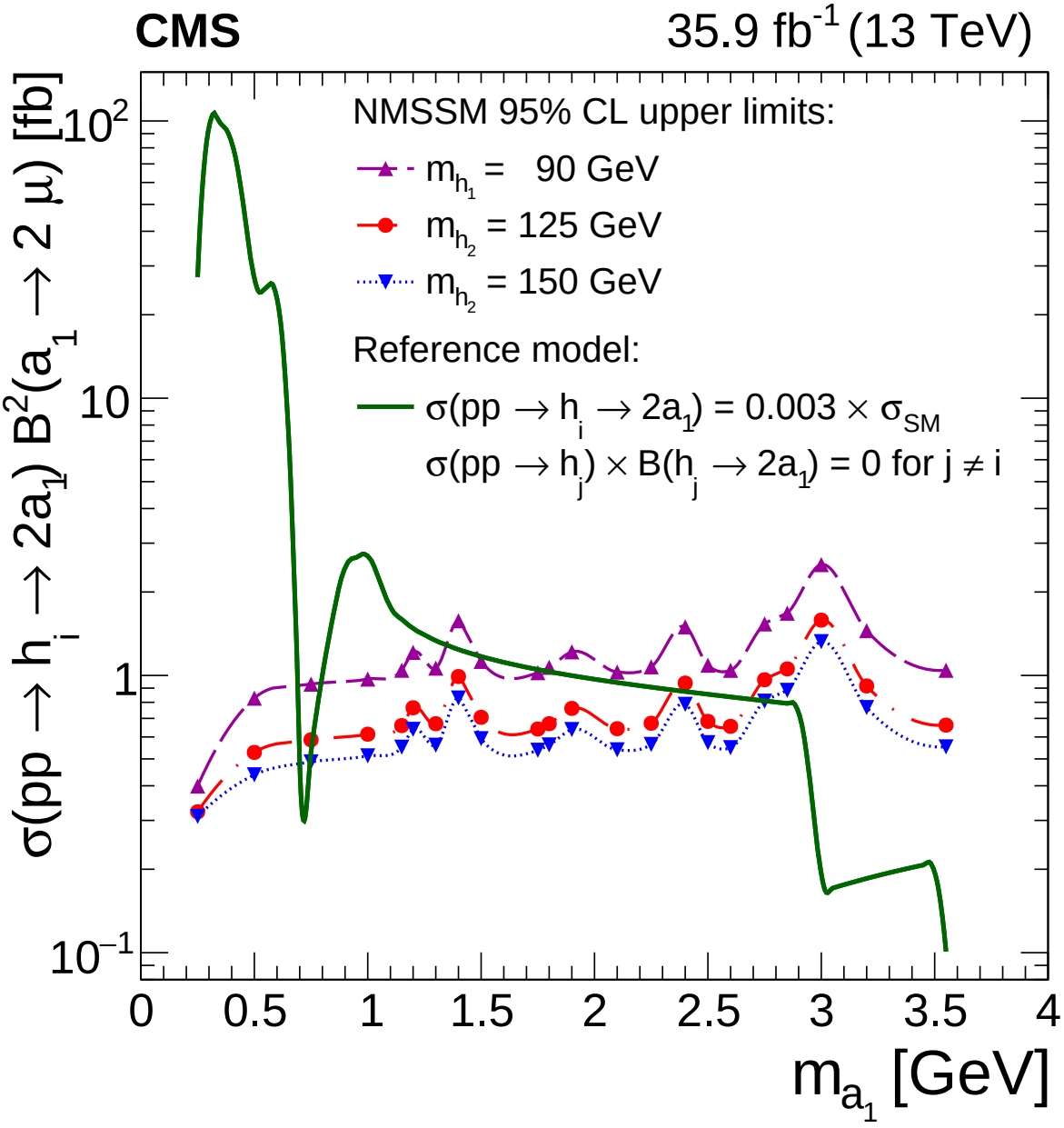

Figure 7.50: The 95% CL upper limits on $\sigma(pp \to h_{1,2}) \times B(h_{1,2} \to 2a_1) \times B^2(a_1 \to 2\mu)$ as functions of m_{a_1}. Observed limits are shown for three cases: $m_{h_1} = 90$ GeV (purple dashed curve), $m_{h_1} = 125$ GeV (red dash-dotted curve) and $m_{h_1} = 150$ GeV (blue dotted curve). The observed limits are compared to predicted ones for a simplified model with parameters $B(h_1 \to 2a_1) = 0.3\%$, $\sigma(pp \to h_1) = \sigma_{\mathrm{SM}}(m_{h_1} = 125\ \mathrm{GeV})$ [92], $\sigma(pp \to h_2) \times B(h_2 \to 2a_1) = 0$ and $B(a_1 \to 2\mu) = 7.7\%$. The branching fraction $B(a_1 \to 2\mu)$ is taken from Ref. [115] for NMSSM parameter $\tan\beta = 20$.

In case this contribution is sizeable, the result is a more conservative limit on $(\sigma \times B)_{\mathrm{h_1}}$.

The second category is similar to the first. We have $(\sigma \times B)_{\mathrm{h_2}} \leq (\sigma \times B)_{\mathrm{h_1}} + (\sigma \times B)_{\mathrm{h_2}} \leq X$. Again, we neglect the the SM-like Higgs boson term $(\sigma \times B)_{\mathrm{h_1}}$. Depending on the actual size of the limit may be exact or conservative, as in the first case.

In the third category we have $(\sigma \times B)_{h_{\mathrm{SM}}} \leq (\sigma \times B)_{h_{\mathrm{SM}}} + (\sigma \times B)_{h_{\mathrm{BSM}}} \leq X$, but the BSM-like Higgs boson contribution is negligible because its production cross section is suppressed. In this case, a limit on BSM decays of the SM-like Higgs boson B_{BSM} can be set. If $(\sigma \times B)_{h_{\mathrm{BSM}}}$ is not negligible, the limit on B_{BSM} is more conservative than the exact limit.

Figure 7.51 shows the 95% CL upper limits on $\sigma\,(pp \to h_{1,2}) \times B(h_{1,2} \to 2a_1) \times B^2(a_1 \to 2\mu)$ versus m_h. For $m_h < 125$ GeV, $m_h > 125$ GeV or $m_h = 125$ GeV the result should be interpreted as a limit on h_1, h_2 and h_{SM} respectively. In the last case, this is h_1 or h_2, depending on which of the two is kinematically accessible. The limits are shown for two different values of m_{a_1}. Limits for a simplified model (with parameters mentioned in Fig. 7.50) are also provided. This analysis has improved the 95% CL upper limits on the NMSSM process $\sigma\,(pp \to h_{1,2}) \times B(h_{1,2} \to 2a_1) \times B^2(a_1 \to 2\mu)$ from $0.6 - 1.6$ fb [47] to $0.3 - 1.1$ fb at $90 - 150$ GeV.

7.7.4 Interpretation in the Context of MSSMD

The model independent limits can also be interpreted as 95% CL limits on $\sigma(pp \to h) \times B(h \to 2\gamma_{\mathrm{D}} + X) \times B^2(\gamma_{\mathrm{D}} \to \mu\mu)$ in the context of the MSSMD benchmark model. This is done as follows:

$$\sigma(pp \to h) \times B(h \to 2\gamma_{\mathrm{D}} + X) \times B^2(\gamma_{\mathrm{D}} \to \mu\mu) < \frac{N(m_{\mu\mu})}{\mathcal{L} \times \bar{r} \times \alpha_{\mathrm{gen}}}, \tag{7.22}$$

with $\mathcal{L}$ the integrated luminosity, $\bar{r}$ the full reconstruction efficiency in data and α_{gen} the generator level acceptance. Let $\sigma(pp \to h) \times B(h \to 2a + X)$ be normalized to the cross section of SM Higgs boson production according to $\sigma(pp \to h) \times B(h \to 2a + X) = \sigma(pp \to h_{\mathrm{SM}}) \times K$, with K an "effective" branching fraction. Depending on the value of K a limit on the branching fraction

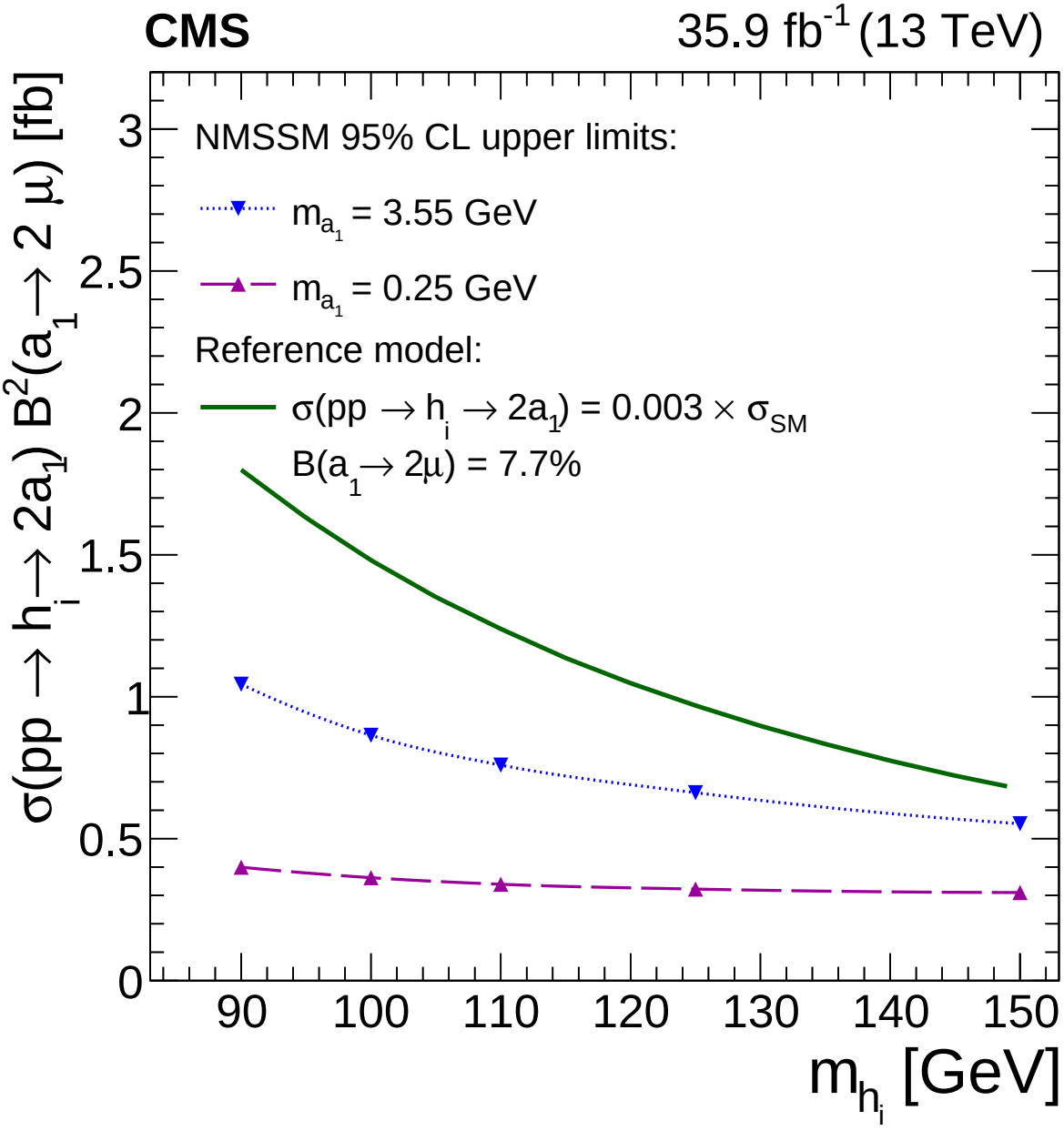

Figure 7.51: The 95% CL upper limits as functions of m_{h_1}, for the NMSSM case, on $\sigma(pp \to h_{1,2}) \times B(h_{1,2} \to 2a_1) \times B^2(a_1 \to 2\mu)$ with $m_{a_1} = 0.25$ GeV (dashed curve), $m_{a_1} = 2$ GeV (dash-dotted curve) and $m_{a_1} = 3.55$ GeV (dotted curve). As an illustration, the limits are compared to the predicted rate (solid curve) obtained using a simplified scenario with $\sigma(pp \to h_1) = \sigma_{\mathrm{SM}}(m_{h_1})$ [179], $\sigma(pp \to h_2) \times B(h_2 \to 2a_1) = 0$, $B(h_1 \to 2a_1) = 0.3\%$, and $B(a_1 \to 2\mu) = 7.7\%$. The chosen $B(a_1 \to 2\mu)$ is taken from [115] for $m_{a_1} = 2$ GeV and NMSSM parameter $\tan\beta = 20$.

$B(h \to 2\gamma_{\rm D} + X)$ can be set:

$$\sigma(pp \to h_{\rm SM}) \times K < \frac{N(m_{\mu\mu})}{\mathcal{L} \times \bar{r} \times \alpha_{\rm gen} \times B^2(\gamma_{\rm D} \to \mu\mu)} \tag{7.23}$$

or

$$B^2(\gamma_{\rm D} \to \mu\mu) < \frac{N(m_{\mu\mu})}{\mathcal{L} \times \bar{r} \times \alpha_{\rm gen} \times \sigma(pp \to h_{\rm SM}) \times K} \tag{7.24}$$

These limits can be derived for each MSSMD sample with a certain $(m_{\gamma_{\rm D}}, c\tau_{\gamma_{\rm D}})$ in the 2D parameter space, and for a few K values. By rewriting $c\tau_{\gamma_{\rm D}}$ in terms of $m_{\gamma_{\rm D}}$ and ε, limits can be obtained in the $(m_{\gamma_{\rm D}}, \varepsilon)$ parameter space.

7.7.4.1 Derivation of $(m_{\gamma_{\rm D}}, \varepsilon)$

The partial width of dark photon decay into a pair of leptons ll is given by the expression

$$\Gamma(\gamma_{\rm D} \longrightarrow l^+l^-) = \frac{1}{3}\alpha\varepsilon^2 m_{\gamma_{\rm D}} \sqrt{1 - \frac{4m_l^2}{m_{\gamma_{\rm D}}}} \left(1 + \frac{2m_l^2}{m_{\gamma_{\rm D}}}\right), \tag{7.25}$$

where m_l is the lepton mass. Decays of hadronic particles become available when the dark photon becomes sufficiently massive, $m_{\gamma_{\rm D}} \geq 2m_\pi$. The associated partial width of dark photon decay into a pair of hadrons is

$$\Gamma(\gamma_{\rm D} \longrightarrow hadrons) = \frac{1}{3}\alpha\varepsilon^2 m_{\gamma_{\rm D}} \sqrt{1 - \frac{4m_{hadron}^2}{m_{\gamma_{\rm D}}}} \left(1 + \frac{2m_{hadron}^2}{m_{\gamma_{\rm D}}}\right) R(s = m_{\gamma_{\rm D}}^2) \tag{7.26}$$

where $R = \sigma(e^+e^- \longrightarrow hadrons)/\sigma(e^+e^- \longrightarrow \mu^+\mu^-)$ is the ratio between the production cross sections of hadrons and muons in e^+e^- collisions. The total decay width $\Gamma_{\gamma_{\rm D},\, total}$ is the sum of the decay widths to leptons and hadrons $\Gamma_{\gamma_{\rm D},\, total} = \Gamma(\gamma_{\rm D} \longrightarrow e^+e^-) + \Gamma(\gamma_{\rm D} \longrightarrow \mu^+\mu^-) + \Gamma(\gamma_{\rm D} \longrightarrow \tau^+\tau^-) + \Gamma(\gamma_{\rm D} \longrightarrow hadrons)$. Since the dark photon lifetime is inversely proportional to the total decay width $\tau_{\gamma_{\rm D}} = \hbar/\Gamma_{\gamma_{\rm D},\, total}$, the lifetime can be written as

$$\tau_{\gamma_{\rm D}} = \frac{\hbar}{\Gamma(\gamma_{\rm D} \longrightarrow e^+e^-) + \Gamma(\gamma_{\rm D} \longrightarrow \mu^+\mu^-) + \Gamma(\gamma_{\rm D} \longrightarrow \tau^+\tau^-) + \Gamma(\gamma_{\rm D} \longrightarrow hadrons)} \tag{7.27}$$

The width can be factorized in terms of the dark photon mass and the mixing parameter $\Gamma_{\gamma_D} = \varepsilon^2 f(m_{\gamma_D})^{-1}$, with

$$\frac{1}{f(m_{\gamma_D})} = \frac{1}{3}\alpha m_{\gamma_D}\sqrt{1-\frac{4m_{hadron}^2}{m_{\gamma_D}}}\left(1+\frac{2m_{hadron}^2}{m_{\gamma_D}}\right)R(s=m_{\gamma_D}^2), \tag{7.28}$$

a function that only depends on the dark photon mass. The lifetime is thus a function of the mass and inversely proportional to the kinetic mixing parameter squared $\tau_{\gamma_D} = \frac{\hbar}{\varepsilon^2} f(m_{\gamma_D})$. In the $(m_{\gamma_D}, \varepsilon)$ parameter space, smaller ε is equivalent to longer lifetimes. In terms of displacement in mm, we have

$$c\tau_{\gamma_D}(m_{\gamma_D}, \varepsilon)[\mathrm{mm}] = \frac{1.97\times 10^{-13}}{\varepsilon^2} f(m_{\gamma_D})[\mathrm{mm}], \tag{7.29}$$

7.7.4.2 Interpretation in the $(m_{\gamma_D}, \varepsilon)$ Parameter Space

Figure 7.52 shows the 95% CL limits on $\sigma(pp \to h) \times B(h \to 2\gamma_D + X) \times B^2(\gamma_D \to \mu\mu)$ for $K = 0.1\%, 1\%, 10\%$ and 40% in $(m_{\gamma_D}, \varepsilon)$. Limits from other searches are also provided, including a recent result from a dark photon search by LHCb [65]. This search constrains a large area of the parameter space. The previously published result excluded the MSSMD model with kinetic mixing ε between 5×10^{-6} at 0.25 GeV and 6×10^{-7} at 2 GeV [47]. The current limits improve to 2×10^{-6} at 0.25 GeV and 5×10^{-8} at 8.5 GeV.

7.7.5 Conclusions

The signal region has been unblinded. The data have been found to be consistent with the standard model expectation within the uncertainty. Model independent limits have been set on $\sigma(pp \to 2a) \times B^2(a \to 2\mu)$ as a function of the light boson mass. The results have been interpreted in the context of two benchmark models. In the case of NMSSM, limits on $\sigma(pp \to h_{1,2}) \times B(h_{1,2} \to 2a_1) \times B^2(a_1 \to 2\mu)$ have been set down to $0.3 - 1.1$ fb In the case of MSSMD, new limits have been set on $\sigma(pp \to h) \times B(h \to 2\gamma_D + X) \times B^2(\gamma_D \to \mu\mu)$ in $(m_{\gamma_D}, \varepsilon)$ resulting in the exclusion of a large area of the parameter space.

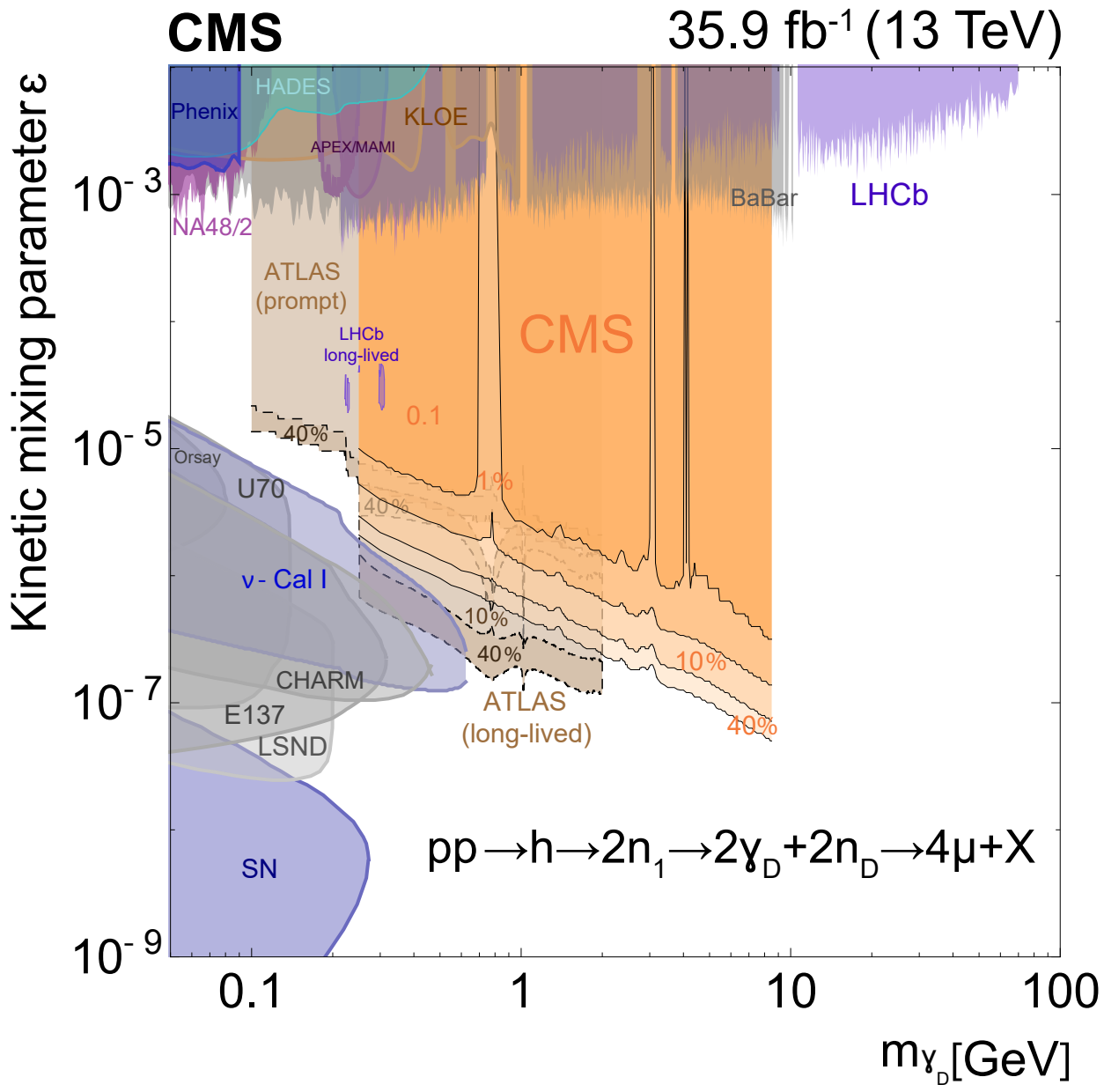

Figure 7.52: 90% CL upper limits (black solid curves) from this search on $\sigma(pp \to h)\, B(h \to 2\gamma_{\mathrm{D}} + X)$ (with $m_{\mathrm{n_1}} = 10$ GeV, $m_{\mathrm{n_D}} = 1$ GeV) in the plane of two of the parameters (ε and $m_{\gamma_{\mathrm{D}}}$) for the MSSMD scenarios, along with constraints from other experiments [18, 20, 22, 23, 40, 57, 65, 187–195] showing the 90% CL exclusion contours. The colored contours represent different values of $B(h \to 2\gamma_{\mathrm{D}} + X)$ in the range 0.1–40%.

8. CONCLUSIONS AND OUTLOOK

In this dissertation a study has been conducted for pair production of new light bosons decaying into pairs of oppositely charged muons, $h \to 2a + X \to 4\mu + X$. The study has been performed on a pp collision data sample collected by the Compact Muon Solenoid experiment in 2016 that corresponds to an integrated luminosity of $35.9\ \mathrm{fb}^{-1}$ at a center-of-mass energy $\sqrt{s} = 13\ \mathrm{TeV}$. Several improvements have been made compared to the previous CMS search. The data have been collected with a new triple-muon trigger, that has an increased sensitivity to signatures with displaced vertices, at a higher center-of-mass energy. The analysis selections have been improved to extend the light boson mass range and the maximum possible displacement of the light boson decay vertex. Nine events have been observed in the signal region, which is consistent with the SM expectation of 7.95 ± 1.83 events. From these observations, a model independent 95% CL upper limit on the product of the cross section, branching fraction, and acceptance, $\sigma(pp \to 2a + X) \times B^2(a \to 2\mu) \times \alpha_{\mathrm{gen}}$, has been set over the mass range $0.25 < m_a < 8.5\ \mathrm{GeV}$. Its value varies between 0.15 and $0.39\ \mathrm{fb}$ in the mass range $0.25 - 8.5\ \mathrm{GeV}$. The model independent limit has been interpreted in the context of the next-to-minimal supersymmetric standard model (NMSSM) and a minimal SUSY model with a $U(1)_{\mathrm{D}}$ dark sector (MSSMD) that allows for light bosons with a nonnegligible lifetime up to $c\tau_{\gamma_{\mathrm{D}}} = 100\ \mathrm{mm}$. In the case of NMSSM, 95% CL limits on $\sigma(pp \to h_{1,2}) \times B(h_{1,2} \to 2a_1) \times B^2(a_1 \to 2\mu)$ have been set over the mass range $0.25 < m_a < 3.55\ \mathrm{GeV}$ of $0.3\ \mathrm{fb}$ to $1.1\ \mathrm{fb}$, improving the existing limits by a factor of 1.5 to 3. In the case of MSSMD, new limits on $\sigma(pp \to h) \times B(h \to 2\gamma_{\mathrm{D}} + X) \times B^2(\gamma_{\mathrm{D}} \to 2\mu)$ constrain previously unexamined ranges of ε in the $(m_{\gamma_{\mathrm{D}}}, \varepsilon)$ plane.

This study can be improved in several ways to continue the search for new light bosons. First of all, further optimization of the event selection for the 2016 dataset could enhance the sensitivity of the search and could set more stringent limits on $\sigma(pp \to 2a + X) \times B^2(a \to 2\mu) \times \alpha_{\mathrm{gen}}$. In addition, the model independent limits can be improved by at least a factor three by using the entire Run-2 dataset collected between 2015 and 2018 ($\approx 140\ \mathrm{fb}^{-1}$). The scope of the analysis

can be expanded by incorporating decay modes with electrons, tau leptons or b quarks to probe the low-mass region (between $2m_e$ and $2m_\mu$) or the high-mass region (between 8.5 and 62.5 GeV). Furthermore, extra production modes may be investigated. While gluon-gluon fusion accounts for $> 85\%$ of the signal yield, extra sensitivity can be expected by including the VBF, Vh and $t\bar{t}h$ production modes. The sensitivity of this study can also be enhanced for displaced signatures by enlarging the fiducial volume in which light bosons can decay. Studies conducted in the context of the CMS Phase-2 Trigger and Muon Upgrade project [143, 147] have shown that it is possible to deploy a L1T sensitive to muon displacements up to $\Delta_{xy} \approx 1$ m. Increasing the fiducial volume from $L_{xy} \approx 10$ cm to 100 cm would constrain a large area in the $(m_{\gamma_\mathrm{D}}, \varepsilon)$ parameter in the case of MSSMD. All these improvements may be taken advantage of to search for evidence of physics beyond the SM with light bosons during the Phase-2 operation of CMS. An expected 3000 fb^{-1} will be collected during the high-luminosity run of the LHC, which would allow to set more stringent limits on $\sigma(pp \to 2a + X) \times B^2(a \to 2\mu) \times \alpha_{\mathrm{gen}}$ by several orders in magnitude.

REFERENCES

[1] S. Glashow, "Partial-symmetries of weak interactions", *Nucl. Phys.* **22** (1961) 579, doi:doi:10.1016/0029-5582(61)90469-2.

[2] S. Weinberg, "A model of leptons", *Phys. Rev. Lett.* **19** (1967) 1264, doi:10.1103/PhysRevLett.19.1264.

[3] A. Salam, "Weak and electromagnetic interactions", *Elementary Particle Theory, Proceedings Of The Nobel Symposium* **C680519** (1968) 367.

[4] S. L. Glashow, J. Iliopoulos, and L. Maiani, "Weak interactions with lepton-hadron symmetry", *Phys. Rev.* **D2** (1970) 1285, doi:10.1103/PhysRevD.2.1285.

[5] M. Veltman, "Perturbation theory of massive Yang-Mills fields", *Nucl. Phys.* **B7** (1968) 637, doi:10.1016/0550-3213(68)90197-1.

[6] G. 't Hooft and M. Veltman, "Regularization and renormalization of gauge fields", *Nucl. Phys.* **B44** (1972) 189, doi:10.1016/0550-3213(72)90279-9.

[7] Particle Data Group Collaboration, "Review of Particle Physics", *Phys. Rev.* **D98** (Aug, 2018) 030001, doi:10.1103/PhysRevD.98.030001.

[8] L. Evans and P. Bryant, "LHC Machine", *JINST* **3** (2008) S08001, doi:10.1088/1748-0221/3/08/S08001.

[9] A. Bross et al., "Search for short-lived particles produced in an electron beam dump", *Phys. Rev. Lett.* **67** (1991) 2942, doi:10.1103/PhysRevLett.67.2942.

[10] E. M. Riordan et al., "Search for short-lived axions in an electron-beam-dump experiment", *Phys. Rev. Lett.* **59** (1987) 755, doi:10.1103/PhysRevLett.59.755.

[11] J. D. Bjorken et al., "Search for neutral metastable penetrating particles produced in the SLAC beam dump", *Phys. Rev.* **D38** (1988) 3375, doi:10.1103/PhysRevD.38.3375.

[12] S. N. Gninenko, "Constraints on dark photons from π^0 decays", *Phys. Rev.* **D87** (2013) 035030, doi:10.1103/PhysRevD.87.035030.

[13] WASA-at-COSY Collaboration, "Search for a dark photon in the $\pi^0 \to e^+e^-\gamma$ decay", *Phys. Lett.* **B726** (2013) 187, doi:10.1016/j.physletb.2013.08.055.

[14] J. Blumlein et al., "Limits on neutral light scalar and pseudoscalar particles in a proton beam dump experiment", *Z. Phys.* **C51** (1991) 341, doi:10.1007/BF01548556.

[15] A. Konaka et al., "Search for Neutral Particles in Electron-Beam-Dump Experiment", *Phys. Rev. Lett.* **57** (1986) 659, doi:10.1103/PhysRevLett.57.659.

[16] M. Davier and H. Nguyen Ngoc, "An Unambiguous Search for a Light Higgs Boson", *Phys. Lett.* **B229** (1989) 150, doi:10.1016/0370-2693(89)90174-3.

[17] S. N. Gninenko, "Stringent limits on the $\pi^0 \to \gamma X$, $X \to e^+e^-$ decay from neutrino experiments and constraints on new light gauge bosons", *Phys. Rev.* **D85** (2012) 055027, doi:10.1103/PhysRevD.85.055027.

[18] S. N. Gninenko, "Constraints on sub-GeV hidden sector gauge bosons from a search for heavy neutrino decays", *Phys. Lett.* **B713** (2012) 244, doi:10.1016/j.physletb.2012.06.002.

[19] R. Essig, P. Schuster, N. Toro, and B. Wojtsekhowski, "An Electron Fixed Target Experiment to Search for a New Vector Boson A' Decaying to e+e-", *JHEP* **02** (2011) 009, doi:10.1007/JHEP02(2011)009.

[20] APEX Collaboration, "Search for a New Gauge Boson in Electron-Nucleus Fixed-Target Scattering by the APEX Experiment", *Phys. Rev. Lett.* **107** (2011) 191804, doi:10.1103/PhysRevLett.107.191804.

[21] A1 Collaboration, "Search at the Mainz Microtron for Light Massive Gauge Bosons Relevant for the Muon $g-2$ Anomaly", *Phys. Rev. Lett.* **112** (2014) 221802, doi:10.1103/PhysRevLett.112.221802.

[22] HADES Collaboration, "Searching a Dark Photon with HADES", *Phys. Lett.* **B731** (2014) 265, doi:10.1016/j.physletb.2014.02.035.

[23] PHENIX Collaboration, "Search for dark photons from neutral meson decays in $p+p$ and d + Au collisions at $\sqrt{s_{NN}} = 200$ GeV", *Phys. Rev.* **C91** (2015) 031901, doi:10.1103/PhysRevC.91.031901.

[24] DØ Collaboration, "Search for NMSSM Higgs bosons in the $h \to aa \to \mu\mu\mu\mu, \mu\mu\tau\tau$ channels using $p\bar{p}$ collisions at $\sqrt{s} = 1.96$ TeV", *Phys. Rev. Lett.* **103** (2009) 061801, doi:10.1103/PhysRevLett.103.061801.

[25] CLEO Collaboration, "Search for very light CP-odd Higgs boson in radiative decays of $\Upsilon(1S)$", *Phys. Rev. Lett.* **101** (2008) 151802, doi:10.1103/PhysRevLett.101.151802.

[26] KLOE-2 Collaboration, "Limit on the production of a light vector gauge boson in phi meson decays with the KLOE detector", *Phys. Lett.* **B720** (2013) 111, doi:10.1016/j.physletb.2013.01.067.

[27] BESIII Collaboration, "Search for a light exotic particle in J/ψ radiative decays", *Phys. Rev.* **D85** (2012) 092012, doi:10.1103/PhysRevD.85.092012.

[28] BESIII Collaboration, "Search for a light CP-odd Higgs boson in radiative decays of J/ψ", *Phys. Rev.* **D93** (2016) 052005, doi:10.1103/PhysRevD.93.052005.

[29] OPAL Collaboration, "Decay mode independent searches for new scalar bosons with the OPAL detector at LEP", *Eur. Phys. J.* **C27** (2003) 311, doi:10.1140/epjc/s2002-01115-1.

[30] OPAL Collaboration, "Search for a low mass CP-odd Higgs boson in e^+e^- collisions with the OPAL detector at LEP-2", *Eur. Phys. J.* **C27** (2003) 483, doi:10.1140/epjc/s2003-01139-y.

[31] ALEPH, DELPHI, L3, OPAL, LEP Working Group for Higgs Boson Searches, "Search for neutral MSSM Higgs bosons at LEP", *Eur. Phys. J.* **C47** (2006) 547, doi:10.1140/epjc/s2006-02569-7.

[32] BaBar Collaboration, B. Aubert et al., "Search for Dimuon Decays of a Light Scalar in Radiative Transitions tau(3S) —> gamma A0", in *2009 Aspen Winter Conference on Astronomy: THIRTY YEARS OF MAGNETARS: NEW FRONTIERS Aspen, Colorado, February 1-7, 2009*. 2009. arXiv:0902.2176.

[33] BaBar Collaboration, "Search for dimuon decays of a light scalar boson in radiative transitions $\Upsilon \to \gamma A_0$", *Phys. Rev. Lett.* **103** (2009) 081803, doi:10.1103/PhysRevLett.103.081803, arXiv:0905.4539.

[34] BaBar Collaboration, "Search for Hadronic Decays of a Light Higgs Boson in the Radiative Decay $\Upsilon \to \gamma A^0$", *Phys. Rev. Lett.* **107** (2011) 221803, doi:10.1103/PhysRevLett.107.221803.

[35] BaBar Collaboration, "Search for a low-mass scalar Higgs boson decaying to a tau pair in single-photon decays of $\Upsilon(1S)$", *Phys. Rev.* **D88** (2013) 071102, doi:10.1103/PhysRevD.88.071102.

[36] BaBar Collaboration, "Search for a light Higgs resonance in radiative decays of the $\Upsilon(1S)$ with a charm tag", *Phys. Rev.* **D91** (2015) 071102, doi:10.1103/PhysRevD.91.071102.

[37] J. D. Bjorken, R. Essig, P. Schuster, and N. Toro, "New fixed-target experiments to search for dark gauge forces", *Phys. Rev.* **D80** (2009) 075018, doi:10.1103/PhysRevD.80.075018.

[38] LSND Collaboration, "Search for $\pi^0 \to \nu_\mu \overline{\nu}_\mu$ Decays in the LSND Detector", *Phys. Rev. Lett.* **92** (2004) 091801, doi:10.1103/PhysRevLett.92.091801.

[39] LSND Collaboration, "Evidence for neutrino oscillations from the observation of anti-neutrino(electron) appearance in a anti-neutrino(muon) beam", *Phys. Rev.* **D64** (2001) 112007, doi:10.1103/PhysRevD.64.112007.

[40] J. B. Dent, F. Ferrer, and L. M. Krauss, "Constraints on Light Hidden Sector Gauge Bosons from Supernova Cooling", arXiv:1201.2683.

[41] M. Pospelov, "Secluded U(1) below the weak scale", *Phys. Rev.* **D80** (2009) 095002, doi:10.1103/PhysRevD.80.095002.

[42] H. Davoudiasl, H.-S. Lee, and W. J. Marciano, "Dark side of Higgs diphoton decays and muon $g-2$", *Phys. Rev.* **D86** (2012) 095009, doi:10.1103/PhysRevD.86.095009.

[43] M. Endo, K. Hamaguchi, and G. Mishima, "Constraints on hidden photon models from electron $g-2$ and hydrogen spectroscopy", *Phys. Rev.* **D86** (2012) 095029, doi:10.1103/PhysRevD.86.095029.

[44] CMS Collaboration, "Search for light resonances decaying into pairs of muons as a signal of new physics", *JHEP* **07** (2011) 098, doi:10.1007/JHEP07(2011)098.

[45] CMS Collaboration, "Search for a light pseudoscalar Higgs boson in the dimuon decay channel in pp collisions at $\sqrt{s} = 7$ TeV", *Phys. Rev. Lett.* **109** (2012) 121801, doi:10.1103/PhysRevLett.109.121801.

[46] CMS Collaboration, "Search for a non-standard-model Higgs boson decaying to a pair of new light bosons in four-muon final states", *Phys. Lett.* **B726** (2013) 564, doi:10.1016/j.physletb.2013.09.009.

[47] CMS Collaboration, "A search for pair production of new light bosons decaying into muons", *Phys. Lett.* **B752** (2016) 146, doi:10.1016/j.physletb.2015.10.067.

[48] CMS Collaboration, "A Search for Beyond Standard Model Light Bosons Decaying into Muon Pairs", Technical Report CMS-PAS-HIG-16-035, CERN, Geneva, 2016.

[49] CMS Collaboration, "Search for a very light NMSSM Higgs boson produced in decays of the 125 GeV scalar boson and decaying into τ leptons in pp collisions at $\sqrt{s} = 8$ TeV", *JHEP* **01** (2016) 079, doi:10.1007/JHEP01(2016)079.

[50] CMS Collaboration, "Search for Higgs Decays to New Light Bosons in Boosted Tau Final States", Technical Report CMS-PAS-HIG-14-022, CERN, Geneva, 2015.

[51] CMS Collaboration, "Search for the exotic decay of the Higgs boson to a pair of light pseudoscalars in the final state with two b quarks and two τ leptons", Technical Report CMS-PAS-HIG-17-024, CERN, Geneva, 2018.

[52] CMS Collaboration, "Search for the exotic decay of the Higgs boson to a pair of light pseudoscalars in the final state of two muons and two τ leptons at $\sqrt{s} = 13$ TeV.", Technical Report CMS-PAS-HIG-17-029, CERN, Geneva, 2018.

[53] CMS Collaboration, "Search for exotic decays of the Higgs boson to a pair of new light bosons with two muon and two b jets in final states", Technical Report CMS-PAS-HIG-14-041, CERN, Geneva, 2016.

[54] CMS Collaboration, "Search for light bosons in decays of the 125 GeV Higgs boson in proton-proton collisions at $\sqrt{s} = 8$ TeV", *JHEP* **10** (2017) 076, doi:10.1007/JHEP10(2017)076.

[55] ATLAS Collaboration, "A search for a light CP-odd Higgs boson decaying to $\mu^+\mu^-$ in ATLAS", Technical Report ATLAS-CONF-2011-020, CERN, Geneva, 2011.

[56] ATLAS Collaboration, "Search for displaced muonic lepton jets from light Higgs boson decay in proton-proton collisions at $\sqrt{s} = 7$ TeV with the ATLAS detector", *Phys. Lett.* **B721** (2013) 32, doi:10.1016/j.physletb.2013.02.058.

[57] ATLAS Collaboration, "Search for long-lived neutral particles decaying into lepton jets in proton–proton collisions at $\sqrt{s} = 8$ TeV with the ATLAS detector", *JHEP* **11** (2014) 88, doi:10.1007/JHEP11(2014)088, arXiv:1409.0746.

[58] ATLAS Collaboration, "Search for new light gauge bosons in Higgs boson decays to four-lepton final states in pp collisions at $\sqrt{s} = 8$ TeV with the ATLAS detector at the LHC", *Phys. Rev.* **D92** (2015) 092001, doi:10.1103/PhysRevD.92.092001.

[59] ATLAS Collaboration, "Search for Higgs boson decays to beyond-the-Standard-Model light bosons in four-lepton events with the ATLAS detector at $\sqrt{s} = 13$ TeV", *JHEP* **06** (2018) 166, doi:10.1007/JHEP06(2018)166, arXiv:1802.03388.

[60] ATLAS Collaboration, "Search for the Higgs boson produced in association with a W boson and decaying to four b-quarks via two spin-zero particles in pp collisions at 13 TeV with the ATLAS detector", *Eur. Phys. J.* **C76** (2016) 605, doi:10.1140/epjc/s10052-016-4418-9.

[61] ATLAS Collaboration, "Search for a Higgs boson decaying to four photons through light CP-odd scalar coupling using $4.9\ \mathrm{fb}^{-1}$ of $7\ \mathrm{TeV}$ pp collision data taken with ATLAS detector at the LHC", Technical Report ATLAS-CONF-2012-079, CERN, Geneva, 2012.

[62] ATLAS Collaboration, "Search for new phenomena in events with at least three photons collected in pp collisions at $\sqrt{s}$ = 8 TeV with the ATLAS detector", *Eur. Phys. J.* **C76** (2016) 210, doi:10.1140/epjc/s10052-016-4034-8.

[63] ATLAS Collaboration, "Search for Higgs boson decays into pairs of light (pseudo)scalar particles in the $\gamma\gamma jj$ final state in pp collisions at $\sqrt{s} = 13$ TeV with the ATLAS detector", *Phys. Lett.* **B782** (2018) 750–767, doi:10.1016/j.physletb.2018.06.011, arXiv:1803.11145.

[64] ATLAS Collaboration, "Search for the Higgs boson produced in association with a vector boson and decaying into two spin-zero particles in the $H \to aa \to 4b$ channel in pp collisions at $\sqrt{s} = 13$ TeV with the ATLAS detector", *JHEP* **10** (2018) 031, doi:10.1007/JHEP10(2018)031, arXiv:1806.07355.

[65] LHCb Collaboration, "Search for Dark Photons Produced in 13 TeV pp Collisions", *Phys. Rev. Lett.* **120** (2018) 061801, doi:10.1103/PhysRevLett.120.061801.

[66] LHCb Collaboration, "Search for Higgs-like bosons decaying into long-lived exotic particles", *Eur. Phys. J.* **C76** (2016) 664, doi:10.1140/epjc/s10052-016-4489-7.

[67] M. Maniatis, "The next-to-minimal supersymmetric extension of the standard model reviewed", *Int. J. Mod. Phys. A* **25** (2010) 3505, doi:10.1142/S0217751X10049827.

[68] N. Arkani-Hamed, D. P. Finkbeiner, T. R. Slatyer, and N. Weiner, "A theory of dark matter", *Phys. Rev.* **D79** (2009) 015014, doi:10.1103/PhysRevD.79.015014.

[69] M. Baumgart et al., "Non-Abelian dark sectors and their collider signatures", *JHEP* **04** (2009) 014, doi:10.1088/1126-6708/2009/04/014.

[70] A. Falkowski, J. T. Ruderman, T. Volansky, and J. Zupan, "Hidden Higgs decaying to lepton jets", *JHEP* **05** (2010) 077, doi:10.1007/JHEP05(2010)077.

[71] CMS Collaboration, "Performance of the CMS muon detector and muon reconstruction with proton-proton collisions at $\sqrt{s} = 13$ TeV", *JINST* **13** (2018) P06015, doi:10.1088/1748-0221/13/06/P06015, arXiv:1804.04528.

[72] F. Englert and R. Brout, "Broken symmetry and the mass of gauge vector mesons", *Phys. Rev. Lett.* **13** (1964) 321, doi:10.1103/PhysRevLett.13.321.

[73] P. W. Higgs, "Broken symmetries and the masses of gauge bosons", *Phys. Rev. Lett.* **13** (1964) 508, doi:10.1103/PhysRevLett.13.508.

[74] G. S. Guralnik, C. R. Hagen, and T. W. B. Kibble, "Global conservation laws and massless particles", *Phys. Rev. Lett.* **13** (1964) 585, doi:10.1103/PhysRevLett.13.585.

[75] P. W. Anderson, "Plasmons, Gauge Invariance, and Mass", *Phys. Rev.* **130** (1963) 439, doi:10.1103/PhysRev.130.439.

[76] J. Schwinger, "Gauge Invariance and Mass", *Phys. Rev.* **125** (1962) 397, doi:10.1103/PhysRev.125.397.

[77] SNO Collaboration, "Measurement of the Rate of $\nu_e + d \rightarrow p + p + e^-$ Interactions Produced by ^8B Solar Neutrinos at the Sudbury Neutrino Observatory", *Phys. Rev. Lett.* **87** (Jul, 2001) 071301, doi:10.1103/PhysRevLett.87.071301.

[78] Z. Maki, M. Nakagawa, and S. Sakata, "Remarks on the Unified Model of Elementary Particles", *Prog. Theor. Phys.* **28** (1962) 870, doi:10.1143/PTP.28.870.

[79] B. Pontecorvo, "Inverse beta processes and nonconservation of lepton charge", *Sov. Phys. JETP* **7** (1958) 172.

[80] G. C. Branco et al., "Theory and phenomenology of two-Higgs-doublet models", *Phys. Rept.* **516** (2012) 1–102, doi:10.1016/j.physrep.2012.02.002, arXiv:1106.0034.

[81] S. P. Martin, "A Supersymmetry primer", *Adv. Ser. Direct. High Energy Phys.* **21** (2010) 1, doi:10.1142/9789814307505_0001.

[82] J. Ellis, "Higgs Physics", in *Proceedings, 2013 European School of High-Energy Physics (ESHEP 2013): Paradfurdo, Hungary, June 5-18, 2013*, p. 117. 2015. doi:10.5170/CERN-2015-004.117.

[83] P. Langacker, "The standard model and beyond", *Boca Raton, USA: CRC Press* (2010) 663.

[84] ALEPH and DELPHI and L3 and OPAL Collaborations and LEP Working Group for Higgs boson searches, "Search for the standard model Higgs boson at LEP", *Phys. Lett.* **B565** (2003) 61, doi:10.1016/S0370-2693(03)00614-2.

[85] CDF and DØ Collaboration, "Combination of Tevatron Searches for the Standard Model Higgs Boson in the W^+W^- Decay Mode", *Phys. Rev. Lett.* **104** (2010) 061802, doi:10.1103/PhysRevLett.104.061802.

[86] LEP Electroweak Working Group, "Precision Electroweak Measurements and Constraints on the Standard Model", Technical Report CERN-PH-EP-2010-095, CERN, Geneva, 2010. arXiv:1012.2367.

[87] CMS Collaboration, "Observation of a new boson at a mass of 125 GeV with the CMS experiment at the LHC", *Phys. Lett.* **B716** (2012) 30, doi:10.1016/j.physletb.2012.08.021.

[88] ATLAS Collaboration, "Observation of a new particle in the search for the Standard Model Higgs boson with the ATLAS detector at the LHC", *Phys. Lett.* **B716** (2012) 1, doi:10.1016/j.physletb.2012.08.020.

[89] J. Ellis, M. K. Gaillard, and D. V. Nanopoulos, "A Historical Profile of the Higgs Boson", in *The standard theory of particle physics: Essays to celebrate CERN's 60th anniversary*, L. Maiani and L. Rolandi, eds., p. 255. 2016. doi:10.1142/9789814733519_0014.

[90] ATLAS Collaboration, "Evidence for the spin-0 nature of the Higgs boson using ATLAS data", *Physics Letters B* **726** (2013) 120, doi:https://doi.org/10.1016/j.physletb.2013.08.026.

[91] ATLAS and CMS Collaboration, "Measurements of the Higgs boson production and decay rates and constraints on its couplings from a combined ATLAS and CMS analysis of the LHC pp collision data at $\sqrt{s} = 7$ and 8 TeV", *JHEP* **08** (2016) 045, doi:10.1007/JHEP08(2016)045.

[92] LHC Higgs Cross Section Working Group, "Handbook of LHC Higgs Cross Sections: 4. Deciphering the Nature of the Higgs Sector", Technical Report FERMILAB-FN-1025-T, CERN-2017-002-M, CERN, Geneva, 2016. doi:10.23731/CYRM-2017-002.

[93] CMS Collaboration, "Summaries of CMS cross section measurements". https://twiki.cern.ch/twiki/bin/view/CMSPublic/PhysicsResultsCombined. Online; Accessed: 2018-06-06.

[94] Supernova Search Team Collaboration, "Observational evidence from supernovae for an accelerating universe and a cosmological constant", *Astron. J.* **116** (1998) 1009–1038, doi:10.1086/300499, arXiv:astro-ph/9805201.

[95] Supernova Cosmology Project Collaboration, "Measurements of Omega and Lambda from 42 high redshift supernovae", *Astrophys. J.* **517** (1999) 565, doi:10.1086/307221, arXiv:astro-ph/9812133.

[96] K. Becker, M. Becker, and J. H. Schwarz, "String theory and M-theory: A modern introduction". Cambridge University Press, 2006.

[97] M. J. Strassler and K. M. Zurek, "Echoes of a hidden valley at hadron colliders", *Phys. Lett.* **B651** (2007) 374, doi:10.1016/j.physletb.2007.06.055, arXiv:hep-ph/0604261.

[98] Y. Nomura and J. Thaler, "Dark Matter through the Axion Portal", *Phys. Rev.* **D79** (2009) 075008, doi:10.1103/PhysRevD.79.075008, arXiv:0810.5397.

[99] S. Dodelson and L. M. Widrow, "Sterile-neutrinos as dark matter", *Phys. Rev. Lett.* **72** (1994) 17–20, doi:10.1103/PhysRevLett.72.17, arXiv:hep-ph/9303287.

[100] C. P. Burgess, M. Pospelov, and T. ter Veldhuis, "The Minimal model of nonbaryonic dark matter: A Singlet scalar", *Nucl. Phys.* **B619** (2001) 709–728, doi:10.1016/S0550-3213(01)00513-2, arXiv:hep-ph/0011335.

[101] B. Holdom, "Two U(1)'s and ϵ charge shifts", *Phys. Lett.* **B166** (1986) 196, doi:10.1016/0370-2693(86)91377-8.

[102] K. R. Dienes, C. F. Kolda, and J. March-Russell, "Kinetic mixing and the supersymmetric gauge hierarchy", *Nucl. Phys.* **B492** (1997) 104, doi:10.1016/S0550-3213(97)00173-9.

[103] C. Cheung, J. T. Ruderman, L.-T. Wang, and I. Yavin, "Kinetic mixing as the origin of light dark scales", *Phys. Rev.* **D80** (2009) 035008, doi:10.1103/PhysRevD.80.035008.

[104] J. Jaeckel, J. Redondo, and A. Ringwald, "Signatures of a hidden cosmic microwave background", *Phys. Rev. Lett.* **101** (2008) 131801, doi:10.1103/PhysRevLett.101.131801, arXiv:0804.4157.

[105] Fermi LAT Collaboration, "Measurement of separate cosmic-ray electron and positron spectra with the Fermi Large Area Telescope", *Phys. Rev. Lett.* **108** (2012) 011103, doi:10.1103/PhysRevLett.108.011103.

[106] AMS Collaboration, "First Result from the Alpha Magnetic Spectrometer on the International Space Station: Precision Measurement of the Positron Fraction in Primary Cosmic Rays of 0.5–350 GeV", *Phys. Rev. Lett.* **110** (2013) 141102, doi:10.1103/PhysRevLett.110.141102.

[107] AMS Collaboration, "High Statistics Measurement of the Positron Fraction in Primary Cosmic Rays of 0.5–500 GeV with the Alpha Magnetic Spectrometer on the International Space Station", *Phys. Rev. Lett.* **113** (2014) 121101, doi:10.1103/PhysRevLett.113.121101.

[108] PAMELA Collaboration, "An anomalous positron abundance in cosmic rays with energies 1.5-100 GeV", *Nature* **458** (2009) 607, doi:10.1038/nature07942.

[109] I. Cholis, D. P. Finkbeiner, L. Goodenough, and N. Weiner, "The PAMELA Positron Excess from Annihilations into a Light Boson", *JCAP* **0912** (2009) 007, doi:10.1088/1475-7516/2009/12/007.

[110] M. Goodsell, J. Jaeckel, J. Redondo, and A. Ringwald, "Naturally Light Hidden Photons in LARGE Volume String Compactifications", *JHEP* **11** (2009) 027, doi:10.1088/1126-6708/2009/11/027, arXiv:0909.0515.

[111] V. Braun, Y.-H. He, and B. A. Ovrut, "Supersymmetric Hidden Sectors for Heterotic Standard Models", *JHEP* **09** (2013) 008, doi:10.1007/JHEP09(2013)008, arXiv:1301.6767.

[112] G. Jungman, M. Kamionkowski, and K. Griest, "Supersymmetric dark matter", *Phys. Rept.* **267** (1996) 195, doi:10.1016/0370-1573(95)00058-5, arXiv:hep-ph/9506380.

[113] M. Cicoli, M. Goodsell, J. Jaeckel, and A. Ringwald, "Testing String Vacua in the Lab: From a Hidden CMB to Dark Forces in Flux Compactifications", *JHEP* **07** (2011) 114, doi:10.1007/JHEP07(2011)114, arXiv:1103.3705.

[114] M. Cicoli, M. Goodsell, and A. Ringwald, "The type IIB string axiverse and its low-energy phenomenology", *JHEP* **10** (2012) 146, doi:10.1007/JHEP10(2012)146, arXiv:1206.0819.

[115] R. Dermisek and J. F. Gunion, "New constraints on a light CP-odd Higgs boson and related NMSSM ideal Higgs scenarios", *Phys. Rev.* **D81** (2010) 075003, doi:10.1103/PhysRevD.81.075003.

[116] M. Abdullah et al., "Coherent elastic neutrino nucleus scattering as a probe of a Z' through kinetic and mass mixing effects", *Phys. Rev.* **D98** (2018) 015005, doi:10.1103/PhysRevD.98.015005, arXiv:1803.01224.

[117] M. Bauer, P. Foldenauer, and J. Jaeckel, "Hunting All the Hidden Photons", *JHEP* **07** (2018) 094, doi:10.1007/JHEP07(2018)094, arXiv:1803.05466.

[118] ATLAS Collaboration, "Search for long-lived neutral particles decaying into displaced lepton jets in proton-proton collisions at $\sqrt{s}$ = 13 TeV with the ATLAS detector", Technical Report ATLAS-CONF-2016-042, CERN, 2016.

[119] ATLAS Collaboration, "A search for pairs of highly collimated photon-jets in pp collisions at $\sqrt{s}$ = 13 TeV with the ATLAS detector", *Phys. Rev.* **D99** (2019), no. 1, 012008, doi:10.1103/PhysRevD.99.012008, arXiv:1808.10515.

[120] CMS Collaboration, "Search for an exotic decay of the Higgs boson to a pair of light pseudoscalars in the final state with two muons and two b quarks in pp collisions at 13 TeV", doi:10.1016/j.physletb.2019.06.021, arXiv:1812.06359.

[121] J. Alwall et al., "The automated computation of tree-level and next-to-leading order differential cross sections, and their matching to parton shower simulations", *JHEP* **07** (2014) 079, doi:10.1007/JHEP07(2014)079.

[122] T. Sjöstrand, S. Mrenna, and P. Z. Skands, "A Brief Introduction to PYTHIA 8.1", *Comput. Phys. Commun.* **178** (2008) 852, doi:10.1016/j.cpc.2008.01.036.

[123] S. Jadach, Z. Was, R. Decker, and J. H. Kuhn, "The tau decay library TAUOLA: Version 2.4", *Comput. Phys. Commun.* **76** (1993) 361, doi:10.1016/0010-4655(93)90061-G.

[124] P. M. Nadolsky et al., "Implications of CTEQ global analysis for collider observables", *Phys. Rev.* **D78** (2008) 013004, doi:10.1103/PhysRevD.78.013004, arXiv:0802.0007.

[125] NNPDF Collaboration, "Parton distributions with QED corrections", *Nucl. Phys.* **B877** (2013) 290, doi:10.1016/j.nuclphysb.2013.10.010.

[126] NNPDF Collaboration, "Unbiased global determination of parton distributions and their uncertainties at NNLO and at LO", *Nucl. Phys.* **B855** (2012) 153, doi:10.1016/j.nuclphysb.2011.09.024.

[127] ATLAS Collaboration, "The ATLAS Experiment at the CERN Large Hadron Collider", *JINST* **3** (2008) S08003, doi:10.1088/1748-0221/3/08/S08003.

[128] ALICE Collaboration, "The ALICE experiment at the CERN LHC", *JINST* **3** (2008) S08002, doi:10.1088/1748-0221/3/08/S08002.

[129] CMS Collaboration, "The CMS experiment at the CERN LHC", *JINST* **3** (2008) S08004, doi:10.1088/1748-0221/3/08/S08004.

[130] LHCb Collaboration, "The LHCb Detector at the LHC", *JINST* **3** (2008) S08005, doi:10.1088/1748-0221/3/08/S08005.

[131] TOTEM Collaboration, "The TOTEM experiment at the CERN Large Hadron Collider", *JINST* **3** (2008) S08007, doi:10.1088/1748-0221/3/08/S08007.

[132] LHCf Collaboration, "The LHCf detector at the CERN Large Hadron Collider", *JINST* **3** (2008) S08006, doi:10.1088/1748-0221/3/08/S08006.

[133] R. Steerenberg, "Batch Compression Merging and Splitting (BCMS)", Apr, 2017. General Photo.

[134] CMS Collaboration, "CMS Technical Design Report for the Pixel Detector Upgrade", Technical Report CERN-LHCC-2012-016. CMS-TDR-11, CERN, Geneva, 2012.

[135] CMS Collaboration, "The Phase-2 Upgrade of the CMS Tracker", Technical Report CERN-LHCC-2017-009. CMS-TDR-014, CERN, Geneva, 2017.

[136] P. Adzic, "Energy resolution of the barrel of the CMS Electromagnetic Calorimeter", *JINST* **2** (2007) P04004, doi:10.1088/1748-0221/2/04/P04004.

[137] CMS Collaboration, "The CMS electromagnetic calorimeter barrel upgrade for High-Luminosity LHC", *Journal of Physics: Conference Series* **587** (2015) 012016, doi:10.1088/1742-6596/587/1/012016.

[138] D. Contardo et al., "Technical Proposal for the Phase-II Upgrade of the CMS Detector", Technical Report CERN-LHCC-2015-010. LHCC-P-008. CMS-TDR-15-02, CERN, Geneva, 2015.

[139] CMS Collaboration, "The Phase-2 Upgrade of the CMS Endcap Calorimeter", Technical Report CERN-LHCC-2017-023. CMS-TDR-019, CERN, Geneva, 2017.

[140] CMS Collaboration, "Precise Mapping of the Magnetic Field in the CMS Barrel Yoke using Cosmic Rays", *JINST* **5** (2010) T03021, doi:10.1088/1748-0221/5/03/T03021.

[141] CMS Collaboration, "The CMS muon project: Technical Design Report". Technical Design Report CMS. CERN, Geneva, 1997.

[142] CMS Collaboration, "Performance of the CMS Drift Tube Chambers with Cosmic Rays", *JINST* **5** (2009) T03015, doi:10.1088/1748-0221/5/03/T03015.

[143] C. Lourenco, "The Phase-2 Upgrade of the CMS Muon Detectors", Technical Report CERN-LHCC-2017-012. CMS-TDR-016, CERN, Geneva, 2017.

[144] CMS Collaboration, "Radiation background with the CMS RPCs at the LHC", *JINST* **10** (2015) C05031, doi:10.1088/1748-0221/10/05/C05031.

[145] CMS Collaboration, "CMS Luminosity Measurements for the 2016 Data Taking Period", Technical Report CMS-PAS-LUM-17-001, CERN, Geneva, 2017.

[146] CMS Collaboration, "The CMS trigger system", *JINST* **12** (2017) P01020, doi:10.1088/1748-0221/12/01/P01020, arXiv:1609.02366.

[147] CMS Collaboration, "The Phase-2 Upgrade of the CMS L1 Trigger Interim Technical Design Report", Technical Report CERN-LHCC-2017-013. CMS-TDR-017, CERN, Geneva, 2017.

[148] CMS Collaboration, "CMS Technical Design Report for the Level-1 Trigger Upgrade", Technical Report CERN-LHCC-2013-011. CMS-TDR-12, CERN, Geneva, 2013.

[149] J. Allison et al., "Geant4 developments and applications", *IEEE Trans. Nucl. Sci.* **53** (2006) 270, doi:10.1109/TNS.2006.869826.

[150] J. Shiers, "The Worldwide LHC Computing Grid (worldwide LCG)", *Computer Physics Communications* **177** (2007) 219, doi:https://doi.org/10.1016/j.cpc.2007.02.021. Proceedings of the Conference on Computational Physics 2006.

[151] CMS Collaboration, "The CMS Data Aggregation System", Technical Report CMS-CR-2010-036, CERN, Geneva, 2010.

[152] D. Spiga et al., "The CMS Remote Analysis Builder (CRAB)", *Lect. Notes Comput. Sci.* **4873** (2007) 580, doi:10.1007/978-3-540-77220-0_52.

[153] CMS Collaboration, "Particle-flow reconstruction and global event description with the CMS detector", *JINST* **12** (2017) P10003, doi:10.1088/1748-0221/12/10/P10003.

[154] D. Barney, "CMS Detector Slice", (2016). CMS Collection.

[155] CMS Collaboration, "Muon Reconstruction and Identification. Improvements for Run-2 and First Results with 2015 Run Data", Technical Report CMS-DP-2015-015, CERN, Geneva, 2015.

[156] CMS Collaboration, "The CMS muon system in Run2: preparation, status and first results", *PoS* **EPS-HEP2015** (2015) 237, arXiv:1510.05424.

[157] CMS Collaboration, "Muon Identification and Isolation efficiency on full 2016 dataset", Technical Report CMS-DP-2017-007, CERN, Geneva, 2017.

[158] M. Cacciari, G. P. Salam, and G. Soyez, "The Anti-k(t) jet clustering algorithm", *JHEP* **04** (2008) 063, doi:10.1088/1126-6708/2008/04/063.

[159] CMS Collaboration, "A search for pair production of new light bosons decaying into muons at $\sqrt{s} = 13$ TeV", Technical Report CMS-PAS-HIG-18-003, CERN, Geneva, 2018.

[160] CMS Collaboration, "A search for pair production of new light bosons decaying into muons in proton-proton collisions at 13 TeV", *Submitted to: Phys. Lett.* (2018) arXiv:1812.00380.

[161] ATLAS and CMS Collaboration, LHC Higgs Combination Group, "Procedure for the LHC Higgs boson search combination in Summer 2011", Technical Report CMS-NOTE-2011-005. ATL-PHYS-PUB-2011-11, CERN, Geneva, Aug, 2011.

[162] T. Sjöstrand et al., "An Introduction to PYTHIA 8.2", *Comput. Phys. Commun.* **191** (2015) 159, doi:10.1016/j.cpc.2015.01.024.

[163] P. Skands, S. Carrazza, and J. Rojo, "Tuning PYTHIA 8.1: the Monash 2013 Tune", *Eur. Phys. J.* **C74** (2014) 3024, doi:10.1140/epjc/s10052-014-3024-y.

[164] J. Alwall et al., "MadGraph/MadEvent v4: the new web generation", *JHEP* **09** (2007) 028, doi:10.1088/1126-6708/2007/09/028.

[165] P. Meade and M. Reece, "BRIDGE: Branching ratio inquiry / decay generated events", arXiv:hep-ph/0703031.

[166] J. Alwall et al., "A Standard format for Les Houches event files", *Comput. Phys. Commun.* **176** (2007) 300, doi:10.1016/j.cpc.2006.11.010.

[167] CMS Collaboration, "CMS Web Based Monitoring". https://cmswbm.cern.ch/. Online; Accessed: 2017-05-1.

[168] J. Pivarski, A. Safonov, and A. Tatarinov, "Search for collimated groups of muons", *CMS Note* **2010/462** (2010).

[169] C. H. Kom, A. Kulesza, and W. J. Stirling, "Pair Production of J/ψ as a Probe of Double Parton Scattering at LHCb", *Phys. Rev. Lett.* **107** (2011) 082002, doi:10.1103/PhysRevLett.107.082002.

[170] M. Bahr et al., "Herwig++ Physics and Manual", *Eur. Phys. J.* **C58** (2008) 639, doi:10.1140/epjc/s10052-008-0798-9.

[171] CMS Collaboration, "Search for supersymmetry in pp collisions at $\sqrt{s} = 13$ TeV in the single-lepton final state using the sum of masses of large-radius jets", *JHEP* **08** (2016) 122, doi:10.1007/JHEP08(2016)122.

[172] A. Pukhov, "CalcHEP 2.3: MSSM, structure functions, event generation, batchs, and generation of matrix elements for other packages", (2004). arXiv:hep-ph/0412191.

[173] CMS Collaboration, "Studies of Higgs boson production in the four-lepton final state at $\sqrt{s}$ = 13 TeV", CMS Physics Analysis Summary CMS-PAS-HIG-15-004, 2016.

[174] M. Botje et al., "The PDF4LHC working group interim recommendations", technical report, CERN, Geneva, 2011. arXiv:1101.0538.

[175] S. Alekhin et al., "The PDF4LHC Working Group Interim Report", technical report, CERN, Geneva, 2011. arXiv:1101.0536.

[176] R. D. Ball et al., "Parton distributions with LHC data", *Nucl. Phys.* **B867** (2013) 244, doi:10.1016/j.nuclphysb.2012.10.003.

[177] J. Butterworth et al., "PDF4LHC recommendations for LHC Run II", *Journal of Physics G* **43** (2016) 023001, doi:10.1088/0954-3899/43/2/023001.

[178] J. M. Campbell and R. Ellis, "Loops and Legs in Quantum Field Theory MCFM for the Tevatron and the LHC", *Nucl. Phys.* **B205** (2010) 10, doi:10.1016/j.nuclphysbps.2010.08.011.

[179] LHC Higgs Cross Section Working Group, "Handbook of LHC Higgs Cross Sections: 1. Inclusive Observables", doi:10.5170/CERN-2011-002, arXiv:1101.0593.

[180] CMS Collaboration, "CMS Tracking POG Performance Plots for year 2016", Technical Report CMS-DP-2016-012, CERN, Geneva, 2016.

[181] CMS Collaboration, "Measurement of the WZ production cross section in pp collisions at $\sqrt{s} = 13$ TeV", *Phys. Lett.* **B766** (2017) 268, doi:10.1016/j.physletb.2017.01.011.

[182] A. L. Read, "Presentation of search results: The CL(s) technique", *J. Phys.* **G28** (2002) 2693, doi:10.1088/0954-3899/28/10/313.

[183] T. Junk, "Confidence level computation for combining searches with small statistics", *Nucl. Instrum. Meth.* **A434** (1999) 435, doi:10.1016/S0168-9002(99)00498-2.

[184] ATLAS and CMS Collaboration, "Procedure for the LHC Higgs boson search combination in summer 2011", Technical Report ATL-PHYS-PUB-2011-011, ATL-COM-PHYS-2011-818, CMS-NOTE-2011-005, CERN, Geneva, 2011.

[185] CMS Collaboration, "Combined results of searches for the standard model Higgs boson in pp collisions at $\sqrt{s} = 7$ TeV", *Phys. Lett.* **B710** (2012) 26, doi:10.1016/j.physletb.2012.02.064.

[186] CMS Collaboration, "Observation of a new boson with mass near 125 GeV in pp collisions at $\sqrt{s}$ = 7 and 8 TeV", *JHEP* **1306** (2013) 081, doi:10.1007/JHEP06(2013)081.

[187] KLOE-2 Collaboration, "Search for light vector boson production in $e^+e^- \to \mu^+\mu^-\gamma$ interactions with the KLOE experiment", *Phys. Lett.* **B736** (2014) 459, doi:10.1016/j.physletb.2014.08.005.

[188] A. Adare et al., "Search at the Mainz Microtron for Light Massive Gauge Bosons Relevant for the Muon g-2 Anomaly", *Phys. Rev. Lett.* **112** (2014) 221802, doi:10.1103/PhysRevLett.112.221802.

[189] BaBar Collaboration, "Search for a Dark Photon in e^+e^- Collisions at BaBar", *Phys. Rev. Lett.* **113** (2014) 201801, doi:10.1103/PhysRevLett.113.201801.

[190] A. Fradette, M. Pospelov, J. Pradler, and A. Ritz, "Cosmological constraints on very dark photons", *Phys. Rev.* **D90** (2014) 035022, doi:10.1103/PhysRevD.90.035022.

[191] R. Essig et al., "Working Group Report: New Light Weakly Coupled Particles", in *Proceedings, 2013 Community Summer Study on the Future of U.S. Particle Physics: Snowmass on the Mississippi (CSS2013): Minneapolis, MN, USA, July 29-August 6, 2013*. 2013. arXiv:1311.0029.

[192] H. K. Dreiner, J. Fortin, and L. U. C. Hanhart, "Supernova Constraints on MeV Dark Sectors from e+ e- Annihilations", *Phys. Rev.* **D89** (2014) 105015, doi:10.1103/PhysRevD.89.105015.

[193] J. B. J. Blumlein, "New Exclusion Limits for Dark Gauge Forces from Beam-Dump Data", *Phys. Lett.* **B701** (2011) 155, doi:10.1016/j.physletb.2011.05.046, arXiv:1104.2747.

[194] R. Essig, R. Harnik, J. Kaplan, and N. Toro, "Discovering New Light States at Neutrino Experiments", *Phys. Rev.* **D82** (2010) 113008, doi:10.1103/PhysRevD.82.113008.

[195] A. R. Brian Batell, Maxim Pospelov, "Exploring Portals to a Hidden Sector Through Fixed Targets", *Phys. Rev.* **D80** (2009) 095024, doi:10.1103/PhysRevD.80.095024.

APPENDIX A

MONTE CARLO SAMPLES

Table A.1: NMSSM signal Monte Carlo mass points.

$m_{h_{1/2}}$ [GeV]	m_a [GeV]	Number of events	$m_{h_{1/2}}$ [GeV]	m_a [GeV]	Number of events
90	0.25	200,000	110	2.00	198,634
90	0.50	200,000	110	3.00	200,000
90	0.75	200,000	110	3.55	200,000
90	1.00	200,000	125	0.25	200,000
90	2.00	200,000	125	0.50	200,000
90	3.00	199,308	125	0.75	195,695
90	3.55	200,000	125	1.00	198,388
100	0.25	199,065	125	2.00	200,000
100	0.50	199,215	125	3.00	200,000
100	0.75	200,000	125	3.55	200,000
100	1.00	198,250	150	0.25	200,000
100	2.00	200,000	150	0.50	200,000
100	3.00	198,865	150	0.75	200,000
100	3.55	200,000	150	1.00	200,000
110	0.25	199,065	150	2.00	200,000
110	0.50	199,215	150	3.00	199,065
110	0.75	200,000	150	3.55	200,000
110	1.00	198,250			

Table A.2: Electroweak Monte Carlo samples.

Dataset name	Number of events
/EWK_13TeV_CALCHEP_50K_batch1_GEN_SIM_v1_TAMU/ jrorie-EWK_13TeV_CALCHEP_50K_batch1_RAW2DIGI_L1Reco_RECO _v1_TAMU- 2ddd25030f7878ebc0ae5f7f9cd4b430/USER	50,000
/EWK_13TeV_CALCHEP_50K_batch2_GEN_SIM_v3_TAMU/ jrorie-EWK_13TeV_CALCHEP_50K_batch2_RAW2DIGI_L1Reco_RECO _v1_TAMU- 2ddd25030f7878ebc0ae5f7f9cd4b430/USER	50,000
Total	100,000

Table A.3: Drell-Yan + jets Monte Carlo sample for muon isolation studies.

Dataset name	Number of events
/DYJetsToLL_M-50_TuneCUETP8M1_13TeV-madgraphMLM-pythia8 /RunIISummer16DR80Premix-PUMoriond17_80X_mcRun2 _asymptotic_2016_TrancheIV_v6_ext1-v1/AODSIM	49,748,967

Table A.4: J/ψ Monte Carlo sample for muon isolation studies.

Dataset name	Number of events
/JpsiToMuMu_JpsiPt8_TuneCUEP8M1_13TeV-pythia8 /RunIISummer16DR80Premix-PUMoriond17_80X_mcRun2 _asymptotic_2016_TrancheIV_v6-v1/AODSIM	29,589,560

Table A.5: MSSMD signal Monte Carlo m_{γ_D} and $c\tau_{\gamma_D}$ points. Note that for all samples $m_h = 125$ GeV, $m_{n_1} = 10$ GeV and $m_{n_D} = 1$ GeV.

m_{γ_D} [GeV]	$c\tau_{\gamma_D}$ [mm]	Number of events	m_{γ_D} [GeV]	$c\tau_{\gamma_D}$ [mm]	Number of events
0.25	0	19400	0.7	0	76800
0.25	0.05	19200	0.7	0.5	19400
0.25	0.1	97900	0.7	1	144000
0.25	0.5	98100	0.7	20	677400
0.25	1	52100	0.7	100	231100
0.25	2	294400	1	0	77999
0.25	5	295800	1	5	170200
0.25	20	1155200	1	20	303300
0.25	100	1048700	1	100	115400
0.4	0	97900	5	0	79400
0.4	0.5	98800	5	20	78300
0.4	1	281600	5	100	227600
0.4	2	296400	8.5	0	79099
0.4	5	146200	8.5	2	276700
0.4	20	581200	8.5	20	708100
0.4	100	623400	8.5	100	918100

Table A.6: Monte Carlo samples for the trigger scale factor studies.

Process	Dataset name	Number of events
$WZ \to 3l\nu$	/WZTo3LNu_TuneCUETP8M1_13TeV-powheg-pythia8/ RunIISummer16DR80Premix-PUMoriond17_80X_mcRun2 _asymptotic_2016_TrancheIV_v6_ext1-v3/AODSIM	18,000,000
$ttW \to 3l\nu$	/TTWJetsToLNu_TuneCUETP8M1_13TeV-amcatnloFXFX-madspin -pythia8/RunIISummer16DR80Premix-PUMoriond17_80X_mcRun2 _asymptotic_2016_TrancheIV_v6_ext1-v3/AODSIM	2,160,168
$ttZ \to ll\nu\nu$	/TTZToLLNuNu_M-10_TuneCUETP8M1_13TeV-amcatnloFXFX-madspin -pythia8/RunIISummer16DR80Premix-PUMoriond17_80X_mcRun2 _asymptotic_2016_TrancheIV_v6_ext1-v3/AODSIM	5,934,228

APPENDIX B

REAL DATA SAMPLES

Table B.1: MuOnia data samples used in the double J/ψ background determination.

Dataset name	Run range	Number of events
/MuOnia/Run2016B-07Aug17_ver1-v1/AOD	272760-273017	514,469
/MuOnia/Run2016B-07Aug17_ver2-v1/AOD	273150-275376	31,260,711
/MuOnia/Run2016C-07Aug17-v1/AOD	275656-276283	12,779,404
/MuOnia/Run2016D-07Aug17-v1/AOD	276315-276811	21,150,419
/MuOnia/Run2016E-07Aug17-v1/AOD	276831-277420	17,460,298
/MuOnia/Run2016F-07Aug17-v1/AOD	277932-278808	12,415,886
/MuOnia/Run2016G-07Aug17-v1/AOD	278820-280385	35,301,548
/MuOnia/Run2016H-07Aug17-v1/AOD	284036-284068	38,094,977
Total	272760-284068	169,208,466

Table B.2: Charmonium data samples used in the muon identification scale factor studies.

Dataset name	Run range	Number of events
/Charmonium/Run2016B-07Aug17_ver1-v1/AOD	272760-273017	1,190,746
/Charmonium/Run2016B-07Aug17_ver2-v1/AOD	273150-275376	51,713,106
/Charmonium/Run2016C-07Aug17-v1/AOD	275656-276283	19,535,374
/Charmonium/Run2016D-07Aug17-v1/AOD	276315-276811	32,176,529
/Charmonium/Run2016E-07Aug17-v1/AOD	276831-277420	27,626,916
/Charmonium/Run2016F-07Aug17-v1/AOD	277932-278808	21,339,582
/Charmonium/Run2016G-07Aug17-v1/AOD	278820-280385	62,080,523
/Charmonium/Run2016H-07Aug17-v1/AOD	284036-284068	71,189,433
Total	272760-284068	286,852,209

Table B.3: MET data samples for the trigger scale factor studies.

Dataset name	Run range	Number of events
/MET/Run2016B-07Aug17_ver1-v1/AOD	272760-273017	583,427
/MET/Run2016B-07Aug17_ver2-v1/AOD	273150-275376	35,987,712
/MET/Run2016C-07Aug17-v1/AOD	275656-276283	17,381,222
/MET/Run2016D-07Aug17-v1/AOD	276315-276811	20,947,429
/MET/Run2016E-07Aug17-v1/AOD	276831-277420	22,348,402
/MET/Run2016F-07Aug17-v1/AOD	277932-278808	13,319,829
/MET/Run2016G-07Aug17-v1/AOD	278820-280385	26,974,131
/MET/Run2016H-07Aug17-v1/AOD	284036-284068	1,129,511
Total	272760-284068	178,148,113

APPENDIX C

GENERATOR LEVEL KINEMATICS

C.1 NMSSM

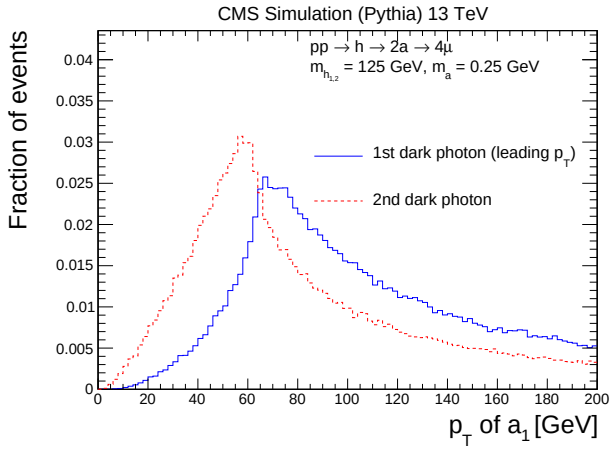

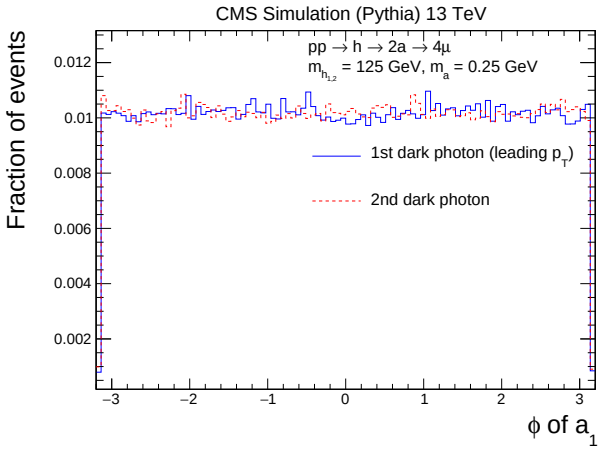

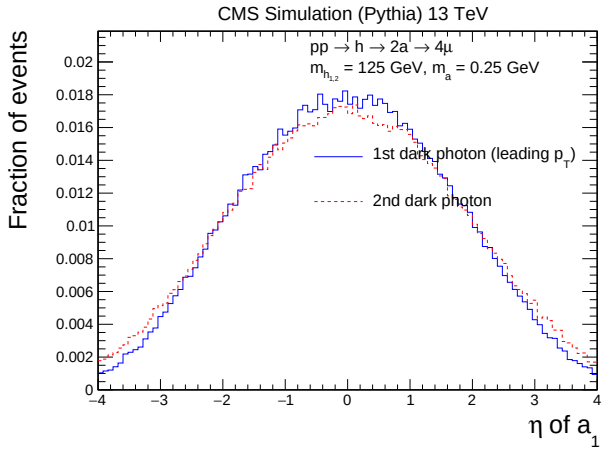

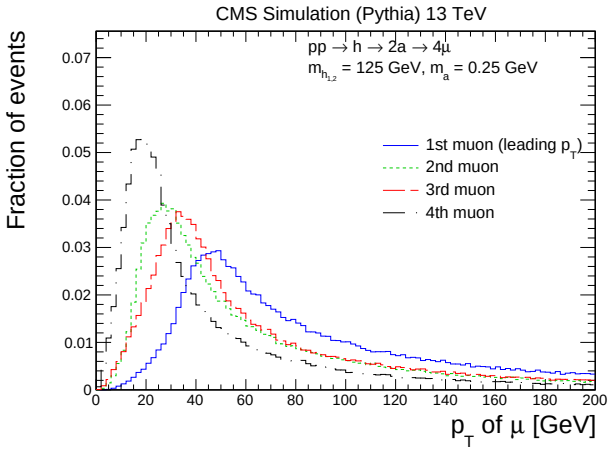

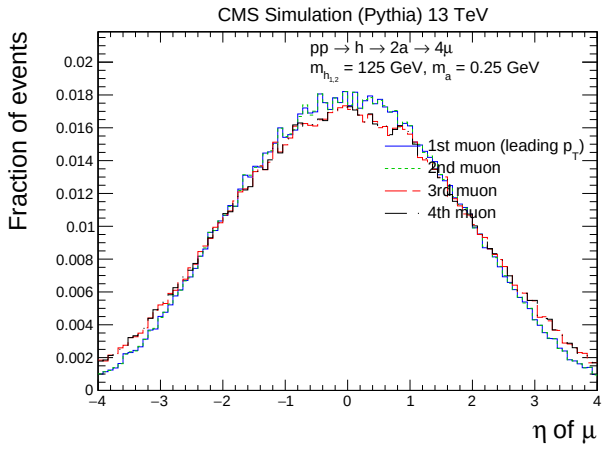

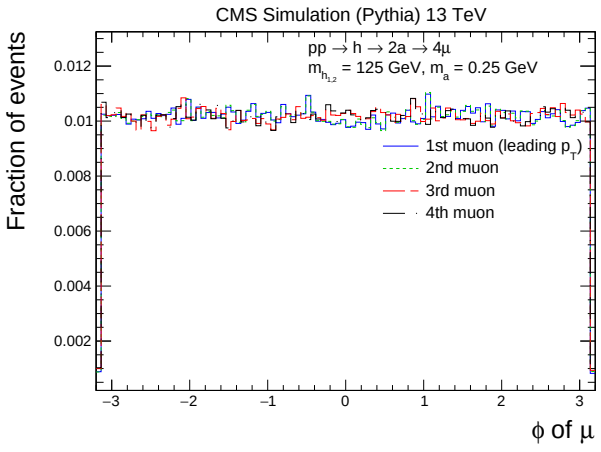

C.2 MSSMD

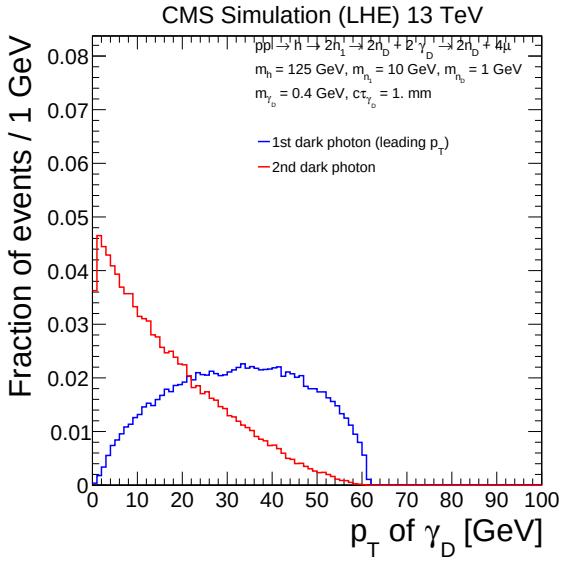
CMS Simulation (LHE) 13 TeV
Fraction of events / 1 GeV
p_T of γ_D [GeV]
1st dark photon (leading p_T)
2nd dark photon

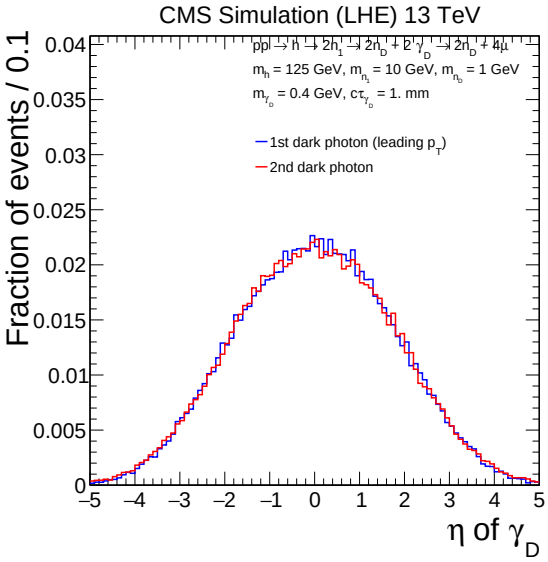
CMS Simulation (LHE) 13 TeV
Fraction of events / 0.1
η of γ_D
1st dark photon (leading p_T)
2nd dark photon

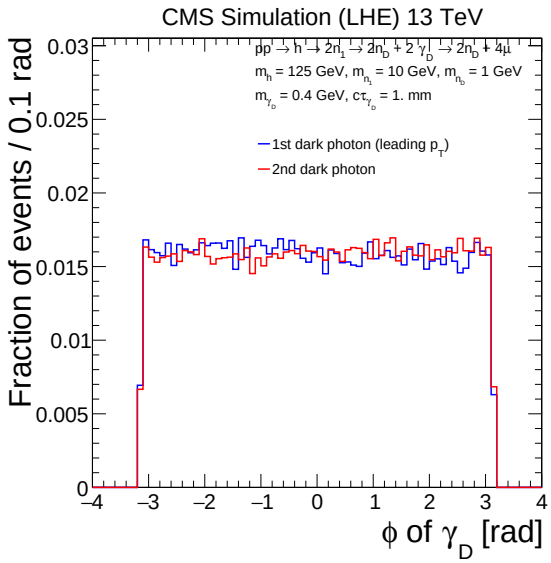
CMS Simulation (LHE) 13 TeV
Fraction of events / 0.1 rad
ϕ of γ_D [rad]
1st dark photon (leading p_T)
2nd dark photon

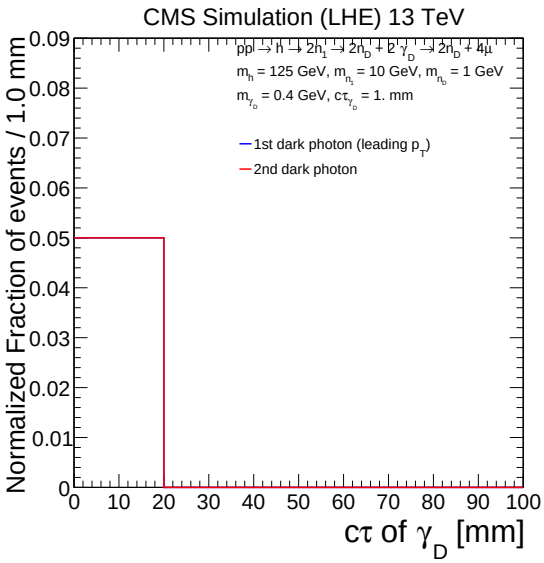
CMS Simulation (LHE) 13 TeV
Normalized Fraction of events / 1.0 mm
cτ of γ_D [mm]
1st dark photon (leading p_T)
2nd dark photon

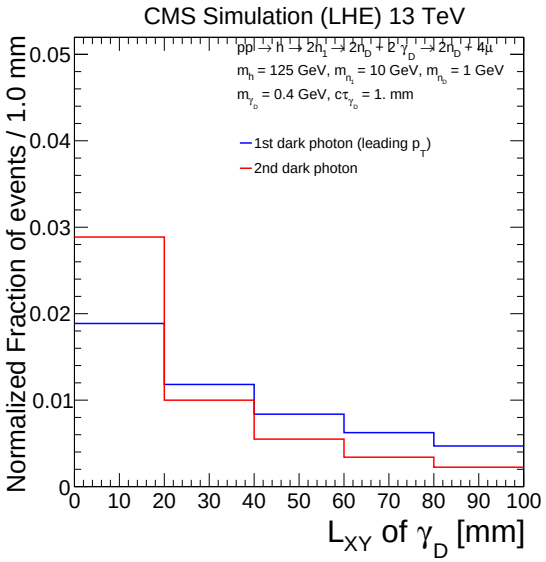
CMS Simulation (LHE) 13 TeV
Normalized Fraction of events / 1.0 mm
L_{XY} of γ_D [mm]
1st dark photon (leading p_T)
2nd dark photon

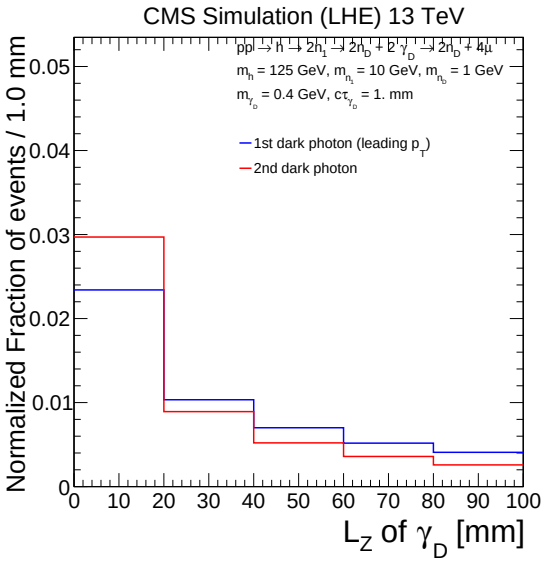
CMS Simulation (LHE) 13 TeV
Normalized Fraction of events / 1.0 mm
L_Z of γ_D [mm]
1st dark photon (leading p_T)
2nd dark photon

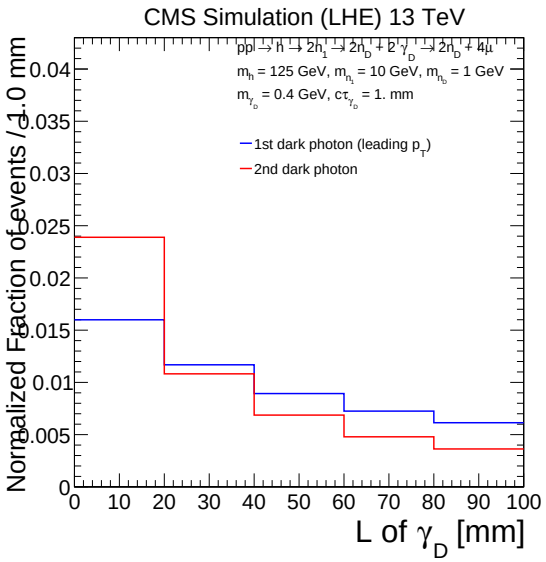
CMS Simulation (LHE) 13 TeV
Normalized Fraction of events / 1.0 mm
L of γ_D [mm]
1st dark photon (leading p_T)
2nd dark photon

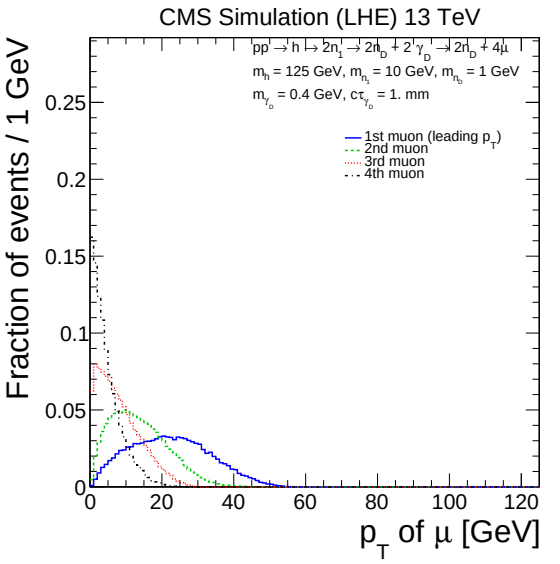
CMS Simulation (LHE) 13 TeV
Fraction of events / 1 GeV
p_T of μ [GeV]
1st muon (leading p_T)
2nd muon
3rd muon
4th muon

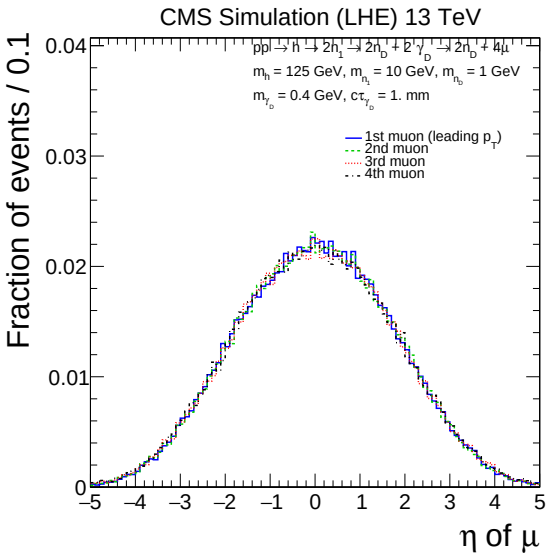
CMS Simulation (LHE) 13 TeV
Fraction of events / 0.1
η of μ
1st muon (leading p_T)
2nd muon
3rd muon
4th muon

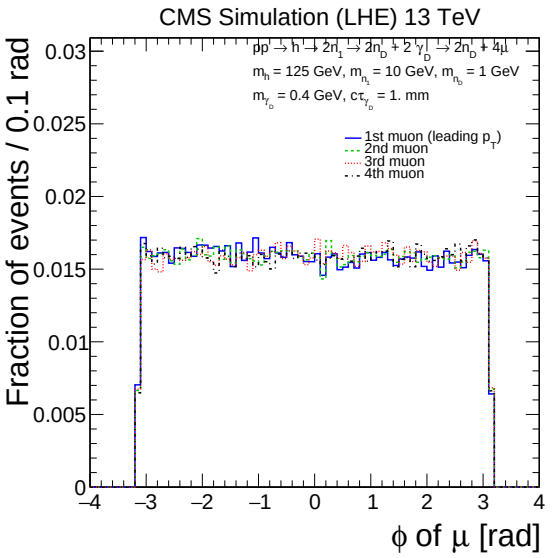
CMS Simulation (LHE) 13 TeV
Fraction of events / 0.1 rad
ϕ of μ [rad]
1st muon (leading p_T)
2nd muon
3rd muon
4th muon

APPENDIX D

PLOTS OF DISTANCE BETWEEN VERTICES

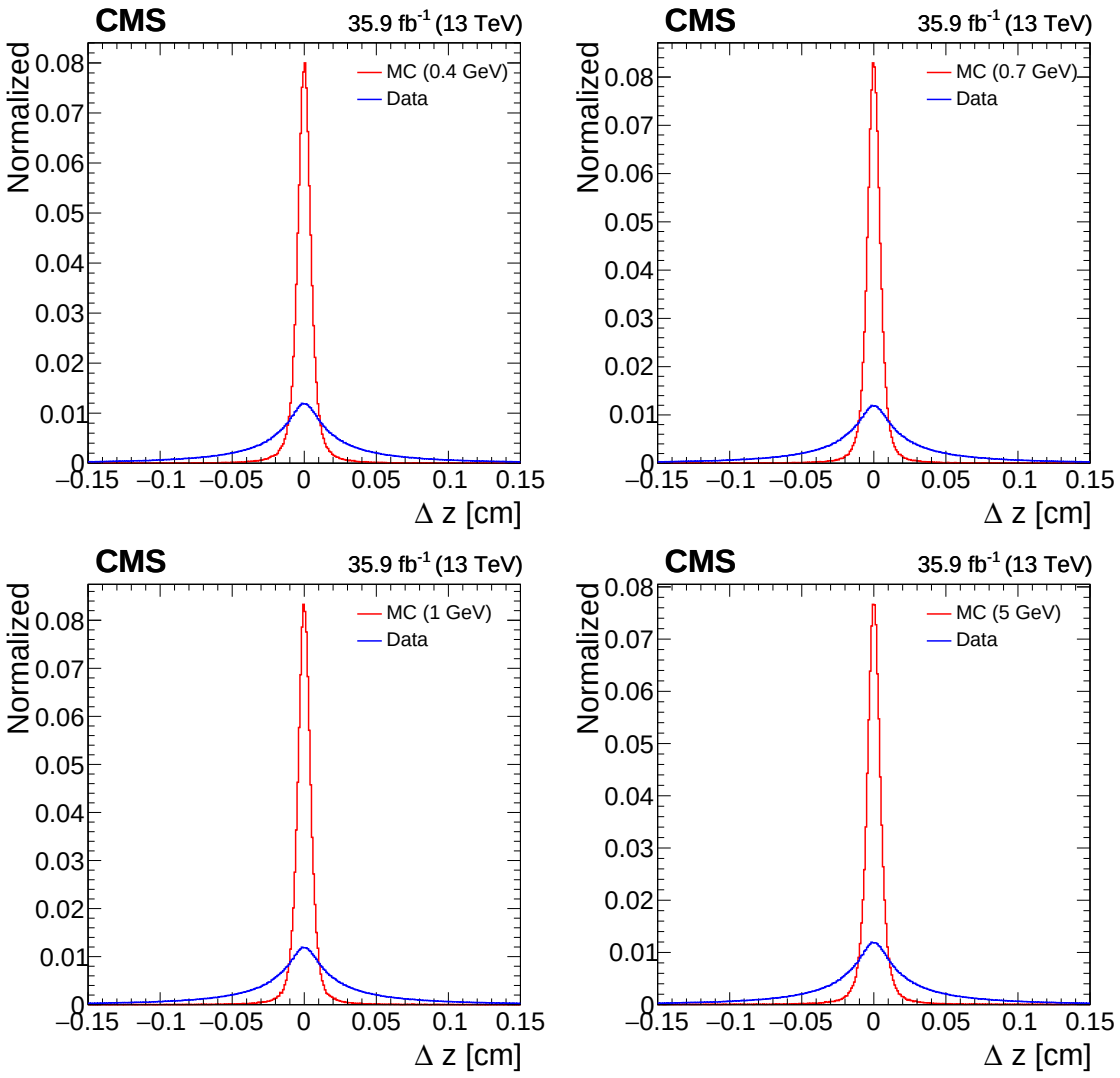

Figure D.1: Distance between vertices measured for two dimuons ($\Delta z = z_{(\mu\mu)_1} - z_{(\mu\mu)_1}$) in the MSSMD simulated sample with $m_h = 125$ GeV, and for dimuon and orphan muon ($\Delta z = z_{\mu\mu} - z$) in events from the bb-background enriched part of the DoubleMuon data sample.

APPENDIX E

PLOTS OF DIMUON ISOLATION

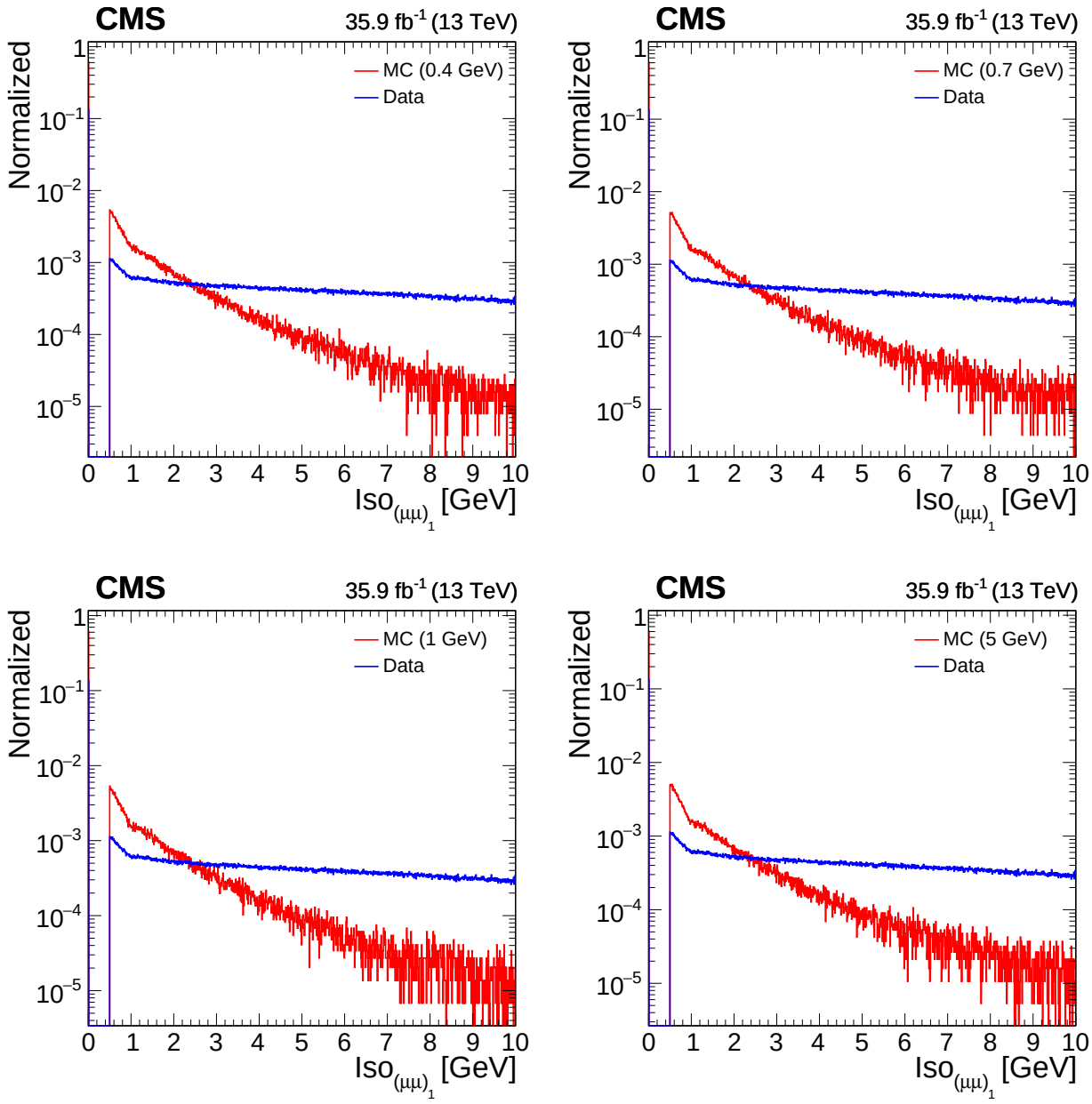

Figure E.1: Dimuon isolation for MSSMD simulated samples with $m_h = 125$ GeV, and for a bb-background enriched part of the DoubleMuon data sample in the range $0 - 10$ GeV.

Table F.1: Acceptances and efficiencies of the event selection for NMSSM benchmark models with $m_h = 90$ GeV and $m_{a_1} = 0.25,\ 0.5$ GeV.

Sample	$m_{h_{1,2}} = 90$ GeV, $m_{a_1} = 0.25$ GeV			$m_{h_{1,2}} = 90$ GeV, $m_{a_1} = 0.5$ GeV		
Selection	Events	Tot. Eff.	Rel. Eff.	Events	Tot. Eff.	Rel. Eff.
All events	200000	1.0000 ± 0.0000	1.0000 ± 0.0000	200000	1.0000 ± 0.0000	1.0000 ± 0.0000
Basic Gen level selections						
$p_{\mathrm{T}_1} > 17$ GeV, $\lvert\eta_1\rvert < 0.9$	87490	0.4374 ± 0.0011	0.4374 ± 0.0011	92109	0.4605 ± 0.0011	0.4605 ± 0.0011
$p_{\mathrm{T}_2} > 8$ GeV, $\lvert\eta_2\rvert < 2.4$	86689	0.4334 ± 0.0011	0.9908 ± 0.0003	87924	0.4396 ± 0.0011	0.9546 ± 0.0007
$p_{\mathrm{T}_3} > 8$ GeV, $\lvert\eta_3\rvert < 2.4$	79856	0.3993 ± 0.0011	0.9212 ± 0.0009	73519	0.3676 ± 0.0011	0.8362 ± 0.0012
$p_{\mathrm{T}_4} > 8$ GeV, $\lvert\eta_4\rvert < 2.4$	69837	0.3492 ± 0.0011	0.8745 ± 0.0012	33836	0.1692 ± 0.0008	0.4602 ± 0.0018
$L_{xy} < 9.8$ cm, $L_z < 46.5$ cm	69837	0.3492 ± 0.0011	1.0000 ± 0.0000	33836	0.1692 ± 0.0008	1.0000 ± 0.0000
Online selection						
Trigger	114815	0.5741 ± 0.0011	0.5741 ± 0.0011	102053	0.5103 ± 0.0011	0.5103 ± 0.0011
Basic Reco level selections						
Good primary vertex	114815	0.5741 ± 0.0011	1.0000 ± 0.0000	102053	0.5103 ± 0.0011	1.0000 ± 0.0000
$p_{\mathrm{T}_1} > 17$ GeV, $\lvert\eta_1\rvert < 0.9$	73003	0.3650 ± 0.0011	0.6358 ± 0.0014	66830	0.3341 ± 0.0011	0.6549 ± 0.0015
$p_{\mathrm{T}_2} > 8$ GeV, $\lvert\eta_2\rvert < 2.4$	72974	0.3649 ± 0.0011	0.9996 ± 0.0001	66800	0.3340 ± 0.0011	0.9996 ± 0.0001
$p_{\mathrm{T}_3} > 8$ GeV, $\lvert\eta_3\rvert < 2.4$	72015	0.3601 ± 0.0011	0.9869 ± 0.0004	65233	0.3262 ± 0.0010	0.9765 ± 0.0006
$p_{\mathrm{T}_4} > 8$ GeV, $\lvert\eta_4\rvert < 2.4$	58507	0.2925 ± 0.0010	0.8124 ± 0.0015	31375	0.1569 ± 0.0008	0.4810 ± 0.0020
Extra Reco level selections						
Two muon-jets	56687	0.2834 ± 0.0010	0.9689 ± 0.0007	27263	0.1363 ± 0.0008	0.8689 ± 0.0019
Two dimuons	56658	0.2833 ± 0.0010	0.9995 ± 0.0001	27254	0.1363 ± 0.0008	0.9997 ± 0.0001
Pixel hit requirement	56238	0.2812 ± 0.0010	0.9926 ± 0.0004	27225	0.1361 ± 0.0008	0.9989 ± 0.0002
$\lvert z_{(\mu\mu)_1} - z_{(\mu\mu)_2}\rvert < 0.1$ cm	56030	0.2801 ± 0.0010	0.9963 ± 0.0003	27154	0.1358 ± 0.0008	0.9974 ± 0.0003
$\mathrm{Iso}_{(\mu\mu)_{1,2}} < 2$ GeV	45342	0.2267 ± 0.0009	0.8092 ± 0.0017	21848	0.1092 ± 0.0007	0.8046 ± 0.0024
$m_{(\mu\mu)_1} \approx m_{(\mu\mu)_2}$	45205	0.2260 ± 0.0009	0.9970 ± 0.0003	21784	0.1089 ± 0.0007	0.9971 ± 0.0004
α_{gen}			0.3492 ± 0.0011			0.1692 ± 0.0008
ϵ_{full}			0.2260 ± 0.0009			0.1089 ± 0.0007
$\epsilon_{\mathrm{full}}/\alpha_{\mathrm{gen}}$			0.6473 ± 0.0018			0.6438 ± 0.0026

Table F.2: Acceptances and efficiencies of the event selection for NMSSM benchmark models with $m_h = 90$ GeV and $m_{a_1} = 0.5,\ 1$ GeV.

Sample	$m_{h_{1,2}} = 90$ GeV, $m_{a_1} = 0.75$ GeV			$m_{h_{1,2}} = 90$ GeV, $m_{a_1} = 1$ GeV		
Selection	Events	Tot. Eff.	Rel. Eff.	Events	Tot. Eff.	Rel. Eff.
All events	200000	1.0000 ± 0.0000	1.0000 ± 0.0000	200000	1.0000 ± 0.0000	1.0000 ± 0.0000
Basic Gen level selections						
$p_{\mathrm{T}_1} > 17$ GeV, $\lvert\eta_1\rvert < 0.9$	92437	0.4622 ± 0.0011	0.4622 ± 0.0011	92521	0.4626 ± 0.0011	0.4626 ± 0.0011
$p_{\mathrm{T}_2} > 8$ GeV, $\lvert\eta_2\rvert < 2.4$	87923	0.4396 ± 0.0011	0.9512 ± 0.0007	87868	0.4393 ± 0.0011	0.9497 ± 0.0007
$p_{\mathrm{T}_3} > 8$ GeV, $\lvert\eta_3\rvert < 2.4$	71588	0.3579 ± 0.0011	0.8142 ± 0.0013	70651	0.3533 ± 0.0011	0.8041 ± 0.0013
$p_{\mathrm{T}_4} > 8$ GeV, $\lvert\eta_4\rvert < 2.4$	30322	0.1516 ± 0.0008	0.4236 ± 0.0018	28962	0.1448 ± 0.0008	0.4099 ± 0.0019
$L_{xy} < 9.8$ cm, $L_z < 46.5$ cm	30322	0.1516 ± 0.0008	1.0000 ± 0.0000	28962	0.1448 ± 0.0008	1.0000 ± 0.0000
Online selection						
Trigger	98848	0.4942 ± 0.0011	0.4942 ± 0.0011	97735	0.4887 ± 0.0011	0.4887 ± 0.0011
Basic Reco level selections						
Good primary vertex	98848	0.4942 ± 0.0011	1.0000 ± 0.0000	97735	0.4887 ± 0.0011	1.0000 ± 0.0000
$p_{\mathrm{T}_1} > 17$ GeV, $\lvert\eta_1\rvert < 0.9$	64755	0.3238 ± 0.0010	0.6551 ± 0.0015	63961	0.3198 ± 0.0010	0.6544 ± 0.0015
$p_{\mathrm{T}_2} > 8$ GeV, $\lvert\eta_2\rvert < 2.4$	64728	0.3236 ± 0.0010	0.9996 ± 0.0001	63948	0.3197 ± 0.0010	0.9998 ± 0.0001
$p_{\mathrm{T}_3} > 8$ GeV, $\lvert\eta_3\rvert < 2.4$	63180	0.3159 ± 0.0010	0.9761 ± 0.0006	62424	0.3121 ± 0.0010	0.9762 ± 0.0006
$p_{\mathrm{T}_4} > 8$ GeV, $\lvert\eta_4\rvert < 2.4$	28237	0.1412 ± 0.0008	0.4469 ± 0.0020	26939	0.1347 ± 0.0008	0.4315 ± 0.0020
Extra Reco level selections						
Two muon-jets	24358	0.1218 ± 0.0007	0.8626 ± 0.0020	23249	0.1162 ± 0.0007	0.8630 ± 0.0021
Two dimuons	24344	0.1217 ± 0.0007	0.9994 ± 0.0002	23232	0.1162 ± 0.0007	0.9993 ± 0.0002
Pixel hit requirement	24334	0.1217 ± 0.0007	0.9996 ± 0.0001	23229	0.1161 ± 0.0007	0.9999 ± 0.0001
$\lvert z_{(\mu\mu)_1} - z_{(\mu\mu)_2}\rvert < 0.1$ cm	24295	0.1215 ± 0.0007	0.9984 ± 0.0003	23205	0.1160 ± 0.0007	0.9990 ± 0.0002
$\mathrm{Iso}_{(\mu\mu)_{1,2}} < 2$ GeV	19638	0.0982 ± 0.0007	0.8083 ± 0.0025	18732	0.0937 ± 0.0007	0.8072 ± 0.0026
$m_{(\mu\mu)_1} \approx m_{(\mu\mu)_2}$	19492	0.0975 ± 0.0007	0.9926 ± 0.0006	18527	0.0926 ± 0.0006	0.9891 ± 0.0008
α_{gen}			0.1516 ± 0.0008			0.1448 ± 0.0008
ϵ_{full}			0.0975 ± 0.0007			0.0926 ± 0.0006
$\epsilon_{\mathrm{full}}/\alpha_{\mathrm{gen}}$			0.6428 ± 0.0028			0.6397 ± 0.0028

Table F.3: Acceptances and efficiencies of the event selection for NMSSM benchmark models with $m_h = 90$ GeV and $m_{a_1} = 2,\ 3$ GeV.

Sample	$m_{h_{1,2}} = 90$ GeV, $m_{a_1} = 2$ GeV			$m_{h_{1,2}} = 90$ GeV, $m_{a_1} = 3$ GeV		
Selection	Events	Tot. Eff.	Rel. Eff.	Events	Tot. Eff.	Rel. Eff.
All events	200000	1.0000 ± 0.0000	1.0000 ± 0.0000	199308	1.0000 ± 0.0000	1.0000 ± 0.0000
Basic Gen level selections						
$p_{\mathrm{T}_1} > 17$ GeV, $\lvert\eta_1\rvert < 0.9$	93027	0.4651 ± 0.0011	0.4651 ± 0.0011	92655	0.4649 ± 0.0011	0.4649 ± 0.0011
$p_{\mathrm{T}_2} > 8$ GeV, $\lvert\eta_2\rvert < 2.4$	88299	0.4415 ± 0.0011	0.9492 ± 0.0007	87862	0.4408 ± 0.0011	0.9483 ± 0.0007
$p_{\mathrm{T}_3} > 8$ GeV, $\lvert\eta_3\rvert < 2.4$	70051	0.3503 ± 0.0011	0.7933 ± 0.0014	69577	0.3491 ± 0.0011	0.7919 ± 0.0014
$p_{\mathrm{T}_4} > 8$ GeV, $\lvert\eta_4\rvert < 2.4$	27857	0.1393 ± 0.0008	0.3977 ± 0.0018	27625	0.1386 ± 0.0008	0.3970 ± 0.0019
$L_{xy} < 9.8$ cm, $L_z < 46.5$ cm	27857	0.1393 ± 0.0008	1.0000 ± 0.0000	27625	0.1386 ± 0.0008	1.0000 ± 0.0000
Online selection						
Trigger	96007	0.4800 ± 0.0011	0.4800 ± 0.0011	94878	0.4760 ± 0.0011	0.4760 ± 0.0011
Basic Reco level selections						
Good primary vertex	96007	0.4800 ± 0.0011	1.0000 ± 0.0000	94878	0.4760 ± 0.0011	1.0000 ± 0.0000
$p_{\mathrm{T}_1} > 17$ GeV, $\lvert\eta_1\rvert < 0.9$	63396	0.3170 ± 0.0010	0.6603 ± 0.0015	62644	0.3143 ± 0.0010	0.6603 ± 0.0015
$p_{\mathrm{T}_2} > 8$ GeV, $\lvert\eta_2\rvert < 2.4$	63378	0.3169 ± 0.0010	0.9997 ± 0.0001	62629	0.3142 ± 0.0010	0.9998 ± 0.0001
$p_{\mathrm{T}_3} > 8$ GeV, $\lvert\eta_3\rvert < 2.4$	61895	0.3095 ± 0.0010	0.9766 ± 0.0006	61179	0.3070 ± 0.0010	0.9768 ± 0.0006
$p_{\mathrm{T}_4} > 8$ GeV, $\lvert\eta_4\rvert < 2.4$	26187	0.1309 ± 0.0008	0.4231 ± 0.0020	26007	0.1305 ± 0.0008	0.4251 ± 0.0020
Extra Reco level selections						
Two muon-jets	22528	0.1126 ± 0.0007	0.8603 ± 0.0021	22516	0.1130 ± 0.0007	0.8658 ± 0.0021
Two dimuons	22511	0.1126 ± 0.0007	0.9992 ± 0.0002	22496	0.1129 ± 0.0007	0.9991 ± 0.0002
Pixel hit requirement	22508	0.1125 ± 0.0007	0.9999 ± 0.0001	22491	0.1128 ± 0.0007	0.9998 ± 0.0001
$\lvert z_{(\mu\mu)_1} - z_{(\mu\mu)_2}\rvert < 0.1$ cm	22493	0.1125 ± 0.0007	0.9993 ± 0.0002	22478	0.1128 ± 0.0007	0.9994 ± 0.0002
$\mathrm{Iso}_{(\mu\mu)_{1,2}} < 2$ GeV	18138	0.0907 ± 0.0006	0.8064 ± 0.0026	18059	0.0906 ± 0.0006	0.8034 ± 0.0027
$m_{(\mu\mu)_1} \approx m_{(\mu\mu)_2}$	17696	0.0885 ± 0.0006	0.9756 ± 0.0011	17383	0.0872 ± 0.0006	0.9626 ± 0.0014
α_{gen}			0.1393 ± 0.0008			0.1386 ± 0.0008
ϵ_{full}			0.0885 ± 0.0006			0.0872 ± 0.0006
$\epsilon_{\mathrm{full}}/\alpha_{\mathrm{gen}}$			0.6352 ± 0.0029			0.6292 ± 0.0029

Table F.4: Acceptances and efficiencies of the event selection for NMSSM benchmark models with $m_h = 100$ GeV and $m_{a_1} = 0.25,\ 0.5$ GeV.

Sample	$m_{h_{1,2}} = 100$ GeV, $m_{a_1} = 0.25$ GeV			$m_{h_{1,2}} = 100$ GeV, $m_{a_1} = 0.5$ GeV		
Selection	Events	Tot. Eff.	Rel. Eff.	Events	Tot. Eff.	Rel. Eff.
All events	199065	1.0000 ± 0.0000	1.0000 ± 0.0000	199215	1.0000 ± 0.0000	1.0000 ± 0.0000
Basic Gen level selections						
$p_{\mathrm{T}_1} > 17$ GeV, $\lvert\eta_1\rvert < 0.9$	93494	0.4697 ± 0.0011	0.4697 ± 0.0011	96955	0.4867 ± 0.0011	0.4867 ± 0.0011
$p_{\mathrm{T}_2} > 8$ GeV, $\lvert\eta_2\rvert < 2.4$	92701	0.4657 ± 0.0011	0.9915 ± 0.0003	92545	0.4645 ± 0.0011	0.9545 ± 0.0007
$p_{\mathrm{T}_3} > 8$ GeV, $\lvert\eta_3\rvert < 2.4$	85163	0.4278 ± 0.0011	0.9187 ± 0.0009	79529	0.3992 ± 0.0011	0.8594 ± 0.0011
$p_{\mathrm{T}_4} > 8$ GeV, $\lvert\eta_4\rvert < 2.4$	77741	0.3905 ± 0.0011	0.9128 ± 0.0010	40784	0.2047 ± 0.0009	0.5128 ± 0.0018
$L_{xy} < 9.8$ cm, $L_z < 46.5$ cm	77741	0.3905 ± 0.0011	1.0000 ± 0.0000	40784	0.2047 ± 0.0009	1.0000 ± 0.0000
Online selection						
Trigger	118548	0.5955 ± 0.0011	0.5955 ± 0.0011	108286	0.5436 ± 0.0011	0.5436 ± 0.0011
Basic Reco level selections						
Good primary vertex	118548	0.5955 ± 0.0011	1.0000 ± 0.0000	108286	0.5436 ± 0.0011	1.0000 ± 0.0000
$p_{\mathrm{T}_1} > 17$ GeV, $\lvert\eta_1\rvert < 0.9$	78344	0.3936 ± 0.0011	0.6609 ± 0.0014	72873	0.3658 ± 0.0011	0.6730 ± 0.0014
$p_{\mathrm{T}_2} > 8$ GeV, $\lvert\eta_2\rvert < 2.4$	78315	0.3934 ± 0.0011	0.9996 ± 0.0001	72846	0.3657 ± 0.0011	0.9996 ± 0.0001
$p_{\mathrm{T}_3} > 8$ GeV, $\lvert\eta_3\rvert < 2.4$	77389	0.3888 ± 0.0011	0.9882 ± 0.0004	71346	0.3581 ± 0.0011	0.9794 ± 0.0005
$p_{\mathrm{T}_4} > 8$ GeV, $\lvert\eta_4\rvert < 2.4$	64718	0.3251 ± 0.0010	0.8363 ± 0.0013	37630	0.1889 ± 0.0009	0.5274 ± 0.0019
Extra Reco level selections						
Two muon-jets	62810	0.3155 ± 0.0010	0.9705 ± 0.0007	32800	0.1646 ± 0.0008	0.8716 ± 0.0017
Two dimuons	62779	0.3154 ± 0.0010	0.9995 ± 0.0001	32786	0.1646 ± 0.0008	0.9996 ± 0.0001
Pixel hit requirement	62214	0.3125 ± 0.0010	0.9910 ± 0.0004	32749	0.1644 ± 0.0008	0.9989 ± 0.0002
$\lvert z_{(\mu\mu)_1} - z_{(\mu\mu)_2}\rvert < 0.1$ cm	61986	0.3114 ± 0.0010	0.9963 ± 0.0002	32658	0.1639 ± 0.0008	0.9972 ± 0.0003
$\mathrm{Iso}_{(\mu\mu)_{1,2}} < 2$ GeV	49744	0.2499 ± 0.0010	0.8025 ± 0.0016	26471	0.1329 ± 0.0008	0.8106 ± 0.0022
$m_{(\mu\mu)_1} \approx m_{(\mu\mu)_2}$	49547	0.2489 ± 0.0010	0.9960 ± 0.0003	26356	0.1323 ± 0.0008	0.9957 ± 0.0004
α_{gen}			0.3905 ± 0.0011			0.2047 ± 0.0009
ϵ_{full}			0.2489 ± 0.0010			0.1323 ± 0.0008
$\epsilon_{\mathrm{full}}/\alpha_{\mathrm{gen}}$			0.6373 ± 0.0017			0.6462 ± 0.0024

Table F.5: Acceptances and efficiencies of the event selection for NMSSM benchmark models with $m_h = 100$ GeV and $m_{a_1} = 0.75,\ 1$ GeV.

Sample	$m_{h_{1,2}} = 100$ GeV, $m_{a_1} = 0.75$ GeV			$m_{h_{1,2}} = 100$ GeV, $m_{a_1} = 1$ GeV		
Selection	Events	Tot. Eff.	Rel. Eff.	Events	Tot. Eff.	Rel. Eff.
All events	200000	1.0000 ± 0.0000	1.0000 ± 0.0000	198250	1.0000 ± 0.0000	1.0000 ± 0.0000
Basic Gen level selections						
$p_{\mathrm{T}_1} > 17$ GeV, $\lvert\eta_1\rvert < 0.9$	98057	0.4903 ± 0.0011	0.4903 ± 0.0011	97141	0.4900 ± 0.0011	0.4900 ± 0.0011
$p_{\mathrm{T}_2} > 8$ GeV, $\lvert\eta_2\rvert < 2.4$	93159	0.4658 ± 0.0011	0.9500 ± 0.0007	92106	0.4646 ± 0.0011	0.9482 ± 0.0007
$p_{\mathrm{T}_3} > 8$ GeV, $\lvert\eta_3\rvert < 2.4$	77827	0.3891 ± 0.0011	0.8354 ± 0.0012	76235	0.3845 ± 0.0011	0.8277 ± 0.0012
$p_{\mathrm{T}_4} > 8$ GeV, $\lvert\eta_4\rvert < 2.4$	36480	0.1824 ± 0.0009	0.4687 ± 0.0018	34629	0.1747 ± 0.0009	0.4542 ± 0.0018
$L_{xy} < 9.8$ cm, $L_z < 46.5$ cm	36480	0.1824 ± 0.0009	1.0000 ± 0.0000	34629	0.1747 ± 0.0009	1.0000 ± 0.0000
Online selection						
Trigger	105381	0.5269 ± 0.0011	0.5269 ± 0.0011	102914	0.5191 ± 0.0011	0.5191 ± 0.0011
Basic Reco level selections						
Good primary vertex	105381	0.5269 ± 0.0011	1.0000 ± 0.0000	102914	0.5191 ± 0.0011	1.0000 ± 0.0000
$p_{\mathrm{T}_1} > 17$ GeV, $\lvert\eta_1\rvert < 0.9$	70876	0.3544 ± 0.0011	0.6726 ± 0.0014	69460	0.3504 ± 0.0011	0.6749 ± 0.0015
$p_{\mathrm{T}_2} > 8$ GeV, $\lvert\eta_2\rvert < 2.4$	70851	0.3543 ± 0.0011	0.9996 ± 0.0001	69439	0.3503 ± 0.0011	0.9997 ± 0.0001
$p_{\mathrm{T}_3} > 8$ GeV, $\lvert\eta_3\rvert < 2.4$	69345	0.3467 ± 0.0011	0.9787 ± 0.0005	67936	0.3427 ± 0.0011	0.9784 ± 0.0006
$p_{\mathrm{T}_4} > 8$ GeV, $\lvert\eta_4\rvert < 2.4$	33857	0.1693 ± 0.0008	0.4882 ± 0.0019	32231	0.1626 ± 0.0008	0.4744 ± 0.0019
Extra Reco level selections						
Two muon-jets	29268	0.1463 ± 0.0008	0.8645 ± 0.0019	27810	0.1403 ± 0.0008	0.8628 ± 0.0019
Two dimuons	29259	0.1463 ± 0.0008	0.9997 ± 0.0001	27801	0.1402 ± 0.0008	0.9997 ± 0.0001
Pixel hit requirement	29249	0.1462 ± 0.0008	0.9997 ± 0.0001	27797	0.1402 ± 0.0008	0.9999 ± 0.0001
$\lvert z_{(\mu\mu)_1} - z_{(\mu\mu)_2}\rvert < 0.1$ cm	29189	0.1459 ± 0.0008	0.9979 ± 0.0003	27767	0.1401 ± 0.0008	0.9989 ± 0.0002
$\mathrm{Iso}_{(\mu\mu)_{1,2}} < 2$ GeV	23403	0.1170 ± 0.0007	0.8018 ± 0.0023	22237	0.1122 ± 0.0007	0.8008 ± 0.0024
$m_{(\mu\mu)_1} \approx m_{(\mu\mu)_2}$	23225	0.1161 ± 0.0007	0.9924 ± 0.0006	21973	0.1108 ± 0.0007	0.9881 ± 0.0007
α_{gen}			0.1824 ± 0.0009			0.1747 ± 0.0009
ϵ_{full}			0.1161 ± 0.0007			0.1108 ± 0.0007
$\epsilon_{\mathrm{full}}/\alpha_{\mathrm{gen}}$			0.6367 ± 0.0025			0.6345 ± 0.0026

Table F.6: Acceptances and efficiencies of the event selection for NMSSM benchmark models with $m_h = 100$ GeV and $m_{a_1} = 2,\ 3$ GeV.

Sample	$m_{h_{1,2}} = 100$ GeV, $m_{a_1} = 2$ GeV			$m_{h_{1,2}} = 100$ GeV, $m_{a_1} = 3$ GeV		
Selection	Events	Tot. Eff.	Rel. Eff.	Events	Tot. Eff.	Rel. Eff.
All events	200000	1.0000 ± 0.0000	1.0000 ± 0.0000	198865	1.0000 ± 0.0000	1.0000 ± 0.0000
Basic Gen level selections						
$p_{\mathrm{T}_1} > 17$ GeV, $\lvert\eta_1\rvert < 0.9$	98468	0.4923 ± 0.0011	0.4923 ± 0.0011	98026	0.4929 ± 0.0011	0.4929 ± 0.0011
$p_{\mathrm{T}_2} > 8$ GeV, $\lvert\eta_2\rvert < 2.4$	93521	0.4676 ± 0.0011	0.9498 ± 0.0007	93107	0.4682 ± 0.0011	0.9498 ± 0.0007
$p_{\mathrm{T}_3} > 8$ GeV, $\lvert\eta_3\rvert < 2.4$	76550	0.3828 ± 0.0011	0.8185 ± 0.0013	76071	0.3825 ± 0.0011	0.8170 ± 0.0013
$p_{\mathrm{T}_4} > 8$ GeV, $\lvert\eta_4\rvert < 2.4$	33727	0.1686 ± 0.0008	0.4406 ± 0.0018	33470	0.1683 ± 0.0008	0.4400 ± 0.0018
$L_{xy} < 9.8$ cm, $L_z < 46.5$ cm	33727	0.1686 ± 0.0008	1.0000 ± 0.0000	33470	0.1683 ± 0.0008	1.0000 ± 0.0000
Online selection						
Trigger	102492	0.5125 ± 0.0011	0.5125 ± 0.0011	101082	0.5083 ± 0.0011	0.5083 ± 0.0011
Basic Reco level selections						
Good primary vertex	102492	0.5125 ± 0.0011	1.0000 ± 0.0000	101082	0.5083 ± 0.0011	1.0000 ± 0.0000
$p_{\mathrm{T}_1} > 17$ GeV, $\lvert\eta_1\rvert < 0.9$	69642	0.3482 ± 0.0011	0.6795 ± 0.0015	68971	0.3468 ± 0.0011	0.6823 ± 0.0015
$p_{\mathrm{T}_2} > 8$ GeV, $\lvert\eta_2\rvert < 2.4$	69629	0.3481 ± 0.0011	0.9998 ± 0.0001	68950	0.3467 ± 0.0011	0.9997 ± 0.0001
$p_{\mathrm{T}_3} > 8$ GeV, $\lvert\eta_3\rvert < 2.4$	68124	0.3406 ± 0.0011	0.9784 ± 0.0006	67542	0.3396 ± 0.0011	0.9796 ± 0.0005
$p_{\mathrm{T}_4} > 8$ GeV, $\lvert\eta_4\rvert < 2.4$	31682	0.1584 ± 0.0008	0.4651 ± 0.0019	31480	0.1583 ± 0.0008	0.4661 ± 0.0019
Extra Reco level selections						
Two muon-jets	27379	0.1369 ± 0.0008	0.8642 ± 0.0019	27171	0.1366 ± 0.0008	0.8631 ± 0.0019
Two dimuons	27362	0.1368 ± 0.0008	0.9994 ± 0.0002	27154	0.1365 ± 0.0008	0.9994 ± 0.0002
Pixel hit requirement	27357	0.1368 ± 0.0008	0.9998 ± 0.0001	27152	0.1365 ± 0.0008	0.9999 ± 0.0001
$\lvert z_{(\mu\mu)_1} - z_{(\mu\mu)_2}\rvert < 0.1$ cm	27333	0.1367 ± 0.0008	0.9991 ± 0.0002	27133	0.1364 ± 0.0008	0.9993 ± 0.0002
$\mathrm{Iso}_{(\mu\mu)_{1,2}} < 2$ GeV	21849	0.1092 ± 0.0007	0.7994 ± 0.0024	21667	0.1090 ± 0.0007	0.7985 ± 0.0024
$m_{(\mu\mu)_1} \approx m_{(\mu\mu)_2}$	21291	0.1065 ± 0.0007	0.9745 ± 0.0011	20937	0.1053 ± 0.0007	0.9663 ± 0.0012
α_{gen}			0.1686 ± 0.0008			0.1683 ± 0.0008
ϵ_{full}			0.1065 ± 0.0007			0.1053 ± 0.0007
$\epsilon_{\mathrm{full}}/\alpha_{\mathrm{gen}}$			0.6313 ± 0.0026			0.6255 ± 0.0026

Table F.7: Acceptances and efficiencies of the event selection for NMSSM benchmark models with $m_h = 110$ GeV and $m_{a_1} = 0.25$ GeV.

Sample	$m_{h_{1,2}} = 110$ GeV, $m_{a_1} = 0.25$ GeV		
Selection	Events	Tot. Eff.	Rel. Eff.
All events	200000	1.0000 ± 0.0000	1.0000 ± 0.0000
Basic Gen level selections			
$p_{\mathrm{T}_1} > 17$ GeV, $\lvert\eta_1\rvert < 0.9$	98832	0.4942 ± 0.0011	0.4942 ± 0.0011
$p_{\mathrm{T}_2} > 8$ GeV, $\lvert\eta_2\rvert < 2.4$	98032	0.4902 ± 0.0011	0.9919 ± 0.0003
$p_{\mathrm{T}_3} > 8$ GeV, $\lvert\eta_3\rvert < 2.4$	89512	0.4476 ± 0.0011	0.9131 ± 0.0009
$p_{\mathrm{T}_4} > 8$ GeV, $\lvert\eta_4\rvert < 2.4$	83808	0.4190 ± 0.0011	0.9363 ± 0.0008
$L_{xy} < 9.8$ cm, $L_z < 46.5$ cm	83808	0.4190 ± 0.0011	1.0000 ± 0.0000
Online selection			
Trigger	122318	0.6116 ± 0.0011	0.6116 ± 0.0011
Basic Reco level selections			
Good primary vertex	122318	0.6116 ± 0.0011	1.0000 ± 0.0000
$p_{\mathrm{T}_1} > 17$ GeV, $\lvert\eta_1\rvert < 0.9$	82451	0.4123 ± 0.0011	0.6741 ± 0.0013
$p_{\mathrm{T}_2} > 8$ GeV, $\lvert\eta_2\rvert < 2.4$	82418	0.4121 ± 0.0011	0.9996 ± 0.0001
$p_{\mathrm{T}_3} > 8$ GeV, $\lvert\eta_3\rvert < 2.4$	81477	0.4074 ± 0.0011	0.9886 ± 0.0004
$p_{\mathrm{T}_4} > 8$ GeV, $\lvert\eta_4\rvert < 2.4$	69103	0.3455 ± 0.0011	0.8481 ± 0.0013
Extra Reco level selections			
Two muon-jets	67151	0.3358 ± 0.0011	0.9718 ± 0.0006
Two dimuons	67114	0.3356 ± 0.0011	0.9994 ± 0.0001
Pixel hit requirement	66500	0.3325 ± 0.0011	0.9909 ± 0.0004
$\lvert z_{(\mu\mu)_1} - z_{(\mu\mu)_2}\rvert < 0.1$ cm	66229	0.3311 ± 0.0011	0.9959 ± 0.0002
$\mathrm{Iso}_{(\mu\mu)_{1,2}} < 2$ GeV	53391	0.2670 ± 0.0010	0.8062 ± 0.0015
$m_{(\mu\mu)_1} \approx m_{(\mu\mu)_2}$	53158	0.2658 ± 0.0010	0.9956 ± 0.0003
α_{gen}			0.4190 ± 0.0011
ϵ_{full}			0.2658 ± 0.0010
$\epsilon_{\mathrm{full}}/\alpha_{\mathrm{gen}}$			0.6343 ± 0.0017

Table F.8: Acceptances and efficiencies of the event selection for NMSSM benchmark models with $m_h = 110$ GeV and $m_{a_1} = 0.75,\ 1$ GeV.

Sample	$m_{h_{1,2}} = 110$ GeV, $m_{a_1} = 0.75$ GeV			$m_{h_{1,2}} = 110$ GeV, $m_{a_1} = 1$ GeV		
Selection	Events	Tot. Eff.	Rel. Eff.	Events	Tot. Eff.	Rel. Eff.
All events	199065	1.0000 ± 0.0000	1.0000 ± 0.0000	197097	1.0000 ± 0.0000	1.0000 ± 0.0000
Basic Gen level selections						
$p_{\mathrm{T}_1} > 17$ GeV, $\lvert\eta_1\rvert < 0.9$	101665	0.5107 ± 0.0011	0.5107 ± 0.0011	101218	0.5135 ± 0.0011	0.5135 ± 0.0011
$p_{\mathrm{T}_2} > 8$ GeV, $\lvert\eta_2\rvert < 2.4$	96713	0.4858 ± 0.0011	0.9513 ± 0.0007	96012	0.4871 ± 0.0011	0.9486 ± 0.0007
$p_{\mathrm{T}_3} > 8$ GeV, $\lvert\eta_3\rvert < 2.4$	82352	0.4137 ± 0.0011	0.8515 ± 0.0011	81050	0.4112 ± 0.0011	0.8442 ± 0.0012
$p_{\mathrm{T}_4} > 8$ GeV, $\lvert\eta_4\rvert < 2.4$	41515	0.2085 ± 0.0009	0.5041 ± 0.0017	39722	0.2015 ± 0.0009	0.4901 ± 0.0018
$L_{xy} < 9.8$ cm, $L_z < 46.5$ cm	41515	0.2085 ± 0.0009	1.0000 ± 0.0000	39722	0.2015 ± 0.0009	1.0000 ± 0.0000
Online selection						
Trigger	109866	0.5519 ± 0.0011	0.5519 ± 0.0011	107405	0.5449 ± 0.0011	0.5449 ± 0.0011
Basic Reco level selections						
Good primary vertex	109866	0.5519 ± 0.0011	1.0000 ± 0.0000	107405	0.5449 ± 0.0011	1.0000 ± 0.0000
$p_{\mathrm{T}_1} > 17$ GeV, $\lvert\eta_1\rvert < 0.9$	75305	0.3783 ± 0.0011	0.6854 ± 0.0014	73872	0.3748 ± 0.0011	0.6878 ± 0.0014
$p_{\mathrm{T}_2} > 8$ GeV, $\lvert\eta_2\rvert < 2.4$	75285	0.3782 ± 0.0011	0.9997 ± 0.0001	73857	0.3747 ± 0.0011	0.9998 ± 0.0001
$p_{\mathrm{T}_3} > 8$ GeV, $\lvert\eta_3\rvert < 2.4$	73771	0.3706 ± 0.0011	0.9799 ± 0.0005	72439	0.3675 ± 0.0011	0.9808 ± 0.0005
$p_{\mathrm{T}_4} > 8$ GeV, $\lvert\eta_4\rvert < 2.4$	38413	0.1930 ± 0.0009	0.5207 ± 0.0018	36770	0.1866 ± 0.0009	0.5076 ± 0.0019
Extra Reco level selections						
Two muon-jets	33214	0.1669 ± 0.0008	0.8647 ± 0.0017	31729	0.1610 ± 0.0008	0.8629 ± 0.0018
Two dimuons	33202	0.1668 ± 0.0008	0.9996 ± 0.0001	31709	0.1609 ± 0.0008	0.9994 ± 0.0001
Pixel hit requirement	33182	0.1667 ± 0.0008	0.9994 ± 0.0001	31700	0.1608 ± 0.0008	0.9997 ± 0.0001
$\lvert z_{(\mu\mu)_1} - z_{(\mu\mu)_2}\rvert < 0.1$ cm	33106	0.1663 ± 0.0008	0.9977 ± 0.0003	31659	0.1606 ± 0.0008	0.9987 ± 0.0002
$\mathrm{Iso}_{(\mu\mu)_{1,2}} < 2$ GeV	26483	0.1330 ± 0.0008	0.7999 ± 0.0022	25418	0.1290 ± 0.0008	0.8029 ± 0.0022
$m_{(\mu\mu)_1} \approx m_{(\mu\mu)_2}$	26260	0.1319 ± 0.0008	0.9916 ± 0.0006	25069	0.1272 ± 0.0008	0.9863 ± 0.0007
α_{gen}			0.2085 ± 0.0009			0.2015 ± 0.0009
ϵ_{full}			0.1319 ± 0.0008			0.1272 ± 0.0008
$\epsilon_{\mathrm{full}}/\alpha_{\mathrm{gen}}$			0.6325 ± 0.0024			0.6311 ± 0.0024

Table F.9: Acceptances and efficiencies of the event selection for NMSSM benchmark models with $m_h = 110$ GeV and $m_{a_1} = 2,\ 3$ GeV.

Sample	$m_{h_{1,2}} = 110$ GeV, $m_{a_1} = 2$ GeV			$m_{h_{1,2}} = 110$ GeV, $m_{a_1} = 3$ GeV		
Selection	Events	Tot. Eff.	Rel. Eff.	Events	Tot. Eff.	Rel. Eff.
All events	198634	1.0000 ± 0.0000	1.0000 ± 0.0000	200000	1.0000 ± 0.0000	1.0000 ± 0.0000
Basic Gen level selections						
$p_{\mathrm{T}_1} > 17$ GeV, $\lvert\eta_1\rvert < 0.9$	101807	0.5125 ± 0.0011	0.5125 ± 0.0011	102786	0.5139 ± 0.0011	0.5139 ± 0.0011
$p_{\mathrm{T}_2} > 8$ GeV, $\lvert\eta_2\rvert < 2.4$	96587	0.4863 ± 0.0011	0.9487 ± 0.0007	97581	0.4879 ± 0.0011	0.9494 ± 0.0007
$p_{\mathrm{T}_3} > 8$ GeV, $\lvert\eta_3\rvert < 2.4$	80783	0.4067 ± 0.0011	0.8364 ± 0.0012	81648	0.4082 ± 0.0011	0.8367 ± 0.0012
$p_{\mathrm{T}_4} > 8$ GeV, $\lvert\eta_4\rvert < 2.4$	38572	0.1942 ± 0.0009	0.4775 ± 0.0018	38481	0.1924 ± 0.0009	0.4713 ± 0.0017
$L_{xy} < 9.8$ cm, $L_z < 46.5$ cm	38572	0.1942 ± 0.0009	1.0000 ± 0.0000	38481	0.1924 ± 0.0009	1.0000 ± 0.0000
Online selection						
Trigger	106587	0.5366 ± 0.0011	0.5366 ± 0.0011	106995	0.5350 ± 0.0011	0.5350 ± 0.0011
Basic Reco level selections						
Good primary vertex	106587	0.5366 ± 0.0011	1.0000 ± 0.0000	106995	0.5350 ± 0.0011	1.0000 ± 0.0000
$p_{\mathrm{T}_1} > 17$ GeV, $\lvert\eta_1\rvert < 0.9$	73667	0.3709 ± 0.0011	0.6911 ± 0.0014	74170	0.3708 ± 0.0011	0.6932 ± 0.0014
$p_{\mathrm{T}_2} > 8$ GeV, $\lvert\eta_2\rvert < 2.4$	73653	0.3708 ± 0.0011	0.9998 ± 0.0001	74155	0.3708 ± 0.0011	0.9998 ± 0.0001
$p_{\mathrm{T}_3} > 8$ GeV, $\lvert\eta_3\rvert < 2.4$	72236	0.3637 ± 0.0011	0.9808 ± 0.0005	72750	0.3638 ± 0.0011	0.9811 ± 0.0005
$p_{\mathrm{T}_4} > 8$ GeV, $\lvert\eta_4\rvert < 2.4$	35970	0.1811 ± 0.0009	0.4980 ± 0.0019	35996	0.1800 ± 0.0009	0.4948 ± 0.0019
Extra Reco level selections						
Two muon-jets	31112	0.1566 ± 0.0008	0.8649 ± 0.0018	31132	0.1557 ± 0.0008	0.8649 ± 0.0018
Two dimuons	31085	0.1565 ± 0.0008	0.9991 ± 0.0002	31099	0.1555 ± 0.0008	0.9989 ± 0.0002
Pixel hit requirement	31079	0.1565 ± 0.0008	0.9998 ± 0.0001	31096	0.1555 ± 0.0008	0.9999 ± 0.0001
$\lvert z_{(\mu\mu)_1} - z_{(\mu\mu)_2}\rvert < 0.1$ cm	31054	0.1563 ± 0.0008	0.9992 ± 0.0002	31073	0.1554 ± 0.0008	0.9993 ± 0.0002
$\mathrm{Iso}_{(\mu\mu)_{1,2}} < 2$ GeV	24836	0.1250 ± 0.0007	0.7998 ± 0.0023	24860	0.1243 ± 0.0007	0.8001 ± 0.0023
$m_{(\mu\mu)_1} \approx m_{(\mu\mu)_2}$	24140	0.1215 ± 0.0007	0.9720 ± 0.0010	23930	0.1196 ± 0.0007	0.9626 ± 0.0012
α_{gen}			0.1942 ± 0.0009			0.1924 ± 0.0009
ϵ_{full}			0.1215 ± 0.0007			0.1196 ± 0.0007
$\epsilon_{\mathrm{full}}/\alpha_{\mathrm{gen}}$			0.6258 ± 0.0025			0.6219 ± 0.0025

Table F.10: Acceptances and efficiencies of the event selection for NMSSM benchmark models with $m_h = 125$ GeV and $m_{a_1} = 0.25,\ 0.5$ GeV.

Sample	$m_{h_{1,2}} = 125$ GeV, $m_{a_1} = 0.25$ GeV			$m_{h_{1,2}} = 125$ GeV, $m_{a_1} = 0.5$ GeV		
Selection	Events	Tot. Eff.	Rel. Eff.	Events	Tot. Eff.	Rel. Eff.
All events	200000	1.0000 ± 0.0000	1.0000 ± 0.0000	200000	1.0000 ± 0.0000	1.0000 ± 0.0000
Basic Gen level selections						
$p_{\mathrm{T}_1} > 17$ GeV, $\lvert\eta_1\rvert < 0.9$	105303	0.5265 ± 0.0011	0.5265 ± 0.0011	107340	0.5367 ± 0.0011	0.5367 ± 0.0011
$p_{\mathrm{T}_2} > 8$ GeV, $\lvert\eta_2\rvert < 2.4$	104555	0.5228 ± 0.0011	0.9929 ± 0.0003	102519	0.5126 ± 0.0011	0.9551 ± 0.0006
$p_{\mathrm{T}_3} > 8$ GeV, $\lvert\eta_3\rvert < 2.4$	94856	0.4743 ± 0.0011	0.9072 ± 0.0009	90431	0.4522 ± 0.0011	0.8821 ± 0.0010
$p_{\mathrm{T}_4} > 8$ GeV, $\lvert\eta_4\rvert < 2.4$	90982	0.4549 ± 0.0011	0.9592 ± 0.0006	54814	0.2741 ± 0.0010	0.6061 ± 0.0016
$L_{xy} < 9.8$ cm, $L_z < 46.5$ cm	90982	0.4549 ± 0.0011	1.0000 ± 0.0000	54814	0.2741 ± 0.0010	1.0000 ± 0.0000
Online selection						
Trigger	126394	0.6320 ± 0.0011	0.6320 ± 0.0011	119772	0.5989 ± 0.0011	0.5989 ± 0.0011
Basic Reco level selections						
Good primary vertex	126394	0.6320 ± 0.0011	1.0000 ± 0.0000	119772	0.5989 ± 0.0011	1.0000 ± 0.0000
$p_{\mathrm{T}_1} > 17$ GeV, $\lvert\eta_1\rvert < 0.9$	87495	0.4375 ± 0.0011	0.6922 ± 0.0013	83496	0.4175 ± 0.0011	0.6971 ± 0.0013
$p_{\mathrm{T}_2} > 8$ GeV, $\lvert\eta_2\rvert < 2.4$	87471	0.4374 ± 0.0011	0.9997 ± 0.0001	83455	0.4173 ± 0.0011	0.9995 ± 0.0001
$p_{\mathrm{T}_3} > 8$ GeV, $\lvert\eta_3\rvert < 2.4$	86480	0.4324 ± 0.0011	0.9887 ± 0.0004	82025	0.4101 ± 0.0011	0.9829 ± 0.0004
$p_{\mathrm{T}_4} > 8$ GeV, $\lvert\eta_4\rvert < 2.4$	73741	0.3687 ± 0.0011	0.8527 ± 0.0012	49932	0.2497 ± 0.0010	0.6087 ± 0.0017
Extra Reco level selections						
Two muon-jets	71608	0.3580 ± 0.0011	0.9711 ± 0.0006	43500	0.2175 ± 0.0009	0.8712 ± 0.0015
Two dimuons	71558	0.3578 ± 0.0011	0.9993 ± 0.0001	43486	0.2174 ± 0.0009	0.9997 ± 0.0001
Pixel hit requirement	70741	0.3537 ± 0.0011	0.9886 ± 0.0004	43441	0.2172 ± 0.0009	0.9990 ± 0.0002
$\lvert z_{(\mu\mu)_1} - z_{(\mu\mu)_2}\rvert < 0.1$ cm	70383	0.3519 ± 0.0011	0.9949 ± 0.0003	43288	0.2164 ± 0.0009	0.9965 ± 0.0003
$\mathrm{Iso}_{(\mu\mu)_{1,2}} < 2$ GeV	56343	0.2817 ± 0.0010	0.8005 ± 0.0015	34480	0.1724 ± 0.0008	0.7965 ± 0.0019
$m_{(\mu\mu)_1} \approx m_{(\mu\mu)_2}$	56039	0.2802 ± 0.0010	0.9946 ± 0.0003	34288	0.1714 ± 0.0008	0.9944 ± 0.0004
α_{gen}			0.4549 ± 0.0011			0.2741 ± 0.0010
ϵ_{full}			0.2802 ± 0.0010			0.1714 ± 0.0008
$\epsilon_{\mathrm{full}}/\alpha_{\mathrm{gen}}$			0.6159 ± 0.0016			0.6255 ± 0.0021

Table F.11: Acceptances and efficiencies of the event selection for NMSSM benchmark models with $m_h = 125$ GeV and $m_{a_1} = 0.75,\ 1$ GeV.

Sample	$m_{h_{1,2}} = 125$ GeV, $m_{a_1} = 0.75$ GeV			$m_{h_{1,2}} = 125$ GeV, $m_{a_1} = 1$ GeV		
Selection	Events	Tot. Eff.	Rel. Eff.	Events	Tot. Eff.	Rel. Eff.
All events	195695	1.0000 ± 0.0000	1.0000 ± 0.0000	198389	1.0000 ± 0.0000	1.0000 ± 0.0000
Basic Gen level selections						
$p_{\mathrm{T}_1} > 17$ GeV, $\lvert\eta_1\rvert < 0.9$	105445	0.5388 ± 0.0011	0.5388 ± 0.0011	106979	0.5392 ± 0.0011	0.5392 ± 0.0011
$p_{\mathrm{T}_2} > 8$ GeV, $\lvert\eta_2\rvert < 2.4$	100131	0.5117 ± 0.0011	0.9496 ± 0.0007	101631	0.5123 ± 0.0011	0.9500 ± 0.0007
$p_{\mathrm{T}_3} > 8$ GeV, $\lvert\eta_3\rvert < 2.4$	86611	0.4426 ± 0.0011	0.8650 ± 0.0011	87296	0.4400 ± 0.0011	0.8590 ± 0.0011
$p_{\mathrm{T}_4} > 8$ GeV, $\lvert\eta_4\rvert < 2.4$	48016	0.2454 ± 0.0010	0.5544 ± 0.0017	46795	0.2359 ± 0.0010	0.5361 ± 0.0017
$L_{xy} < 9.8$ cm, $L_z < 46.5$ cm	48016	0.2454 ± 0.0010	1.0000 ± 0.0000	46795	0.2359 ± 0.0010	1.0000 ± 0.0000
Online selection						
Trigger	113791	0.5815 ± 0.0011	0.5815 ± 0.0011	113996	0.5746 ± 0.0011	0.5746 ± 0.0011
Basic Reco level selections						
Good primary vertex	113791	0.5815 ± 0.0011	1.0000 ± 0.0000	113996	0.5746 ± 0.0011	1.0000 ± 0.0000
$p_{\mathrm{T}_1} > 17$ GeV, $\lvert\eta_1\rvert < 0.9$	79570	0.4066 ± 0.0011	0.6993 ± 0.0014	79933	0.4029 ± 0.0011	0.7012 ± 0.0014
$p_{\mathrm{T}_2} > 8$ GeV, $\lvert\eta_2\rvert < 2.4$	79552	0.4065 ± 0.0011	0.9998 ± 0.0001	79910	0.4028 ± 0.0011	0.9997 ± 0.0001
$p_{\mathrm{T}_3} > 8$ GeV, $\lvert\eta_3\rvert < 2.4$	78152	0.3994 ± 0.0011	0.9824 ± 0.0005	78484	0.3956 ± 0.0011	0.9822 ± 0.0005
$p_{\mathrm{T}_4} > 8$ GeV, $\lvert\eta_4\rvert < 2.4$	44264	0.2262 ± 0.0009	0.5664 ± 0.0018	43137	0.2174 ± 0.0009	0.5496 ± 0.0018
Extra Reco level selections						
Two muon-jets	38246	0.1954 ± 0.0009	0.8640 ± 0.0016	37272	0.1879 ± 0.0009	0.8640 ± 0.0017
Two dimuons	38222	0.1953 ± 0.0009	0.9994 ± 0.0001	37240	0.1877 ± 0.0009	0.9991 ± 0.0002
Pixel hit requirement	38195	0.1952 ± 0.0009	0.9993 ± 0.0001	37217	0.1876 ± 0.0009	0.9994 ± 0.0001
$\lvert z_{(\mu\mu)_1} - z_{(\mu\mu)_2}\rvert < 0.1$ cm	38101	0.1947 ± 0.0009	0.9975 ± 0.0003	37163	0.1873 ± 0.0009	0.9985 ± 0.0002
$\mathrm{Iso}_{(\mu\mu)_{1,2}} < 2$ GeV	30426	0.1555 ± 0.0008	0.7986 ± 0.0021	29523	0.1488 ± 0.0008	0.7944 ± 0.0021
$m_{(\mu\mu)_1} \approx m_{(\mu\mu)_2}$	30120	0.1539 ± 0.0008	0.9899 ± 0.0006	29122	0.1468 ± 0.0008	0.9864 ± 0.0007
α_{gen}			0.2454 ± 0.0010			0.2359 ± 0.0010
ϵ_{full}			0.1539 ± 0.0008			0.1468 ± 0.0008
$\epsilon_{\mathrm{full}}/\alpha_{\mathrm{gen}}$			0.6273 ± 0.0022			0.6223 ± 0.0022

Table F.12: Acceptances and efficiencies of the event selection for NMSSM benchmark models with $m_h = 125$ GeV and $m_{a_1} = 2,\ 3$ GeV.

Sample	$m_{h_{1,2}} = 125$ GeV, $m_{a_1} = 2$ GeV			$m_{h_{1,2}} = 125$ GeV, $m_{a_1} = 3$ GeV		
Selection	Events	Tot. Eff.	Rel. Eff.	Events	Tot. Eff.	Rel. Eff.
All events	200001	1.0000 ± 0.0000	1.0000 ± 0.0000	200001	1.0000 ± 0.0000	1.0000 ± 0.0025
Basic Gen level selections						
$p_{\mathrm{T}_1} > 17$ GeV, $\lvert\eta_1\rvert < 0.9$	108063	0.5403 ± 0.0011	0.5403 ± 0.0011	108342	0.5417 ± 0.0011	0.5417 ± 0.0011
$p_{\mathrm{T}_2} > 8$ GeV, $\lvert\eta_2\rvert < 2.4$	102538	0.5127 ± 0.0011	0.9489 ± 0.0007	102787	0.5139 ± 0.0011	0.9487 ± 0.0007
$p_{\mathrm{T}_3} > 8$ GeV, $\lvert\eta_3\rvert < 2.4$	87363	0.4368 ± 0.0011	0.8520 ± 0.0011	87284	0.4364 ± 0.0011	0.8492 ± 0.0011
$p_{\mathrm{T}_4} > 8$ GeV, $\lvert\eta_4\rvert < 2.4$	45674	0.2284 ± 0.0009	0.5228 ± 0.0017	44992	0.2250 ± 0.0009	0.5155 ± 0.0017
$L_{xy} < 9.8$ cm, $L_z < 46.5$ cm	45674	0.2284 ± 0.0009	1.0000 ± 0.0000	44992	0.2250 ± 0.0009	1.0000 ± 0.0000
Online selection						
Trigger	113664	0.5683 ± 0.0011	0.5683 ± 0.0011	112965	0.5648 ± 0.0011	0.5648 ± 0.0023
Basic Reco level selections						
Good primary vertex	113664	0.5683 ± 0.0011	1.0000 ± 0.0000	112965	0.5648 ± 0.0011	1.0000 ± 0.0000
$p_{\mathrm{T}_1} > 17$ GeV, $\lvert\eta_1\rvert < 0.9$	80094	0.4005 ± 0.0011	0.7047 ± 0.0014	79822	0.3991 ± 0.0011	0.7066 ± 0.0014
$p_{\mathrm{T}_2} > 8$ GeV, $\lvert\eta_2\rvert < 2.4$	80076	0.4004 ± 0.0011	0.9998 ± 0.0001	79808	0.3990 ± 0.0011	0.9998 ± 0.0000
$p_{\mathrm{T}_3} > 8$ GeV, $\lvert\eta_3\rvert < 2.4$	78744	0.3937 ± 0.0011	0.9834 ± 0.0005	78459	0.3923 ± 0.0011	0.9831 ± 0.0005
$p_{\mathrm{T}_4} > 8$ GeV, $\lvert\eta_4\rvert < 2.4$	42467	0.2123 ± 0.0009	0.5393 ± 0.0018	41944	0.2097 ± 0.0009	0.5346 ± 0.0018
Extra Reco level selections						
Two muon-jets	36561	0.1828 ± 0.0009	0.8609 ± 0.0017	36118	0.1806 ± 0.0009	0.8611 ± 0.0017
Two dimuons	36535	0.1827 ± 0.0009	0.9993 ± 0.0001	36076	0.1804 ± 0.0009	0.9988 ± 0.0002
Pixel hit requirement	36529	0.1826 ± 0.0009	0.9998 ± 0.0001	36068	0.1803 ± 0.0009	0.9998 ± 0.0001
$\lvert z_{(\mu\mu)_1} - z_{(\mu\mu)_2}\rvert < 0.1$ cm	36493	0.1825 ± 0.0009	0.9990 ± 0.0002	36041	0.1802 ± 0.0009	0.9993 ± 0.0001
$\mathrm{Iso}_{(\mu\mu)_{1,2}} < 2$ GeV	29060	0.1453 ± 0.0008	0.7963 ± 0.0021	28608	0.1430 ± 0.0008	0.7938 ± 0.0021
$m_{(\mu\mu)_1} \approx m_{(\mu\mu)_2}$	28251	0.1413 ± 0.0008	0.9722 ± 0.0010	27522	0.1376 ± 0.0008	0.9620 ± 0.0011
α_{gen}			0.2284 ± 0.0009			0.2250 ± 0.0009
ϵ_{full}			0.1413 ± 0.0008			0.1376 ± 0.0008
$\epsilon_{\mathrm{full}}/\alpha_{\mathrm{gen}}$			0.6185 ± 0.0023			0.6117 ± 0.0023

Table F.13: Acceptances and efficiencies of the event selection for NMSSM benchmark models with $m_h = 150$ GeV and $m_{a_1} = 0.25,\ 0.5$ GeV.

Sample	$m_{h_{1,2}} = 150$ GeV, $m_{a_1} = 0.25$ GeV			$m_{h_{1,2}} = 150$ GeV, $m_{a_1} = 0.5$ GeV		
Selection	Events	Tot. Eff.	Rel. Eff.	Events	Tot. Eff.	Rel. Eff.
All events	200001	1.0000 ± 0.0000	1.0000 ± 0.0000	200001	1.0000 ± 0.0000	1.0000 ± 0.6343
Basic Gen level selections						
$p_{\mathrm{T}_1} > 17$ GeV, $\lvert\eta_1\rvert < 0.9$	112770	0.5638 ± 0.0011	0.5638 ± 0.0011	114310	0.5715 ± 0.0011	0.5715 ± 0.0011
$p_{\mathrm{T}_2} > 8$ GeV, $\lvert\eta_2\rvert < 2.4$	112162	0.5608 ± 0.0011	0.9946 ± 0.0002	109658	0.5483 ± 0.0011	0.9593 ± 0.0006
$p_{\mathrm{T}_3} > 8$ GeV, $\lvert\eta_3\rvert < 2.4$	100458	0.5023 ± 0.0011	0.8957 ± 0.0009	97405	0.4870 ± 0.0011	0.8883 ± 0.0010
$p_{\mathrm{T}_4} > 8$ GeV, $\lvert\eta_4\rvert < 2.4$	98493	0.4925 ± 0.0011	0.9804 ± 0.0004	66806	0.3340 ± 0.0011	0.6859 ± 0.0015
$L_{xy} < 9.8$ cm, $L_z < 46.5$ cm	98493	0.4925 ± 0.0011	1.0000 ± 0.0000	66806	0.3340 ± 0.0011	1.0000 ± 0.0000
Online selection						
Trigger	130811	0.6541 ± 0.0011	0.6541 ± 0.0011	127017	0.6351 ± 0.0011	0.6351 ± 0.0011
Basic Reco level selections						
Good primary vertex	130811	0.6541 ± 0.0011	1.0000 ± 0.0000	127017	0.6351 ± 0.0011	1.0000 ± 0.0000
$p_{\mathrm{T}_1} > 17$ GeV, $\lvert\eta_1\rvert < 0.9$	92628	0.4631 ± 0.0011	0.7081 ± 0.0013	90404	0.4520 ± 0.0011	0.7117 ± 0.0013
$p_{\mathrm{T}_2} > 8$ GeV, $\lvert\eta_2\rvert < 2.4$	92587	0.4629 ± 0.0011	0.9996 ± 0.0001	90372	0.4519 ± 0.0011	0.9996 ± 0.0001
$p_{\mathrm{T}_3} > 8$ GeV, $\lvert\eta_3\rvert < 2.4$	91468	0.4573 ± 0.0011	0.9879 ± 0.0004	88985	0.4449 ± 0.0011	0.9847 ± 0.0004
$p_{\mathrm{T}_4} > 8$ GeV, $\lvert\eta_4\rvert < 2.4$	77555	0.3878 ± 0.0011	0.8479 ± 0.0012	60339	0.3017 ± 0.0010	0.6781 ± 0.0016
Extra Reco level selections						
Two muon-jets	75263	0.3763 ± 0.0011	0.9704 ± 0.0006	52861	0.2643 ± 0.0010	0.8761 ± 0.6170
Two dimuons	75225	0.3761 ± 0.0011	0.9995 ± 0.0001	52838	0.2642 ± 0.0010	0.9996 ± 0.0001
Pixel hit requirement	74146	0.3707 ± 0.0011	0.9857 ± 0.0004	52754	0.2638 ± 0.0010	0.9984 ± 0.0002
$\lvert z_{(\mu\mu)_1} - z_{(\mu\mu)_2}\rvert < 0.1$ cm	73706	0.3685 ± 0.0011	0.9941 ± 0.0003	52474	0.2624 ± 0.0010	0.9947 ± 0.0003
$\mathrm{Iso}_{(\mu\mu)_{1,2}} < 2$ GeV	58710	0.2935 ± 0.0010	0.7965 ± 0.0015	41458	0.2073 ± 0.0009	0.7901 ± 0.0018
$m_{(\mu\mu)_1} \approx m_{(\mu\mu)_2}$	58218	0.2911 ± 0.0010	0.9916 ± 0.0004	41216	0.2061 ± 0.0009	0.9942 ± 0.0004
α_{gen}			0.4925 ± 0.0011			0.3340 ± 0.0011
ϵ_{full}			0.2911 ± 0.0010			0.2061 ± 0.0009
$\epsilon_{\mathrm{full}}/\alpha_{\mathrm{gen}}$			0.5911 ± 0.0016			0.6170 ± 0.0019

Table F.14: Acceptances and efficiencies of the event selection for NMSSM benchmark models with $m_h = 150$ GeV and $m_{a_1} = 0.75,\ 1$ GeV.

Sample	$m_{h_{1,2}} = 150$ GeV, $m_{a_1} = 0.75$ GeV			$m_{h_{1,2}} = 150$ GeV, $m_{a_1} = 1$ GeV		
Selection	Events	Tot. Eff.	Rel. Eff.	Events	Tot. Eff.	Rel. Eff.
All events	200001	1.0000 ± 0.0000	1.0000 ± 0.0000	200001	1.0000 ± 0.0000	1.0000 ± 0.0000
Basic Gen level selections						
$p_{\mathrm{T}_1} > 17$ GeV, $\lvert\eta_1\rvert < 0.9$	114774	0.5739 ± 0.0011	0.5739 ± 0.0011	114733	0.5737 ± 0.0011	0.5737 ± 0.0011
$p_{\mathrm{T}_2} > 8$ GeV, $\lvert\eta_2\rvert < 2.4$	109455	0.5473 ± 0.0011	0.9537 ± 0.0006	109226	0.5461 ± 0.0011	0.9520 ± 0.0006
$p_{\mathrm{T}_3} > 8$ GeV, $\lvert\eta_3\rvert < 2.4$	96123	0.4806 ± 0.0011	0.8782 ± 0.0010	95293	0.4765 ± 0.0011	0.8724 ± 0.0010
$p_{\mathrm{T}_4} > 8$ GeV, $\lvert\eta_4\rvert < 2.4$	59862	0.2993 ± 0.0010	0.6228 ± 0.0016	57543	0.2877 ± 0.0010	0.6039 ± 0.0016
$L_{xy} < 9.8$ cm, $L_z < 46.5$ cm	59862	0.2993 ± 0.0010	1.0000 ± 0.0000	57543	0.2877 ± 0.0010	1.0000 ± 0.0000
Online selection						
Trigger	124129	0.6206 ± 0.0011	0.6206 ± 0.0011	123291	0.6165 ± 0.0011	0.6165 ± 0.0011
Basic Reco level selections						
Good primary vertex	124129	0.6206 ± 0.0011	1.0000 ± 0.0000	123291	0.6165 ± 0.0011	1.0000 ± 0.0000
$p_{\mathrm{T}_1} > 17$ GeV, $\lvert\eta_1\rvert < 0.9$	88901	0.4445 ± 0.0011	0.7162 ± 0.0013	87923	0.4396 ± 0.0011	0.7131 ± 0.0013
$p_{\mathrm{T}_2} > 8$ GeV, $\lvert\eta_2\rvert < 2.4$	88877	0.4444 ± 0.0011	0.9997 ± 0.0001	87898	0.4395 ± 0.0011	0.9997 ± 0.0001
$p_{\mathrm{T}_3} > 8$ GeV, $\lvert\eta_3\rvert < 2.4$	87477	0.4374 ± 0.0011	0.9842 ± 0.0004	86494	0.4325 ± 0.0011	0.9840 ± 0.0004
$p_{\mathrm{T}_4} > 8$ GeV, $\lvert\eta_4\rvert < 2.4$	54653	0.2733 ± 0.0010	0.6248 ± 0.0016	52475	0.2624 ± 0.0010	0.6067 ± 0.0017
Extra Reco level selections						
Two muon-jets	47372	0.2369 ± 0.0010	0.8668 ± 0.0015	45254	0.2263 ± 0.0009	0.8624 ± 0.0015
Two dimuons	47344	0.2367 ± 0.0010	0.9994 ± 0.0001	45229	0.2261 ± 0.0009	0.9994 ± 0.0001
Pixel hit requirement	47309	0.2365 ± 0.0010	0.9993 ± 0.0001	45209	0.2260 ± 0.0009	0.9996 ± 0.0001
$\lvert z_{(\mu\mu)_1} - z_{(\mu\mu)_2}\rvert < 0.1$ cm	47159	0.2358 ± 0.0009	0.9968 ± 0.0003	45108	0.2255 ± 0.0009	0.9978 ± 0.0002
$\mathrm{Iso}_{(\mu\mu)_{1,2}} < 2$ GeV	37329	0.1866 ± 0.0009	0.7916 ± 0.0019	35730	0.1787 ± 0.0009	0.7921 ± 0.0019
$m_{(\mu\mu)_1} \approx m_{(\mu\mu)_2}$	36951	0.1848 ± 0.0009	0.9899 ± 0.0005	35147	0.1757 ± 0.0009	0.9837 ± 0.0007
α_{gen}			0.2993 ± 0.0010			0.2877 ± 0.0010
ϵ_{full}			0.1848 ± 0.0009			0.1757 ± 0.0009
$\epsilon_{\mathrm{full}}/\alpha_{\mathrm{gen}}$			0.6173 ± 0.0020			0.6108 ± 0.0020

Table F.15: Acceptances and efficiencies of the event selection for NMSSM benchmark models with $m_h = 150$ GeV and $m_{a_1} = 2,\ 3$ GeV.

Sample	$m_{h_{1,2}} = 150$ GeV, $m_{a_1} = 2$ GeV			$m_{h_{1,2}} = 150$ GeV, $m_{a_1} = 3$ GeV		
Selection	Events	Tot. Eff.	Rel. Eff.	Events	Tot. Eff.	Rel. Eff.
All events	200001	1.0000 ± 0.0000	1.0000 ± 0.0000	199066	1.0000 ± 0.0000	1.0000 ± 0.0000
Basic Gen level selections						
$p_{\mathrm{T}_1} > 17$ GeV, $\lvert\eta_1\rvert < 0.9$	115039	0.5752 ± 0.0011	0.5752 ± 0.0011	114421	0.5748 ± 0.0011	0.5748 ± 0.0011
$p_{\mathrm{T}_2} > 8$ GeV, $\lvert\eta_2\rvert < 2.4$	109461	0.5473 ± 0.0011	0.9515 ± 0.0006	108903	0.5471 ± 0.0011	0.9518 ± 0.0006
$p_{\mathrm{T}_3} > 8$ GeV, $\lvert\eta_3\rvert < 2.4$	94815	0.4741 ± 0.0011	0.8662 ± 0.0010	94412	0.4743 ± 0.0011	0.8669 ± 0.0010
$p_{\mathrm{T}_4} > 8$ GeV, $\lvert\eta_4\rvert < 2.4$	55447	0.2772 ± 0.0010	0.5848 ± 0.0016	54660	0.2746 ± 0.0010	0.5790 ± 0.0016
$L_{xy} < 9.8$ cm, $L_z < 46.5$ cm	55447	0.2772 ± 0.0010	1.0000 ± 0.0000	54660	0.2746 ± 0.0010	1.0000 ± 0.0000
Online selection						
Trigger	121653	0.6083 ± 0.0011	0.6083 ± 0.0011	120156	0.6036 ± 0.0011	0.6036 ± 0.0011
Basic Reco level selections						
Good primary vertex	121653	0.6083 ± 0.0011	1.0000 ± 0.0000	120156	0.6036 ± 0.0011	1.0000 ± 0.0000
$p_{\mathrm{T}_1} > 17$ GeV, $\lvert\eta_1\rvert < 0.9$	87463	0.4373 ± 0.0011	0.7190 ± 0.0013	86651	0.4353 ± 0.0011	0.7212 ± 0.0013
$p_{\mathrm{T}_2} > 8$ GeV, $\lvert\eta_2\rvert < 2.4$	87446	0.4372 ± 0.0011	0.9998 ± 0.0000	86636	0.4352 ± 0.0011	0.9998 ± 0.0000
$p_{\mathrm{T}_3} > 8$ GeV, $\lvert\eta_3\rvert < 2.4$	86106	0.4305 ± 0.0011	0.9847 ± 0.0004	85371	0.4289 ± 0.0011	0.9854 ± 0.0004
$p_{\mathrm{T}_4} > 8$ GeV, $\lvert\eta_4\rvert < 2.4$	51202	0.2560 ± 0.0010	0.5946 ± 0.0017	50640	0.2544 ± 0.0010	0.5932 ± 0.0017
Extra Reco level selections						
Two muon-jets	44103	0.2205 ± 0.0009	0.8614 ± 0.0015	43657	0.2193 ± 0.0009	0.8621 ± 0.0015
Two dimuons	44063	0.2203 ± 0.0009	0.9991 ± 0.0001	43612	0.2191 ± 0.0009	0.9990 ± 0.0002
Pixel hit requirement	44050	0.2202 ± 0.0009	0.9997 ± 0.0001	43605	0.2190 ± 0.0009	0.9998 ± 0.0001
$\lvert z_{(\mu\mu)_1} - z_{(\mu\mu)_2}\rvert < 0.1$ cm	44008	0.2200 ± 0.0009	0.9990 ± 0.0001	43555	0.2188 ± 0.0009	0.9989 ± 0.0002
$\mathrm{Iso}_{(\mu\mu)_{1,2}} < 2$ GeV	34723	0.1736 ± 0.0008	0.7890 ± 0.0019	34217	0.1719 ± 0.0008	0.7856 ± 0.0020
$m_{(\mu\mu)_1} \approx m_{(\mu\mu)_2}$	33696	0.1685 ± 0.0008	0.9704 ± 0.0009	32919	0.1654 ± 0.0008	0.9621 ± 0.0010
α_{gen}			0.2772 ± 0.0010			0.2746 ± 0.0010
ϵ_{full}			0.1685 ± 0.0008			0.1654 ± 0.0008
$\epsilon_{\mathrm{full}}/\alpha_{\mathrm{gen}}$			0.6077 ± 0.0021			0.6023 ± 0.0021

Table G.1: Acceptances and efficiencies of the event selection for MSSMD benchmark models with $m_{\gamma_D} = 0.25$ GeV and $c\tau_{\gamma_D} = 0,\ 0.05$ mm.

Sample	$m_{\gamma_D} = 0.25$ GeV, $c\tau_{\gamma_D} = 0$ mm			$m_{\gamma_D} = 0.25$ GeV, $c\tau_{\gamma_D} = 0.05$ mm		
Selection	Events	Tot. Eff. [%]	Rel. Eff.	Events	Tot. Eff.	Rel. Eff.
All events	19400	1.0000 ± 0.0000	1.0000 ± 0.0000	19200	1.0000 ± 0.0000	1.0000 ± 0.0000
Basic Gen level selections						
$p_{\mathrm{T}_1} > 17$ GeV, $\lvert\eta_1\rvert < 0.9$	6160	0.3175 ± 0.0033	0.3175 ± 0.0033	6092	0.3173 ± 0.0034	0.3173 ± 0.0034
$p_{\mathrm{T}_2} > 8$ GeV, $\lvert\eta_2\rvert < 2.4$	6041	0.3114 ± 0.0033	0.9807 ± 0.0018	5951	0.3099 ± 0.0033	0.9769 ± 0.0019
$p_{\mathrm{T}_3} > 8$ GeV, $\lvert\eta_3\rvert < 2.4$	4024	0.2074 ± 0.0029	0.6661 ± 0.0061	3995	0.2081 ± 0.0029	0.6713 ± 0.0061
$p_{\mathrm{T}_4} > 8$ GeV, $\lvert\eta_4\rvert < 2.4$	2622	0.1352 ± 0.0025	0.6516 ± 0.0075	2666	0.1389 ± 0.0025	0.6673 ± 0.0075
$L_{xy} < 9.8$ cm, $L_z < 46.5$ cm	2622	0.1352 ± 0.0025	1.0000 ± 0.0000	2654	0.1382 ± 0.0025	0.9955 ± 0.0013
Online selection						
Trigger	6065	0.3126 ± 0.0033	0.3126 ± 0.0033	5907	0.3077 ± 0.0033	0.3077 ± 0.0033
Basic Reco level selections						
Good primary vertex	6065	0.3126 ± 0.0033	1.0000 ± 0.0000	5907	0.3077 ± 0.0033	1.0000 ± 0.0000
$p_{\mathrm{T}_1} > 17$ GeV, $\lvert\eta_1\rvert < 0.9$	3600	0.1856 ± 0.0028	0.5936 ± 0.0063	3559	0.1854 ± 0.0028	0.6025 ± 0.0064
$p_{\mathrm{T}_2} > 8$ GeV, $\lvert\eta_2\rvert < 2.4$	3598	0.1855 ± 0.0028	0.9994 ± 0.0004	3554	0.1851 ± 0.0028	0.9986 ± 0.0006
$p_{\mathrm{T}_3} > 8$ GeV, $\lvert\eta_3\rvert < 2.4$	3490	0.1799 ± 0.0028	0.9700 ± 0.0028	3436	0.1790 ± 0.0028	0.9668 ± 0.0030
$p_{\mathrm{T}_4} > 8$ GeV, $\lvert\eta_4\rvert < 2.4$	2302	0.1187 ± 0.0023	0.6596 ± 0.0080	2300	0.1198 ± 0.0023	0.6694 ± 0.0080
Extra Reco level selections						
Two muon-jets	2221	0.1145 ± 0.0023	0.9648 ± 0.0038	2199	0.1145 ± 0.0023	0.9561 ± 0.0043
Two dimuons	2221	0.1145 ± 0.0023	1.0000 ± 0.0000	2197	0.1144 ± 0.0023	0.9991 ± 0.0006
Pixel hit requirement	2206	0.1137 ± 0.0023	0.9932 ± 0.0017	2171	0.1131 ± 0.0023	0.9882 ± 0.0023
$\lvert z_{(\mu\mu)_1} - z_{(\mu\mu)_2}\rvert < 0.1$ cm	2196	0.1132 ± 0.0023	0.9955 ± 0.0014	2159	0.1124 ± 0.0023	0.9945 ± 0.0016
$\mathrm{Iso}_{(\mu\mu)_{1,2}} < 2$ GeV	1772	0.0913 ± 0.0021	0.8069 ± 0.0084	1751	0.0912 ± 0.0021	0.8110 ± 0.0084
$m_{(\mu\mu)_1} \approx m_{(\mu\mu)_2}$	1769	0.0912 ± 0.0021	0.9983 ± 0.0010	1748	0.0910 ± 0.0021	0.9983 ± 0.0010
α_{gen}			0.1352 ± 0.0025			0.1382 ± 0.0025
ϵ_{full}			0.0912 ± 0.0021			0.0910 ± 0.0021
$\epsilon_{\mathrm{full}}/\alpha_{\mathrm{gen}}$			0.6747 ± 0.0091			0.6586 ± 0.0092

Table G.2: Acceptances and efficiencies of the event selection for MSSMD benchmark models with $m_{\gamma_D} = 0.25$ GeV and $c\tau_{\gamma_D} = 0.1,\ 0.5$ mm.

Sample	$m_{\gamma_D} = 0.25$ GeV, $c\tau_{\gamma_D} = 0.1$ mm			$m_{\gamma_D} = 0.25$ GeV, $c\tau_{\gamma_D} = 0.5$ mm		
Selection	Events	Tot. Eff.	Rel. Eff.	Events	Tot. Eff.	Rel. Eff.
All events	97900	1.0000 ± 0.0000	1.0000 ± 0.0000	98100	1.0000 ± 0.0000	1.0000 ± 0.0000
Basic Gen level selections						
$p_{T_1} > 17$ GeV, $\lvert\eta_1\rvert < 0.9$	31178	0.3185 ± 0.0015	0.3185 ± 0.0015	31515	0.3213 ± 0.0015	0.3213 ± 0.0015
$p_{T_2} > 8$ GeV, $\lvert\eta_2\rvert < 2.4$	30501	0.3116 ± 0.0015	0.9783 ± 0.0008	30851	0.3145 ± 0.0015	0.9789 ± 0.0008
$p_{T_3} > 8$ GeV, $\lvert\eta_3\rvert < 2.4$	20407	0.2084 ± 0.0013	0.6691 ± 0.0027	20480	0.2088 ± 0.0013	0.6638 ± 0.0027
$p_{T_4} > 8$ GeV, $\lvert\eta_4\rvert < 2.4$	13707	0.1400 ± 0.0011	0.6717 ± 0.0033	13706	0.1397 ± 0.0011	0.6692 ± 0.0033
$L_{xy} < 9.8$ cm, $L_z < 46.5$ cm	13318	0.1360 ± 0.0011	0.9716 ± 0.0014	6337	0.0646 ± 0.0008	0.4624 ± 0.0043
Online selection						
Trigger	30167	0.3081 ± 0.0015	0.3081 ± 0.0015	27942	0.2848 ± 0.0014	0.2848 ± 0.0014
Basic Reco level selections						
Good primary vertex	30167	0.3081 ± 0.0015	1.0000 ± 0.0000	27942	0.2848 ± 0.0014	1.0000 ± 0.0000
$p_{T_1} > 17$ GeV, $\lvert\eta_1\rvert < 0.9$	18104	0.1849 ± 0.0012	0.6001 ± 0.0028	16999	0.1733 ± 0.0012	0.6084 ± 0.0029
$p_{T_2} > 8$ GeV, $\lvert\eta_2\rvert < 2.4$	18086	0.1847 ± 0.0012	0.9990 ± 0.0002	16943	0.1727 ± 0.0012	0.9967 ± 0.0004
$p_{T_3} > 8$ GeV, $\lvert\eta_3\rvert < 2.4$	17466	0.1784 ± 0.0012	0.9657 ± 0.0014	15885	0.1619 ± 0.0012	0.9376 ± 0.0019
$p_{T_4} > 8$ GeV, $\lvert\eta_4\rvert < 2.4$	11458	0.1170 ± 0.0010	0.6560 ± 0.0036	9510	0.0969 ± 0.0009	0.5987 ± 0.0039
Extra Reco level selections						
Two muon-jets	10877	0.1111 ± 0.0010	0.9493 ± 0.0020	7939	0.0809 ± 0.0009	0.8348 ± 0.0038
Two dimuons	10872	0.1111 ± 0.0010	0.9995 ± 0.0002	7937	0.0809 ± 0.0009	0.9997 ± 0.0002
Pixel hit requirement	10609	0.1084 ± 0.0010	0.9758 ± 0.0015	5029	0.0513 ± 0.0007	0.6336 ± 0.0054
$\lvert z_{(\mu\mu)_1} - z_{(\mu\mu)_2}\rvert < 0.1$ cm	10569	0.1080 ± 0.0010	0.9962 ± 0.0006	4911	0.0501 ± 0.0007	0.9765 ± 0.0021
$\mathrm{Iso}_{(\mu\mu)_{1,2}} < 2$ GeV	8368	0.0855 ± 0.0009	0.7917 ± 0.0039	3908	0.0398 ± 0.0006	0.7958 ± 0.0058
$m_{(\mu\mu)_1} \approx m_{(\mu\mu)_2}$	8357	0.0854 ± 0.0009	0.9987 ± 0.0004	3901	0.0398 ± 0.0006	0.9982 ± 0.0007
α_{gen}			0.1360 ± 0.0011			0.0646 ± 0.0008
ϵ_{full}			0.0854 ± 0.0009			0.0398 ± 0.0006
$\epsilon_{\mathrm{full}}/\alpha_{\mathrm{gen}}$			0.6275 ± 0.0042			0.6156 ± 0.0061

Table G.3: Acceptances and efficiencies of the event selection for MSSMD benchmark models with $m_{\gamma_D} = 0.25$ GeV and $c\tau_{\gamma_D} = 1,\ 2$ mm.

Sample	$m_{\gamma_D} = 0.25$ GeV, $c\tau_{\gamma_D} = 1$ mm			$m_{\gamma_D} = 0.25$ GeV, $c\tau_{\gamma_D} = 2$ mm		
Selection	Events	Tot. Eff.	Rel. Eff.	Events	Tot. Eff.	Rel. Eff.
All events	52100	1.0000 ± 0.0000	1.0000 ± 0.0000	294400	1.0000 ± 0.0000	1.0000 ± 0.0000
Basic Gen level selections						
$p_{T_1} > 17$ GeV, $\lvert\eta_1\rvert < 0.9$	16812	0.3227 ± 0.0020	0.3227 ± 0.0020	94481	0.3209 ± 0.0009	0.3209 ± 0.0009
$p_{T_2} > 8$ GeV, $\lvert\eta_2\rvert < 2.4$	16475	0.3162 ± 0.0020	0.9800 ± 0.0011	92452	0.3140 ± 0.0009	0.9785 ± 0.0005
$p_{T_3} > 8$ GeV, $\lvert\eta_3\rvert < 2.4$	11017	0.2115 ± 0.0018	0.6687 ± 0.0037	61569	0.2091 ± 0.0007	0.6660 ± 0.0016
$p_{T_4} > 8$ GeV, $\lvert\eta_4\rvert < 2.4$	7368	0.1414 ± 0.0015	0.6688 ± 0.0045	41465	0.1408 ± 0.0006	0.6735 ± 0.0019
$L_{xy} < 9.8$ cm, $L_z < 46.5$ cm	1484	0.0285 ± 0.0007	0.2014 ± 0.0047	2836	0.0096 ± 0.0002	0.0684 ± 0.0012
Online selection						
Trigger	13354	0.2563 ± 0.0019	0.2563 ± 0.0019	57950	0.1968 ± 0.0007	0.1968 ± 0.0007
Basic Reco level selections						
Good primary vertex	13354	0.2563 ± 0.0019	1.0000 ± 0.0000	57950	0.1968 ± 0.0007	1.0000 ± 0.0000
$p_{T_1} > 17$ GeV, $\lvert\eta_1\rvert < 0.9$	8082	0.1551 ± 0.0016	0.6052 ± 0.0042	33811	0.1148 ± 0.0006	0.5835 ± 0.0020
$p_{T_2} > 8$ GeV, $\lvert\eta_2\rvert < 2.4$	8013	0.1538 ± 0.0016	0.9915 ± 0.0010	33171	0.1127 ± 0.0006	0.9811 ± 0.0007
$p_{T_3} > 8$ GeV, $\lvert\eta_3\rvert < 2.4$	7264	0.1394 ± 0.0015	0.9065 ± 0.0033	27852	0.0946 ± 0.0005	0.8396 ± 0.0020
$p_{T_4} > 8$ GeV, $\lvert\eta_4\rvert < 2.4$	3845	0.0738 ± 0.0011	0.5293 ± 0.0059	13057	0.0444 ± 0.0004	0.4688 ± 0.0030
Extra Reco level selections						
Two muon-jets	2891	0.0555 ± 0.0010	0.7519 ± 0.0070	8798	0.0299 ± 0.0003	0.6738 ± 0.0041
Two dimuons	2889	0.0555 ± 0.0010	0.9993 ± 0.0005	8794	0.0299 ± 0.0003	0.9995 ± 0.0002
Pixel hit requirement	1188	0.0228 ± 0.0007	0.4112 ± 0.0092	2501	0.0085 ± 0.0002	0.2844 ± 0.0048
$\lvert z_{(\mu\mu)_1} - z_{(\mu\mu)_2}\rvert < 0.1$ cm	1114	0.0214 ± 0.0006	0.9377 ± 0.0070	2303	0.0078 ± 0.0002	0.9208 ± 0.0054
$\text{Iso}_{(\mu\mu)_{1,2}} < 2$ GeV	894	0.0172 ± 0.0006	0.8025 ± 0.0119	1864	0.0063 ± 0.0001	0.8094 ± 0.0082
$m_{(\mu\mu)_1} \approx m_{(\mu\mu)_2}$	894	0.0172 ± 0.0006	1.0000 ± 0.0000	1862	0.0063 ± 0.0001	0.9989 ± 0.0008
α_{gen}			0.0285 ± 0.0007			0.0096 ± 0.0002
ϵ_{full}			0.0172 ± 0.0006			0.0063 ± 0.0001
$\epsilon_{\text{full}}/\alpha_{\text{gen}}$			0.6024 ± 0.0127			0.6566 ± 0.0089

Table G.4: Acceptances and efficiencies of the event selection for MSSMD benchmark models with $m_{\gamma_D} = 0.25$ GeV and $c\tau_{\gamma_D} = 5,\ 20$ mm.

Sample	$m_{\gamma_D} = 0.25$ GeV, $c\tau_{\gamma_D} = 5$ mm			$m_{\gamma_D} = 0.25$ GeV, $c\tau_{\gamma_D} = 20$ mm		
Selection	Events	Tot. Eff.	Rel. Eff.	Events	Tot. Eff.	Rel. Eff.
All events	295800	1.0000 ± 0.0000	1.0000 ± 0.0000	1155200	1.0000 ± 0.0000	1.0000 ± 0.0000
Basic Gen level selections						
$p_{T_1} > 17$ GeV, $\lvert\eta_1\rvert < 0.9$	94753	0.3203 ± 0.0009	0.3203 ± 0.0009	370951	0.3211 ± 0.0004	0.3211 ± 0.0004
$p_{T_2} > 8$ GeV, $\lvert\eta_2\rvert < 2.4$	92786	0.3137 ± 0.0009	0.9792 ± 0.0005	362825	0.3141 ± 0.0004	0.9781 ± 0.0002
$p_{T_3} > 8$ GeV, $\lvert\eta_3\rvert < 2.4$	61945	0.2094 ± 0.0007	0.6676 ± 0.0015	242335	0.2098 ± 0.0004	0.6679 ± 0.0008
$p_{T_4} > 8$ GeV, $\lvert\eta_4\rvert < 2.4$	41630	0.1407 ± 0.0006	0.6720 ± 0.0019	162845	0.1410 ± 0.0003	0.6720 ± 0.0010
$L_{xy} < 9.8$ cm, $L_z < 46.5$ cm	584	0.0020 ± 0.0001	0.0140 ± 0.0006	154	0.0001 ± 0.0000	0.0009 ± 0.0001
Online selection						
Trigger	28502	0.0964 ± 0.0005	0.0964 ± 0.0005	19886	0.0172 ± 0.0001	0.0172 ± 0.0001
Basic Reco level selections						
Good primary vertex	28502	0.0964 ± 0.0005	1.0000 ± 0.0000	19886	0.0172 ± 0.0001	1.0000 ± 0.0000
$p_{T_1} > 17$ GeV, $\lvert\eta_1\rvert < 0.9$	15563	0.0526 ± 0.0004	0.5460 ± 0.0029	10155	0.0088 ± 0.0001	0.5107 ± 0.0035
$p_{T_2} > 8$ GeV, $\lvert\eta_2\rvert < 2.4$	14877	0.0503 ± 0.0004	0.9559 ± 0.0016	9167	0.0079 ± 0.0001	0.9027 ± 0.0029
$p_{T_3} > 8$ GeV, $\lvert\eta_3\rvert < 2.4$	10851	0.0367 ± 0.0003	0.7294 ± 0.0036	5044	0.0044 ± 0.0001	0.5502 ± 0.0052
$p_{T_4} > 8$ GeV, $\lvert\eta_4\rvert < 2.4$	4240	0.0143 ± 0.0002	0.3907 ± 0.0047	1640	0.0014 ± 0.0000	0.3251 ± 0.0066
Extra Reco level selections						
Two muon-jets	2591	0.0088 ± 0.0002	0.6111 ± 0.0075	947	0.0008 ± 0.0000	0.5774 ± 0.0122
Two dimuons	2588	0.0087 ± 0.0002	0.9988 ± 0.0007	947	0.0008 ± 0.0000	1.0000 ± 0.0000
Pixel hit requirement	493	0.0017 ± 0.0001	0.1905 ± 0.0077	138	0.0001 ± 0.0000	0.1457 ± 0.0115
$\lvert z_{(\mu\mu)_1} - z_{(\mu\mu)_2}\rvert < 0.1$ cm	443	0.0015 ± 0.0001	0.8986 ± 0.0136	119	0.0001 ± 0.0000	0.8623 ± 0.0293
$\mathrm{Iso}_{(\mu\mu)_{1,2}} < 2$ GeV	341	0.0012 ± 0.0001	0.7698 ± 0.0200	90	0.0001 ± 0.0000	0.7563 ± 0.0394
$m_{(\mu\mu)_1} \approx m_{(\mu\mu)_2}$	341	0.0012 ± 0.0001	1.0000 ± 0.0000	90	0.0001 ± 0.0000	1.0000 ± 0.0000
α_{gen}			0.0020 ± 0.0001			0.0001 ± 0.0000
ϵ_{full}			0.0012 ± 0.0001			0.0001 ± 0.0000
$\epsilon_{\mathrm{full}}/\alpha_{\mathrm{gen}}$			0.5839 ± 0.0204			0.5844 ± 0.0397

Table G.5: Acceptances and efficiencies of the event selection for MSSMD benchmark models with $m_{\gamma_D} = 0.25$ GeV, $c\tau_{\gamma_D} = 100$ mm and $m_{\gamma_D} = 0.4$ GeV, $c\tau_{\gamma_D} = 0$ mm

Sample	$m_{\gamma_D} = 0.25$ GeV, $c\tau_{\gamma_D} = 100$ mm			$m_{\gamma_D} = 0.4$ GeV, $c\tau_{\gamma_D} = 0$ mm		
Selection	Events	Tot. Eff.	Rel. Eff.	Events	Tot. Eff.	Rel. Eff.
All events	1048700	1.0000 ± 0.0000	1.0000 ± 0.0000	97900	1.0000 ± 0.0000	1.0000 ± 0.0000
Basic Gen level selections						
$p_{\mathrm{T}_1} > 17$ GeV, $\lvert\eta_1\rvert < 0.9$	336474	0.3208 ± 0.0005	0.3208 ± 0.0005	32982	0.3369 ± 0.0015	0.3369 ± 0.0015
$p_{\mathrm{T}_2} > 8$ GeV, $\lvert\eta_2\rvert < 2.4$	329123	0.3138 ± 0.0005	0.9782 ± 0.0003	30417	0.3107 ± 0.0015	0.9222 ± 0.0015
$p_{\mathrm{T}_3} > 8$ GeV, $\lvert\eta_3\rvert < 2.4$	219579	0.2094 ± 0.0004	0.6672 ± 0.0008	20088	0.2052 ± 0.0013	0.6604 ± 0.0027
$p_{\mathrm{T}_4} > 8$ GeV, $\lvert\eta_4\rvert < 2.4$	147387	0.1405 ± 0.0003	0.6712 ± 0.0010	9614	0.0982 ± 0.0010	0.4786 ± 0.0035
$L_{xy} < 9.8$ cm, $L_z < 46.5$ cm	4	0.0000 ± 0.0000	0.0000 ± 0.0000	9614	0.0982 ± 0.0010	1.0000 ± 0.0000
Online selection						
Trigger	1428	0.0014 ± 0.0000	0.0014 ± 0.0000	30092	0.3074 ± 0.0015	0.3074 ± 0.0015
Basic Reco level selections						
Good primary vertex	1428	0.0014 ± 0.0000	1.0000 ± 0.0000	30092	0.3074 ± 0.0015	1.0000 ± 0.0000
$p_{\mathrm{T}_1} > 17$ GeV, $\lvert\eta_1\rvert < 0.9$	671	0.0006 ± 0.0000	0.4699 ± 0.0132	18419	0.1881 ± 0.0012	0.6121 ± 0.0028
$p_{\mathrm{T}_2} > 8$ GeV, $\lvert\eta_2\rvert < 2.4$	598	0.0006 ± 0.0000	0.8912 ± 0.0120	18406	0.1880 ± 0.0012	0.9993 ± 0.0002
$p_{\mathrm{T}_3} > 8$ GeV, $\lvert\eta_3\rvert < 2.4$	272	0.0003 ± 0.0000	0.4548 ± 0.0204	17841	0.1822 ± 0.0012	0.9693 ± 0.0013
$p_{\mathrm{T}_4} > 8$ GeV, $\lvert\eta_4\rvert < 2.4$	76	0.0001 ± 0.0000	0.2794 ± 0.0272	8975	0.0917 ± 0.0009	0.5031 ± 0.0037
Extra Reco level selections						
Two muon-jets	39	0.0000 ± 0.0000	0.5132 ± 0.0573	8034	0.0821 ± 0.0009	0.8952 ± 0.0032
Two dimuons	39	0.0000 ± 0.0000	1.0000 ± 0.0000	8030	0.0820 ± 0.0009	0.9995 ± 0.0002
Pixel hit requirement	5	0.0000 ± 0.0000	0.1282 ± 0.0535	8022	0.0819 ± 0.0009	0.9990 ± 0.0004
$\lvert z_{(\mu\mu)_1} - z_{(\mu\mu)_2}\rvert < 0.1$ cm	3	0.0000 ± 0.0000	0.6000 ± 0.2191	8002	0.0817 ± 0.0009	0.9975 ± 0.0006
$\mathrm{Iso}_{(\mu\mu)_{1,2}} < 2$ GeV	1	0.0000 ± 0.0000	0.3333 ± 0.2722	6331	0.0647 ± 0.0008	0.7912 ± 0.0045
$m_{(\mu\mu)_1} \approx m_{(\mu\mu)_2}$	1	0.0000 ± 0.0000	1.0000 ± 0.0000	6320	0.0646 ± 0.0008	0.9983 ± 0.0005
α_{gen}			0.0000 ± 0.0000			0.0982 ± 0.0010
ϵ_{full}			0.0000 ± 0.0000			0.0646 ± 0.0008
$\epsilon_{\mathrm{full}}/\alpha_{\mathrm{gen}}$			0.2500 ± 0.2165			0.6574 ± 0.0048

Table G.6: Acceptances and efficiencies of the event selection for MSSMD benchmark models with $m_{\gamma_D} = 0.4$ GeV and $c\tau_{\gamma_D} = 0.5,\ 1$ mm.

Sample	$m_{\gamma_D} = 0.4$ GeV, $c\tau_{\gamma_D} = 0.5$ mm			$m_{\gamma_D} = 0.4$ GeV, $c\tau_{\gamma_D} = 1$ mm		
Selection	Events	Tot. Eff.	Rel. Eff.	Events	Tot. Eff.	Rel. Eff.
All events	98800	1.0000 ± 0.0000	1.0000 ± 0.0000	281600	1.0000 ± 0.0000	1.0000 ± 0.0000
Basic Gen level selections						
$p_{T_1} > 17$ GeV, $\lvert\eta_1\rvert < 0.9$	33187	0.3359 ± 0.0015	0.3359 ± 0.0015	95487	0.3391 ± 0.0009	0.3391 ± 0.0009
$p_{T_2} > 8$ GeV, $\lvert\eta_2\rvert < 2.4$	30495	0.3087 ± 0.0015	0.9189 ± 0.0015	87803	0.3118 ± 0.0009	0.9195 ± 0.0009
$p_{T_3} > 8$ GeV, $\lvert\eta_3\rvert < 2.4$	20221	0.2047 ± 0.0013	0.6631 ± 0.0027	58189	0.2066 ± 0.0008	0.6627 ± 0.0016
$p_{T_4} > 8$ GeV, $\lvert\eta_4\rvert < 2.4$	9572	0.0969 ± 0.0009	0.4734 ± 0.0035	27587	0.0980 ± 0.0006	0.4741 ± 0.0021
$L_{xy} < 9.8$ cm, $L_z < 46.5$ cm	6381	0.0646 ± 0.0008	0.6666 ± 0.0048	9740	0.0346 ± 0.0003	0.3531 ± 0.0029
Online selection						
Trigger	27734	0.2807 ± 0.0014	0.2807 ± 0.0014	73094	0.2596 ± 0.0008	0.2596 ± 0.0008
Basic Reco level selections						
Good primary vertex	27734	0.2807 ± 0.0014	1.0000 ± 0.0000	73094	0.2596 ± 0.0008	1.0000 ± 0.0000
$p_{T_1} > 17$ GeV, $\lvert\eta_1\rvert < 0.9$	17089	0.1730 ± 0.0012	0.6162 ± 0.0029	45218	0.1606 ± 0.0007	0.6186 ± 0.0018
$p_{T_2} > 8$ GeV, $\lvert\eta_2\rvert < 2.4$	17050	0.1726 ± 0.0012	0.9977 ± 0.0004	44978	0.1597 ± 0.0007	0.9947 ± 0.0003
$p_{T_3} > 8$ GeV, $\lvert\eta_3\rvert < 2.4$	16035	0.1623 ± 0.0012	0.9405 ± 0.0018	40733	0.1446 ± 0.0007	0.9056 ± 0.0014
$p_{T_4} > 8$ GeV, $\lvert\eta_4\rvert < 2.4$	7366	0.0746 ± 0.0008	0.4594 ± 0.0039	17364	0.0617 ± 0.0005	0.4263 ± 0.0025
Extra Reco level selections						
Two muon-jets	6234	0.0631 ± 0.0008	0.8463 ± 0.0042	13931	0.0495 ± 0.0004	0.8023 ± 0.0030
Two dimuons	6232	0.0631 ± 0.0008	0.9997 ± 0.0002	13925	0.0494 ± 0.0004	0.9996 ± 0.0002
Pixel hit requirement	4875	0.0493 ± 0.0007	0.7823 ± 0.0052	7448	0.0264 ± 0.0003	0.5349 ± 0.0042
$\lvert z_{(\mu\mu)_1} - z_{(\mu\mu)_2}\rvert < 0.1$ cm	4816	0.0487 ± 0.0007	0.9879 ± 0.0016	7201	0.0256 ± 0.0003	0.9668 ± 0.0021
$\mathrm{Iso}_{(\mu\mu)_{1,2}} < 2$ GeV	3817	0.0386 ± 0.0006	0.7926 ± 0.0058	5726	0.0203 ± 0.0003	0.7952 ± 0.0048
$m_{(\mu\mu)_1} \approx m_{(\mu\mu)_2}$	3813	0.0386 ± 0.0006	0.9990 ± 0.0005	5718	0.0203 ± 0.0003	0.9986 ± 0.0005
α_{gen}			0.0646 ± 0.0008			0.0346 ± 0.0003
ϵ_{full}			0.0386 ± 0.0006			0.0203 ± 0.0003
$\epsilon_{\mathrm{full}}/\alpha_{\mathrm{gen}}$			0.5976 ± 0.0061			0.5871 ± 0.0050

Table G.7: Acceptances and efficiencies of the event selection for MSSMD benchmark models with $m_{\gamma_D} = 0.4$ GeV and $c\tau_{\gamma_D} = 2,\ 5$ mm.

Sample	$m_{\gamma_D} = 0.4$ GeV, $c\tau_{\gamma_D} = 2$ mm			$m_{\gamma_D} = 0.4$ GeV, $c\tau_{\gamma_D} = 5$ mm		
Selection	Events	Tot. Eff.	Rel. Eff.	Events	Tot. Eff.	Rel. Eff.
All events	296400	1.0000 ± 0.0000	1.0000 ± 0.0000	146200	1.0000 ± 0.0000	1.0000 ± 0.0000
Basic Gen level selections						
$p_{T_1} > 17$ GeV, $\lvert\eta_1\rvert < 0.9$	100134	0.3378 ± 0.0009	0.3378 ± 0.0009	49255	0.3369 ± 0.0012	0.3369 ± 0.0012
$p_{T_2} > 8$ GeV, $\lvert\eta_2\rvert < 2.4$	92034	0.3105 ± 0.0008	0.9191 ± 0.0009	45395	0.3105 ± 0.0012	0.9216 ± 0.0012
$p_{T_3} > 8$ GeV, $\lvert\eta_3\rvert < 2.4$	60730	0.2049 ± 0.0007	0.6599 ± 0.0016	30007	0.2052 ± 0.0011	0.6610 ± 0.0022
$p_{T_4} > 8$ GeV, $\lvert\eta_4\rvert < 2.4$	28891	0.0975 ± 0.0005	0.4757 ± 0.0020	14310	0.0979 ± 0.0008	0.4769 ± 0.0029
$L_{xy} < 9.8$ cm, $L_z < 46.5$ cm	3802	0.0128 ± 0.0002	0.1316 ± 0.0020	457	0.0031 ± 0.0001	0.0319 ± 0.0015
Online selection						
Trigger	64545	0.2178 ± 0.0008	0.2178 ± 0.0008	18968	0.1297 ± 0.0009	0.1297 ± 0.0009
Basic Reco level selections						
Good primary vertex	64545	0.2178 ± 0.0008	1.0000 ± 0.0000	18968	0.1297 ± 0.0009	1.0000 ± 0.0000
$p_{T_1} > 17$ GeV, $\lvert\eta_1\rvert < 0.9$	39109	0.1319 ± 0.0006	0.6059 ± 0.0019	10804	0.0739 ± 0.0007	0.5696 ± 0.0036
$p_{T_2} > 8$ GeV, $\lvert\eta_2\rvert < 2.4$	38657	0.1304 ± 0.0006	0.9884 ± 0.0005	10446	0.0715 ± 0.0007	0.9669 ± 0.0017
$p_{T_3} > 8$ GeV, $\lvert\eta_3\rvert < 2.4$	33080	0.1116 ± 0.0006	0.8557 ± 0.0018	8016	0.0548 ± 0.0006	0.7674 ± 0.0041
$p_{T_4} > 8$ GeV, $\lvert\eta_4\rvert < 2.4$	12541	0.0423 ± 0.0004	0.3791 ± 0.0027	2509	0.0172 ± 0.0003	0.3130 ± 0.0052
Extra Reco level selections						
Two muon-jets	9313	0.0314 ± 0.0003	0.7426 ± 0.0039	1725	0.0118 ± 0.0003	0.6875 ± 0.0093
Two dimuons	9310	0.0314 ± 0.0003	0.9997 ± 0.0002	1724	0.0118 ± 0.0003	0.9994 ± 0.0006
Pixel hit requirement	3041	0.0103 ± 0.0002	0.3266 ± 0.0049	401	0.0027 ± 0.0001	0.2326 ± 0.0102
$\lvert z_{(\mu\mu)_1} - z_{(\mu\mu)_2}\rvert < 0.1$ cm	2857	0.0096 ± 0.0002	0.9395 ± 0.0043	367	0.0025 ± 0.0001	0.9152 ± 0.0139
$\mathrm{Iso}_{(\mu\mu)_{1,2}} < 2$ GeV	2250	0.0076 ± 0.0002	0.7875 ± 0.0077	287	0.0020 ± 0.0001	0.7820 ± 0.0216
$m_{(\mu\mu)_1} \approx m_{(\mu\mu)_2}$	2245	0.0076 ± 0.0002	0.9978 ± 0.0010	285	0.0019 ± 0.0001	0.9930 ± 0.0049
α_{gen}			0.0128 ± 0.0002			0.0031 ± 0.0001
ϵ_{full}			0.0076 ± 0.0002			0.0019 ± 0.0001
$\epsilon_{\mathrm{full}}/\alpha_{\mathrm{gen}}$			0.5905 ± 0.0080			0.6236 ± 0.0227

Table G.8: Acceptances and efficiencies of the event selection for MSSMD benchmark models with $m_{\gamma_D} = 0.4$ GeV and $c\tau_{\gamma_D} = 20,\ 100$ mm.

Sample	$m_{\gamma_D} = 0.4$ GeV, $c\tau_{\gamma_D} = 20$ mm			$m_{\gamma_D} = 0.4$ GeV, $c\tau_{\gamma_D} = 100$ mm		
Selection	Events	Tot. Eff.	Rel. Eff.	Events	Tot. Eff.	Rel. Eff.
All events	581200	1.0000 ± 0.0000	1.0000 ± 0.0000	623400	1.0000 ± 0.0000	1.0000 ± 0.0000
Basic Gen level selections						
$p_{T_1} > 17$ GeV, $\lvert\eta_1\rvert < 0.9$	196990	0.3389 ± 0.0006	0.3389 ± 0.0006	210808	0.3382 ± 0.0006	0.3382 ± 0.0006
$p_{T_2} > 8$ GeV, $\lvert\eta_2\rvert < 2.4$	181018	0.3115 ± 0.0006	0.9189 ± 0.0006	193725	0.3108 ± 0.0006	0.9190 ± 0.0006
$p_{T_3} > 8$ GeV, $\lvert\eta_3\rvert < 2.4$	119508	0.2056 ± 0.0005	0.6602 ± 0.0011	127543	0.2046 ± 0.0005	0.6584 ± 0.0011
$p_{T_4} > 8$ GeV, $\lvert\eta_4\rvert < 2.4$	57076	0.0982 ± 0.0004	0.4776 ± 0.0014	60868	0.0976 ± 0.0004	0.4772 ± 0.0014
$L_{xy} < 9.8$ cm, $L_z < 46.5$ cm	133	0.0002 ± 0.0000	0.0023 ± 0.0002	4	0.0000 ± 0.0000	0.0001 ± 0.0000
Online selection						
Trigger	16344	0.0281 ± 0.0002	0.0281 ± 0.0002	1543	0.0025 ± 0.0001	0.0025 ± 0.0001
Basic Reco level selections						
Good primary vertex	16344	0.0281 ± 0.0002	1.0000 ± 0.0000	1543	0.0025 ± 0.0001	1.0000 ± 0.0000
$p_{T_1} > 17$ GeV, $\lvert\eta_1\rvert < 0.9$	8587	0.0148 ± 0.0002	0.5254 ± 0.0039	775	0.0012 ± 0.0000	0.5023 ± 0.0127
$p_{T_2} > 8$ GeV, $\lvert\eta_2\rvert < 2.4$	7930	0.0136 ± 0.0002	0.9235 ± 0.0029	668	0.0011 ± 0.0000	0.8619 ± 0.0124
$p_{T_3} > 8$ GeV, $\lvert\eta_3\rvert < 2.4$	4741	0.0082 ± 0.0001	0.5979 ± 0.0055	312	0.0005 ± 0.0000	0.4671 ± 0.0193
$p_{T_4} > 8$ GeV, $\lvert\eta_4\rvert < 2.4$	1259	0.0022 ± 0.0001	0.2656 ± 0.0064	55	0.0001 ± 0.0000	0.1763 ± 0.0216
Extra Reco level selections						
Two muon-jets	765	0.0013 ± 0.0000	0.6076 ± 0.0138	26	0.0000 ± 0.0000	0.4727 ± 0.0673
Two dimuons	765	0.0013 ± 0.0000	1.0000 ± 0.0000	26	0.0000 ± 0.0000	1.0000 ± 0.0000
Pixel hit requirement	112	0.0002 ± 0.0000	0.1464 ± 0.0128	1	0.0000 ± 0.0000	0.0385 ± 0.0377
$\lvert z_{(\mu\mu)_1} - z_{(\mu\mu)_2}\rvert < 0.1$ cm	96	0.0002 ± 0.0000	0.8571 ± 0.0331	1	0.0000 ± 0.0000	1.0000 ± 0.0000
$\mathrm{Iso}_{(\mu\mu)_{1,2}} < 2$ GeV	79	0.0001 ± 0.0000	0.8229 ± 0.0390	1	0.0000 ± 0.0000	1.0000 ± 0.0000
$m_{(\mu\mu)_1} \approx m_{(\mu\mu)_2}$	78	0.0001 ± 0.0000	0.9873 ± 0.0126	1	0.0000 ± 0.0000	1.0000 ± 0.0000
α_{gen}			0.0002 ± 0.0000			0.0000 ± 0.0000
ϵ_{full}			0.0001 ± 0.0000			0.0000 ± 0.0000
$\epsilon_{\mathrm{full}}/\alpha_{\mathrm{gen}}$			0.5865 ± 0.0427			0.2500 ± 0.2165

Table G.9: Acceptances and efficiencies of the event selection for MSSMD benchmark models with $m_{\gamma_{\mathrm{D}}} = 0.7$ GeV and $c\tau_{\gamma_{\mathrm{D}}} = 0,\ 0.05$ mm.

Sample	$m_{\gamma_D} = 0.7$ GeV, $c\tau_{\gamma_D} = 0$ mm			$m_{\gamma_D} = 0.7$ GeV, $c\tau_{\gamma_D} = 0.5$ mm		
Selection	Events	Tot. Eff.	Rel. Eff.	Events	Tot. Eff.	Rel. Eff.
All events	76800	1.0000 ± 0.0000	1.0000 ± 0.0000	19400	1.0000 ± 0.0000	1.0000 ± 0.0000
Basic Gen level selections						
$p_{\mathrm{T}_1} > 17$ GeV, $\lvert\eta_1\rvert < 0.9$	26147	0.3405 ± 0.0017	0.3405 ± 0.0017	6648	0.3427 ± 0.0034	0.3427 ± 0.0034
$p_{\mathrm{T}_2} > 8$ GeV, $\lvert\eta_2\rvert < 2.4$	23820	0.3102 ± 0.0017	0.9110 ± 0.0018	6064	0.3126 ± 0.0033	0.9122 ± 0.0035
$p_{\mathrm{T}_3} > 8$ GeV, $\lvert\eta_3\rvert < 2.4$	15760	0.2052 ± 0.0015	0.6616 ± 0.0031	4009	0.2066 ± 0.0029	0.6611 ± 0.0061
$p_{\mathrm{T}_4} > 8$ GeV, $\lvert\eta_4\rvert < 2.4$	7131	0.0929 ± 0.0010	0.4525 ± 0.0040	1804	0.0930 ± 0.0021	0.4500 ± 0.0079
$L_{xy} < 9.8$ cm, $L_z < 46.5$ cm	7131	0.0929 ± 0.0010	1.0000 ± 0.0000	1582	0.0815 ± 0.0020	0.8769 ± 0.0077
Online selection						
Trigger	23336	0.3039 ± 0.0017	0.3039 ± 0.0017	5671	0.2923 ± 0.0033	0.2923 ± 0.0033
Basic Reco level selections						
Good primary vertex	23336	0.3039 ± 0.0017	1.0000 ± 0.0000	5671	0.2923 ± 0.0033	1.0000 ± 0.0000
$p_{\mathrm{T}_1} > 17$ GeV, $\lvert\eta_1\rvert < 0.9$	14430	0.1879 ± 0.0014	0.6184 ± 0.0032	3528	0.1819 ± 0.0028	0.6221 ± 0.0064
$p_{\mathrm{T}_2} > 8$ GeV, $\lvert\eta_2\rvert < 2.4$	14421	0.1878 ± 0.0014	0.9994 ± 0.0002	3521	0.1815 ± 0.0028	0.9980 ± 0.0007
$p_{\mathrm{T}_3} > 8$ GeV, $\lvert\eta_3\rvert < 2.4$	13989	0.1821 ± 0.0014	0.9700 ± 0.0014	3358	0.1731 ± 0.0027	0.9537 ± 0.0035
$p_{\mathrm{T}_4} > 8$ GeV, $\lvert\eta_4\rvert < 2.4$	6656	0.0867 ± 0.0010	0.4758 ± 0.0042	1556	0.0802 ± 0.0020	0.4634 ± 0.0086
Extra Reco level selections						
Two muon-jets	5877	0.0765 ± 0.0010	0.8830 ± 0.0039	1371	0.0707 ± 0.0018	0.8811 ± 0.0082
Two dimuons	5876	0.0765 ± 0.0010	0.9998 ± 0.0002	1370	0.0706 ± 0.0018	0.9993 ± 0.0007
Pixel hit requirement	5872	0.0765 ± 0.0010	0.9993 ± 0.0003	1253	0.0646 ± 0.0018	0.9146 ± 0.0076
$\lvert z_{(\mu\mu)_1} - z_{(\mu\mu)_2}\rvert < 0.1$ cm	5861	0.0763 ± 0.0010	0.9981 ± 0.0006	1247	0.0643 ± 0.0018	0.9952 ± 0.0020
$\mathrm{Iso}_{(\mu\mu)_{1,2}} < 2$ GeV	4669	0.0608 ± 0.0009	0.7966 ± 0.0053	969	0.0499 ± 0.0016	0.7771 ± 0.0118
$m_{(\mu\mu)_1} \approx m_{(\mu\mu)_2}$	4643	0.0605 ± 0.0009	0.9944 ± 0.0011	959	0.0494 ± 0.0016	0.9897 ± 0.0032
α_{gen}			0.0929 ± 0.0010			0.0815 ± 0.0020
ϵ_{full}			0.0605 ± 0.0009			0.0494 ± 0.0016
$\epsilon_{\mathrm{full}}/\alpha_{\mathrm{gen}}$			0.6511 ± 0.0056			0.6062 ± 0.0123

Table G.10: Acceptances and efficiencies of the event selection for MSSMD benchmark models with $m_{\gamma_D} = 0.7$ GeV and $c\tau_{\gamma_D} = 1,\ 20$ mm.

Sample	$m_{\gamma_D} = 0.7$ GeV, $c\tau_{\gamma_D} = 1$ mm			$m_{\gamma_D} = 0.7$ GeV, $c\tau_{\gamma_D} = 20$ mm		
Selection	Events	Tot. Eff.	Rel. Eff.	Events	Tot. Eff.	Rel. Eff.
All events	144000	1.0000 ± 0.0000	1.0000 ± 0.0000	677400	1.0000 ± 0.0000	1.0000 ± 0.0000
Basic Gen level selections						
$p_{T_1} > 17$ GeV, $\lvert\eta_1\rvert < 0.9$	48722	0.3383 ± 0.0012	0.3383 ± 0.0012	231533	0.3418 ± 0.0006	0.3418 ± 0.0006
$p_{T_2} > 8$ GeV, $\lvert\eta_2\rvert < 2.4$	44342	0.3079 ± 0.0012	0.9101 ± 0.0013	210649	0.3110 ± 0.0006	0.9098 ± 0.0006
$p_{T_3} > 8$ GeV, $\lvert\eta_3\rvert < 2.4$	29159	0.2025 ± 0.0011	0.6576 ± 0.0023	138098	0.2039 ± 0.0005	0.6556 ± 0.0010
$p_{T_4} > 8$ GeV, $\lvert\eta_4\rvert < 2.4$	13175	0.0915 ± 0.0008	0.4518 ± 0.0029	62408	0.0921 ± 0.0004	0.4519 ± 0.0013
$L_{xy} < 9.8$ cm, $L_z < 46.5$ cm	7989	0.0555 ± 0.0006	0.6064 ± 0.0043	370	0.0005 ± 0.0000	0.0059 ± 0.0003
Online selection						
Trigger	39015	0.2709 ± 0.0012	0.2709 ± 0.0012	37356	0.0551 ± 0.0003	0.0551 ± 0.0003
Basic Reco level selections						
Good primary vertex	39015	0.2709 ± 0.0012	1.0000 ± 0.0000	37356	0.0551 ± 0.0003	1.0000 ± 0.0000
$p_{T_1} > 17$ GeV, $\lvert\eta_1\rvert < 0.9$	24114	0.1675 ± 0.0010	0.6181 ± 0.0025	20766	0.0307 ± 0.0002	0.5559 ± 0.0026
$p_{T_2} > 8$ GeV, $\lvert\eta_2\rvert < 2.4$	24050	0.1670 ± 0.0010	0.9973 ± 0.0003	19641	0.0290 ± 0.0002	0.9458 ± 0.0016
$p_{T_3} > 8$ GeV, $\lvert\eta_3\rvert < 2.4$	22437	0.1558 ± 0.0010	0.9329 ± 0.0016	13288	0.0196 ± 0.0002	0.6765 ± 0.0033
$p_{T_4} > 8$ GeV, $\lvert\eta_4\rvert < 2.4$	9843	0.0684 ± 0.0007	0.4387 ± 0.0033	3625	0.0054 ± 0.0001	0.2728 ± 0.0039
Extra Reco level selections						
Two muon-jets	8296	0.0576 ± 0.0006	0.8428 ± 0.0037	2406	0.0036 ± 0.0001	0.6637 ± 0.0078
Two dimuons	8291	0.0576 ± 0.0006	0.9994 ± 0.0003	2404	0.0035 ± 0.0001	0.9992 ± 0.0006
Pixel hit requirement	6071	0.0422 ± 0.0005	0.7322 ± 0.0049	346	0.0005 ± 0.0000	0.1439 ± 0.0072
$\lvert z_{(\mu\mu)_1} - z_{(\mu\mu)_2}\rvert < 0.1$ cm	6001	0.0417 ± 0.0005	0.9885 ± 0.0014	294	0.0004 ± 0.0000	0.8497 ± 0.0192
$\mathrm{Iso}_{(\mu\mu)_{1,2}} < 2$ GeV	4757	0.0330 ± 0.0005	0.7927 ± 0.0052	235	0.0003 ± 0.0000	0.7993 ± 0.0234
$m_{(\mu\mu)_1} \approx m_{(\mu\mu)_2}$	4729	0.0328 ± 0.0005	0.9941 ± 0.0011	234	0.0003 ± 0.0000	0.9957 ± 0.0042
α_{gen}			0.0555 ± 0.0006			0.0005 ± 0.0000
ϵ_{full}			0.0328 ± 0.0005			0.0003 ± 0.0000
$\epsilon_{\mathrm{full}}/\alpha_{\mathrm{gen}}$			0.5919 ± 0.0055			0.6324 ± 0.0251

Table G.11: Acceptances and efficiencies of the event selection for MSSMD benchmark models with $m_{\gamma_D} = 0.7$ GeV, $c\tau_{\gamma_D} = 100$ mm and $m_{\gamma_D} = 1$ GeV, $c\tau_{\gamma_D} = 0$ mm.

Sample	$m_{\gamma_D} = 0.7$ GeV, $c\tau_{\gamma_D} = 100$ mm			$m_{\gamma_D} = 1$ GeV, $c\tau_{\gamma_D} = 0$ mm		
Selection	Events	Tot. Eff.	Rel. Eff.	Events	Tot. Eff.	Rel. Eff.
All events	231100	1.0000 ± 0.0000	1.0000 ± 0.0000	77999	1.0000 ± 0.0000	1.0000 ± 0.0000
Basic Gen level selections						
$p_{T_1} > 17$ GeV, $\lvert\eta_1\rvert < 0.9$	78603	0.3401 ± 0.0010	0.3401 ± 0.0010	26774	0.3433 ± 0.0017	0.3433 ± 0.0017
$p_{T_2} > 8$ GeV, $\lvert\eta_2\rvert < 2.4$	71546	0.3096 ± 0.0010	0.9102 ± 0.0010	24398	0.3128 ± 0.0017	0.9113 ± 0.0017
$p_{T_3} > 8$ GeV, $\lvert\eta_3\rvert < 2.4$	46981	0.2033 ± 0.0008	0.6567 ± 0.0018	16187	0.2075 ± 0.0015	0.6635 ± 0.0030
$p_{T_4} > 8$ GeV, $\lvert\eta_4\rvert < 2.4$	21031	0.0910 ± 0.0006	0.4476 ± 0.0023	7110	0.0912 ± 0.0010	0.4392 ± 0.0039
$L_{xy} < 9.8$ cm, $L_z < 46.5$ cm	12	0.0001 ± 0.0000	0.0006 ± 0.0002	7110	0.0912 ± 0.0010	1.0000 ± 0.0000
Online selection						
Trigger	1363	0.0059 ± 0.0002	0.0059 ± 0.0002	23874	0.3061 ± 0.0017	0.3061 ± 0.0017
Basic Reco level selections						
Good primary vertex	1363	0.0059 ± 0.0002	1.0000 ± 0.0000	23874	0.3061 ± 0.0017	1.0000 ± 0.0000
$p_{T_1} > 17$ GeV, $\lvert\eta_1\rvert < 0.9$	708	0.0031 ± 0.0001	0.5194 ± 0.0135	14771	0.1894 ± 0.0014	0.6187 ± 0.0031
$p_{T_2} > 8$ GeV, $\lvert\eta_2\rvert < 2.4$	631	0.0027 ± 0.0001	0.8912 ± 0.0117	14763	0.1893 ± 0.0014	0.9995 ± 0.0002
$p_{T_3} > 8$ GeV, $\lvert\eta_3\rvert < 2.4$	304	0.0013 ± 0.0001	0.4818 ± 0.0199	14308	0.1834 ± 0.0014	0.9692 ± 0.0014
$p_{T_4} > 8$ GeV, $\lvert\eta_4\rvert < 2.4$	73	0.0003 ± 0.0000	0.2401 ± 0.0245	6678	0.0856 ± 0.0010	0.4667 ± 0.0042
Extra Reco level selections						
Two muon-jets	46	0.0002 ± 0.0000	0.6301 ± 0.0565	5877	0.0753 ± 0.0009	0.8801 ± 0.0040
Two dimuons	46	0.0002 ± 0.0000	1.0000 ± 0.0000	5872	0.0753 ± 0.0009	0.9991 ± 0.0004
Pixel hit requirement	6	0.0000 ± 0.0000	0.1304 ± 0.0497	5870	0.0753 ± 0.0009	0.9997 ± 0.0002
$\lvert z_{(\mu\mu)_1} - z_{(\mu\mu)_2}\rvert < 0.1$ cm	6	0.0000 ± 0.0000	1.0000 ± 0.0000	5864	0.0752 ± 0.0009	0.9990 ± 0.0004
$\mathrm{Iso}_{(\mu\mu)_{1,2}} < 2$ GeV	6	0.0000 ± 0.0000	1.0000 ± 0.0000	4626	0.0593 ± 0.0008	0.7889 ± 0.0053
$m_{(\mu\mu)_1} \approx m_{(\mu\mu)_2}$	6	0.0000 ± 0.0000	1.0000 ± 0.0000	4582	0.0587 ± 0.0008	0.9905 ± 0.0014
α_{gen}			0.0001 ± 0.0000			0.0912 ± 0.0010
ϵ_{full}			0.0000 ± 0.0000			0.0587 ± 0.0008
$\epsilon_{\mathrm{full}}/\alpha_{\mathrm{gen}}$			0.5000 ± 0.1443			0.6444 ± 0.0057

Table G.12: Acceptances and efficiencies of the event selection for MSSMD benchmark models with $m_{\gamma_D} = 1$ GeV and $c\tau_{\gamma_D} = 5, 20$ mm.

Sample	$m_{\gamma_D} = 1$ GeV, $c\tau_{\gamma_D} = 5$ mm			$m_{\gamma_D} = 1$ GeV, $c\tau_{\gamma_D} = 20$ mm		
Selection	Events	Tot. Eff.	Rel. Eff.	Events	Tot. Eff.	Rel. Eff.
All events	170200	1.0000 ± 0.0000	1.0000 ± 0.0000	303300	1.0000 ± 0.0000	1.0000 ± 0.0000
Basic Gen level selections						
$p_{T_1} > 17$ GeV, $\lvert\eta_1\rvert < 0.9$	58196	0.3419 ± 0.0011	0.3419 ± 0.0011	104206	0.3436 ± 0.0009	0.3436 ± 0.0009
$p_{T_2} > 8$ GeV, $\lvert\eta_2\rvert < 2.4$	52792	0.3102 ± 0.0011	0.9071 ± 0.0012	94863	0.3128 ± 0.0008	0.9103 ± 0.0009
$p_{T_3} > 8$ GeV, $\lvert\eta_3\rvert < 2.4$	34733	0.2041 ± 0.0010	0.6579 ± 0.0021	62487	0.2060 ± 0.0007	0.6587 ± 0.0015
$p_{T_4} > 8$ GeV, $\lvert\eta_4\rvert < 2.4$	15199	0.0893 ± 0.0007	0.4376 ± 0.0027	27422	0.0904 ± 0.0005	0.4388 ± 0.0020
$L_{xy} < 9.8$ cm, $L_z < 46.5$ cm	2125	0.0125 ± 0.0003	0.1398 ± 0.0028	360	0.0012 ± 0.0001	0.0131 ± 0.0007
Online selection						
Trigger	36654	0.2154 ± 0.0010	0.2154 ± 0.0010	24914	0.0821 ± 0.0005	0.0821 ± 0.0005
Basic Reco level selections						
Good primary vertex	36653	0.2154 ± 0.0010	1.0000 ± 0.0000	24914	0.0821 ± 0.0005	1.0000 ± 0.0000
$p_{T_1} > 17$ GeV, $\lvert\eta_1\rvert < 0.9$	22724	0.1335 ± 0.0008	0.6200 ± 0.0025	14414	0.0475 ± 0.0004	0.5786 ± 0.0031
$p_{T_2} > 8$ GeV, $\lvert\eta_2\rvert < 2.4$	22490	0.1321 ± 0.0008	0.9897 ± 0.0007	13850	0.0457 ± 0.0004	0.9609 ± 0.0016
$p_{T_3} > 8$ GeV, $\lvert\eta_3\rvert < 2.4$	19587	0.1151 ± 0.0008	0.8709 ± 0.0022	10146	0.0335 ± 0.0003	0.7326 ± 0.0038
$p_{T_4} > 8$ GeV, $\lvert\eta_4\rvert < 2.4$	7445	0.0437 ± 0.0005	0.3801 ± 0.0035	3082	0.0102 ± 0.0002	0.3038 ± 0.0046
Extra Reco level selections						
Two muon-jets	5773	0.0339 ± 0.0004	0.7754 ± 0.0048	2152	0.0071 ± 0.0002	0.6982 ± 0.0083
Two dimuons	5766	0.0339 ± 0.0004	0.9988 ± 0.0005	2152	0.0071 ± 0.0002	1.0000 ± 0.0000
Pixel hit requirement	1817	0.0107 ± 0.0002	0.3151 ± 0.0061	347	0.0011 ± 0.0001	0.1612 ± 0.0079
$\lvert z_{(\mu\mu)_1} - z_{(\mu\mu)_2}\rvert < 0.1$ cm	1701	0.0100 ± 0.0002	0.9362 ± 0.0057	299	0.0010 ± 0.0001	0.8617 ± 0.0185
$\text{Iso}_{(\mu\mu)_{1,2}} < 2$ GeV	1350	0.0079 ± 0.0002	0.7937 ± 0.0098	238	0.0008 ± 0.0001	0.7960 ± 0.0233
$m_{(\mu\mu)_1} \approx m_{(\mu\mu)_2}$	1333	0.0078 ± 0.0002	0.9874 ± 0.0030	237	0.0008 ± 0.0001	0.9958 ± 0.0042
α_{gen}			0.0125 ± 0.0003			0.0012 ± 0.0001
ϵ_{full}			0.0078 ± 0.0002			0.0008 ± 0.0001
$\epsilon_{\text{full}}/\alpha_{\text{gen}}$			0.6273 ± 0.0105			0.6583 ± 0.0250

Table G.13: Acceptances and efficiencies of the event selection for MSSMD benchmark models with $m_{\gamma_D} = 1$ GeV, $c\tau_{\gamma_D} = 100$ mm and $m_{\gamma_D} = 5$ GeV, $c\tau_{\gamma_D} = 0$ mm

Sample	$m_{\gamma_D} = 1$ GeV, $c\tau_{\gamma_D} = 100$ mm			$m_{\gamma_D} = 5$ GeV, $c\tau_{\gamma_D} = 0$ mm		
Selection	Events	Tot. Eff.	Rel. Eff.	Events	Tot. Eff.	Rel. Eff.
All events	115400	1.0000 ± 0.0000	1.0000 ± 0.0000	79400	1.0000 ± 0.0000	1.0000 ± 0.0000
Basic Gen level selections						
$p_{T_1} > 17$ GeV, $\lvert\eta_1\rvert < 0.9$	39995	0.3466 ± 0.0014	0.3466 ± 0.0014	35254	0.4440 ± 0.0018	0.4440 ± 0.0018
$p_{T_2} > 8$ GeV, $\lvert\eta_2\rvert < 2.4$	36407	0.3155 ± 0.0014	0.9103 ± 0.0014	33472	0.4216 ± 0.0018	0.9495 ± 0.0012
$p_{T_3} > 8$ GeV, $\lvert\eta_3\rvert < 2.4$	23838	0.2066 ± 0.0012	0.6548 ± 0.0025	24446	0.3079 ± 0.0016	0.7303 ± 0.0024
$p_{T_4} > 8$ GeV, $\lvert\eta_4\rvert < 2.4$	10489	0.0909 ± 0.0008	0.4400 ± 0.0032	8302	0.1046 ± 0.0011	0.3396 ± 0.0030
$L_{xy} < 9.8$ cm, $L_z < 46.5$ cm	5	0.0000 ± 0.0000	0.0005 ± 0.0002	8302	0.1046 ± 0.0011	1.0000 ± 0.0000
Online selection						
Trigger	1124	0.0097 ± 0.0003	0.0097 ± 0.0003	33147	0.4175 ± 0.0018	0.4175 ± 0.0018
Basic Reco level selections						
Good primary vertex	1124	0.0097 ± 0.0003	1.0000 ± 0.0000	33147	0.4175 ± 0.0018	1.0000 ± 0.0000
$p_{T_1} > 17$ GeV, $\lvert\eta_1\rvert < 0.9$	615	0.0053 ± 0.0002	0.5472 ± 0.0148	21397	0.2695 ± 0.0016	0.6455 ± 0.0026
$p_{T_2} > 8$ GeV, $\lvert\eta_2\rvert < 2.4$	562	0.0049 ± 0.0002	0.9138 ± 0.0113	21390	0.2694 ± 0.0016	0.9997 ± 0.0001
$p_{T_3} > 8$ GeV, $\lvert\eta_3\rvert < 2.4$	296	0.0026 ± 0.0001	0.5267 ± 0.0211	20855	0.2627 ± 0.0016	0.9750 ± 0.0011
$p_{T_4} > 8$ GeV, $\lvert\eta_4\rvert < 2.4$	61	0.0005 ± 0.0001	0.2061 ± 0.0235	7851	0.0989 ± 0.0011	0.3765 ± 0.0034
Extra Reco level selections						
Two muon-jets	38	0.0003 ± 0.0001	0.6230 ± 0.0621	6906	0.0870 ± 0.0010	0.8796 ± 0.0037
Two dimuons	38	0.0003 ± 0.0001	1.0000 ± 0.0000	6902	0.0869 ± 0.0010	0.9994 ± 0.0003
Pixel hit requirement	4	0.0000 ± 0.0000	0.1053 ± 0.0498	6901	0.0869 ± 0.0010	0.9999 ± 0.0001
$\lvert z_{(\mu\mu)_1} - z_{(\mu\mu)_2}\rvert < 0.1$ cm	4	0.0000 ± 0.0000	1.0000 ± 0.0000	6898	0.0869 ± 0.0010	0.9996 ± 0.0003
$\text{Iso}_{(\mu\mu)_{1,2}} < 2$ GeV	1	0.0000 ± 0.0000	0.2500 ± 0.2165	5476	0.0690 ± 0.0009	0.7939 ± 0.0049
$m_{(\mu\mu)_1} \approx m_{(\mu\mu)_2}$	1	0.0000 ± 0.0000	1.0000 ± 0.0000	5220	0.0657 ± 0.0009	0.9533 ± 0.0029
α_{gen}			0.0000 ± 0.0000			0.1046 ± 0.0011
ϵ_{full}			0.0000 ± 0.0000			0.0657 ± 0.0009
$\epsilon_{\text{full}}/\alpha_{\text{gen}}$			0.2000 ± 0.1789			0.6288 ± 0.0053

Table G.14: Acceptances and efficiencies of the event selection for MSSMD benchmark models with $m_{\gamma_D} = 5$ GeV and $c\tau_{\gamma_D} = 20,\ 100$ mm.

Sample	$m_{\gamma_D} = 5$ GeV, $c\tau_{\gamma_D} = 20$ mm			$m_{\gamma_D} = 5$ GeV, $c\tau_{\gamma_D} = 100$ mm		
Selection	Events	Tot. Eff.	Rel. Eff.	Events	Tot. Eff.	Rel. Eff.
All events	78300	1.0000 ± 0.0000	1.0000 ± 0.0000	227600	1.0000 ± 0.0000	1.0000 ± 0.0000
Basic Gen level selections						
$p_{T_1} > 17$ GeV, $\lvert\eta_1\rvert < 0.9$	34982	0.4468 ± 0.0018	0.4468 ± 0.0018	101990	0.4481 ± 0.0010	0.4481 ± 0.0010
$p_{T_2} > 8$ GeV, $\lvert\eta_2\rvert < 2.4$	33192	0.4239 ± 0.0018	0.9488 ± 0.0012	96799	0.4253 ± 0.0010	0.9491 ± 0.0007
$p_{T_3} > 8$ GeV, $\lvert\eta_3\rvert < 2.4$	23953	0.3059 ± 0.0016	0.7216 ± 0.0025	70180	0.3083 ± 0.0010	0.7250 ± 0.0014
$p_{T_4} > 8$ GeV, $\lvert\eta_4\rvert < 2.4$	7946	0.1015 ± 0.0011	0.3317 ± 0.0030	23802	0.1046 ± 0.0006	0.3392 ± 0.0018
$L_{xy} < 9.8$ cm, $L_z < 46.5$ cm	1456	0.0186 ± 0.0005	0.1832 ± 0.0043	256	0.0011 ± 0.0001	0.0108 ± 0.0007
Online selection						
Trigger	21111	0.2696 ± 0.0016	0.2696 ± 0.0016	16336	0.0718 ± 0.0005	0.0718 ± 0.0005
Basic Reco level selections						
Good primary vertex	21111	0.2696 ± 0.0016	1.0000 ± 0.0000	16336	0.0718 ± 0.0005	1.0000 ± 0.0000
$p_{T_1} > 17$ GeV, $\lvert\eta_1\rvert < 0.9$	13837	0.1767 ± 0.0014	0.6554 ± 0.0033	10185	0.0447 ± 0.0004	0.6235 ± 0.0038
$p_{T_2} > 8$ GeV, $\lvert\eta_2\rvert < 2.4$	13739	0.1755 ± 0.0014	0.9929 ± 0.0007	9901	0.0435 ± 0.0004	0.9721 ± 0.0016
$p_{T_3} > 8$ GeV, $\lvert\eta_3\rvert < 2.4$	12276	0.1568 ± 0.0013	0.8935 ± 0.0026	7436	0.0327 ± 0.0004	0.7510 ± 0.0043
$p_{T_4} > 8$ GeV, $\lvert\eta_4\rvert < 2.4$	3985	0.0509 ± 0.0008	0.3246 ± 0.0042	1936	0.0085 ± 0.0002	0.2604 ± 0.0051
Extra Reco level selections						
Two muon-jets	3097	0.0396 ± 0.0007	0.7772 ± 0.0066	1380	0.0061 ± 0.0002	0.7128 ± 0.0103
Two dimuons	3093	0.0395 ± 0.0007	0.9987 ± 0.0006	1380	0.0061 ± 0.0002	1.0000 ± 0.0000
Pixel hit requirement	1185	0.0151 ± 0.0004	0.3831 ± 0.0087	253	0.0011 ± 0.0001	0.1833 ± 0.0104
$\lvert z_{(\mu\mu)_1} - z_{(\mu\mu)_2}\rvert < 0.1$ cm	1116	0.0143 ± 0.0004	0.9418 ± 0.0068	221	0.0010 ± 0.0001	0.8735 ± 0.0209
$\mathrm{Iso}_{(\mu\mu)_{1,2}} < 2$ GeV	870	0.0111 ± 0.0004	0.7796 ± 0.0124	178	0.0008 ± 0.0001	0.8054 ± 0.0266
$m_{(\mu\mu)_1} \approx m_{(\mu\mu)_2}$	843	0.0108 ± 0.0004	0.9690 ± 0.0059	172	0.0008 ± 0.0001	0.9663 ± 0.0135
α_{gen}			0.0186 ± 0.0005			0.0011 ± 0.0001
ϵ_{full}			0.0108 ± 0.0004			0.0008 ± 0.0001
$\epsilon_{\mathrm{full}}/\alpha_{\mathrm{gen}}$			0.5790 ± 0.0129			0.6719 ± 0.0293

Table G.15: Acceptances and efficiencies of the event selection for MSSMD benchmark models with $m_{\gamma_D} = 8.5$ GeV and $c\tau_{\gamma_D} = 0,\ 2$ mm.

Sample	$m_{\gamma_D} = 8.5$ GeV, $c\tau_{\gamma_D} = 0$ mm			$m_{\gamma_D} = 8.5$ GeV, $c\tau_{\gamma_D} = 2$ mm		
Selection	Events	Tot. Eff.	Rel. Eff.	Events	Tot. Eff.	Rel. Eff.
All events	79099	1.0000 ± 0.0000	1.0000 ± 0.0000	276700	1.0000 ± 0.0000	1.0000 ± 0.0000
Basic Gen level selections						
$p_{T_1} > 17$ GeV, $\lvert\eta_1\rvert < 0.9$	44037	0.5567 ± 0.0018	0.5567 ± 0.0018	153847	0.5560 ± 0.0009	0.5560 ± 0.0009
$p_{T_2} > 8$ GeV, $\lvert\eta_2\rvert < 2.4$	42211	0.5336 ± 0.0018	0.9585 ± 0.0010	147153	0.5318 ± 0.0009	0.9565 ± 0.0005
$p_{T_3} > 8$ GeV, $\lvert\eta_3\rvert < 2.4$	35071	0.4434 ± 0.0018	0.8308 ± 0.0018	122355	0.4422 ± 0.0009	0.8315 ± 0.0010
$p_{T_4} > 8$ GeV, $\lvert\eta_4\rvert < 2.4$	16205	0.2049 ± 0.0014	0.4621 ± 0.0027	56138	0.2029 ± 0.0008	0.4588 ± 0.0014
$L_{xy} < 9.8$ cm, $L_z < 46.5$ cm	16205	0.2049 ± 0.0014	1.0000 ± 0.0000	55479	0.2005 ± 0.0008	0.9883 ± 0.0005
Online selection						
Trigger	45282	0.5725 ± 0.0018	0.5725 ± 0.0018	153549	0.5549 ± 0.0009	0.5549 ± 0.0009
Basic Reco level selections						
Good primary vertex	45282	0.5725 ± 0.0018	1.0000 ± 0.0000	153549	0.5549 ± 0.0009	1.0000 ± 0.0000
$p_{T_1} > 17$ GeV, $\lvert\eta_1\rvert < 0.9$	32152	0.4065 ± 0.0017	0.7100 ± 0.0021	109385	0.3953 ± 0.0009	0.7124 ± 0.0012
$p_{T_2} > 8$ GeV, $\lvert\eta_2\rvert < 2.4$	32144	0.4064 ± 0.0017	0.9998 ± 0.0001	109365	0.3952 ± 0.0009	0.9998 ± 0.0000
$p_{T_3} > 8$ GeV, $\lvert\eta_3\rvert < 2.4$	31723	0.4011 ± 0.0017	0.9869 ± 0.0006	107415	0.3882 ± 0.0009	0.9822 ± 0.0004
$p_{T_4} > 8$ GeV, $\lvert\eta_4\rvert < 2.4$	15651	0.1979 ± 0.0014	0.4934 ± 0.0028	52836	0.1910 ± 0.0007	0.4919 ± 0.0015
Extra Reco level selections						
Two muon-jets	13716	0.1734 ± 0.0013	0.8764 ± 0.0026	46186	0.1669 ± 0.0007	0.8741 ± 0.0014
Two dimuons	13700	0.1732 ± 0.0013	0.9988 ± 0.0003	46149	0.1668 ± 0.0007	0.9992 ± 0.0001
Pixel hit requirement	13700	0.1732 ± 0.0013	1.0000 ± 0.0000	45812	0.1656 ± 0.0007	0.9927 ± 0.0004
$\lvert z_{(\mu\mu)_1} - z_{(\mu\mu)_2}\rvert < 0.1$ cm	13695	0.1731 ± 0.0013	0.9996 ± 0.0002	45500	0.1644 ± 0.0007	0.9932 ± 0.0004
$\text{Iso}_{(\mu\mu)_{1,2}} < 2$ GeV	10750	0.1359 ± 0.0012	0.7850 ± 0.0035	36011	0.1301 ± 0.0006	0.7915 ± 0.0019
$m_{(\mu\mu)_1} \approx m_{(\mu\mu)_2}$	10105	0.1278 ± 0.0012	0.9400 ± 0.0023	33898	0.1225 ± 0.0006	0.9413 ± 0.0012
α_{gen}			0.2049 ± 0.0014			0.2005 ± 0.0008
ϵ_{full}			0.1278 ± 0.0012			0.1225 ± 0.0006
$\epsilon_{\text{full}}/\alpha_{\text{gen}}$			0.6236 ± 0.0038			0.6110 ± 0.0021

Table G.16: Acceptances and efficiencies of the event selection for MSSMD benchmark models with $m_{\gamma_D} = 8.5$ GeV and $c\tau_{\gamma_D} = 20,\ 100$ mm.

Sample	$m_{\gamma_D} = 8.5$ GeV, $c\tau_{\gamma_D} = 20$ mm			$m_{\gamma_D} = 8.5$ GeV, $c\tau_{\gamma_D} = 100$ mm		
Selection	Events	Tot. Eff.	Rel. Eff.	Events	Tot. Eff.	Rel. Eff.
All events	708100	1.0000 ± 0.0000	1.0000 ± 0.0000	918100	1.0000 ± 0.0000	1.0000 ± 0.0000
Basic Gen level selections						
$p_{T_1} > 17$ GeV, $\lvert\eta_1\rvert < 0.9$	394162	0.5566 ± 0.0006	0.5566 ± 0.0006	510675	0.5562 ± 0.0005	0.5562 ± 0.0005
$p_{T_2} > 8$ GeV, $\lvert\eta_2\rvert < 2.4$	377302	0.5328 ± 0.0006	0.9572 ± 0.0003	488761	0.5324 ± 0.0005	0.9571 ± 0.0003
$p_{T_3} > 8$ GeV, $\lvert\eta_3\rvert < 2.4$	313365	0.4425 ± 0.0006	0.8305 ± 0.0006	406687	0.4430 ± 0.0005	0.8321 ± 0.0005
$p_{T_4} > 8$ GeV, $\lvert\eta_4\rvert < 2.4$	144443	0.2040 ± 0.0005	0.4609 ± 0.0009	187200	0.2039 ± 0.0004	0.4603 ± 0.0008
$L_{xy} < 9.8$ cm, $L_z < 46.5$ cm	43590	0.0616 ± 0.0003	0.3018 ± 0.0012	4346	0.0047 ± 0.0001	0.0232 ± 0.0003
Online selection						
Trigger	291037	0.4110 ± 0.0006	0.4110 ± 0.0006	115795	0.1261 ± 0.0003	0.1261 ± 0.0003
Basic Reco level selections						
Good primary vertex	291037	0.4110 ± 0.0006	1.0000 ± 0.0000	115795	0.1261 ± 0.0003	1.0000 ± 0.0000
$p_{T_1} > 17$ GeV, $\lvert\eta_1\rvert < 0.9$	211189	0.2982 ± 0.0005	0.7256 ± 0.0008	82097	0.0894 ± 0.0003	0.7090 ± 0.0013
$p_{T_2} > 8$ GeV, $\lvert\eta_2\rvert < 2.4$	210375	0.2971 ± 0.0005	0.9961 ± 0.0001	80317	0.0875 ± 0.0003	0.9783 ± 0.0005
$p_{T_3} > 8$ GeV, $\lvert\eta_3\rvert < 2.4$	195018	0.2754 ± 0.0005	0.9270 ± 0.0006	63149	0.0688 ± 0.0003	0.7862 ± 0.0014
$p_{T_4} > 8$ GeV, $\lvert\eta_4\rvert < 2.4$	86419	0.1220 ± 0.0004	0.4431 ± 0.0011	22792	0.0248 ± 0.0002	0.3609 ± 0.0019
Extra Reco level selections						
Two muon-jets	67898	0.0959 ± 0.0003	0.7857 ± 0.0014	15009	0.0163 ± 0.0001	0.6585 ± 0.0031
Two dimuons	67859	0.0958 ± 0.0003	0.9994 ± 0.0001	15002	0.0163 ± 0.0001	0.9995 ± 0.0002
Pixel hit requirement	35593	0.0503 ± 0.0003	0.5245 ± 0.0019	3760	0.0041 ± 0.0001	0.2506 ± 0.0035
$\lvert z_{(\mu\mu)_1} - z_{(\mu\mu)_2}\rvert < 0.1$ cm	33385	0.0471 ± 0.0003	0.9380 ± 0.0013	3321	0.0036 ± 0.0001	0.8832 ± 0.0052
$\mathrm{Iso}_{(\mu\mu)_{1,2}} < 2$ GeV	26708	0.0377 ± 0.0002	0.8000 ± 0.0022	2669	0.0029 ± 0.0001	0.8037 ± 0.0069
$m_{(\mu\mu)_1} \approx m_{(\mu\mu)_2}$	25586	0.0361 ± 0.0002	0.9580 ± 0.0012	2575	0.0028 ± 0.0001	0.9648 ± 0.0036
α_{gen}			0.0616 ± 0.0003			0.0047 ± 0.0001
ϵ_{full}			0.0361 ± 0.0002			0.0028 ± 0.0001
$\epsilon_{\mathrm{full}}/\alpha_{\mathrm{gen}}$			0.5870 ± 0.0024			0.5925 ± 0.0075

APPENDIX H

EXTRA TRIGGER SCALE FACTOR PLOTS

H.1 Data vs Monte Carlo Comparisons

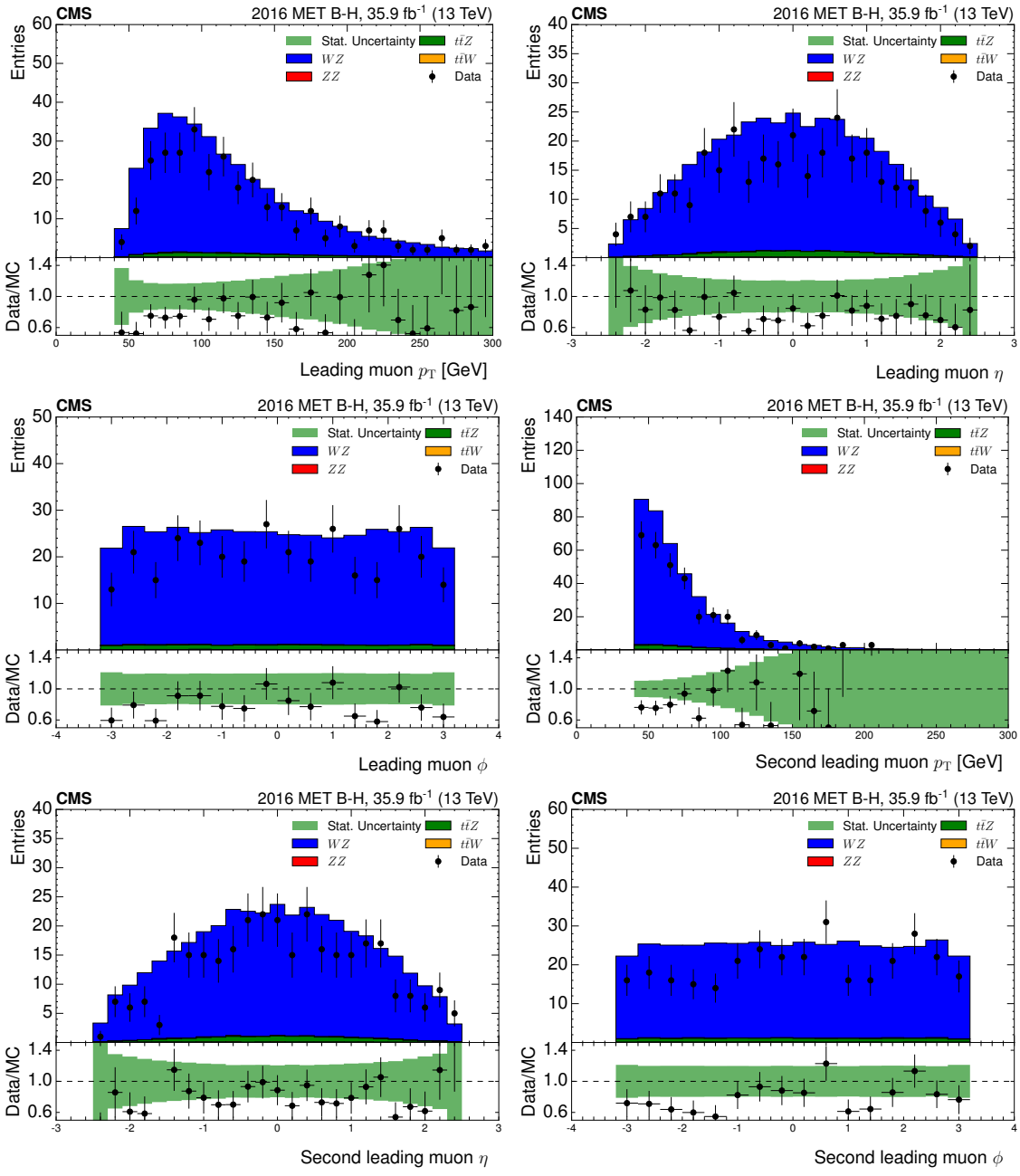

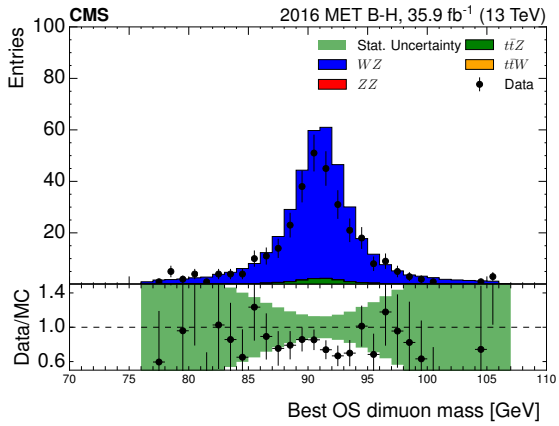
CMS
2016 MET B-H, 35.9 fb-1 (13 TeV)
Entries
Stat. Uncertainty
tt̄Z
WZ
tt̄W
ZZ
Data
Data/MC
Best OS dimuon mass [GeV]

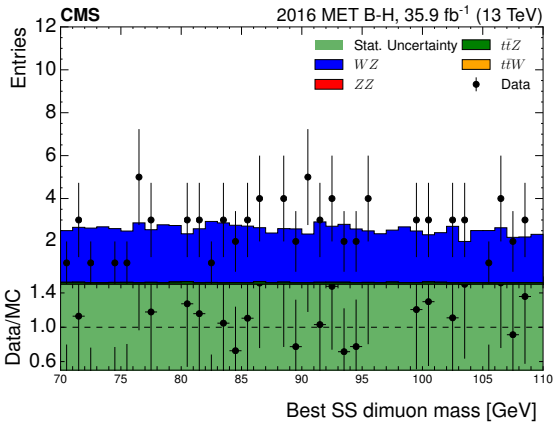
CMS
2016 MET B-H, 35.9 fb-1 (13 TeV)
Entries
Stat. Uncertainty
tt̄Z
WZ
tt̄W
ZZ
Data
Data/MC
Best SS dimuon mass [GeV]

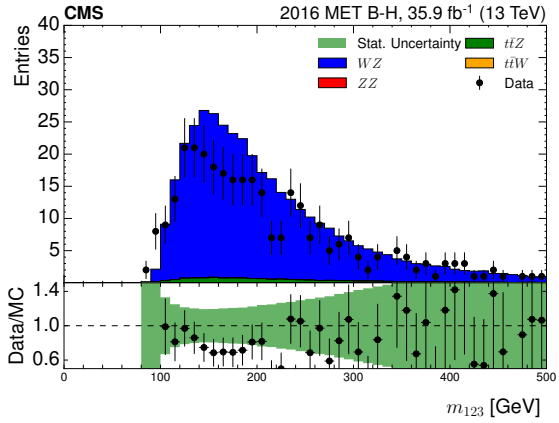
CMS
2016 MET B-H, 35.9 fb-1 (13 TeV)
Entries
Stat. Uncertainty
tt̄Z
WZ
tt̄W
ZZ
Data
Data/MC
m123 [GeV]

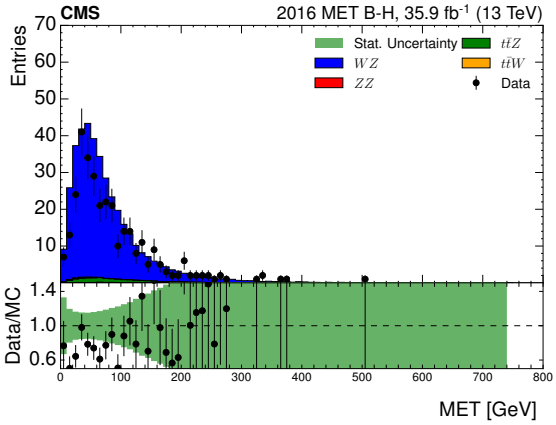
CMS
2016 MET B-H, 35.9 fb-1 (13 TeV)
Entries
Stat. Uncertainty
tt̄Z
WZ
tt̄W
ZZ
Data
Data/MC
MET [GeV]

H.2 Trigger Efficiencies

H.2.1 $pp \to WZ$

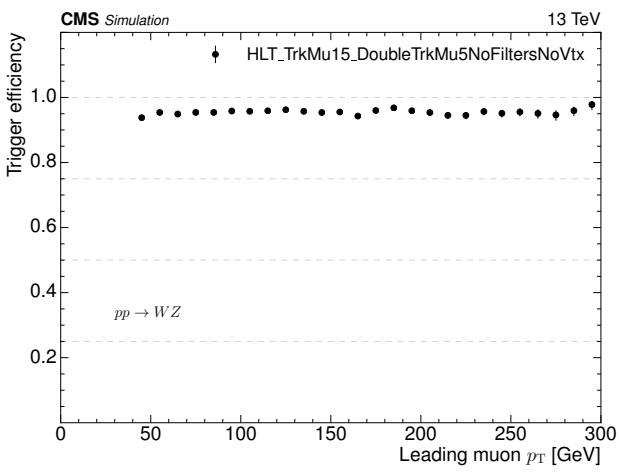

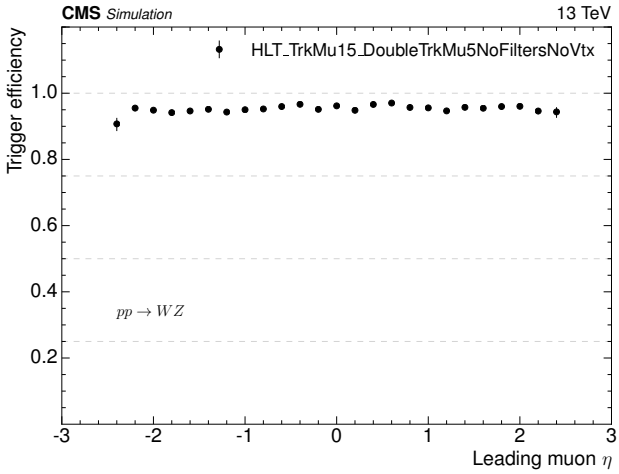

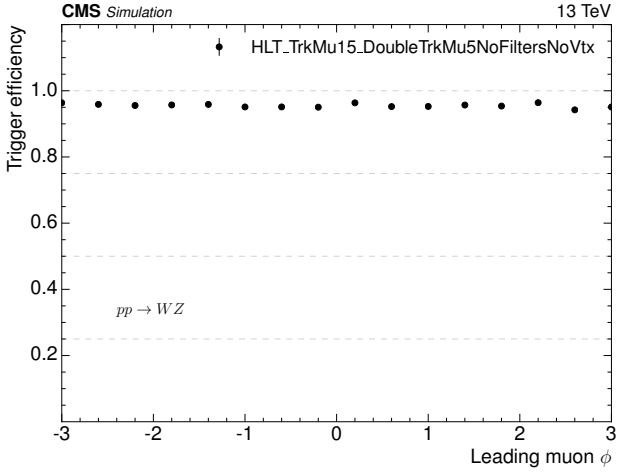

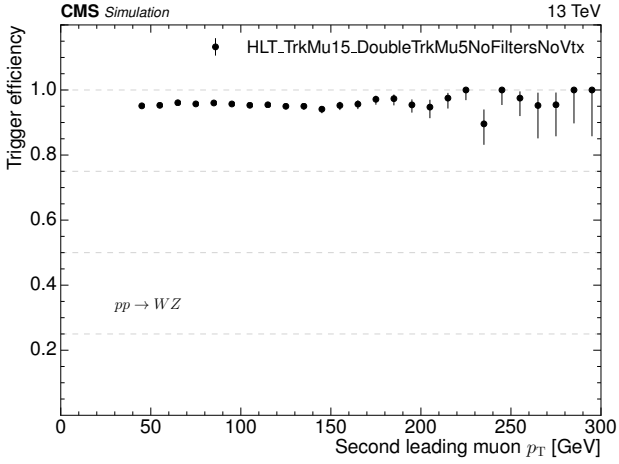

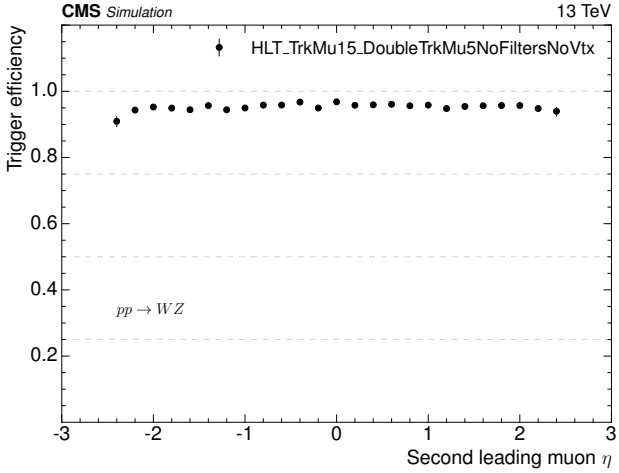

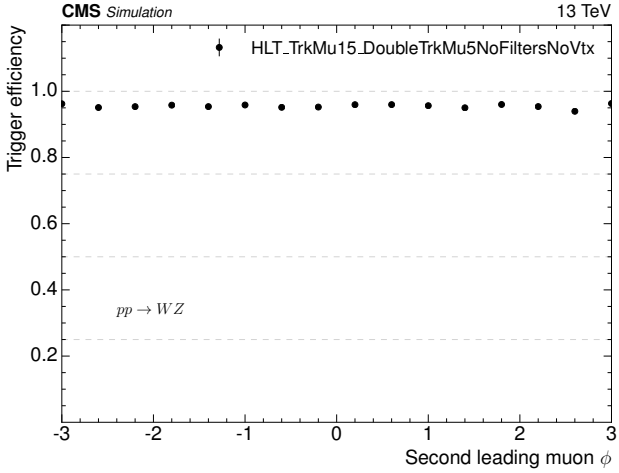

H.2.2 $pp \to ZZ$

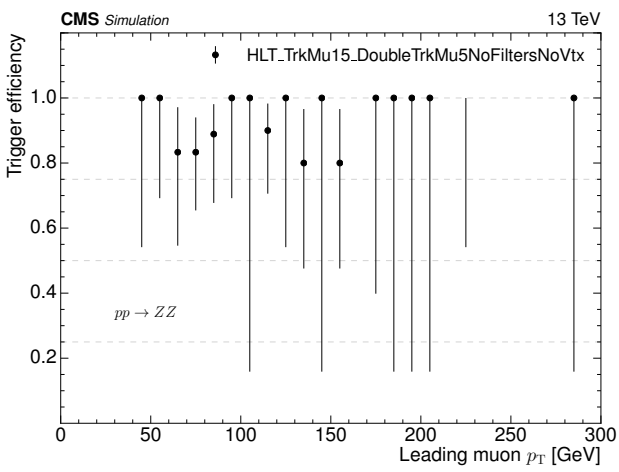
CMS Simulation
13 TeV
HLT_TrkMu15_DoubleTrkMu5NoFiltersNoVtx
Trigger efficiency
$pp \to ZZ$
Leading muon p_T [GeV]

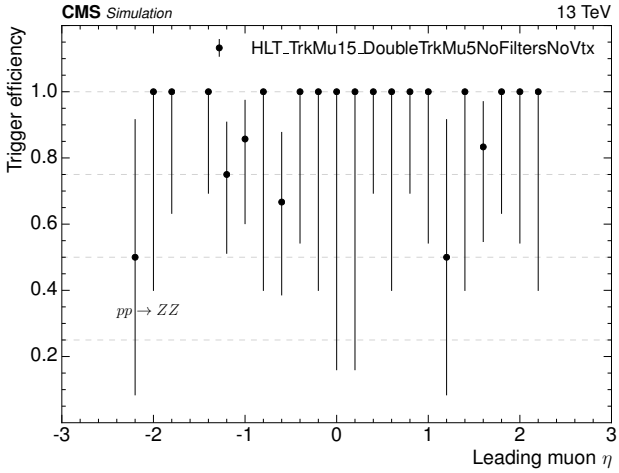
CMS Simulation
13 TeV
HLT_TrkMu15_DoubleTrkMu5NoFiltersNoVtx
Trigger efficiency
$pp \to ZZ$
Leading muon η

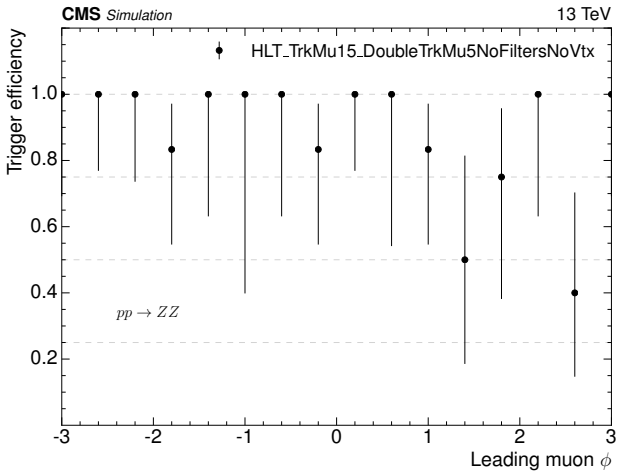
CMS Simulation
13 TeV
HLT_TrkMu15_DoubleTrkMu5NoFiltersNoVtx
Trigger efficiency
$pp \to ZZ$
Leading muon ϕ

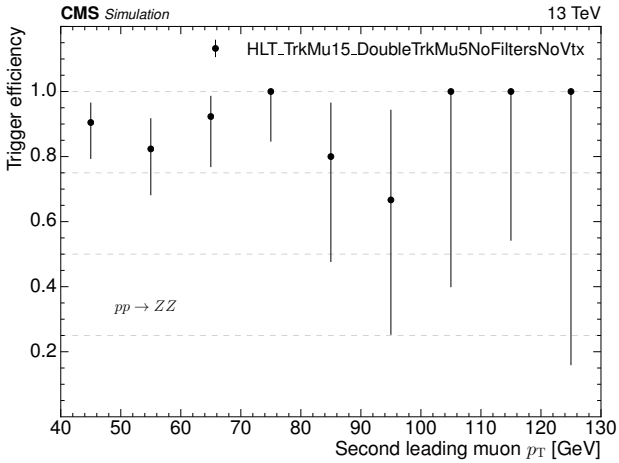
CMS Simulation
13 TeV
HLT_TrkMu15_DoubleTrkMu5NoFiltersNoVtx
Trigger efficiency
$pp \to ZZ$
Second leading muon p_T [GeV]

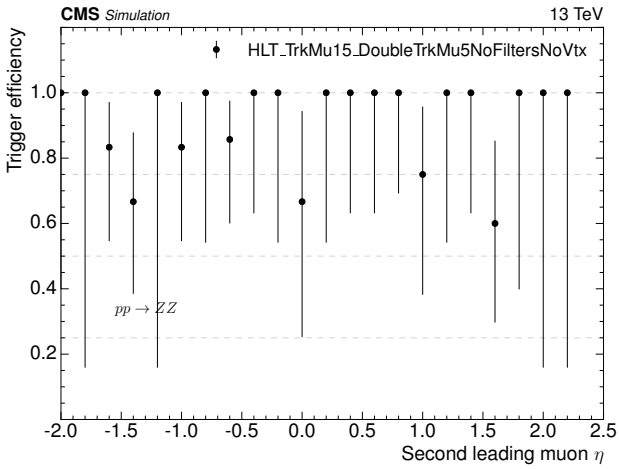
CMS Simulation
13 TeV
HLT_TrkMu15_DoubleTrkMu5NoFiltersNoVtx
Trigger efficiency
$pp \to ZZ$
Second leading muon η

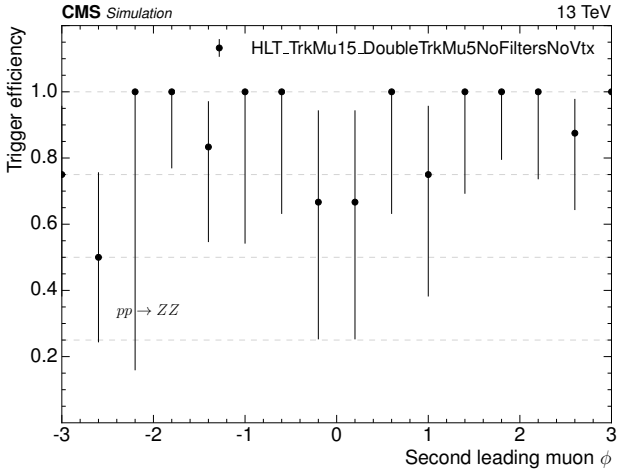
CMS Simulation
13 TeV
HLT_TrkMu15_DoubleTrkMu5NoFiltersNoVtx
Trigger efficiency
$pp \to ZZ$
Second leading muon ϕ

H.2.3 $pp \to t\bar{t}W$

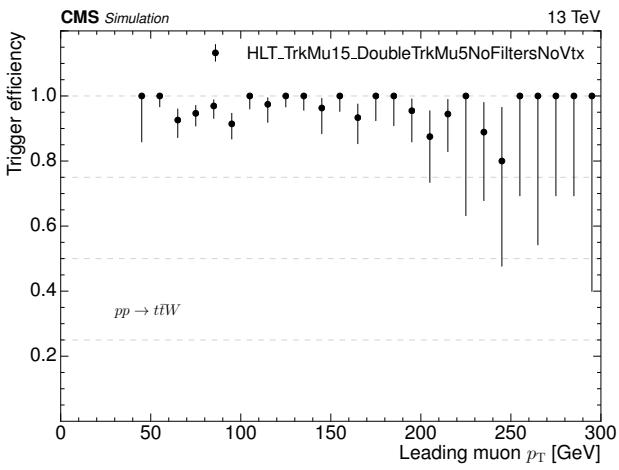

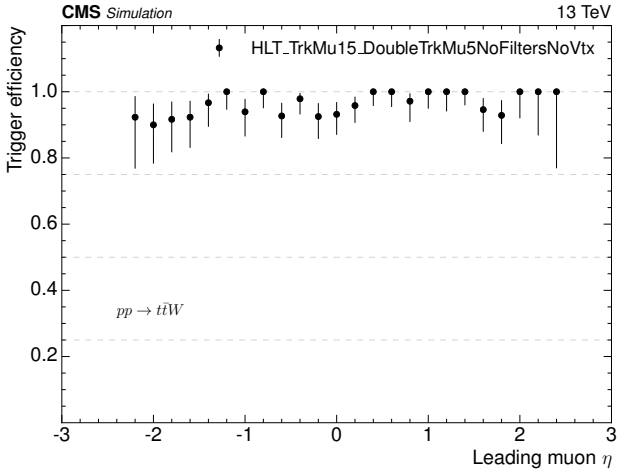

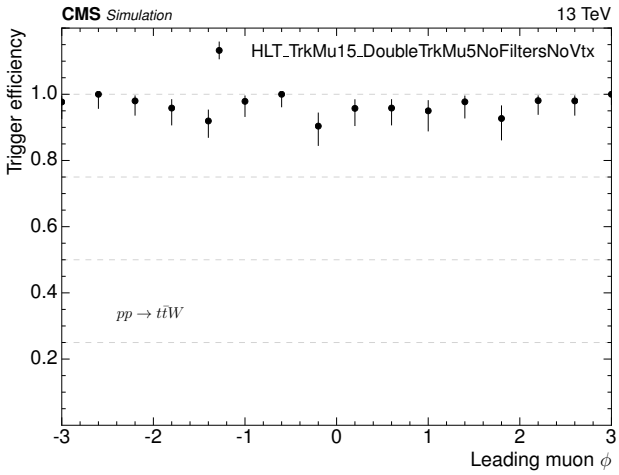

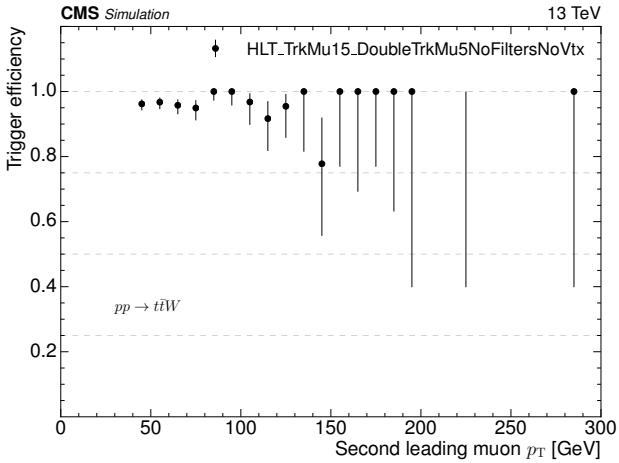

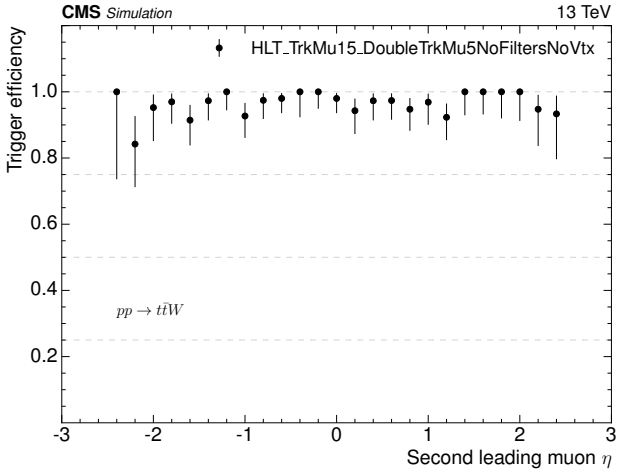

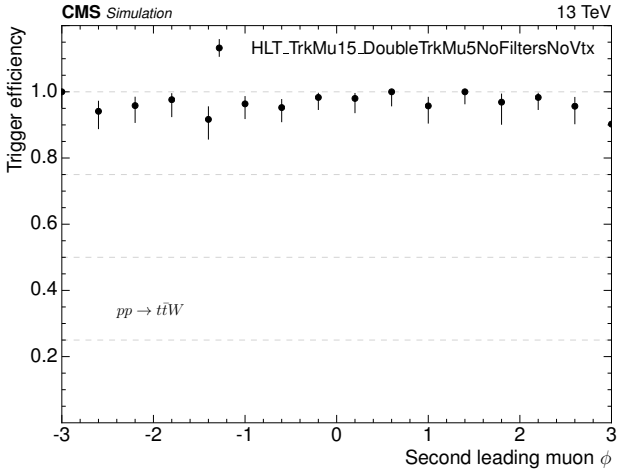

H.2.4 $pp \to t\bar{t}Z$

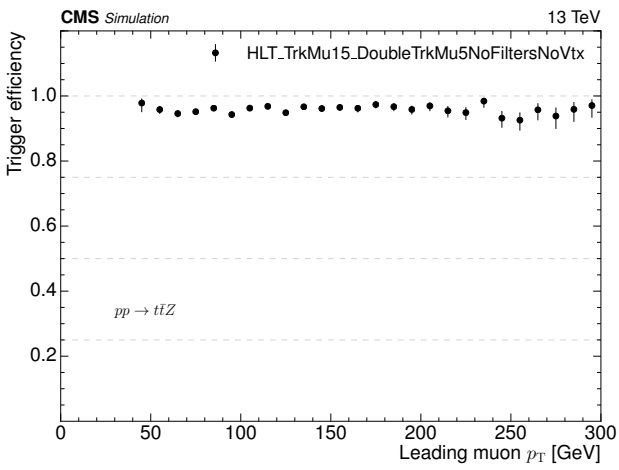

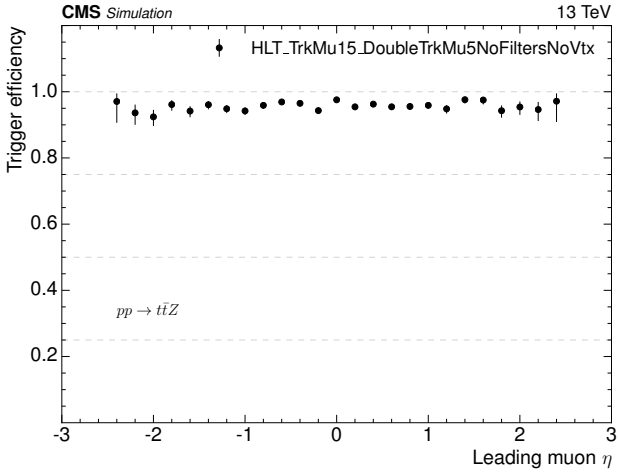

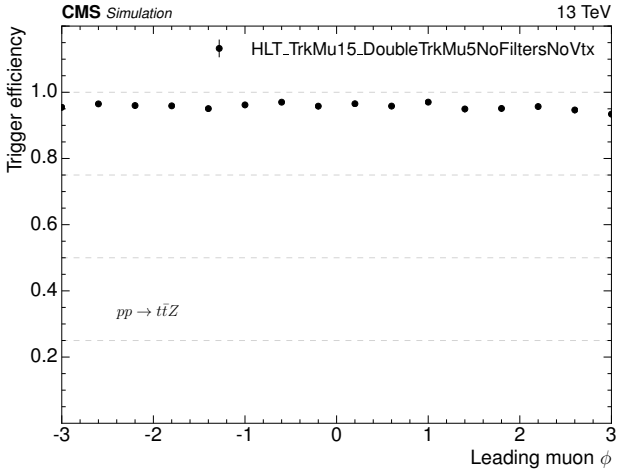

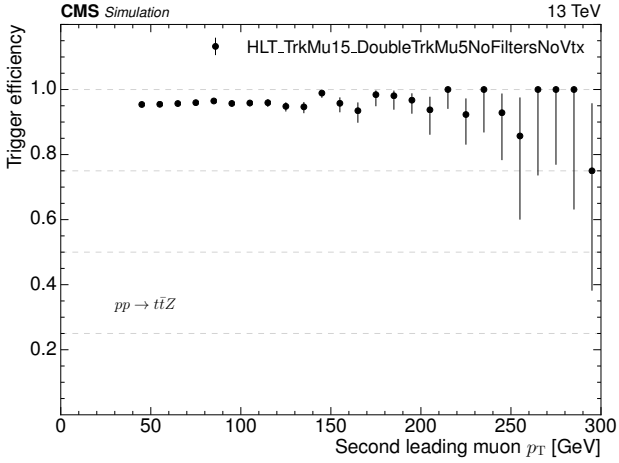

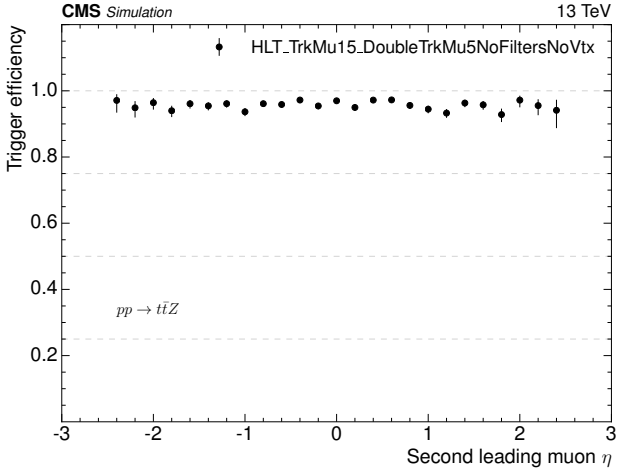

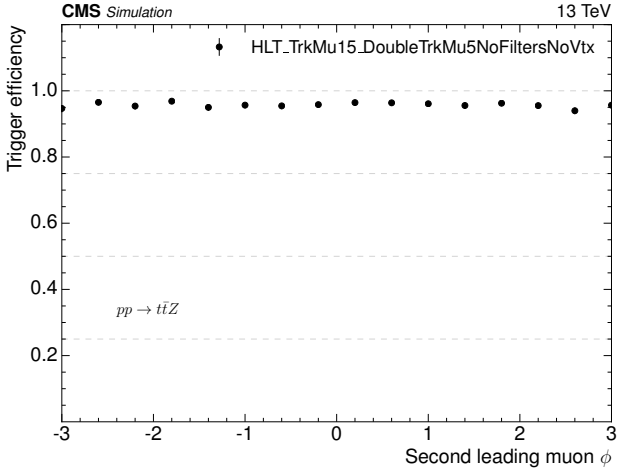

H.2.5 Data

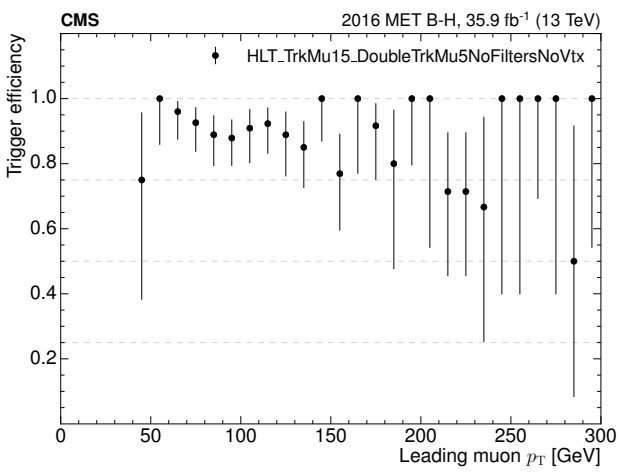
CMS
2016 MET B-H, 35.9 fb-1 (13 TeV)
HLT_TrkMu15_DoubleTrkMu5NoFiltersNoVtx
Trigger efficiency
Leading muon p_T [GeV]

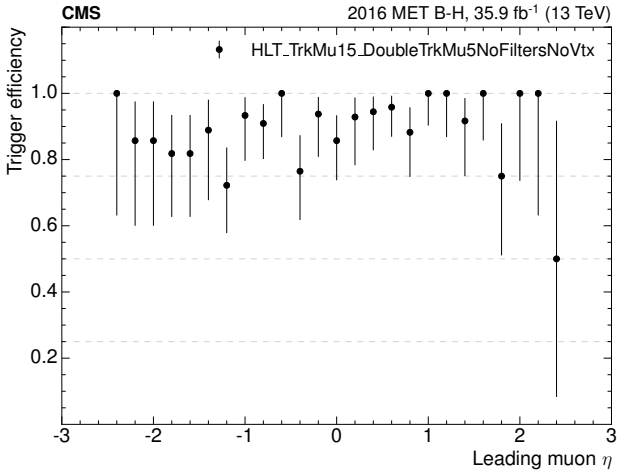
CMS
2016 MET B-H, 35.9 fb-1 (13 TeV)
HLT_TrkMu15_DoubleTrkMu5NoFiltersNoVtx
Trigger efficiency
Leading muon η

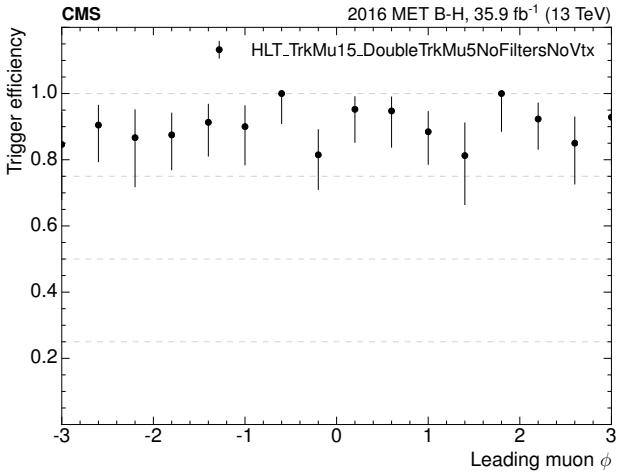
CMS
2016 MET B-H, 35.9 fb-1 (13 TeV)
HLT_TrkMu15_DoubleTrkMu5NoFiltersNoVtx
Trigger efficiency
Leading muon ϕ

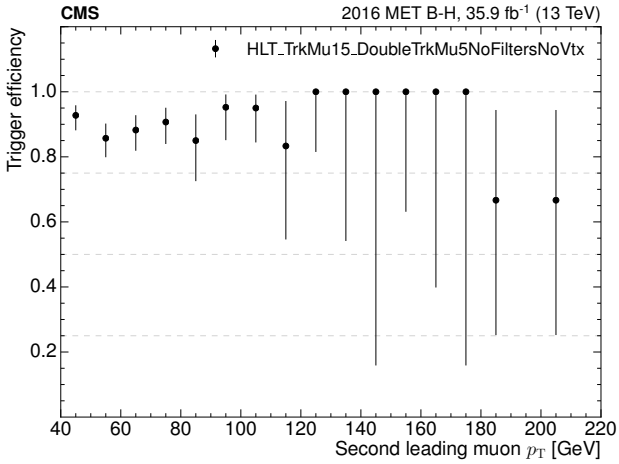
CMS
2016 MET B-H, 35.9 fb-1 (13 TeV)
HLT_TrkMu15_DoubleTrkMu5NoFiltersNoVtx
Trigger efficiency
Second leading muon p_T [GeV]

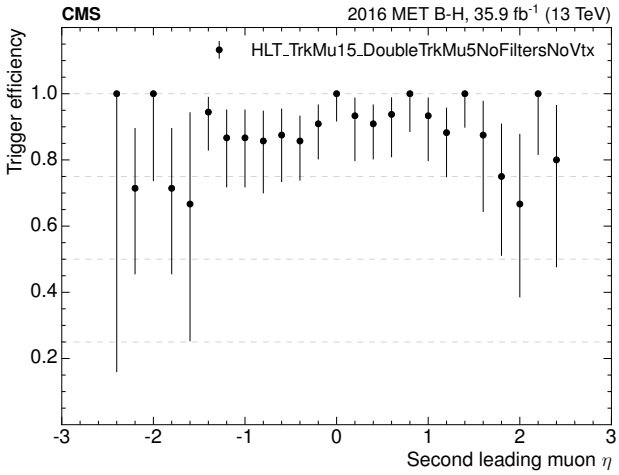
CMS
2016 MET B-H, 35.9 fb-1 (13 TeV)
HLT_TrkMu15_DoubleTrkMu5NoFiltersNoVtx
Trigger efficiency
Second leading muon η

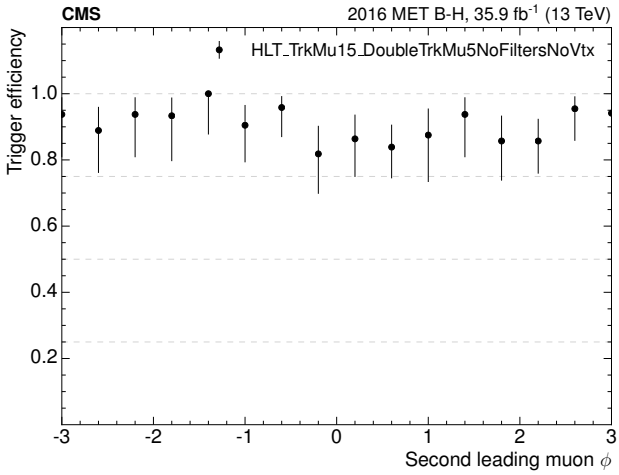
CMS
2016 MET B-H, 35.9 fb-1 (13 TeV)
HLT_TrkMu15_DoubleTrkMu5NoFiltersNoVtx
Trigger efficiency
Second leading muon ϕ